AASERT under Grant F49620-95-1-0386
NOAA under Grant #NA37RJ0202-ITEM14
AFOSR under Grant #F49620-95-1-0132
DOE/ARM under Grant #DE-FG03-95ER61958

THE EFFECTS OF RADIATIVE AND MICROPHYSICAL PROCESSES ON SIMULATED WARM AND TRANSITION SEASON ARCTIC STRATUS

by Jerry Youngblood Harrington

William R. Cotton, P.I.

Colorado State University

DEPARTMENT OF ATMOSPHERIC SCIENCE

PAPER NO. 637

THE EFFECTS OF RADIATIVE AND MICROPHYSICAL PROCESSES ON SIMULATED WARM AND TRANSITION SEASON ARCTIC STRATUS

by

Jerry Youngblood Harrington

Department of Atmospheric Science

Colorado State University

Fort Collins, CO 80523

Augmentation Awards for Science and Engineering Research Training

under Contract F49620-95-1-0386

NOAA/FAA

under contract #NA37RJ0202-ITEM14

AFOSR

under grant #F49620-95-1-0132

DOE-ARM

under grant #DE-FG03-95ER61958

October 17, 1997

Atmospheric Science Paper No. 637

ABSTRACT

THE EFFECTS OF RADIATIVE AND MICROPHYSICAL PROCESSES ON SIMULATED WARM AND TRANSITION SEASON ARCTIC STRATUS

A cloud-resolving model (CRM) version of RAMS, coupled to explicit bin resolving microphysics and a new two-stream radiative transfer code is used to study various aspects of Arctic stratus clouds (ASC). The two-stream radiative transfer model is coupled in a consistent fashion to the bulk microphysical parameterization of Walko *et al.* (1995), an explicit liquid bin microphysical model (*e.g.* Feingold *et al.* 1996a) and a mixed-phase microphysical model (Reisin *et al.* , 1996). These models are used to study both warm (summer) season and transition (fall and spring) season ASC. Equations are developed for the inclusion of the radiative term in the drop growth equation and the effect is studied in a trajectory parcel model (TPM) and the CRM.

Arctic stratus simulated with the new CRM framework compared well with the observations of Curry (1986). Along with CCN concentrations, it is shown that drop distribution shape and optical property methods strongly impact cloud evolution through their effect on the radiative properties. Broader cloud top distributions lead to clouds with more shallow depths and circulation strengths as more shortwave radiation is absorbed while the opposite occurs for narrow distribution functions. Radiative-cloud interactions using mean effective radii are shown to be problematic, while conserving r_e and N of the distribution function (as per Hu and Stamnes, 1993) produces similar cloud evolution as compared to detailed computations. Radiative effects on drop vapor deopsition growth can produce drizzle about 30 minutes earlier and is strongly dependent upon cloud top residence time of the parcels. The same set of trajectories assists drizzle production in the radiation and no-radiation cases. Not only is the growth of larger drops enhanced by the radiative effect, but drops

with $r < 10\mu m$ are caused to evaporate; the effects together constitute a method of spectral broadening at cloud top. Simulations with the CRM show a smaller impact of the radiative influence; this is attributed to the spurious production of cloud top supersaturations by Eulerian models (Stevens *et al.* , 1996a).

Simulations of transition season ASC shows that boundary layer stability is strongly dependent upon ice processes, illustrating that the rapid reduction in fall stratus cloud cover may be forced, in part, by microphysical processes. Cloud stability is shown to be strongly dependent upon the cloud temperature, ice concentration, precipitation rate and the indirect effects of ice crystals on cloud top radiative cooling while ice aggregation has a weak effect. Transitions from predominately mixed to stable boundary layers occur and are a function of ice sublimation and precipitation; ice habit strongly constrains the effect. Frequently observed autumnal stable layers may be formed in this fashion. A new method of multiple cloud layer formation is discussed and occurs through the rapid loss of ice from the upper cloud layer, which moistens and cools (sublimation and radiation) the lower layers causing droplet activation.

Jerry Youngblood Harrington
Department of Atmospheric Science
Colorado State University
Fort Collins, Colorado 80523
Fall 1997

ACKNOWLEDGEMENTS

It would be difficult to overstate the importance of the various people with whom I have worked, associated with, and become friends with throughout the coarse of my research career at CSU. First and foremost, my advisor Bill Cotton has been an unwavering source of support, scientific ideas, and friendly discourse throughout my six years under his tutelage. He has been kind enough to let me wander in my own directions (which must required some bravery!), suggesting courses of action when necessary. More than an advisor, Bill has been a good friend both in and outside of the department. My committee members, Sonia Kreidenweis, David Krueger and Graeme Stephens must also be thanked for undertaking the enormous task of reviewing this dissertation and serving as committee members. I have had the joy of working closely with both Graeme and Sonia over the years which has been to my intellectual benefit.

Collaborative works with Graham Feingold, Tamir Reisin, and Peter Q. Olsson have been not only fruitful, but extremely enjoyable. Peter, Graham and Tamir have been an enormous source of ideas, conversation and friendship. Working with Graham over the past year has benefited me more than I can possibly express. Members of the Cotton and Pielke groups must be thanked for both technical and emotional support (which is more important than many people realize). Bob Walko, not only for his all around RAMS knowledge, has been a large source of support particularly when my code development was giving me headaches. Members of the Stephens' group, Philip Gabriel, Paul Stackhouse and Tim Schneider are warmly thanked for the collaborative research we've done. Hans Verlinde (Penn State) and Piotr Flatau (Scripps) are thanked for help with some of the initial development stages of the radiative transfer model. Bjorn Stevens is thanked for his assistance with the RAMS code. Tom Chase is thanked for his assistance in coupling the radiation model to the RAMS surface model. To all those brave enough to use the new

radiation code and run to me with problems, I am indebted. Discussions of Arctic stratus (liquid and mixed-phase) with Andreas Reuter were most enligthening. Many LaTeX and postscript problems were solved through communications with Brenda Thompson, Ligia Bernardet and Tom Chase. The poster presentation skills of Debra Youngblood Harrington were called upon frequently and her help was very much appreciated.

My office mates Tom Chase, Cathy Finley and Mark Sellers are thanked for insightful discussions on many relevant topics (including MRHLF). Brian Gaudet, Andrew Heidinger, Ligia Bernardet, Tara Jensen, Louie Grasso, Gordon Beck, Brenda Thompson, Abby Hodges, Chris Clarke and all those I have so carelessly forgotten are thanked most warmly for their support and camaraderie.

My family, with their unconditional love and support, have been one of the strong points of my success and deserve praise beyond what I can give. I am also indebted to my family-in-law, Judie Youngblood, Mike Youngblood, David Youngblood, John Youngblood and Tim Youngblood for being so supportive of this entire endeavor. David, John and Tim are thanked in particular for keeping up a friendship over such a great distance.

Finally, and definitely never least, I would like to thank my wife, Debra Youngblood Harrington for her unconditional support, love, and life; if it were not for her I'd surely never have made it.

This research was supported in part by the Augmentation Awards for Science and Engineering Training under contract F49620-95-1-0386, NOAA/FAA under contract # NA37RJ0202-ITEM14, AFOSR under grant # F49620-95-1-0132, and DOE-ARM under grant # DE-FG03-95ER61958.

TABLE OF CONTENTS

LIST OF FIGURES

LIST OF TABLES

Chapter 1

INTRODUCTION

Interest in Arctic cloud research has remained a relatively sparse field of inquiry until recent climate simulations suggested that the Arctic is particularly sensitive to climate perturbations. Experiments within the Arctic region for the purpose of understanding Arctic cloudiness have been sparse and limited to a span of essentially 30 years (with most of the predominant research having been done over the past 20 years). The attendant difficulties of taking measurements in the Arctic Basin coupled with the fact that few people live in the region have been prime reasons for the lack of information.

In this chapter, we discuss the previous research that has been conducted on Arctic stratus clouds (ASC). The focus is not only on the microphysical nature of ASC, but also upon ASC as they relate to other scientific questions. This leads to a discussion of unanswered questions that remain in association with ASC in general. We begin by giving an outline of the current knowledge (observations and modelling) of these clouds (§1.1 and 1.2), this discussion is somewhat detailed and is given for the person interested in the details of the current state of knowledge. A brief synopsis of the outstanding questions about ASC that are directly addressed by this research as relates to previous knowledge is given in §1.3. The reader who is uninterested in the details given in §1.1 and 1.2 may easily skip to this section. Connections are then made to our research strategy and the primary objectives of this work (§1.4).

1.1 Preliminaries: Recent interest in Arctic cloudiness

From the vantage point of scientific research today, ASC are interesting because they are a link in the puzzle of how the Arctic climate may respond to climate change events. Doubling CO_2 experiments such as those presented by Walsh and Crane (1992) show an

interesting "polar amplification" affect in which the Arctic region experiences an 8 to 16°C increase in temperatures as compared to 1.5 to 4°C at lower latitudes. A response which Curry *et al.* (1995) showed is intimately linked to the sea ice-albedo feedback mechanism. Interrelations among sea-ice and cloud cover seem to be quite important in studies of the Arctic climate. Sea-ice equilibrium thickness may be strongly influenced by increases and decrease in cloud fractional coverage (Curry *et al.* , 1993) coupled with changes in cloud microphysical properties. The sea-ice system greatly affects the surface-atmosphere physical relations through its large albedo, which reflects more radiation back to space than do clouds, and through its insulating effects whereby the overlying atmosphere has little contact with the underlying, relatively warmer ocean waters . Thus, how clouds affect the sea-ice thickness can have drastic effects on the energy budget of the Arctic. The possible strengths of such effects have been illustrated in climate modelling sensitivities in which Arctic sea-ice is removed. In one particular numerical experiment Royer *et al.* (1990) showed that the removal of sea-ice caused a reduction in low cloud cover from around 65% down to 40% . Once the sea-ice was removed, and the warmer ocean waters exposed, convective motions were increased and low cloud amounts decreased due to subsidence warming and drying. The corresponding evaporation from the ocean surface increased convection providing a positive feedback. Other modelling studies such as Dümenil and Schröder (1989) which used a different convective parameterization scheme, showed increases in cloud cover rather than the decreases shown by Royer *et al.* (1990). Therefore, how Arctic cloudiness would respond to sea-ice reductions, and how this would feed back into sea-ice and the radiation budget is not well understood and further study is warranted, especially if sea-ice thicknesses are as sensitive to cloud cover as has been suggested.

While these relations are inextricably linked to the radiation budget as modulated by the cloud cover/sea-ice interactions, the clouds, themselves are also modulated by vertical distributions of temperature, water vapor amounts, cloud condensation nuclei (CCN) and ice nuclei (IN) concentrations, compositions and vertical profiles; not to mention large scale forcing mechanisms. Large scale pollution events, as discussed by Shaw (1986), cause aerosol concentrations to increase and thereby affect the radiative, microphysical

and dynamical properties of ASC. These affects might then feedback into the Arctic heat budget.

The impact on the Arctic heat budget is also dependent upon the seasonal cycle of Arctic clouds and their associated composition. Seasonally, ASC have a peak in cloud fraction between 70 and 90% throughout the summer months (Herman and Goody, 1976) and, during a rapid transition period in the fall, low cloud climatologies show that this amount rapidly decreases to values between 20 and 50% . Recently, it has been shown that low level clear-sky ice crystal precipitation, having been highly unaccounted for in low cloud climatologies, may boost the percentage of cloud fraction to values much higher than once thought (Curry *et al.* , 1990). That this may have an impact on the radiation budget of the Arctic has been explored by Curry *et al.* (1993) where it was shown that these precipitation events can increase down-welling IR radiation at the surface by as much as 80 $W\ m^{-2}$, which then affects the sea-ice and atmospheric thermal properties. This transition regime and wintertime cloudiness are not well understood. Clear sky ice crystal precipitation is frequent, however Witte (1968) has also noted predominately liquid phase ASC occurring in the depths of winter at temperatures of -32°C. In any case, low level cloudiness in the Arctic undergoes a transition between predominately liquid phase summertime ASC to mixed-phase and ice clouds in the fall, spring and winter. Both summertime and mixed-phase ASC are persistent (less so in the case of mixed-phase clouds) and driven strongly by cloud top radiative cooling.

Even though the climate issues are highly relevant, overlooked in many instances is the fact that this region contains some of the most unique cloud features on the globe, particularly as concerns low level stratus clouds[1]. In summertime, these clouds can have complex moisture and temperature profiles (Curry, 1986), some with increases in humidity above the inversion that affects entrainment processes. The clouds often exist in multiple layers and may persist over the ocean for extended periods of time (Herman and Goody, 1976). Prevailing synoptic conditions appear not to be of prime importance in the development of

---

[1] The fact that few papers exist on the topic of cloud-scale processes and cloud-scale modelling of ASC illustrates this point.

these clouds, as it was shown by Curry and Herman (1985b) that ASC formation seems to be predominately related to changes in air mass characteristics as the flow is directed over the ice pack with synoptic-scale fluctuations superimposed. During the transition-season, persistent mixed-phase clouds have been observed with complex features similar to the summertime clouds. Wintertime may produce ice clouds generated by plumes emanating from leads. Wintertime clear-sky ice crystal precipitation is a feature that may be more wide-spread than previously documented (Curry *et al.* , 1996) and may be an important source of ice for the ice pack and an important term in the IR budget of winter (with downwelling IR fluxes to the surface of 40 to 80 Wm^{-2}).

All of these unique microphysical, radiative and corresponding dynamical properties are unique to the Arctic region and have remained essentially untouched (especially by cloud modelers). In particular, the fall, spring and wintertime cloudy situations have received little attention until the recent interest in Arctic clouds, their seasonal cycles and associated affects which was spawned by climate research interests. In the next section we touch on the physical characteristics of ASC with particular emphasis placed on cloud-scale processes.

1.2 Microphysical, radiative, and dynamical characteristics of ASC: An overview

In the next few subsections we present a thumbnail outline of the current state of knowledge associated with ASC. Even though there are many attendant side issues associated with climate and the like, we focus on the physical processes directly related to ASC. The subsections are broken down into two, the first covering summertime ASC and the second covering fall, spring and wintertime cloudiness with the focus placed on the transition seasons.

1.2.1 Summertime ASC

The microphysical data base for summertime ASC is more extensive than for low clouds throughout the rest of the year, most likely being due to the fact that wintertime measurements are difficult at best (Curry *et al.* , 1996). Some early microphysical measurements of summertime clouds had been accomplished (*e.g.* Dergach *et al.* , 1960;

Witte, 1968) but it was not until the Arctic Stratus Experiment (ASE) in June of 1980 that extensive microphysical, radiation and turbulence data were collected simultaneously and analyzed for a variety of ASC situations. Indeed, most of the information associated with ASC properties are related to these experiments. Before this experiment, summertime ASC were believed to be simple, homogeneous systems that occur as persistent layers over large portions of the Arctic basin (Jayaweera and Ohtake, 1973). Profiles of liquid water and drop concentrations were assumed to be quite similar to those measured in lower latitude stratus clouds (*i.e.* LWC that increase with height above cloud base and fairly constant concentrations of drops within the cloud). The Arctic stratus experiments showed that these clouds exist in complex environments with sometimes few similarities to their lower latitude counterparts.

Microphysics

Microphysically, the bulk of the observations show cloud layers from 100 to 500 meters in thickness with liquid water contents (LWC) ranging from 0.05 to 0.5 $g\ m^{-3}$ and liquid water paths (LWP) of 11 to 130 $g\ m^{-2}$. Supersaturations are usually small with values less than 1% . Cloud droplet concentrations vary from values as low as 50 cm^{-3} to values as large as 500 cm^{-3} . Distributions (Herman and Curry, 1984; Tsay and Jayaweera, 1984) showed small mean droplet radii ranging over 2 to 7 μm, although distribution dispersions showed larger values which Curry *et al.* (1996) consider consistent with observed drizzle from the cloud layers. Curry (1986) attributed the large drop dispersions to turbulent fluctuations in vertical motion causing spurious variations in the supersaturation field and postulated that radiative cooling may be assisting the process of distribution broadening at cloud top. However, recently Curry (1995) has suggested that dynamics may be of secondary importance in terms of shaping the drop size distribution. Examining the drop size data given in Herman and Curry (1984) for these cases shows that the drop size distribution function is quite flat[2] over the 1 to 10 μm radius range and falls rapidly

[2]This flat area may be purely a function of instrumentation error and, therefore, erroneous (Reuter, personal communication).

with little or no concentration beyond 20 μm radius. This shows that the large drop size dispersions are due to broad spectra at small sizes and not to any measured drizzle mode. The drop in concentration above 10 μm is also shown by Tsay and Jayaweera (1984) for these cases. Their results illustrated that the distributions in ASC can be bi-modal near cloud top and mono-modal near cloud base, however the bimodality existed at small sizes and trailed off rapidly above about 12 μm. Thus, it seems that the distribution breadths so measured may not have been indicative of drizzle production. Measurements of large drops during these cases has been suggested (Curry *et al.* , 1996) but the spectral data do not explicitly show it.

Cloud condensation nuclei (CCN) concentrations were shown by Radke *et al.* , (1976) to have values of about 90 cm^{-3} at $S = 1\%$ and postulated to be mostly sulfate. The recent data of the ASE show that concentrations of CCN can be much higher with values ranging between 100 and 500 cm^{-3} (Curry, 1986). The large range in CCN concentration values in the Arctic seem to be related to large scale pollution events (Shaw, 1986) caused by advection from Eurasia and the lower North American continent. Data bases for CCN over the Arctic are quite sparse but have recently been enhanced by the measurements of Hegg *et al.* (1995). Their results show large values in CCN concentrations consistent with Curry (1986), however, the most fascinating result of their study was the finding that the CCN during April were not dominated by sulfate mass. The CCN spectra showed that about half of the mass of CCN activated below $S = 1\%$ was not sulfate; most of the sulfate mass was shown to be associated with aerosol much too small to be CCN. The authors, therefore, postulated that organics may be playing a role in drop activation. In-situ production of CCN aloft was suggested as a mechanism to explain the fact that the c and k in the $N_{ccn} = cS^k$ relation were significantly correlated with height.

Radiative processes

Radiatively, ASC have solar optical depths that range from 2 to 24 with reflectance and transmission functions varying between 0.2-0.82 and 0.8-0.25, respectively (Herman and Curry, 1984). Cloud absorptivities for these cases are more difficult to ascertain and, therefore, have large discrepancies shortwave heating rates range from about 0.4 to 1.6 K

h^{-1} (Curry, 1986) while longwave cooling appears to occur over depths of from 100 to 300 meters with maximum rates of from -2 to -7 $K\ h^{-1}$, as computed by Curry and Herman (1985a). Cloud emissivities for the ASE cases ranged from 0.4 to 1.0 with the predominant value of 0.85 being associated with clouds of liquid water path (LWP) of about 20 $g\ m^{-2}$. Clouds thinner than about 320 m appear to have emissivities much less than 1 (Herman, 1975). Unlike lower latitude clouds, it was found that the broadband emissivity of ASC is not well represented by the window region value. This fact appears to be due to water vapor lines outside of the window region that are not saturated in the Arctic atmosphere (Curry and Herman, 1985). The radiative extinction length, which describes the distance below cloud top over which $1 - e^{-1}$ of the net longwave flux is reduced, attained values of between 30 and 120 m. This variable has been used to explain how much of the longwave cooling is made available for generating mixed-layer convection.

Microphysical, radiative and dynamic interactions

The interactions amongst radiation and microphysics affects the turbulent structure of the stratus cloud layers (and vice-versa). In one of the very few papers that discusses the inter-relations of these processes, Curry (1986) showed that the ASC of the Arctic Stratus Experiment are not maintained by surface moisture and heat fluxes. Curry (1986) also showed that entrainment at the top of the cloud layers did not seem to penetrate deeply into the cloud interior (only about 50 m) and, hence, may not be an important dissipation mechanism. In fact, it was shown that entrainment moistened some cloud layers as water vapor mixing ratio (r_v) increases above cloud top. Radiative cooling was shown to affect mixed-layer convection to some degree (about 10 %), however, in many instances was offset to a large extent by cloud top condensation and entrainment effects. The large LWCs at cloud top were, however, postulated to be a function of the radiative cooling. Most of the cloud decks examined were dominated by longwave cooling as the shortwave heating was small in comparison. Turbulence statistics show that $< w'w' >$ ranged between 0.01 and 0.16 $m^2\ s^{-2}$ with the largest values occurring usually at cloud base but, at times, also at cloud top. Values of $< w'\theta_v' >$ ranged from -0.0149 to 0.009 $K\ m\ s^{-1}$ with minimum values usually associated with cloud top (entrainment and other

heating effects) and areas below cloud base. Maxima usually occurred just below cloud top where buoyancy production is a maximum in stratus driven by cloud top radiative cooling. Moisture fluxes ($< w'r_v' >$) usually ranged from -43 $\times$ 10^{-4} to 40 $\times$ 10^{-4} g m^{-3} m s^{-1} almost always attaining positive values within the cloud layer and at cloud top, suggesting the entrainment of air with lower moisture content. In only one case was $< w'r_v' >$ negative at cloud top, suggesting that cloud top was being moistened by larger r_v values above the inversion. The fluxes of liquid water were normally positively correlated with vertical motion showing the effects of advection of liquid water and the condensation/evaporation process occurring within updrafts and downdrafts, respectively. Even though turbulent statistical correlations were derived for the extensive ASE data base, causal relations could only be speculated at as information about temporal processes are not available. As pointed out by Curry (1986), no detailed modelling studies of the inter-relations of microphysics, radiation and cloud-scale dynamics existed at that time for ASC (this is still predominately true). The interactions of these processes are likely to be very important in producing the unique features of summertime ASC.

Radiation effects on drop growth

The effects of longwave cooling on the growth of water droplets has been postulated to be a potentially important mechanism for the production of large droplets capable of initiating the collision-coalescence process (Roach, 1976; Barkstrom, 1978, Austin *et al.* , 1995) within stratiform clouds and fog layers. Cloud top radiative cooling is dominated by the droplets that exist there and such cooling of the droplets at the tops of clouds allows the heat generated during condensation to be dissipated more rapidly than through standard diffusion, thus allowing for faster condensation. If such enhanced condensation can produce droplets with radii greater than 20μm in a sufficient time, then enhanced collection should occur. Since summertime ASC can be somewhat tenuous with low LWC, this effect maybe particularly important for drizzle production within these clouds. In addition, the unique radiative environment that these clouds persist in (continuous SW heating) makes the SW portion of the problem particularly important.

While this topic has generated some interest in the microphysics community, the process has yet to be included in detailed microphysical modelling situations with a thorough discussion of the attendant physics. Fuchs (1959) appears to have been the first to discuss the radiative term in the vapor growth equations, however in his short discussion both the drop and its local environment are considered to be radiating as blackbodies. Since the temperature differences between the drop and the environment are not large, Fuchs shows that the effect can be neglected when considering growth from the vapor. This treatment, however, ignored the fact that droplets at cloud boundaries may gain or loose significant radiant energy through large differentials in the incident fluxes. Early works have considered this effect on the heat budget of an isolated drop existing at cloud top (Roach, 1976; Barkstrom, 1978). Studies such as these showed that not only is condensation enhanced, but that larger droplets (20 μm and greater) can grow through radiative cooling in classically subsaturated environments. Since the radiative effect on condensation is larger for bigger droplets, one would expect to see a differential effect on a population of droplets. This result was briefly discussed in a paper by Guzzi and Rizzi (1980), in which it was shown that longwave cooling had the effect of allowing large droplets to grow while suppressing the growth of smaller drops (collision-coalescence was not addressed in this study). The drop populations examined, however, consisted of droplets with radii no larger than 10 μm, therefore not showing what the effects of collection size drops would have on the growth of smaller droplets.

More recently, Austin *et al.* (1995) considered the radiative cooling effect in a mixed-layer model of stratocumulus clouds which included the effects of collision-coalescence on the evolution of the drop spectrum. While the results for the growth of individual droplets substantiated results published earlier, the information gained on the effects of collision-coalescence showed that significant numbers of droplets with $r > 25\mu m$ were produced thus initiating significant collision-coalescence. Their results illustrated that the time required for the onset of precipitation may be reduced by as much as a factor of four. These interesting results were, however, obtained from a simplified model with a specified population of droplets existing at cloud top and longwave cooling parameterized by the simplified function given in Roach (1976).

Modelling of microphysical processes including the radiative term in droplet growth has been completely confined to one-dimensional models of stratocumulus and fog. All results have shown that significant production of large droplets occurs in reasonable times. Ackerman *et al.* (1995) utilized the effect in an explicit microphysical framework coupled to a one-dimensional stratocumulus model. Their results showed that cloud top liquid water contents and supersaturations were reduced while optical depth and longwave cooling from cloud top were increased substantially over simulations without the radiative term included in the condensation growth equation. These results are similar to those discussed by Bott *et al.* (1990) in which the radiative term was included in a 1-D fog model. All previous works (except Austin *et al.* , 1995) have either consider simple isolated drops or populations of drops without collision-coalescence effects in simplified frameworks or the radiative effect has been included within a modelling framework including complicating processes that make it difficult to separate out the microphysical effects. In addition, all studies (except Ackerman *et al.* ,1995) exclude the effects of shortwave radiation on the problem. Indeed, there appears to be a gap in the link between understanding the radiative-vapor growth phenomenon in simplified frameworks and the inclusion of the process in a detailed numerical simulation. Since this effect has potential importance for drizzling ASC, we focus on examining this effect in Chapter 6. Section 1.3 discusses our strategy for the examination of this problem.

Formation and persistence

The formation of summertime ASC, unlike mid and upper-level clouds, seems to be somewhat insensitive to synoptic conditions (Curry and Herman, 1985). These clouds tend to form under a variety of conditions as a warm, moist air mass is modified while it flows over the Arctic basin. The clouds are normally situated in stably stratified environments, at times with strong shear (Curry, 1986) of the horizontal winds. Arctic stratus are a persistent feature lasting for days and without any dominant dissipation mechanism (Herman, 1975). The clouds may exist as single or multiple layer features depending upon the flow and small (cloud) scale processes (Tsay and Jayaweera, 1984). This is significantly different from subtropical stratocumulus. While subtropical stratocumulus share

similar characteristics with a small subset of ASC (*i.e.* strong mixed-layer cases with large buoyancy production of TKE), in general the above conditions differ greatly from stratocumulus processes. The persistent SW heating, little to no effect of surface fluxes from highly reflective ice surfaces, small effect of synoptic forcing, persistence within strongly stable layers with sometimes large wind shear, and the possibility of mixed-phase clouds (summer included) combine to produce the unique features of Arctic stratus.

The layering of summertime ASC is a feature that is still not well understood. At this time, there are at least three theories for this phenomenon (Curry *et al.* , 1996). Herman and Goody (1976) showed with a one-dimensional model that the absorption of weak, persistent solar radiation during the polar day causes increases in temperatures within the middle of an initially solid cloud deck. Over a period of 1-2 days of this relatively constant effect, droplets in the interior of the cloud evaporate as dew points increase, eventually leaving two cloud layers. The upper cloud deck in their study is maintained by cloud top radiative cooling while the lower deck is maintained by cooling to the colder underlying surface. McInnes and Curry (1995) propose that radiative cooling of air near the boundary layer temperature and moisture inversion may cause the formation of the upper deck while the lower deck is formed by the cooling of warm, moist air overlying a cooler surface. Tsay and Jayaweera (1984) proposed that upper cloud decks may be formed by weak vertical ascent with the lower cloud deck being formed by advection and mixing of warm and cold air. It is not known which of these processes is the primary mechanism for layering, whether the processes operate together, or whether they operate at all. Indeed, all of these mechanisms concentrate on double layer systems and none consider systems with more than two decks (Hobbs and Rango, 1997). It may be that various combinations of these mechanisms work to help form true multi-layered cloud decks.

The persistence of these clouds decks was postulated by Herman (1975) to be due to the lack of any strong dissipative processes. The lack of precipitation, strong radiative heating, convective heating generated at the surface, and the lack of large scale synoptic activity all assist in cloud maintenance. Curry (1986) shows that entrainment into ASC layers seems to be of little importance in the dissipation of these clouds. Since, as discussed above, the

Arctic can undergo pollution events, changes in CCN concentrations and characteristics may be important. If the advected pollutants are potential CCN sources as has been suggested by some (Shaw, 1986; Hegg *et al.* , 1995), then it is possible that clouds with smaller droplets and larger LWC (since precipitation would be suppressed) may occur. If, as has been suggested by Albrecht (1989), the production of drizzle is important in limiting the value of the cloud fraction, then enhancements of CCN concentrations may be a positive feedback upon ASC persistence. Although, as Stevens (1996) has recently shown, the production of drizzle does not necessarily have to lead to lower cloud fractions.

Specifically, with regards to changes in CCN concentrations, there are a number of issues not directly related to the climate issues that need to be resolved before a proper understanding of ASC processes may be reached. For example, we do not know whether cloud-scale dynamics, CCN spectra and chemistry, or cloud top radiative cooling are predominant mechanisms in controlling the drop size spectrum. In relation to this, we are not sure how radiation, microphysics, cloud top entrainment, and turbulent motions are linked in the Arctic Stratus regime. Neither are we sure of how strongly correlated mixed-layer convection is to radiative cooling at cloud top and how cloud-top microphysical/dynamical processes affect this. Changes in CCN concentrations have been postulated to be important in affecting the ASC boundary layer dynamics, however, this has never been elucidated.

Previous modelling

All modelling works on ASC to date have either concentrated on 1-D models with simplified turbulence, radiation, and microphysics (*e.g.* Smith and Kao, 1996; McInnes and Curry, 1994; Finger and Wendling, 1990; Herman and Goody, 1976) for cloud scale studies to large scale studies that employ crude microphysics and radiation (*e.g.* Pinto *et al.* , 1995, Curry and Ebert, 1992; Royer, 1990). Thus, a gap exists in the modelling studies conducted so far which may be filled by the use of detailed, CRM and LES simulations of ASC. The use of detailed CRM and LES dynamical frameworks coupled to explicit, bin resolving microphysics have only recently been used to study the coupled microphysical and dynamical processes in stratocumulus (Stevens *et al.* , 1996; Kogan *et al.* , 1995). In addition, all of these experiments touched on CRM and LES with simplified

radiation schemes (many done with only the effects of LW radiation) and only for sub-tropical marine stratocumulus. The heat budget affects of microphysics on cloud structure are resolved in detail, however the manner in which radiation impacts this heat budget through microphysical interactions is dealt with crudely.

The one-dimensional results of McInnes and Curry (1995) illustrated the primary importance of radiative cooling in TKE production within ASC. Their results showed that ASC can persist within regions of weak large scale ascent, whereas weak large scale descent causes dissipation of the multi-layered system. This result is exactly the opposite of that shown in Smith and Kao (1996) in which large scale subsidence does not affect the dissipation of the cloud layers. In their 1-D modelling study, the larger strength of the cloud top radiative cooling, between -12 and -15 $K\ h^{-1}$ in this study as opposed to -3.13 $K\ h^{-1}$ in McInnes and Curry (1995), was able to keep the layer cool against the heating and stabilizing effects of the large scale subsidence and is the reason for the difference between the results. The radiative results of Smith and Kao (1996), however, produce cooling within an extremely narrow vertical range, over only about $25m$ near cloud top. A reason for the differences appears to be that the Smith and Kao (1996) 1-D model uses $7.5m$ vertical grid-spacing whereas the McInnes and Curry (1995) model uses $50m$ grid-spacing. Turbulent fluxes in the Smith and Kao (1996) cases are strongly over-predicted, especially below the level of cloud base. As drizzle is not included in the simulations, the total water flux has the wrong sign at cloud top and is under-predicted at cloud base (as compared to observations). McInnes and Curry (1995) make the point that surface radiation fluxes (and thus, sea ice heat budget) is strongly dependent upon the cloud properties. Even if this is not the case, the results of these 1-D models should eventually be corroborated by more detailed modelling studies (*i.e.* CRM and, especially, LES simulations), which has not been done to date.

1.2.2 Interactions with ice: Fall, Winter and Spring cloudiness

Due to the extremely sparse nature of the data associated with fall, winter and spring season cloudiness (and ice producing potential) we group information on cloud processes associated with ASC for these seasons together. Traditionally, (Herman and Goody, 1976),

the fall and spring seasons have been seen as "transition" seasons over which low level cloud amounts change rapidly within a relatively short period of time (about one month). During fall, cloud fractions decrease from summertime highs of 70 to 90% down to around 30 % in the winter months (Huschke, 1969), with a subsequent increase in cloud fraction during April and May in spring. This seasonal cycle is of particular interest as the heat budget of the Arctic and subsequent effects on climate may be sensitive to how Arctic cloudiness changes (as mentioned above). Recently, it has been suggested by Curry and Ebert (1992) that low-level cloud amount in the Arctic during winter may be substantially underestimated as standard satellite instruments have difficulty discerning these clouds and surface based observations tend to not include clear sky ice crystal precipitation.

During the transition period of Fall and Spring, it appears that different ice production mechanisms may be at work in each season. Even though little data exist, what does exist is suggestive. Curry *et al.* (1990) showed that significant ice nucleation occurred during April of two years at temperatures as warm as -15 to -20 C (possibly by freezing nucleation). During October, Curry *et al.* (1996) mentioned clouds composed completely of ice crystals at temperatures as high as -14 C. During the winter months, Witte (1968) had reported a case of a predominately liquid phase cloud at temperatures of -32 C. These data illustrates the possibility that ice forming nuclei (IN) may have periods of deficiency in the Arctic and may depend upon pollution events. During strong pollution events, IN may be deactivate if contact with the pollution is made. Coating of the IN, for example, with sulfate particles (which are poor ice nucleating agents) could cause mass deactivation of populations of IN (Borys, 1989). Jayaweera and Ohtake (1973) showed values of IN concentration covering the temperature range of 0 to -20 C of between 0.003 to 1 L^{-1} while Radke *et al.* (1976) reported values of IN concentrations at -20 C of 0.15 L^{-1}. Large values of ice crystal concentrations have been reported and range from 17 to 4210 L^{-1} (Curry *et al.* , 1990) with values as high as 20 cm^{-3} (Pinto *et al.* , 1997) near the base of a mixed-phase cloud deck. The formation of high ice crystal concentrations during the winter months near the surface of the pack ice may be due high ice supersaturations (up to 30% see Curry *et al.* , 1990). Values of water supersaturation over open leads have been reported to be as

high as 200% (Pinto and Curry, 1995) which would strongly influence the concentrations of ice crystals generated near the surface. It should be noted that ice nuclei data gathered at lower latitudes (upon which model parameterizations are built, see Meyers *et al.* , 1992) produce concentrations of only 26 L^{-1} at 30% ice supersaturation. Thus, standard IN formulas do not seem able to capture the high concentrations observed in the Arctic. Equally puzzling from a modelling perspective is the extremely large concentrations of ice shown by Pinto *et al.* (1997). These high concentrations existed near cloud base and were predominately snow. How these larger cloud base concentrations of snow are produced is not known. Mechanisms such as rime-splintering may not be active in these cases as cloud temperatures were near -13 and -18 C.

Ice crystal habits in the Arctic seem to be dominated by plates, columns, and other irregular shapes (*e.g.* Jayaweera and Ohtake, 1973; Curry *et al.* , 1990) with frozen drops occurring at times (Ohtake *et al.* , 1982). As has been noted by Curry *et al.* (1990), no particular relationship for ice crystal habit as a function of ice supersaturation and temperatures, as is evident at lower latitudes, seems to exist.

Little data exist on the mixed-phase clouds that occur during the Fall and Spring transition months. Pinto *et al.* (1997) recently analyzed two cases of mixed-phase clouds that occurred during October over the Beaufort sea during BASE (Beaufort and Arctic Storms Experiment) in 1994 and the conditions under which they formed. Each of the two cases was unique in that one occurred under very stable conditions without much of an attendant mixed-layer while the other showed a substantial cloudy mixed-layer with strong temperature inversions above and below cloud base. In this respect, the data we used to simulate ASC cloud processes is similar to the latter of these two cases. Both cases were quite persistent, lasting for days, partially because they were continually forced by large scale synoptic conditions (water vapor was continually fed into the areas of cloudiness).

Pinto and Curry (1995) have simulated mixed phase clouds that are formed through convection generated over leads. The clouds were forced through flow over the leads and showed that within 6 hours of initialization that a deep cloud layer of ice (small particles), snow and water formed. The simulated cloud slowly lifted with cloud ice and liquid water

dominating the upper portions of the cloud (from 600 to 1400 m) while the lower portion was completely snow (from the surface to 600 m). Mixing ratios of snow and ice produced by the model were significant, attaining mixing ratios as great as 0.1 $g\ kg^{-1}$. Liquid water was less dominant with values of only about 0.01 $g\ kg^{-1}$, the small values of liquid water produced being due to the partitioning of liquid to ice (a simple parameterization of the Bergeron-Findeisen process). The modelling results showed sensitivity of the downwelling IR radiation at the surface to the evolution of the plume generated mixed-phase layer. Downwelling IR at the surface increased by 70 $W\ m^{-2}$ and was shown to vary between an increase of 50 and 90 $W\ m^{-2}$ depending upon the value of the effective radius assumed.

The overall transition from predominately liquid summertime ASC to wintertime cloudiness is not well understood due to the lack of information. A transition occurs during the fall under which the liquid phase clouds of summer must be replaced by cloudiness that contains or is predominately ice. As discussed above, the amount of ice within low-level cloudiness during the transition and cold (winter) season may vary considerably. Low level cloudiness has been shown in the traditional cloud climatologies to decrease over a short period of time during the fall and then to rise again during the spring. This, however, has been cast into doubt as clear-sky ice crystal precipitation has not been considered in the data base. What is not clear, is how stratus-type cloudiness is related to the enhanced low-level cloudiness in the Arctic during winter. Does stratus-type cloudiness disappear as low level ice crystals begin to dominate the cloud fractions in winter? What is clear is that stratus-type cloudiness does exist during the spring and fall with mixed-phase conditions while a possible rapid reduction in this type of cloudiness during the wintertime may occur. What causes this reduction in stratus-type cloudiness, and how and why this is replaced by clear sky ice crystal precipitation during the Arctic winter as the predominant cloud type is not well understood. No modelling studies of these types of mixed-phase ASC during the transition period have been attempted. In particular, the response of ASC to microphysical forcings needs to be examined in detail.

1.3 Outstanding problems in relation to conducted research

The above sections outline the state of knowledge in terms of observations and modelling of summertime ASC, transition season ASC, and the radiative effects on the growth of drops. As the radiative effect is a somewhat separate issue, related to ASC through the heat balance equation for the growth of drops, it may appear to be somewhat out of place. In any case, it is included above in order to motivate the research discussed below and in Chapter 6.

What becomes clear, after a cursory reading of earlier work on summertime ASC, or after a reading of §1.1, 1.2.1 and 1.2.2, is that the state of knowledge in terms of detailed, cloud-scale modelling is quite sparse. Almost all of the modelling work has centered around the June 28, 1980 ASE case because its cloud-capped mixed-layer makes is particularly amiable to 1-D and 2-D modelling studies (McInnes and Curry, 1995). Most modelling studies to date have centered upon discussions of cloud layer evolution during the period surrounding the 28^{th} of June, 1980 (Smith and Kao, 1996) including the formation and dissipation of the lower fog layer. No studies, however have addressed issues related to drizzle production within these clouds layers or the impacts of SW radiation on the evolution of the cloud layers. Because of the sensitivity of these clouds to SW radiation (Herman and Goody, 1976), and since drizzle production can have a large effect on stratocumulus dynamics (Stevens, 1996), studies such as these may shed light on important processes that impact the evolution of ASC decks. In addition, ASC may undergo microphysical modification through large scale pollution events that occur within the Arctic Basin (Shaw, 1986). This alteration of CCN concentrations could also impact the dynamics of the cloud layer through modifications of the radiative and microphysical heat budgets. However, the importance of these various effects upon the dynamical and microphysical structure of ASC layers remains unknown.

In terms of drizzle production, LW and SW radiative heating modify the heat budget of the liquid water drops allowing them to grow faster by condensation at cloud top but slower within the cloud interior where SW heating is a maximum. This impact could cause an alteration of the microphysical and dynamical structure of ASC. The radiative effect,

however, has not been extensively studied by the microphysical community. Most work done to enhance knowledge on a microphysical level have studied the radiative effect with drops (or distributions of drops) poised at cloud top for residence times between 20 to 80 minutes (Roach, 1976; Guzzi and Rizzi, 1980; Austin *et al.* , 1995). In addition, most of these studies are concerned exclusively with the production of large drops that may enhance collision-coalescence (not with the impacts on the drop distribution function). In addition to this, 1-D modelling studies of fog (Bott *et al.* , 1990) and stratocumulus (Ackermann *et al.* , 1995) have been undertaken which examine the radiative effect upon the simulated cloud structure. None of these studies examines in detail the impact of the effect on the drop distribution function under realistic cloud time-scales; nor is it readily evident how this effect may impact the evolution of a particular stratus layer.

Mixed-phase clouds that occur over the Arctic ocean during the transition seasons (fall and spring) have been almost completely ignored by numerical modellers, although these clouds are important for a number of reasons (including the fact that they may affect the freezing of the Arctic ocean; Curry *et al.* , 1997). One of the few modelling studies is that of Pinto and Curry (1995) in which mixed-phase clouds that form due to vapor fluxes over ice leads are simulated with a 1-D model. Certainly, the lack of modelling studies is due to the sparse nature of the data that exist during fall and spring. Indeed, the only experiment that has examined mixed-phase cloud microphysics was the Beaufort Arctic Sea Experiment (BASE) which was conducted in 1994 during autumn. Papers discussing this data set are only recently appearing in the literature (Curry *et al.* , 1997; Pinto, 1997). The persistence of these clouds during autumn (Pinto, 1997) is particularly interesting as mixed-phase clouds are colloidally unstable. The mechanisms behind the stability of these cloud layers and their maintenance does not appear to be known.

1.4 Objectives of this research

Because of the inherent sensitivity of summertime ASC to changes in CCN concentrations as suggested in the literature, we explore sensitivities to this parameter with two-dimensional LES (what are termed cloud-resolving models or CRM) version of RAMS

coupled to the detailed liquid phase microphysical model of Feingold *et al.* (1994) and a detailed radiative transfer scheme. The effects of changes in CCN concentration on the radiative and dynamical properties of simulated ASC are explored. We examine how important CCN changes are to the production of drizzle within the cloud layer, how it affects the radiative properties and how these feed back into the cloud-scale dynamics. Simple radiative couplings are used at first in which gamma function representations of the drop size distributions are used to interact with the radiation. This effectively removes variation in distribution shape from the radiative feedbacks. The effects of changes in drop size distribution shape are explored with an explicit representation of the cloud drop optical properties. These explorations allow us to examine how important various microphysical/radiative couplings are to cloud properties. The hypothesis of Hu and Stamnes (1993), that r_e may be used to characterize cloud optical properties irregardless of distribution shape, is explored within the context of the modelling studies.

Since these clouds are strongly driven by cloud top radiative cooling, drizzle production may be enhanced within these clouds through larger condensational growth rates. Specifically, we examine how the radiative effect (both shortwave and longwave) impacts the evolution of the drop size spectra within two modelling frameworks. The first is a trajectory parcel model (TPM) that is driven with data from the RAMS model runs. This allows for the isolation of important causal relationships. In addition,the framework allows for the examination of how enhanced drizzle production through radiative effects is dependent upon drop cloud top residence times. Since drizzle production cannot be properly elucidated within the TPM framework (drops cannot sediment and there are no dynamic feedbacks), the radiative effect is incorporated into the CRM. The hope being that the TPM results will guide the analysis of the radiative effect in the detailed CRM simulations.

Mixed-phase ASC systems are explored as sensitivities to the liquid cloud. In these cases, we wish to examine/explore whether the rapid decrease in stratus-type cloudiness during fall is forced at all by microphysical mechanisms. In addition, we explore what determines the stability of these mixed-phase clouds which have been postulated to be

persistent features of the autumnal boundary layer (Pinto, 1997). Since the Bergeron-Findeisen process removes liquid water at the expense of ice, it is postulated that certain cloud temperatures and IN concentrations may cause collapsing or stable boundary layers depending upon these parameters. We utilize the explicit ice microphysical model of Reisin *et al.* (1995) coupled to the RAMS dynamical framework and the detailed radiation model in order to explore this hypothesis (the first such coupling, to our knowledge). To test our ideas, a set of sensitivity experiments are constructed around cooled versions of the liquid phase initialization soundings (with RH kept constant). Different coolings are utilized along with different IN concentrations, CCN concentrations and different ice habits to explore the stability of the cloud layer. Sensitivities so constructed are not meant to be case studies by any means. These explorations are considered to be physically plausible situations under which our hypotheses may be explored.

The two-dimensional framework is used for all of these studies as it allowed for more sensitivities to be run with the limited computational resources. The pure liquid phase simulations are not extensively cumbersome in two-dimensions but become much more so when the third dimension is added. This is especially true for the mixed-phase simulations in which the ice microphysical model is used. In these cases even the two-dimensional simulations are extremely costly with three-dimensional simulations being impossible with present computational resources. As has recently been discussed by Stevens (1996), the two-dimensional framework seems adequate for capturing the fundamental physical integrity of the radiative, microphysical and dynamical interactions of the stratus system.

This dissertation is organized in the following manner. In Chapter 2 we discuss (briefly) the RAMS model and, in somewhat more detail, the microphysical models used concentrating on the aspects of the models that relate to the studies at hand. The radiative transfer model and its interaction with the different microphysical models in RAMS is discussed in Chapter 3. Chapter 4 discusses the particular ASC case utilized for these studies, focusing on the cloud-scale details of the microphysics, radiation and turbulent interactions. Simulations of the summertime ASC and sensitivities to CCN concentrations and discussions of the microphysical and radiative interactions are discussed in Chapter 5.

Chapter 6 discusses the radiative couplings to droplet growth mechanisms, introduces the TPM and concludes with added simulations of the summertime ASC including this effect on drop growth in the CRM. In Chapter 7 simulations of the mixed-phase ASC are presented along with discussions of the important microphysical mechanisms for cloud collapse during the transition season. A set of sensitivities that explore the mixed-phase cloud sensitivity to various parameters are studied in Chapter 8. We summarize and suggest topics that need to be explored in the future in Chapter 9.

Chapter 2

METHOD

Various methods may be used to study physical systems that range from the purely observational to the purely theoretical. All methods have their limitations, however a proper discussion of these could fill a volume by itself. Within this work, the method of numerical modelling is used to study various processes associated with Arctic stratus clouds.

The framework of numerical modelling, which consists of sets of equations based in physics, written down and solved on a discrete grid within a computer, provide a quasi-theoretical method for examining causal relations within complex systems. The equations thus solved are approximated in certain ways (and some processes not completely understood or too computationally demanding are approximated by a method called *parameterization*) before even entering the computational framework. Solutions on a discretized grid are never exact and, except for very simple one-dimensional systems, it is impossible to prove that the appropriate solution is even being attained (Thomas, 1995). An excellent discussion of the problems associated with using truncated systems of equations within numerical frameworks has been put forth by Stevens (1996) in which he reasons that, even with formidable limitations imposed by truncation, that results attained by the numerical model coupled to an explicit bin microphysical and detailed radiation schemes are sufficient to capture the, "low-dimensional behavior" of the system.

The results put forth in this dissertation are obtained with a two-dimensional version of the numerical model. This, of course, limits the results further as the nature of the turbulent cascades are different in two dimensions than three dimensions. Thus, standard turbulent truncations (called *closures*) are not appropriate in these situations. However, as has been shown by Stevens (1996), the behavior of the two-dimensional system emulates the

three-dimensional results in such a fashion that the integrity of the radiative/microphysical and dynamical interactions seem to be maintained. Thus, sensitivities conducted in two-dimensions may have counterparts within the three-dimensional realm and we expect that the results presented here will reasonably transfer to three-dimensions. There are points in the discussion where sensitivity results are not well separated from one another and may be affected by initial random perturbation and two-dimensionality. At these points, we make an effort to point out the possible limitations based on our initial assumptions.

2.1 The RAMS Model

A complete description of the Regional Atmospheric Modelling System (RAMS) may be found in the paper by Pielke *et al.* (1995). Herein, suffice it to say that RAMS is a primitive equation numerical model solved on a Eulerian grid. The model is cast in what is termed an LES mode, although since the simulations conducted are two-dimensional and, thus, do not capture the turbulent statistics correctly as does true LES, we stick to the conventional nomenclature in the vernacular of CRM, or cloud-resolving model. The CRM, like the LES framework, consists of a limited domain (in this case 3600 m in the horizontal and 2880 m in the vertical) with a fine enough gird mesh to adequately resolve the cloud-scale motions. Systems that can be examined within such small domains must be able to maintain themselves against dissipation processes. Thus, we call these *self-maintaining* systems. In our case, the horizontal direction is broken into discrete sections of $\Delta x = 60\ m$; the vertical direction begins with 30 m grid spacing which remains constant up to a location just above cloud top (about 1200 m) and, at this point, the grid spacing is stretched to 50 m. This model has been used successfully to examine various properties of marine stratocumulus (Stevens *et al.* , 1996; Feingold *et al.* , 1994) within both two and three-dimensional frameworks. The inherent differences between two and three-dimensional simulations of marine stratocumulus may be found in Stevens (1996). In the present framework, the non-hydrostatic model integrates predictive equations for the u and w components of the wind field, a perturbation form of the Exner function (a pressure variable), total water mixing ratio (r_t), and 52 scalars for the liquid microphysics and 205

scalars for the ice microphysics, along with the ice-liquid water potential temperature (θ_{il}) on a stretched Arakawa C-grid.

2.2 Bulk microphysical representations

Within some of the studies presented in the following chapters, '"bulk" microphysical schemes are used either during the spin-up phase of the model simulations or some sensitivity experiments. The simplest version of the model used assumes an immediate conversion of any supersaturated vapor to liquid water. This water is termed *cloud water* throughout the remainder of this dissertation. Simulations executed with this simple scheme are denoted by adding NM (no microphysics) to the descriptive acronyms. This method of initiation of cloud drops is also utilized within the bulk microphysical modelling framework which is also used for some studies (Walko *et al.* , 1994). This version of the microphysics is termed bulk because it assumes hydrometeor distributions have a gamma function form, given by

$$n(D) = \frac{N_t}{\Gamma(\nu)} \left(\frac{D}{D_n}\right)^{\nu-1} \frac{1}{D_n} exp\left(-\frac{D}{D_n}\right) \tag{2.1}$$

where N_t is the total concentration of a given microphysical species, D_n is the characteristic diameter so named because integrations of the various moments act as if they are "characterized" by a hydrometeor of size D_n, ν is the shape parameter and describes the breadth of the distribution function. In RAMS, ν is not predicted and must be set by looking to observations for assistance. In the current version of the bulk microphysics, only the third moment (mass) of the distribution is predicted. Since $n(D)$ is given in terms of three other variables, two must be specified and the last diagnosed from the equation for the mass-moment. For most of the runs produced in this dissertation, cloud water is assumed to have a shape of $\nu = 6$ (which is a narrow distribution normally associated with the cloud drop spectrum in stratus clouds) while $\nu = 2$ is used for any and all ice species. The second parameter specified is the number concentration (when cloud droplets are considered) and the characteristic diameter (when ice is considered). Of course, one is free to specify other parameters, however, our choices are based on some limited evidence.

The use of the bulk microphysical model that includes ice processes will be denoted by added IM (ice bulk microphysics) to the descriptive acronyms.

The bulk framework includes seven different hydrometeor classes defined in terms of the processes affecting them. The classes defined are given by cloud water, rain, pristine ice, snow, aggregates, graupel and hail. Cloud water was described above, its simple formulation is due to the fact that no detailed information on CCN that can be used for model initialization is currently known. Rain is formed when cloud droplets become big enough to initiate the collision coalescence processes; the form of this parameterization is based on the work of Berry and Reinhardt (1974). Although, recently, Feingold *et al.* (1997) have developed a bin method of dealing with this conversion process (and drop sedimentation) that more realistically captures the production of drizzle (as compared to a detailed bin representation). Pristine ice is the only category in RAMS for which two-moments of the size spectra are predicted (mass and number concentration). This is due to the fact that pristine ice is the initiation category into which ice nucleated through various mechanisms (see Walko *et al.* , 1994) is placed. Pristine ice is grown by vapor deposition although it is allowed to attain a small amount of rime. Snow is produced by vapor-grown pristine ice through an analytical method that converts the larger pristine ice into snow (Harrington *et al.* , 1994). Snow may also attain small amounts of rime. Collection of snow or ice produces aggregates (aggregates may also self-collect as a number depletion mechanism) which may also rime in small amounts. Any significant rimed ice is placed into the graupel and hail categories. For detailed descriptions of these processes see Walko *et al.* (1995).

2.3 Liquid-phase bin microphysics

In order to address issues associated with drizzle, detailed radiative microphysical interactions at cloud top, and the affects of radiation on cloud drop growth a model is needed that accurately represents liquid microphysical processes. The explicit microphysical representations of liquid phase microphysics as described by Tzivion *et al.* (1989) and Feingold *et al.* (1994) have been used to accurately describe the liquid phase processes

within marine stratocumulus clouds (Stevens *et al.* , 1996) and are used within this framework to understand detailed microphysical and radiative interactions. The use of the bin microphysical model is denoted by adding LBM (liquid-phase bin model) to descriptive acronyms.

Condensation, evaporation, and collision-coalescence (through the stochastic collection equation) are solved on a discrete grid utilizing the method of moments described in Tzivion *et al.* (1989). The grid so used is defined by diameter boundaries covering the space 3.125 to 1008 μm, which is sufficient for our purposes. Diameter boundaries are defined in terms of mass doubling where diameter edge $k+1$ is related to edge k by $x_{k+1} = 2x_k$ (where x is the mass). This translates into the following formula for the diameter edges,

$$D_k = 2^{(k-1)/3} D_1 \tag{2.2}$$

where D_1 is 3.125 μm. To define this space requires 25 drop bins in which the bin concentration, N_k, and the total bin mass, M_k, are defined. Thus, the predictive equations require an added 50 scalars for the liquid cloud related processes. Methods of condensation and evaporation are quite important to the processes of the radiative enhancement (or suppression) of the growth of droplets by condensation. In order to accurately represent this process, optical properties that have a bin functional dependence must be derived (as the radiative effect is differential in diameter space, larger and smaller drops must necessarily experience different forcings). We will discuss condensation processes within the bin framework in Chapter 6 which describes radiative enhanced (suppressed) condensation growth based on the bin derived optical properties of Chapter 3.

2.4 Ice-phase bin microphysics

Since our goal in studying mixed-phase clouds is to examine detailed ice-liquid microphysical processes and how they affect the simulated boundary-layer, a detailed ice microphysical representation is necessary. In keeping with the method described in the last section, we utilize the ice microphysical model of Reisin *et al.* (1995). The bin structure and solution methods for this model are analogous to those for the liquid-phase model, the only exception is the differentiation of ice species into three specific classes. In

the ice microphysical model, pristine ice is (as in the bulk model) a category that is grown through the vapor deposition process and is allowed to carry small amounts of rime. In this case, since the distribution function is predicted explicitly, there is no need for a larger snow class of ice which is purely vapor grown (as in the bulk model). Any self-collection of pristine ice is mapped appropriately to the bins of the aggregate distribution. Aggregates may also grow larger by self-collection and may also carry small amounts of rime. Any significant amounts of riming onto pristine ice or aggregates is mapped to the bins of the graupel distribution function. Thus, the ice microphysical model includes 4 classes; the same water class as in the liquid-phase model and three ice classes for a total of 200 extra scalars to be solved for in the numerical model. As would be expected, this presents an enormous computational load for current desk-top workstations. It should be noted that mixed-phase particles are not allowed within the current ice microphysical framework, although this will be included in the future (Reisin, personal communication). Since graupel production within Arctic stratus is small and our modelling efforts (discussed later) show little graupel, there is probably little reason for concern.

In keeping with the methods derived for the liquid microphysical model, we derive optical properties for all of the ice classes consistent with the bin representation. Since this ice settles quickly out of the vicinity of cloud top, it is probably not extremely important for these simulations, however it is done for the sake of completeness and is discussed in Chapter 3.

Chapter 3

TWO-STREAM RADIATIVE TRANSFER MODEL

In this chapter we discuss the development of a two-stream radiative transfer package which is flexible enough to interact with a variety of degrees of microphysical sophistication. The two-stream model (TSM) has been written in such a manner that modification of the model band structure and cloud optical properties may be accomplished with relative ease. At present, the radiation scheme is limited to 3 solar and 5 infrared bands, however in the future these numbers will be expanded to accommodate those who wish a more accurate representation of the radiative fields.

In any TSM one must specify essentially three things. First is the particular approximation to the radiance integrals, $\int_0^1 I(\tau,\mu)d\mu$ and $\int_0^1 \int_0^1 I(\tau,\mu')P(\mu,\mu')d\mu' d\mu$, to be utilized. Approximations such as assuming I constant in μ (which is related to the azimuth angle through the relation, $\mu = cos\theta$) or assuming I is a known function of μ are common. Each method works well in different situations ranging over variations in the solar zenith angle (θ_0), the thickness of the particular cloud layer, and how the extinction is partitioned between scattering and absorption. The second is the way in which gaseous absorption and scattering will be handled by the numerical scheme. Various methods can be utilized to solve the gaseous absorption problem and we will discuss our particular choice below. Finally, one must specify how the cloud hydrometeors scatter and absorb the incident fluxes. These properties are usually treated as "grey" (independent of wavelength) across a given spectral band. This can lead to over-absorption problems in solar broadbands for which there isn't any easy treatment.

We break this chapter into three separate sections in order to address the above in detail. The first section deals with the solution of the two-stream equations and the appropriate radiance approximation for our problems. The second deals with the gaseous

absorption framework and the parameterization of Rayleigh scattering and continuum absorption. Derivation of the cloud optical properties appropriately coupled to the various RAMS microphysical models is discussed in the third.

3.1 Some preliminaries

The two-stream equations are an approximate set of equations for the radiative fluxes. The fluxes are of importance for numerical cloud models as the radiative heating rates are proportional to the net flux divergence within a grid volume. The two-stream set is formulated by first averaging the the one-dimensional, time-independent radiative transfer equation (RTE) azimuthally. This equation may be written in the following form,

$$\mu \frac{dI(\tau,\mu)}{d\tau} = I(\tau,\mu) - J(\tau,\mu) - J_0(\tau,\mu,\mu_0) - B_0(\tau,T) \tag{3.1}$$

where τ is the optical depth, μ is the cosine of the zenith angle, μ_0 is the cosine of the solar zenith angle, and T is the local temperature. The function J is the scattering function for diffuse radiation, J_0 is the source function for solar radiation scattered into the diffuse component, and B_0 is the source function for emitted longwave (LW) radiation. These functions are given by,

$$J(\tau,\mu) = \frac{\omega}{2}\int_{-1}^{1} I(\tau,\mu')P(\mu,\mu')d\mu'$$

$$J_0(\tau,\mu,\mu_0) = \frac{\omega}{4\pi}P(\mu,\mu_0)F_s e^{-\tau/\mu_0}$$

$$B_0(\tau,T) = (1-\omega)B_\lambda[T(\tau)]$$

where μ is the direction we are interested in, μ' is all other directions, $P(\mu,\mu')$ describes the amount of radiation scattered from the μ' direction into the μ direction, $P(\mu,\mu_0)$ describes the amount of solar radiation scattered into the μ direction, F_s is the solar flux in a given band, B_λ is the Planck function at wavelength λ and temperature T, and ω is the single scatter albedo as is illustrated graphically in Fig. 3.1.

Since we are only interested in upwelling (F^+) and downwelling (F^-) fluxes, we integrate the azimuthally-independent RTE to produce a coupled set of ODEs for the fluxes defined as

$$F^{\pm}(\tau) = 2\pi \int_0^{\pm 1} I(\tau, \mu)\mu d\mu. \tag{3.2}$$

Upon integrating, one ends up with two integrals that must be evaluated in some fashion,

$$\int_0^{\pm 1} I(\tau, \mu) d\mu,$$

$$\int_0^{\pm 1} \left[\int_{-1}^{1} I(\tau, \mu') P(\mu, \mu') d\mu' \right] d\mu.$$

This is where the approximation comes in. Since the distribution of the radiance is not known *a priori*, one must come up with some approximation for its dependence upon μ in order to write the differential equations for the fluxes.

Many different methods have been employed over the years to approximate the above integrals so that two coupled equations for the fluxes emerge. Methods vary widely with Gaussian quadrature (Chandrasekhar, 1960), hemispheric mean values of the radiance (Coakly and Chylek, 1975), and radiance written as a function of the first moment (μ) of a Legendre Polynomial expansion (Eddington, 1916) as examples. Since no single approximation method can capture all of the physics in the radiance equations, all methods tend to fail in certain portions of parameter space with errors in the fluxes becoming as large as 20% for some methods (*e.g.* King and Harshvardhan, 1986 and Harshvardhan and King, 1992). In particular, the earlier methods mentioned above tended to fail badly for thin clouds in which scattering is dominated by the strong forward peak in the phase function for droplets. This inaccuracy also causes methods such as Eddington's to produce negative fluxes. The so-called delta-scaling method (Joseph *et al.*, 1976) removed the problem of negative fluxes and improved results by adding a delta-function forward peak to the approximated phase function, $P(\mu, \mu')$, at the point where $\mu = \mu'$. This captured some of the features of the forward scattering by particles, improving results. Our particular choice of approximation, which manifests itself in the reflection (r) and transmission (t) functions for a layer, will be discussed below.

The interaction of the incident fluxes with atmospheric gases and particulates must be specified in some manner so that accurate computations of the heating rates may be realized. We discuss the inclusion of gaseous properties in the sections below however, as the inclusion of cloud optical properties is of paramount importance for our work, we make an effort at this point to discuss some of the various methods which have been used for the inclusion of clouds in two-stream models.

The interaction of the two-stream model with cloud requires the definition of three parameters: the optical depth (τ_p), the single scatter albedo (ω_p) and the asymmetry parameter (g_p). Parameterizations of these properties have ranged from the very simple to complex depending upon the information supplied by the host model and the complexity of the radiative transfer scheme. Possibly the simplest method of computing the optical depth for clouds in climate scale models is based on the assumption that $Q_{ext} \simeq 2$ (Stephens, 1978) leading to optical depths that are proportional to the ratio of LWC to r_e. Longwave emissivity models have made use of emissivity approximations (Stephens, 1978) that are a decaying exponential function of the LWP (as LWP increases emissivity $\rightarrow$ 1).

Parameterizations for models have become more complex in time owing to the need for more detailed cloud/radiative interactions. Broadband models (models that break up the solar and infrared spectra into a few large bandwidths) normally make the assumption that cloud hydrometeor optical properties are "grey" (independent of wavelength) across the band. This assumption has its validity in the fact that the real and complex index of refraction of liquid water and ice vary slowly across appropriately spaced wavelength intervals. It was shown by Slingo and Schrecker (1982) that cloud drop optical properties are well approximated as grey in the solar by weighting the properties by the solar energy and integrating across the bandwidth. This methodology turns out to produce excellent results as long as at least four bands are used within the solar regime. Difficulties with treating the optical properties as grey within the near infrared (NIR) portion of the solar spectrum occur because the complex index of refraction of liquid water and ice varies over several orders of magnitude, thus fine spectral resolution is needed in order to accurately approximate the cloud optical properties. Computations of optical properties are less

sensitive in the infrared as the complex index of refraction varies much less, thus using broader intervals is much less of a problem.

Parameterization of the water drop properties is easily accomplished as the integrals of Slingo and Schrecker (1982) may be accomplished numerically using the Lorenz-Mie theory. As these integrals are expensive to compute, many researchers pre-compute these optical properties either over a range of effective radius (r_e) values or at a fixed r_e value for a given gamma distribution function and then fit the results with some sort of polynomial in r_e (Slingo, 1989). The singular use of r_e to describe cloud drop optical properties may be appropriate as Hu and Stamnes (1993) have shown evidence that suggests cloud drop optical properties are highly dependent on r_e but not the shape of the distribution function.

Methods that simplify the Lorenz-Mie computations, such as the anomalous diffraction theory of van de Hulst (1957), are computationally expedient but tend to overestimate the extinction and underestimate the scattering contribution (as will be discussed later). Recently, Mitchell (1997) has suggested an improvement to the ADT method that "corrects" for some of the missing physics in ADT. As will be shown, this method produces large improvements over ADT with the benefit of reduced computation times over Lorenz-Mie theory.

The parameterization of ice optical properties for cloud models remains a difficult problem as ice crystals have a variety of shapes and orientations, in addition no exact analytical theory exists. Many methods abound for ice optical property computations with perhaps the simplest being the use of equivalent surface area or volume spheres in Lorenz-Mie theory or ADT. The use of equivalent area ice spheres has been discussed by a number of authors (*e. g.* Mitchell and Arnott, 1994; Stackhouse and Stephens, 1991; Wielicki *et al.* , 1990). The use of ice spheres is most likely not appropriate; for example, Stackhouse and Stephens (1991) found that the measured albedo of cirrus clouds was significantly larger than that predicted by theory utilizing ice spheres.

Other parameterizations, such as Fu and Liou (1992) and Ebert and Curry (1992), make use of the work of Takano and Liou (1989) in which the optical properties of randomly oriented hexagonal columns were derived from ray tracing results. Fu and Liou (1992)

compute the optical properties for the ice crystals over a small range of mean effective size (0 to 150 μm) and fit the results with second order polynomials. For all bands in their radiative transfer model, the complex index of refraction is averaged over the band weighted by the solar (or infrared) energy at each wavelength. Optical properties are computed at the central wavelength of each band using the averaged indices of refraction for that band.

Ebert and Curry (1992) follow a similar methodology to Fu and Liou (1992) in that the optical properties are fit as functions of the effective size (here an effective radius derived from observational data). Fits for hexagonal ice covered a slightly smaller range (0 to 140 μm), however fits produced for each of their model bands were linear in r_e; the exception being τ which was fit with an inverse function of r_e.

Mitchell and Arnott (1994), picking up on the Takano and Liou (1989) result showing that ice crystals scatter more and absorb less than equivalent spheres, developed a modified version of ADT for differing ice habits. Their methodology hinges on the computation of an effective distance that a ray passes through an ice crystal which is parameterized for randomly oriented particles as dependent upon the ratio of the ice volume to the projected area. This produces less absorption and more scattering in the ADT results. Mitchell and Arnott (1994) results cover a larger size range than Fu and Liou (1992) or Ebert and Curry (1992) (0 to 500 μm), however, they do not broach the issue of use in a broadband model nor of the appropriateness of the parameterization at larger ice sizes.

Indeed, the coupling of multi-moment, detailed microphysical models with two-stream radiation models is a task that has not yet been accomplished. Detailed bulk microphysical models such as Ferrier *et al.* (1994), Walko *et al.* (1994), and Meyers *et al.* (1997) contain various hydrometeor classes with a broad range of size distributions and methods that predict ice habit in cold clouds, making couplings to radiative transfer schemes difficult. Couplings of explicit bin microphysical models to LES and mesoscale models is becoming more prevalent (*e. g.* Feingold *et al.* , 1994; Olsson *et al.* , 1997; Stevens *et al.* , 1996; Reisin *et al.* , 1996; Kogan *et al.* , 1995) opening the need for couplings between the radiative transfer models and these microphysical schemes. In the section on cloud optical

properties, we describe our schemes for detailed couplings between the two-stream model and microphysical models with varying degrees of complexity.

3.2 Solution of the two-stream equations

In the development of any method, it is always instructive to revisit equation solutions as much can be learned about the structure of the system that one is attempting to model. In addition, the solution method presented here (using matrix methods) is not often used in the literature (with Flatau and Stephens, 1988 and Gabriel *et al.* , 1997 being notable exceptions). Thus, we include a thumbnail sketch of the two-stream solution in Appendix A along with the interaction principle for mulitple plane-parallel layers used in RAMS. This has the added benefit of aiding future users of the model.

3.2.1 Choice of two-stream approximation

For our particular case of Arctic stratus clouds, we deal with more opaque layers (solar $\tau \simeq$ 5-10) at somewhat large solar zenith angles ($\theta_0 \simeq$ 50-70°). Our two-stream code is formulated with two different sets of approximations to the integrals in Eq. 3.3; the first discussed in Ritter and Geleyn (1992) (RG) and the second being the δ-Eddington (DE) approximation (Joseph *et al.*, 1976). Recall that these approximations appear in the reflection and transmission functions; particularly in the γ-terms in the two-stream equations. Derivations of these terms for a variety (but not all) approximations may be found in some references (*e.g.* Meador and Weaver, 1980; Zundkowski *et. al.*, 1985 and Liou, 1982). The coefficients used by Ritter and Geleyn (1992) are given by,

$$\begin{aligned}
\beta_0 &= \frac{4+g}{8(1+g)} \\
\gamma_1 &= U(1-\omega_0)[1-\beta_0(1-f)] \\
\gamma_2 &= U\omega_0\beta_0(1-f) \\
\gamma_3 &= \left[\frac{1}{2} - \frac{3}{4}\frac{g\mu_0}{1+g}\right]\omega_0(1-f) \\
\gamma_4 &= \omega_0(1-f) - \gamma_3 \\
f &= g^2
\end{aligned}$$

where g is the asymmetry parameter and f is the amount of radiation contained in the forward scattering peak of the Heney-Greenstein phase function. These coefficients are derived by considering I as a constant function of μ; backscatter fractions (simply the integral of the phase function) are approximated by utilizing the δ-approximation (Potter, 1970) for both direct and diffuse radiation streams. The method originated in Zundkowski *et al.* (1980) as a way of producing accurate fluxes without backscatter fractions becoming negative.

For the δ-Eddington model the coefficients are given by,

$$\begin{aligned}
\gamma_p &= \frac{g-f}{1-f} \\
\gamma_1 &= \frac{1}{4}[7-\omega_0(4+3\gamma_p)] \\
\gamma_2 &= -\frac{1}{4}[1-\omega_0(4-3\gamma_p)] \\
\gamma_3 &= \frac{1}{4}[2-3g\mu_0] \\
\gamma_4 &= 1-\gamma_3.
\end{aligned}$$

which are derived by assuming that I is a known function of μ ($I = I_0 + I_1\mu$) and then integrating Eq. 3.3 including a δ-function for forward scattering.

Each two-stream approximation works well and fails in certain portions of parameter space as examined by King and Harshvardhan (1986). Their computations, while spanning τ and μ_0 space, only covered two particular single-scatter albedos ($\omega_0 = 1,\ 0.9$). Recently, Gabriel (personal communication) has done a comparison of various two-stream approximations with a 32-stream code spanning τ and ω_0 space for selected μ_0 values. Comparisons of the fluxes at top and bottom of an atmospheric layer were made utilizing a top of the atmosphere downwelling flux of $F_t^- = 1$. According to Gabriel, the δ-Eddington method tends to out perform other two-stream approximations in general and does especially well at large solar zenith angles. His results, however , did not utilize the approximation of Ritter and Geleyn (1992) which our model was originally built on. Since we are interested in large solar zenith angle cases, we show results of the comparison between the 32-stream results of Gabriel with the δ-Eddington and Ritter and Geleyn (1992) approximations for a solar zenith angle of $\theta_0 = 75°$ as motivation for the Arctic stratus simulations.

Figure 3.2 shows the relative error in F^+ at the top of the layer for the two approximations. The plot spans τ and ω space covering a range of $\tau = 0.1 \rightarrow 80$. The relative error is defined as,

$$Error(\%) = \frac{F_{32-strm} - F_{2-strm}}{F_{32-strm}}, \tag{3.3}$$

for upwelling and downwelling fluxes. Plots for the δ-Eddington method were graciously supplied by Gabriel (personal communication). One immediately notices that the δ-Eddington approximation produces good results for optical depths greater than about $\tau = 1$ and covering the whole of ω. The large errors for small optical depths (up to 31 %) occur when the upwelling fluxes are very small; here, the absolute error in the fluxes is small and larger relative errors are predominately due to the division by a very small flux. Ritter and Geleyn's (1992) functions, however, produce significant deviations in the upwelling flux over most of parameter space with a swath of small error existing in the center of the figure.

Figure 3.3 shows the relative error in F^- at the base of the layer for the two approximations. Here, δ-Eddington produces errors on the order of 10 % for most of the parameter space except for a portion at large τ and small ω. Relative errors in this region are large, however the downwelling flux at the base of the layer is small here. The associated absolute error (not shown) is quite small illustrating that this increase in relative error is due to the division by a very small flux. Ritter and Geleyn's (1992) functions show larger errors over most of parameter space with a strong gradient in relative error around $\tau = 5$. Here the error jumps rapidly and we have plotted it only to the 40 % level. As τ increases the error jumps rapidly to values larger than 100 % .

Since we deal with Arctic stratus at large solar zenith angles and optical depths between 5 and 10, the above results in association with the results of Gabriel (personal communication) suggest that the δ-Eddington method is the most appropriate method at for our purposes. Here we should also note that as the solar zenith angle changes the applicability of Ritter and Geleyn's method becomes more appropriate, particularly for $\theta_0 > 50°$.

3.3 Gaseous absorption

The set of two-stream equations discussed above are for a set of monochromatic fluxes. This set of equations now needs to be applied to both the solar and infrared spectra including gases and particulates. Of course, computations of the fluxes at individual wavelengths is too computationally expensive for any sort of modelling application and, therefore, we resort to solving the equations over broad band-widths. Our choice of method is that of the Fast Exponential Sum-Fitting (FESFT) method of Ritter and Geleyn (1992) using their choice of band limits. Some modifications to the number of gaseous absorption and the Planck function integrated over truncated limits. The total number of gaseous absorption coefficients has been reduced and Planck function fits use third-order polynomials. These combined have reduced the computational cost of the model by a factor of 2 while retaining accuracy. For a complete discussion of the gaseous absorption method, band limits, Rayleigh scattering and continuum absorption calculations included in RAMS, see Appendix B.

3.4 Cloud optical properties

The cloud optical properties utilized in the two-stream model are derived in connection to the various microphysical methods utilized in the RAMS model as discussed in the Chapter 2. Note that essentially two microphysical models are routinely used, the first assumes size-spectra determined by analytical gamma distribution functions with fixed shapes, ν, while the second is an explicit (bin) representation of the distribution functions of water and ice, without any prescribed distribution shape dependence.

We derive the cloud optical properties utilizing the solar or infrared energy per wavelength weighting method of Slingo and Schrecker (1982). The advantage of this method is that the absorption and scattering at each wavelength within a given band is weighted by the amount of energy contained at that wavelength. The two-stream model requires three optical parameters for the various hydrometers, the single scatter for particles (ω_p), the extinction coefficient (β_{ext}) and the asymmetry parameter (g). For a given cloud optical

property, σ, the averaging of Slingo and Schrecker (1982) takes the form,

$$\begin{aligned}
\bar{\sigma} &= \frac{1}{\bar{E}} \int_{\Delta\lambda} \left[\int_0^\infty A(D)\sigma(D,m,\lambda)n(D)dD \right] E_\lambda d\lambda \\
\bar{E} &= \int_{\Delta\lambda} E_\lambda d\lambda \\
E_\lambda &= S_\lambda \text{ (Solar)} \qquad E_\lambda = B(\lambda, T_s) \text{ (Infrared)}
\end{aligned}$$

where $A(D)$ is the projected area of the hydrometeor being considered, σ is the optical property being considered (i.e. Q_{ext}), S_λ is the solar energy density, $T_s = 273K$ is the reference temperature for the Planck function, and $n(D)$ is the particular distribution function. For the gamma microphysical model the distribution function (Walko et al., 1995) is given by the generalized gamma distribution (Eq, 2.1). The bin microphysical model has an explicit form of $n(D)$ as discussed in the previous chapter.

3.4.1 Errors in Broadband Solar Optical Properties

Optical properties for cloud hydrometeors can generally be considered grey because the index of refraction does not vary rapidly for most bands. Thus, an average value of the above quantities is suitable. This is, however, not true within the near-IR band ($0.7 \rightarrow 4.64\mu m$) where the complex index of refraction varies over several orders of magnitude. This causes problems as using a single number to characterize absorption causes over-absorption for optically thick clouds. To illustrate the possible magnitude of error, we solved the two-stream equations for a single atmospheric layer composed of liquid water drops that follow the distribution function of Eq. 2.1. The number of droplets was varied along with the characteristic diameter of the distribution function in order to span a realistic parameter space. Computations were done over the solar and near-IR with our 3-band solar model as compared to an accurate representation as given by a 30-band solar model. Relative errors were computed comparing the 3-band to the 30-band results. Derivations of optical properties by this method can lead to errors of up to 44% in the absorption and 9% in the reflection as is shown in Fig. 3.4. To adjust for the over-absorption illustrated in Fig. 3.4 we artificially limited the complex index of refraction, c_i in effect limiting the total amount of absorption possible. This was done by not allowing c_i to become greater than its mean

value in the near-IR region during the integration of Eq. 3.4,

$$\begin{aligned} \bar{c_i} &= \frac{1}{\Delta\lambda}\int_{\lambda_1}^{\lambda_2} c_i(\lambda)d\lambda \\ c_i(\lambda) &= min(c_i(\lambda), \bar{c_i}). \end{aligned} \tag{3.4}$$

Out of all the various methods tested, this method produced the best results in comparison to the 30-band solar model. Figure 3.5 shows that the error in the reflection is never greater than 6% while the absorption error has decreased from values of around 20% to near 9% covering most of the parameter space. This method produces even better results for the ice optical property model and is most likely due to the fact that the ice model (described below) reduces the absorption based on the fact that rays travel a shorter distance, on average, through ice particles than through water drops.

A solution to the integral in Eq. 3.4 requires knowledge of the optical coefficient, σ, for each hydrometeor type (discussed in the following subsections). In the next two subsections we discuss the parameterization of the optical coefficients for the two-stream model. We begin with the liquid phase since this is the simplest case to treat as analytical solutions exist for spherical particles. The ice phase follows and a discussion of how existing spherical particle parameterizations are modified to approximately treat non-spherical ice is discussed.

3.4.2 Liquid-phase parameterization

Accurate computation of the optical properties for liquid drops may be done as an exact analytical solution exists in the Lorenz-Mie theory (van de Hulst, 1957). The Lorenz-Mie solution, however, is an exceedingly cumbersome and computationally expensive method for arriving at the cloud optical properties. This is easily seen upon examination of eq. 3.4 where we note that the integral over the band and the integral over the size must be done numerically as the Lorenz-Mie theory does not afford an analytical solution to these integrals. Of course, one does not want to compute these numerical integrals during a model simulation. Thus, we look for methods that well approximate Lorenz-Mie theory but allow for the size integral to be solved analytically. It is true that there is not an analytical solution for the wavelength integral for any of the methods that we describe

here and, thus, this integral must always be done numerically. We do, however, have a method of fitting the data produced by numerically integrating Eq. 3.4 over the parameter space of the distribution function (this spans only D_n). This procedure will be discussed in the last subsection to this chapter. It may be argued that since the wavelength integral has to be evaluated numerically in any case that there is no reason not to use Lorenz-Mie theory. However, these integrals have to be done not only for a range of D_n values, but it must also be done for various ν values (this is fixed during a RAMS simulation), for all seven hydrometeor classes in RAMS and for all 8 radiation bands. The computations for just a single ν value can take over one week of computer time to produce the necessary fits. Having an analytical solution for the size integral greatly reduces this computational cost, with all of the needed fits being produced in less than one day.

One particular method that has been used widely in the community is the Anomalous Diffraction Theory (ADT) of van de Hulst (1957). In this theory the interference of a ray that passes through a sphere and one that passes outside of the sphere is computed at some large distance from the sphere. From this analysis one can derive the extinction and absorption coefficients for the sphere. The extinction coefficient is given by,

$$\begin{aligned} Q_{ext}(D,\lambda,m) &= 2K(tD) \qquad (3.5) \\ t = u + iv \quad &, \quad u = \frac{2\pi}{\lambda} n_i, \\ v = \frac{2\pi}{\lambda}(n_r - 1) \quad &, \quad m = n_r - i n_i \\ K(x) &= 1 + 2Re\left[\frac{e^{-x}}{x} + \frac{e^{-x} - 1}{x^2}\right] \qquad (3.6) \end{aligned}$$

where m is the complex index of refraction and D is the diameter of the sphere. The absorption coefficient is given as,

$$Q_{abs} = K(wD) \quad , \quad w = \frac{4\pi}{\lambda} n_i. \qquad (3.7)$$

These functions are easily integrated over the gamma distribution (Eq. 2.1), (see Flatau, 1992) producing a closed-form analytical solution that may be used in Eq. 3.4. These functions, however, do produce errors in comparison to Lorenz-Mie theory. Figure 3.6 shows a comparison of ADT to Lorenz-Mie theory at $\lambda = 0.5\mu m$ as a function of drop size.

Note that the extinction and scattering coefficients are significantly less than that predicted from the Lorenz-Mie theory. Figure 3.7 shows the relative error for the ADT derive Q_{ext} and ω_p in comparison to the Lorenz-Mie theory plotted over the solar wavelengths and drop size. The extinction error can become as large as 15% but is usually around 3% for the majority of the wavelength and size space. Error in the single scatter for droplets shows a swath of about 9% error at around $\lambda = 2\mu m$ with the areas immediately above and below containing errors of about 6% . The error in ADT for the IR wavelengths is shown in Fig. 3.8. The error in the extinction has a fan-profile showing areas of error near 15% . The single scatter error in the IR shows errors as large as 15% at the large particle sizes for almost all λ with an area around 100 μm showing lower errors.

It is possible to reduce the error with respect to Lorenz-Mie theory even further as is shown by Mitchell (1997) where the ADT parameterization is extended. Mitchell (1997) parameterizes the "missing physics" in ADT, accounting for such phenomena as internal reflection/refraction, resonance tunneling and edge effects that are not accounted for in standard ADT. In Mitchell's (1997) method, the ADT absorption coefficient is modified by two terms,

$$\begin{aligned} Q_{abs,m} &= (1 + C_{ir} + C_{res})Q_{abs} \\ C_{ir} &= a_{ir} exp\left[\frac{-8\pi n_i D}{3\lambda}\right] \\ C_{res} &= r_a \frac{k^m e^{-\epsilon k}}{k_{max}^m e^{-m}} \end{aligned} \tag{3.8}$$

where Q_{abs} is the standard ADT form given by Eq. 3.7, C_{ir} is the coefficient that corrects for internal reflection/refraction, C_{res} is the coefficient that corrects for resonance tunneling, and the other variables in Eq. 3.8 are given by,

$$\begin{aligned} a_{ir} &= \frac{1}{4} + \frac{1}{4}e^{-1167 n_i}, \\ r_a = 0.7393 n_r - 0.6069 \quad &, \quad m = \frac{1}{2}, \\ k = \frac{D}{\lambda} \quad &, \quad k_{max} = \frac{m}{\epsilon}, \\ \epsilon &= \frac{1}{4} + 0.6\left\{1 - exp\left[-\frac{8\pi n_i}{3}\right]\right\}^2. \end{aligned}$$

The C_{ir} term accounts for the fact that for small absorption, internal reflection and refraction can increase the total amount of absorption by the particle. The C_{res} term accounts for the fact that when $n_r > 1$ resonance may arise that causes the tunneling of photons from outside of the drop to some short distance inside where they may be absorbed. The extinction coefficient is modified by adding terms for the resonance tunneling and edge effects which are given in Mitchell (1997) by,

$$\begin{aligned} Q_{ext,m} &= \left(1 + \frac{C_{res}}{2}\right) Q_{ext} + Q_{edge} \\ Q_{edge} &= 2\left[1 - exp\left(\frac{-0.06\pi D}{\lambda}\right)\right]\left(\frac{piD}{\lambda}\right)^{-2/3}. \end{aligned} \tag{3.9}$$

The edge effect term, Q_{edge}, corrects for the fact that grazing radiation reflected from the edge of a drop may interfere with grazing radiation that was not reflected. See Mitchell (1997) for a more complete description of the physics included in the above terms.

Figures 3.9 and 3.10 show the relative error associated with Mitchell's (1997) modified ADT (MADT) method for both the extinction and droplet single scatter covering the solar and IR regions. These results should be compared with those for standard ADT given in Figs. 3.7 and 3.8. Comparing the solar extinction errors, one immediately notes that MADT produces smaller errors across the entire parameter space. Errors for MADT extinction usually lie between 1.2 and -0.4% where as ADT lies near 3% . At the small particle end errors are drastically reduced by using MADT, however, errors for very small ($\simeq 1 - 4\ \mu m$) radius drops can be as large as 15 % . The error in the single scatter, ω_p, for MADT is also reduced over that for ADT; reductions in relative error of the order of 2% over most of parameter space is quite common. The biggest difference, however, is in the IR region where errors in extinction and single scatter for MADT are significantly reduced over that of standard ADT. Notice that much of the MADT error space contains errors of 2% or less with the largest errors (up to about 8%) existing at small sizes but large wavelengths (where the amount of energy is small). Standard ADT, contains noticeably larger errors with 9 to 15% covering much of the space. The single scatter error is similar showing errors for MADT between 2 and 7% covering much of the space and, again, the largest errors (up to 14%) at small drops sizes and larger wavelengths. Standard ADT

shows small errors (1 to 5%) in a vertical swath between 50 and 100 μm. The small and large particle ends, however, contain significant errors with values up to 15 % .

Since the above MADT formulae may be easily integrated over a gamma size distribution function and they show less error in comparison to Lorenz- Mie theory we choose to use the MADT functions in our integration of Eq. 3.4. The integration of the size distribution for the gamma microphysical model and the parameterization for the bin microphysical model are discussed below in the subsection on microphysical model connections.

Of course, the above functions only produce the parameterizations for Q_{ext} and ω_p; a parameterization is still needed for the asymmetry parameter g_p and this may be attained with Lorenz-Mie theory. As we noted above, it is quite computationally expensive to compute the numerical solution to Eq. 3.4 with Lorenz-Mie theory for the variety of hydrometeor species used in RAMS. To get around this problem we make use of the hypothesis of Hu and Stamnes (1993) that the optical properties for an arbitrary distribution function may be parameterized largely in terms of the effective radius, r_e. The claim being based on the assumption that the optical properties are insensitive to other parameters of the distribution function. Since our range of variation for RAMS is over the D_n and ν space of the distribution function, we may be able to produce data for g_p over D_n for a given ν and then use Hu and Stamnes' (1993) hypothesis to produce g_p at different values of ν. This would require only two pre-calculated solutions to Eq. 3.4; one for water drops at a give ν and one for ice spheres at a given ν. We know that the effective diameter, D_e, is related to D_n by,

$$D_e = \frac{\int D^3 n(D) dD}{\int D^2 n(D) dD} = (\nu + 2) D_n. \tag{3.10}$$

Thus, if we have computed g_p over a range of D_n for a given ν (say, ν_o) and we would like to find g_p for a different ν value (say ν_n) then, according to Hu and Stamnes (1993), we equate the effective diameter of the ν_n distribution to that for which the g_p were computed,

$$D_e^{(n)} = (\nu_o + 2) D_n^{(0)}. \tag{3.11}$$

Now one simply finds the new D_n value (D_n') associated with this $D_e^{(n)}$,

$$D_n' = \frac{D_e^{(n)}}{\nu_n + 2}, \tag{3.12}$$

and then uses this in the derived formulate for g_p as a function of D_n $(g_p(D'_n))$.

Figure 3.11 illustrates this graphically for distributions with shapes ranging from $\nu = 1 \rightarrow 14$ over D_e for g_p and Q_{ext}. Note that the potential error is quite great for narrow distributions. Maximum errors reach to 40% in some cases. Thus, in utilizing the method of Hu and Stamnes (1993) we produce three sets of data for $\nu = 1, 6$, and 14 and interpolate in D_e-space as needed. This produces little error and reduces the number of required computations. Our use of the method advocated by Hu and Stamnes (1994) is limited to computations of g_p. As is shown in Fig. 3.11, errors in Q_{ext} at small droplet sizes can be quite large and, since cloud droplet size distributions can be quite narrow, we choose to utilize MADT theory to produce the extinction and single scatter for droplet size distributions with various ν values. Indeed, errors in the extinction more strongly controls the flux divergence and, hence, the heating/cooling rates within the cloud emphasizing the need for more accuracy in these cases.

It should be noted that the larger errors experienced here as compared to Hu and Stamnes (1993) are due to the fact that we examined narrower distribution functions than was shown in their paper. Errors seem to become much larger once the distribution attains a narrow shape, thus this method is questionable for distributions newly formed through a nucleation process or narrow cloud top spectra.

3.4.3 Ice phase parameterization

Unlike water drops, there isn't an analytical solution for the scattering of non-spherical particles that have sharp edges and sizes similar to the wavelength of light. The closest one may come is the oblate and prolate spheroid solution to the Lorenz-Mie theory (Asano and Sato, 1980). This solution, however, is even more cumbersome than the Lorenz-Mie theory for spheres since the orientation of the particle now plays an important role. This is not the only obstacle to using this solution, it is also extremely unstable for particles with sizes much greater than the wavelength of the incident light[1]. Some researchers have utilized

---

[1]Recently, stable solutions to the scattering problem for oblate and prolate spheroids has been developed. This method allows for extreme prolate and oblate shapes that well approximate plates and columns (Stamnes, personal communication)

equivalent surface area or equivalent volume spheres; however, as is noted in Mitchell and Arnott (1994), this approximation tends to over-estimate the amount of absorption as the path of the radiation through the sphere is longer than it would be through a crystal. To correct for this, Mitchell and Arnott (1994) devised a method where by ADT is modified to account for the shorter path through the crystal. The method of Mitchell and Arnott (1994) is based on the absorption formula for large spheres given by,

$$Q_{abs,l} = 1 - exp\left[-\frac{4\pi n_i}{\lambda} d_{e,s}\right] \tag{3.13}$$

where $d_{e,s}$ is the effective distance a ray passes through the sphere and is given by the ratio of volume to projected area, $d_{e,s} = V/A = 2/3D$. For ice crystals, this same absorption function is postulated to hold except that now the effective distance through the ice particle, d_e, is used along with the term for the integral reflection/refraction correction as per Mitchell *et al.* (1996),

$$Q_{abs,i} = [1 + C_{ir}(d_e)]\left[1 - exp\left(-\frac{4\pi n_i}{\lambda} d_e\right)\right]. \tag{3.14}$$

The parameter d_e is now the ratio of the crystal volume to its projected area. We use formulae from Mitchell and Arnott (1994), Mitchell *et al.* (1987) and Auer and Veal (1970) to produce the values of d_e for three ice classes: hexagonal plates, hexagonal columns and bullet rosettes (5 branches). Figure 3.12 shows a plot of d_e, the projected area $P(L)$, and the volume of various ice habits. The effective distance is much lower for the non-spherical habits than for the ice sphere. This is due to the fact that the volume of the crystal increases by a much smaller amount than the increase in the projected area as the maximum dimension (L) increases. Since we wish to eventually integrate the absorption over a gamma distribution function of maximum crystal dimension, d_e needs to be, at most, a linear function of the maximum crystal dimension, L. Mitchell and Arnott (1994) parameterize d_e by fitting it as a linear function of L over short spans in L so that a linear function may be justified. In Mitchell and Arnott (1994) only a few size ranges are necessary since their parameterization only spans the size range of $L = 1 \rightarrow 500\mu m$. In our case, the size range is considerably greater extending out to 10,000 μm for the cases

of aggregates and snow. In order to account for these possibilities we find that 5 ranges in size are necessary for the linear fit,

$$d_e = a_i + b_i L, \tag{3.15}$$

to be valid. Figure 3.12 shows us that the most variation is at the small size end, and this is where finer size resolution is necessary to make the linear fit work. Table 3.4.3 shows the size ranges used and the coefficients for the d_e fit for each crystal type.

Range (μm)	1-30	30-100	100-500	500-2000	2000-10,000
hex. plates a_i ($\times 10^{-6}$)	0.9642	4.8972	15.903	39.924	88.857
hex. plates b_i	0.3495	0.1896	0.0845	0.0383	0.0164
hex. columns a_i ($\times 10^{-6}$)	0.1728	8.988	30.218	65.702	135.730
hex. columns b_i	0.4490	0.4026	0.1226	0.0520	0.0209
rosettes a_i ($\times 10^{-6}$)	0.9108	3.883	11.517	28.189	65.767
rosettes b_i	0.2660	0.1369	0.0676	0.0352	0.0174

Table 3.1: Coefficients for d_e fit in *mks* units.

The extinction coefficient is computed through Eq. 3.9 for equivalent volume spheres,

$$D_s = \left[\frac{6}{\pi \rho_i} m_i(L)\right]^{1/3}, \tag{3.16}$$

where m_i is the mass and ρ_i is the density of the given crystal habit for the maximum dimension L. Formulas from Mitchell *et al.* (1987) and Auer and Veal (1970) for mass and ice density as a function of maximum dimension are used here (see Harrington *et al.*, 1994 for formulas).

In order to compute the absorption and extinction coefficients, the formulation of the projected area of the ice crystals is needed. The projected area may be put into the general form,

$$P(L) = B_p L^{\alpha_p} + C_p L^{\beta_p}, \tag{3.17}$$

where the above coefficients are a function of the ice habit and size. The values for these coefficients are given in Mitchell and Arnott (1994).

3.4.4 Form of the RAMS parameterization

Within this subsection we discuss the form of the parameterization that is used in the RAMS gamma and bin microphysics. These are based on the methods discussed above with the only exception being the derivations of the optical properties for the bin liquid water model (which uses Lorenz-Mie theory).

The gamma microphysics

Since the distribution function is known for the gamma microphysical model, we may use the modified ADT forms for water and ice and analytically solve the size integral in Eq. 3.4. Let us denote this size integral by,

$$\bar{\beta} = \int_0^\infty A(D)\sigma(D, m, \lambda)n(D)dD. \tag{3.18}$$

This integral has been solved for the liquid and ice ADT extinction, β_{ext}, and absorption, β_{abs}, functions in Mitchell and Arnott (1994) and Mitchell (1997). However, the form of the solution given in these papers is not for the generalized gamma distribution function given by Eq. 2.1. Also, the forms presented in those papers are not particularly elegant and, in addition, the equivalent sphere method for ice presented in Mitchell and Arnott (1994) can become numerically unstable, thus an alternative derivation is presented.

For the liquid water drop parameterization, we solve Eq. 3.18 using the gamma distribution (Eq. 2.1) along with the MADT functions above (Eqs. 3.8 and 3.9) in place of σ. One notices after a little inspection that, in order to solve these integrals, one must in general solve integrals of the form,

$$\kappa = \frac{1}{\bar{A}} \int_0^\infty \frac{\pi}{4} D^2 K(xD) a D^b e^{-cD} n(D) dD, \tag{3.19}$$

where $\bar{A}$ is the total projected area, the general variables x, a, b, and c are not functions of size and the K function is defined in Eq. 3.6. Therefore, it is quite useful to find the solution of this integral as then it is quite easy to simply write down the solution to the integrals involving the extinction and absorption functions. Much manipulation reveals

the solution to this integral to be,

$$\begin{aligned}
\kappa(D_n, x, a, b, c, \nu) &= \kappa_1 + 2Re[\kappa_2 + \kappa_3] \qquad (3.20)\\
\kappa_1 &= \left[\frac{aD_n^b}{(1+cD_n)^{\nu+b+2}}\right]\frac{\Gamma(\nu+b+2)}{\Gamma(\nu+2)}\\
\kappa_2 &= \left[\frac{aD_n^b}{xD_n(1+cD_n+xD_n)^{\nu+b+1}}\right]\frac{\Gamma(\nu+b+1)}{\Gamma(\nu+2)}\\
\kappa_3 &= \frac{aD_n^b}{(xD_n)^2}\left\{\frac{1}{(1+cD_n+xD_n)^{\nu+b}} - \frac{1}{(1+cD_n)^{\nu+b}}\right\}\frac{\Gamma(\nu+b)}{\Gamma(\nu+2)}
\end{aligned}$$

where $\bar{A}$ is the integral of the projected area and is given by,

$$\bar{A} = \int_0^\infty A(D)n(D)dD = N_t\frac{\pi}{4}D_n^2\frac{\Gamma(\nu+2)}{\Gamma(\nu)}. \qquad (3.21)$$

Note the similarity of the κ-function to the K-function for ADT given by Eq. 3.6. The integral to the absorption function may now be written down quite simply. After some simple manipulations the solution can be cast into the form,

$$\beta_{abs} = \bar{A}[\bar{Q}_{abs} + \bar{Q}_{ir} + \bar{Q}_{res}], \qquad (3.22)$$

where $\bar{Q}_{abs}$ is the solution to the integral for the standard ADT formula, $\bar{Q}_{ir}$ is associated with the integral of the internal reflection/refraction term and $\bar{Q}_{res}$ is associated with the integral of the resonance tunneling term. These functions are given by the following,

$$\bar{Q}_{abs} = 1 - \kappa(D_n, 0, 1, 0, y, \nu) \qquad (3.23)$$

$$\bar{Q}_{ir} = \kappa(D_n, 0, a_{ir}, 0, y, \nu) - \kappa(D_n, 0, a_{ir}, 0, 2y, \nu) \qquad (3.24)$$

$$\bar{Q}_{res} = \kappa(D_n, 0, f_{res}, m, \epsilon k', \nu) - \kappa(D_n, 0, f_{res}, m, y + \epsilon k', \nu) \qquad (3.25)$$

where we have defined the following coefficients,

$$\begin{aligned}
y &= \frac{8\pi n_i}{3\lambda}\\
f_{res} &= \frac{r_a}{k_{max}^m \lambda^m e^{-m}}, k' = \frac{1}{\lambda}.
\end{aligned}$$

This function is easily coded and requires little computation time for the integral solution (as compared to Lorenz-Mie theory solutions).

We may use the integral given by Eq. 3.20 to solve for the MADT extinction function giving,

$$\beta_{ext} = \bar{A}\left[\bar{Q}_{ext} + \bar{Q}_{res,e} + \bar{Q}_{edge}\right], \tag{3.26}$$

where $\bar{Q}_{ext}$ is the integral of the standard ADT extinction function, $\bar{Q}_{res,e}$ is the integral of the resonance tunneling term for extinction, and $\bar{Q}_{edge}$ is the integral of the edge effect correction term. Each term is given by the expressions,

$$\begin{aligned}
\bar{Q}_{ext} &= 2\kappa(D_n, t, 1, 0, 0, \nu) \\
\bar{Q}_{res,e} &= \kappa(D_n, t, f_{res}, m, \epsilon k', \nu) \\
\bar{Q}_{edge} &= 2[\kappa(D_n, 0, f_{edge}, -2/3, 0, \nu) - \kappa(D_n, 0, f_{edge}, -2/3, x', \nu)],
\end{aligned} \tag{3.27}$$

where the definitions $f_{edge} = (\pi/\lambda)^{-2/3}$ and $x' = 0.06\pi/\lambda$ are used. As in the case of absorption, these functions are quickly evaluated as compared to numerical solutions of the Lorenz-Mie theory.

Figure 3.13 illustrates the differences between MADT, ADT and Lorenz-Mie theory for Q_{ext} and ω_p. The plots show the results for model band 1 with a distribution shape parameter of $\nu = 2$; the integral over wavelength was computed numerically. MADT consistently produces better results than ADT in comparison to Lorenz-Mie theory. This turns out to be true for all bands over most of parameter space. However, as is shown in Fig. 3.14 for model band 6, there are portions of the domain over which ADT performs better. For characteristic diameters, D_n, between 15 and 40 μm ADT outperforms MADT in predicting the single scatter. The extinction, however is better predicted over the entire space by MADT. When considered in its entirety, MADT consistently improves prediction of the optical properties over ADT.

The ice microphysical optical properties are derived in an analogous fashion with the exception being that the formula for the projected area of the ice particles is used. This method is similar to that presented in Mitchell *et al.* (1996), however, here we use the generalized gamma distribution function given by Eq. 2.1 and cast the solution into a more elegant form. The absorption function given by Eq. 3.14 is used along with Eqs. 3.15

and 3.8 in the integral Eq. 3.4 to obtain an integral for the absorption. Unfortunately, as is shown in Table 3.4.3, the formula for d_e has 5 different bounding sizes. Because of this, we have to solve truncated gamma function integrals. In general, there are three types and these are given by,

$$\begin{aligned}
\beta_{abs,1} &= \int_0^{D_l} P(L)Q_{abs,i}(L,m,\lambda)n(L)dL, \\
\beta_{abs,2} &= \int_{D_l}^{D_h} P(L)Q_{abs,i}(L,m,\lambda)n(L)dL, \\
\beta_{abs,3} &= \int_{D_h}^{\infty} P(L)Q_{abs,i}(L,m,\lambda)n(L)dL,
\end{aligned} \tag{3.28}$$

where D_l is some lower size bound and D_h is some upper size bound. Since all integral solutions follow from the solution to $\beta_{abs,2}$, we solve only this integral. By substituting in the appropriate definitions, and using Eq. 3.20 we find the solution to be,

$$\beta_{abs,2} = \bar{P}_{l,h}[\bar{Q}_{abs,l,h} - \bar{C}_{ir,l,h}] \tag{3.29}$$

where the total projected area $\bar{P}_{l,h}$ is given by,

$$\begin{aligned}
\bar{P}_{l,h} &= \frac{N_t}{\Gamma(\nu)}\{B_p D_n^{\alpha_p}[\gamma(\nu+\alpha_p, D_h/D_n) - \gamma(\nu+\alpha_p, D_l/D_n)] \\
&\quad + C_p D_n^{\beta_p}[\gamma(\nu+\beta_p, D_h/D_n) - \gamma(\nu+\beta_p, D_l/D_n)],
\end{aligned}$$

and the integrated absorption and internal reflection/refraction terms are,

$$\begin{aligned}
\bar{Q}_{abs,l,h} &= 1 - \frac{N_t e^{-Y a_i}}{\Gamma(\nu)}[\psi_{l,h}(D_n, B_p, \alpha_p, b_i, Y, \nu) - \psi_{l,h}(D_n, C_p, \beta_p, b_i, Y, \nu)] \\
\bar{C}_{ir,l,h} &= \frac{N_t a_{ir} e^{-Y a_i}}{\Gamma(\nu)}[\psi_{l,h}(D_n, B_p, \alpha_p, b_i, Y, \nu) - \psi_{l,h}(D_n, C_p, \beta_p, b_i, Y, \nu)] \\
&\quad + \frac{N_t a_{ir} e^{-2Y a_i}}{\Gamma(\nu)}[\psi_{l,h}(D_n, B_p, \alpha_p, b_i, 2Y, \nu) - \psi_{l,h}(D_n, C_p, \beta_p, b_i, 2Y, \nu)].
\end{aligned}$$

The $\psi_{l,h}$ function is defined by the incomplete integral from D_l to D_h,

$$\begin{aligned}
Y &= \frac{4\pi n_i}{\lambda} \\
\psi_{l,h}(D_n, a, b, c, x, \nu) &= \frac{a D_n^b}{\bar{P}_{l,h}} \frac{1}{(1+xcD_n)^{\nu+b}}[\gamma(\nu+b, f(x)D_h/D_n) \\
&\quad - \gamma(\nu+b, f(x)D_l/D_n)] \\
f(x) &= 1 + x b_i D_n.
\end{aligned}$$

The γ-functions are the solution to the truncated gamma integral (Abramowitz and Stegun, 1972) given by,

$$\gamma(\nu, Y) = \int_0^Y X^{\nu-1} e^{-X} dX. \tag{3.30}$$

The solutions for any values of D_l and D_h may be obtained from the above solution. Of course, we will also want solutions that range over the limits $D_l \to \infty$ and $0 \to D_h$ by simply extending D_h to infinity and D_l to zero in the solution for $\beta_{abs,2}$. This is accomplished by simply taking the appropriate limit of the incomplete gamma functions that appear in $\psi_{l,h}$ above,

$$G(D_l, D_h) = \gamma(\nu + \alpha, fD_h/D_n) - \gamma(\nu + \alpha, fD_l/D_n). \tag{3.31}$$

Taking the limit as $D_l \to 0$ produces the solution for the integral over the limits $0 \to D_h$,

$$\lim_{D_l \to 0} = \gamma(\nu + \alpha, fD_h/D_n), \tag{3.32}$$

which gives us the solution to the integral in $\beta_{abs,1}$. The solution for the limits $D_l \to \infty$ is found by taking the limit,

$$\lim_{D_h \to \infty} = \Gamma(\nu + \alpha) - \gamma(\nu + \alpha, fD_l/D_n), \tag{3.33}$$

which gives the solution to the integral in $\beta_{abs,3}$. Using the solutions given by Eq. 3.29 one may write the total solution to the absorption integral by breaking it into truncated integrals for each of the size limits for d_e given in Table 3.4.3.

The extinction coefficient for each band is found for the ice particles by following the method suggested in Mitchell and Arnott (1994). This method, as discussed above, makes an equivalent mass sphere distribution out of the ice mass distribution. In Mitchell and Arnott (1994), this is accomplished by considering the mass and number median size (the size that splits the mass and number distributions into equal parts) of the ice distribution function,

$$\int_0^{\bar{D}_m} \alpha_i D^{\beta_i} n(D) dD = \frac{1}{2} \int_0^{\infty} \alpha_i D^{\beta_i} n(D) dD, \tag{3.34}$$

where the mass of the ice particles is represented by the function, $m_i(D) = \alpha_i D^{\beta_i}$ where D is the maximum dimension (L). The mass and number median size for a generalized gamma may be expressed as,

$$\bar{D}_m = (\nu + \beta_i - 0.332) D_n, \tag{3.35}$$

and

$$\bar{D}_{nm} = (\nu - 0.332)D_n, \tag{3.36}$$

respectively. Mitchell and Arnott (1994) then use the spherical mass equivalent size given by Eq. 3.16 to deduce a new set of mass median sizes for equivalent mass spheres. These forms are then used to derive new values for ν, D_n and N_t for the equivalent mass sphere distribution function. This method appears to be somewhat unphysical because the newly derived concentration, $N_{t,s}$, is not equal to the old concentration, N_t. The value for $N_{t,s}$ can be greater or less than N_t and, for very narrow distributions $N_{t,s}$ can become infinite with appropriate bounding being troublesome. An equivalent method for deriving the equivalent mass spheres is to conserve the number and mass moments (holding ν constant) and then deriving a new value of D_n for the spherical particle distribution function ($D_{n,s}$). Consider the integral of the total mass of the distribution function for non-spherical ice

$$M_{ns} = \int_0^\infty m_i(D)n(D)dD = N_t\alpha_i D_n^{\beta_i}\frac{\Gamma(\nu+\beta_i)}{\Gamma(\nu)} \tag{3.37}$$

and for spherical ice,

$$M_s = \int_0^\infty m_s(D)n(D)dD = N_t\frac{\pi}{6}\rho_i D_{n,s}^3\frac{\Gamma(\nu+3)}{\Gamma(\nu)}. \tag{3.38}$$

If we conserve number and mass of the distributions we can then find a new characteristic diameter for the equivalent mass sphere distribution function which is given by,

$$D_{n,s} = D_n^{\beta_i/3}\left[\frac{6\alpha_i}{\pi\rho_i}\frac{\Gamma(\nu+\beta_i)}{\Gamma(\nu+3)}\right]^{1/3}. \tag{3.39}$$

Thus, our method of computing an equivalent mass sphere distribution function consists of simply finding a new D_n. Tests of this method with that of Mitchell and Arnott (1994) show that exactly the same results are obtained. However, our method is numerically stable as N_t is conserved (cannot become infinite) and, therefore, appears.to be a more attractive form of the solution. This value of $D_{n,s}$ is then used in the equation for extinction given by the MADT (Eq. 3.26) but is modified as in Mitchell and Arnott (1994) for the projected area of the non-spherical ice as,

$$\beta_{ext,i} = \beta_{ext}\frac{\bar{P}}{\bar{A}} \tag{3.40}$$

where $\bar{P}$ is the integrated projected area of the non-spherical ice. The asymmetry parameter computations are produced in an analogous fashion. Figure 3.15 illustrates the optical properties for the non-spherical ice (band 6). The effect of the reduced effective distance through the ice (as compared to a sphere) is immediately noticed. The single scatter increases considerably in comparison to the spheres. Similarly, the extinction also increases being due to the fact that MADT is used for the spheres and that being a decrease in D_n (over the D_n of the crystals) occurs when equivalent spheres are produced.

The solution to the above extinction and absorption integrals for water drops and ice are produced for normalized spectra, $N_t = 1$, and a fixed value of the distribution shape, ν. The solutions are then obtained over the range of D_n that occur within RAMS for 13 hydrometeor classes (7 total species with 3 ice habits for pristine ice, snow and aggregates) and 8 radiation bands. For each band and hydrometeor class, we fit the extinction, β_{ext}, the single scatter, ω_p, and the asymmetry parameter g_p with simple functions of the form,

$$\begin{aligned} \omega_p &= w_0 + w_1 e^{w_2 D_n} + w_3 e^{w_4 D_n} \\ g_p &= g_0 + g_1 e^{g_2 D_n} + g_3 e^{g_4 D_n} \\ \beta_{ext} &= b_0 D_n^{b_1} \end{aligned} \tag{3.41}$$

where $w_0 \rightarrow w_4$, $g_0 \rightarrow g_4$ and b_0,b_1 are the fit coefficients for the single scatter, asymmetry, and extinction respectively. These fits work extremely well for all bands, with accumulated errors (errors added for all 100 points used in the fit) of no greater than 2 percent and most of the time being less than 1. Errors for individual points never became larger than 1 percent themselves. Since exponentials are expensive to compute in a numerical code, we produce tables of the exponential function and of the function $D_n^{b_1}$. Optical properties for all of the seven hydrometeor classes in RAMS are combined following Slingo and Schrecker (1982),

$$\begin{aligned} \tau_p &= \sum_{i=1}^{N_h} \tau_{p,i} \\ \omega_p &= \frac{\sum_{i=1}^{N_h} \omega_{p,i}\tau_{p,i}}{\sum_{i=1}^{N_h} \tau_{p,i}} \\ g_p &= \frac{\sum_{i=1}^{N_h} g_{p,i}\omega_{p,i}\tau_{p,i}}{\sum_{i=1}^{N_h} \omega_{p,i}\tau_{p,i}} \end{aligned}$$

where N_h is the number of hydrometeor classes utilized by the model.

The bin microphysics

Unfortunately, these fits are not usable for the bin microphysical model in which the shape of the distribution function varies as a function of the environment. It might be possible to use these fits if one uses the method of Hu and Stamnes (1993) discussed above. However, there are many times when the cloud drop distribution at cloud top (where LW cooling is the largest) is quite narrow and, as we saw above, substantial errors in the extinction and single scatter can be incurred if we simply use predetermined extinction and scattering for a gamma distribution and then look-up equivalent r_e values. Since distribution shape may be important (as we will discuss in Chapter 5) and since we wish to include the effects of radiation in the growth of drops within the bin microphysical framework, in this section we develop a method for computing the cloud optical properties directly from the bin model information.

In the bin microphysical model, as discussed in the last chapter, we know the number concentration and mass of droplets within a bin which is defined by bounding sizes (or edges). In order to compute the integral in Eq. 3.4 we must know the form of the distribution function, $n(D)$. If we break up the integral into a discrete sum, which is exact for the bin model, we obtain

$$\begin{aligned} \bar{\sigma} &= \frac{1}{\bar{E}} \int_{\Delta\lambda} E_\lambda \sum_{k=1}^{N_{bins}} A(\bar{D}_k)\sigma(\bar{D}_k, m, \lambda) N_k d\lambda \\ \bar{D}_k &= \left(\frac{M_k}{\alpha_m N_k}\right)^{1/3} \end{aligned}$$

where N_k is the concentration in the bin, M_k is the total bin mass mixing-ratio, and α_m is a factor containing miscellaneous coefficients. Note that the difficulty here is that we must compute this integral before-hand. Since size and wavelength are intimately connected through σ, this is impossible for the general case as $\bar{D}_k$ varies in time. If we had *a priori* knowledge of $\bar{D}_k$ we could easily compute this integral exactly (in the bin sense) for the normalized case ($N_k = 1$) and then multiply by the appropriate concentration later on.

In order to solve this problem we attempted two different approaches. The first was to assume that we could replace $\bar{D}_k$ with the average of the bin edges, $\bar{D}_{e,k}$, in the σ

function. This assumption is based on the hypothesis that changes in size within each bin affect the optical properties in a minimal fashion. This was felt to possibly be the case as bin resolution is the finest at the small drop end of the spectrum, where the optical properties vary the most. This assumption removes the time dependent $\bar{D}_k$ from the σ-function, effectively decoupling the λ and D integrals. Our integral becomes after a simple rearrangement,

$$\begin{aligned} \bar{\sigma} &= \sum_{k=1}^{N_{bins}} A(\bar{D}_k) N_k \bar{\sigma}_k \\ \bar{\sigma}_k &= \frac{1}{\bar{E}} \int_{\Delta\lambda} E_\lambda \sigma(\bar{D}_{e,k}, m, \lambda). \end{aligned} \tag{3.42}$$

We will call this method the *mean bin method.* The second method followed Tzivion *et al.* (1987) and assumed that the concentration was a linear function of mass within a bin,

$$N_k(m) = a_k(t) + b_k(t)m, \tag{3.43}$$

where $a(t)$ and $b(t)$ are time-varying coefficients that essentially allow us to account for the fact that $\bar{D}_k$ will vary in time. The assumption being that the distribution within each bin can be well approximated by a linear function. This amounts to a separation of variables as the σ-integral now breaks into two parts, each with the time-dependent term separated from the wavelength term which must be computed before-hand,

$$\bar{\sigma} = \sum_{k=1}^{N_{bins}} a_k(t)\bar{\sigma}_{k,1} + b_k(t)\bar{\sigma}_{k,2}. \tag{3.44}$$

We will term this the *linear bin method.* After doing extensive tests with both methods, it was found that the simple mean bin method performs as well as the more complex linear method with a reduction in computational cost (since fewer terms must be computed).

For the computation of the extinction, scattering and the asymmetry, we use the Lorenz-Mie theory. Here, since we are computing integrals over 25 size bins and for only one class of hydrometeors (drops) we are able to do the computations rather quickly and utilize the more exact theory. The computations of the extinction, single scatter and asymmetry for the bin model take on the form (for a particular two-stream band),

$$\beta_{ext} = \sum_{k=1}^{N_{bins}} A(\bar{D}_k) N_k Q_{k,ext}$$

$$\begin{aligned}
\beta_{abs} &= \sum_{k=1}^{N_{bins}} A(\bar{D}_k) N_k Q_{k,abs} \\
\omega_p &= \frac{1}{\beta_{ext}} \sum_{k=1}^{N_{bins}} A(\bar{D}_k) N_k Q_{k,ext} \omega_k \\
g_p &= \frac{1}{A_t} \sum_{k=1}^{N_{bins}} A(\bar{D}_k) N_k g_k \\
A_t &= \sum_{k=1}^{N_{bins}} A(\bar{D}_k) N_k
\end{aligned} \tag{3.45}$$

where $Q_{k,ext}$, ω_k, and g_k are the band integrated quantities discussed above, and A_t is the total projected area. This method is also used for the ice bin model of Reisin *et al.* (1995) with the extinction and single scatter functions replaced with the theory of Mitchell and Arnott (1994), Eqs. 3.14 and 3.9. The asymmetry parameter uses the Lorenz-Mie theory results with the equivalent mass sphere approximation of Eq. 3.16. All of the above given approximations seem to work extremely well.

Tests of the bin mean method were conducted on a variety of gamma distribution functions, the solutions to which are known. Gamma distributions of a given shape, ν, were broken up in the same fashion as is done in the bin microphysical model for drops. The number concentration and mass within a bin were computed by truncating the gamma distribution,

$$\begin{aligned}
N_k &= \int_{D_k}^{D_{k+1}} n(D) dD \\
M_k &= \int_{D_k}^{D_{k+1}} m(D) n(D) dD.
\end{aligned}$$

The optical properties were then found by applying the method given in Eq. 3.45; comparisons being made with fine resolution numerical solutions to the integrals with Lorenz-Mie theory. A number of different combinations of distribution shapes, including bi-modality were utilized in the tests. Most of the tests produced similar errors with the largest being around 2% . Figure 3.16 illustrates the accuracy of this approach using 25 drop bins for a gamma distribution with $\nu = 2$ for band 5. Here we plot the optical properties over the mean size of the distribution function. Note that the differences between the bin method and the accurate solution are miniscule. Figure 3.17 shows the relative error associated

with the optical properties derived with the bin method. Errors are quite small with the largest values reaching to about 1.2% for the asymmetry factor. The ice bin model shows similar small errors. Figure 3.18 shows the bin ice model results compared to an analytical solution to the gamma distribution for band 5. As is shown, the ice bin mean method produces small errors as compared to the analytical solution. Errors never become larger than about 0.6% . More extensive tests have shown that the largest errors may reach 2% . Plots for g_p are not shown as they are similar to those shown in the water drop bin model plots discussed above.

The sort of result presented in these three figures is representative of the results for other distribution functions. Overall the method works extremely well, producing little error and, therefore, we have used this as our connection between the bin microphysics and the radiation model. Note that we have also included the data for the absorption coefficient in these plots. In a later chapter we will tie the vapor growth of droplets into the radiation by including a radiative heating/cooling term. This term requires knowledge of the absorption coefficient for each bin, as presented above.

3.5 Possible improvements

Possible improvements to this model includes reduction in band width to produce better accuracy in the gaseous absorption and cloud optical properties. A possible method for even larger computational gains in the gaseous absorption problem that is related to the FESFT method is the "effective extinction" (EE) method of Edwards (1996). In this method one could take advantage of the fact that profiles of gases such as CO_2 and O_3 do not vary during most model simulations. At this point, since the optical depth of this gas must be computed with time varying quantities such as cloud hydrometeor optical properties, one must always do somewhat redundant computations involving the non-time varying gases. The EE method offers a way out of this. In the method one computes a single, average effective extinction coefficient for the non-varying gaseous profiles ($\bar{K}(z)$). This single coefficient then takes the place of the 1 through 5 coefficients normally used to compute the gaseous absorption. The advantage is in the reduction of the number of

required solutions of the two-stream equations; at this point, time invariant gases may require as many as five solutions to the two-stream equations while the EE method would require only one solution. One could compute a set of these $\bar{K}$ profiles for each gas that does not vary in time and then use them in the model computations.

Recently, Gabriel *et al.* (1997) have developed an adjoint two-stream method that allows for the use of perturbation theory as a possible way of reducing computational costs. The method works by finding the adjoint of the two-stream equations and then, in a method analogous to that of classical and quantum physics, form an equation for deviations from a given base state know as the *perturbation equation.* The idea being that one could compute the fluxes (or heating rates) for a given base-state atmosphere. Deviations from this base state in terms of gas amounts are then used as input into the perturbation equation and new fluxes associated with the "perturbed" state are derived. This would allow for fewer overall computations and, therefore, the ability to improve the speed of the overall two-stream solution. Gabriel *et al.* (1997) also put forth the idea that the largest k in the correlated-k method could be used as the base state, with all other ks in that band being the perturbations. Again, the idea is to reduce the number of computations by using the perturbation equation to quickly produce the fluxes for other k values. The methods seems promising as a simple set of one layer atmosphere tests showed. The method, however, does show limits and needs to be extensively tested in a multiple-layer system. One big disadvantage of the method is that one particular form of the perturbation equation (termed the exponential method) does not conserve energy under large scattering perturbations. The method may also have promise for including more streams in the radiation computations (a possible advantage for high latitude radiative computations) as it may be possible to treat further streams as perturbations, thus reducing the computational costs of using 4 and 6 stream methods in numerical models.

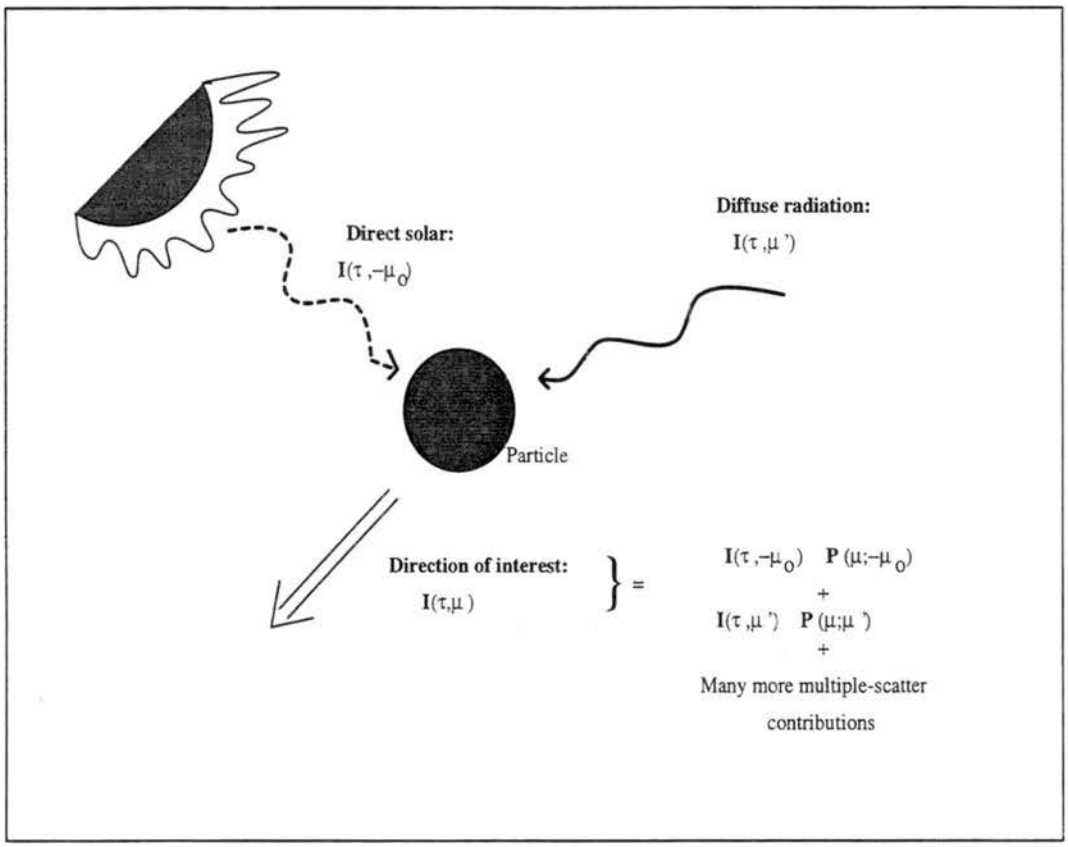

Figure 3.1: Illustration of the phase function. Radiation is scattered by the particle into the direction of interest. Sources of the scattered radiation may be direct solar radiation or diffuse (multiply scattered) radiation.

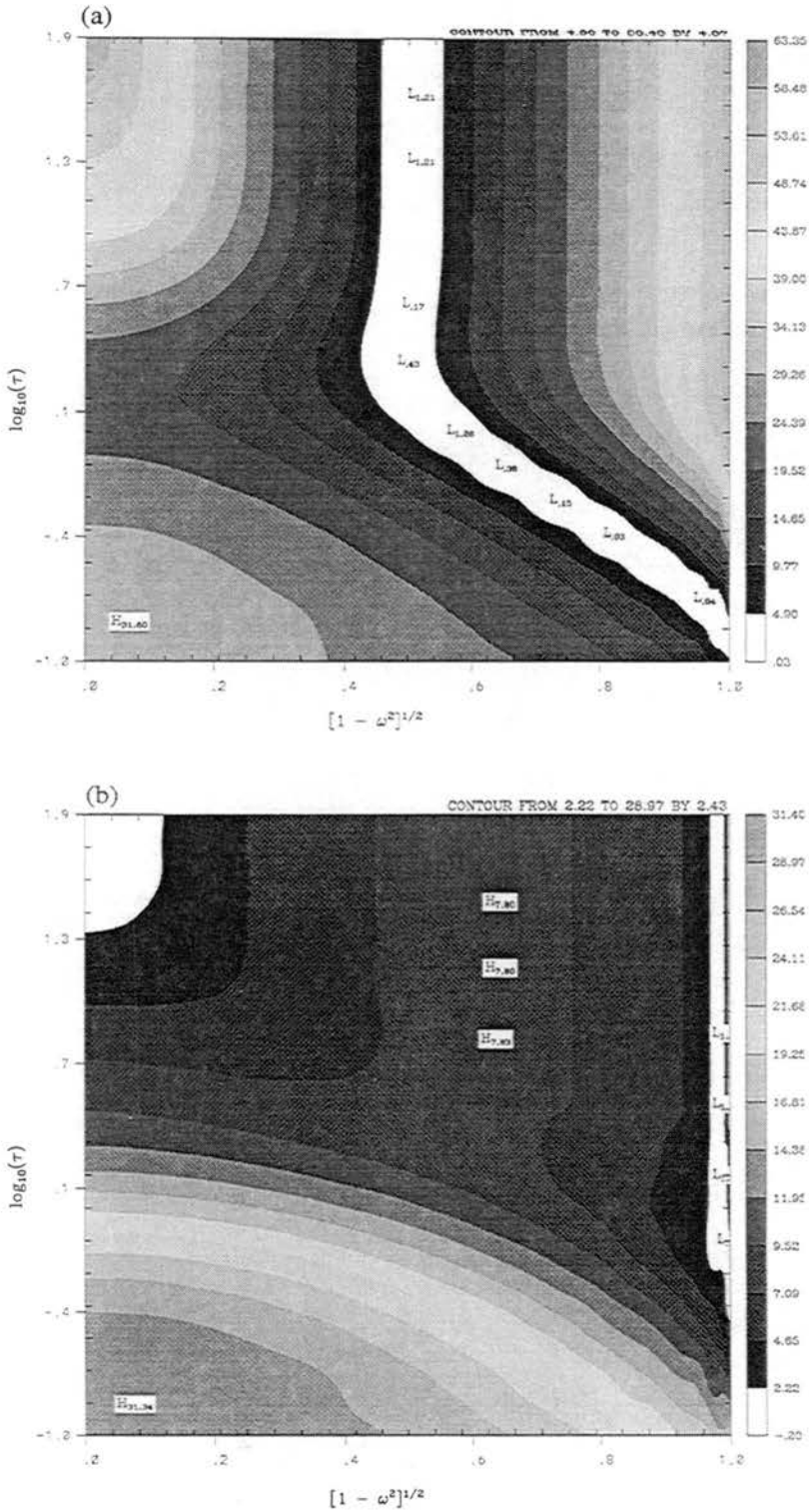

Figure 3.2: Comparison of the two-stream approximations of: a) Ritter and Geleyn (1992) and b)δ-Eddington (courtesy of Gabriel, personal communication). Contour plots are of the relative error in F^+ at the top of the layer as compared to 32-stream computations of Gabriel. The incident flux was $F_t^- = 1$ and $\theta_0 = 75°$.

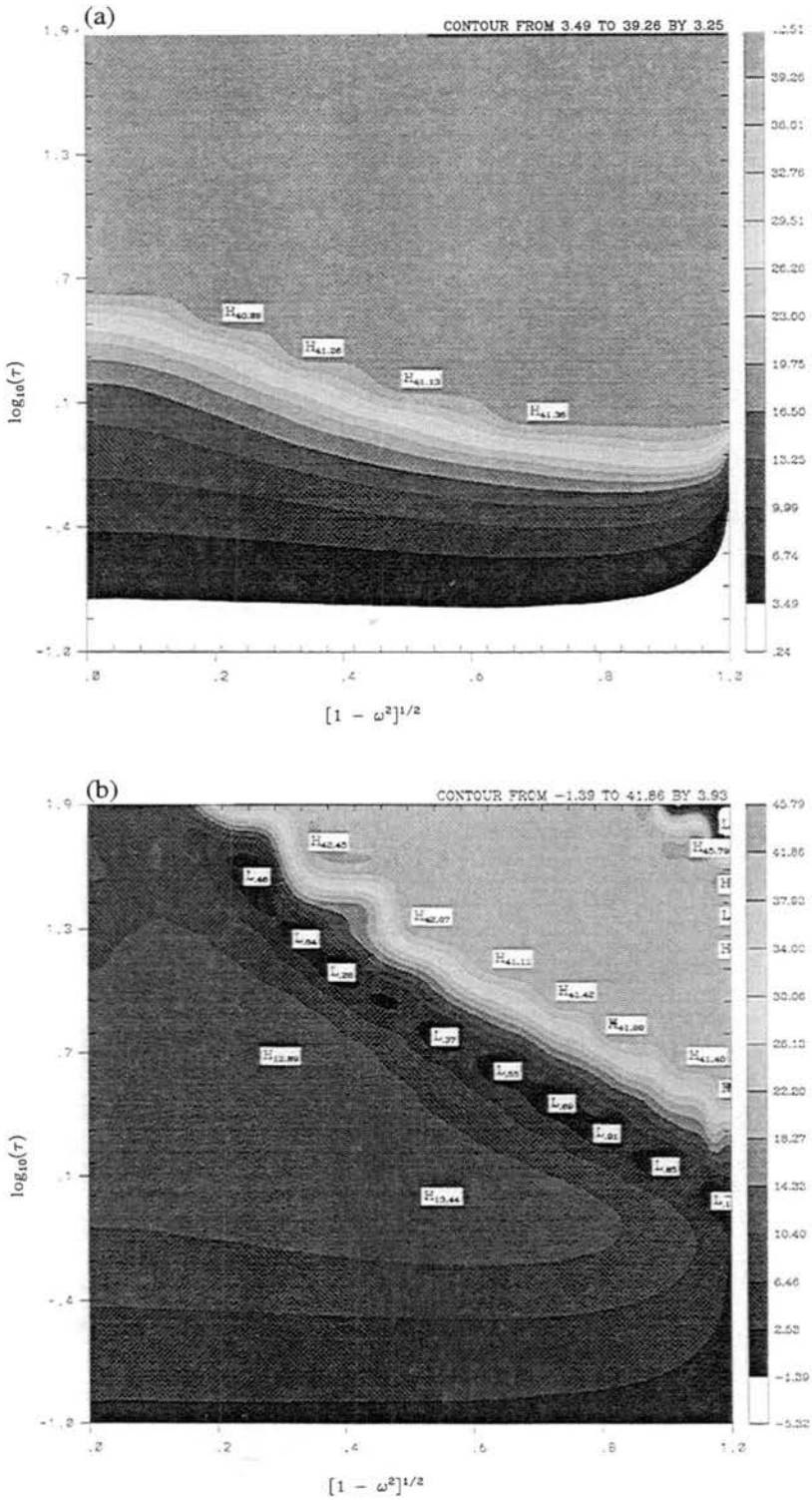

Figure 3.3: Comparison of the two-stream approximations of: a) Ritter and Geleyn (1992) and b)δ-Eddington (courtesy of Gabriel, personal communication). Contour plots are of the relative error in F^- at the bottom of the layer as compared to 32-stream computations of Gabriel. The incident flux was $F_t^- = 1$ and $\theta_0 = 75°$.

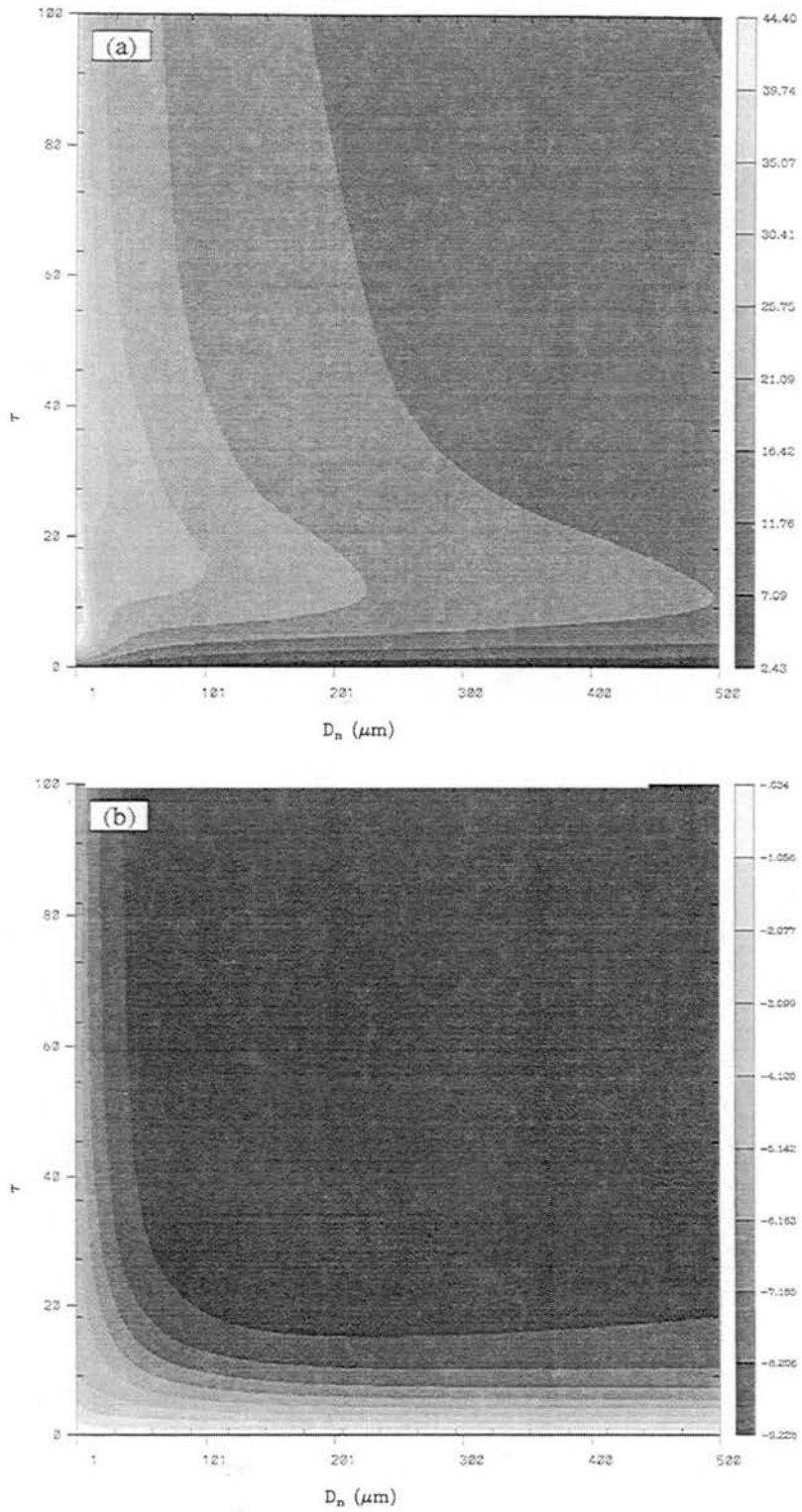

Figure 3.4: Relative error in absorption (a) and reflection (b) for water drops with no correction to c_i (3-band compared to 30-band solar model).

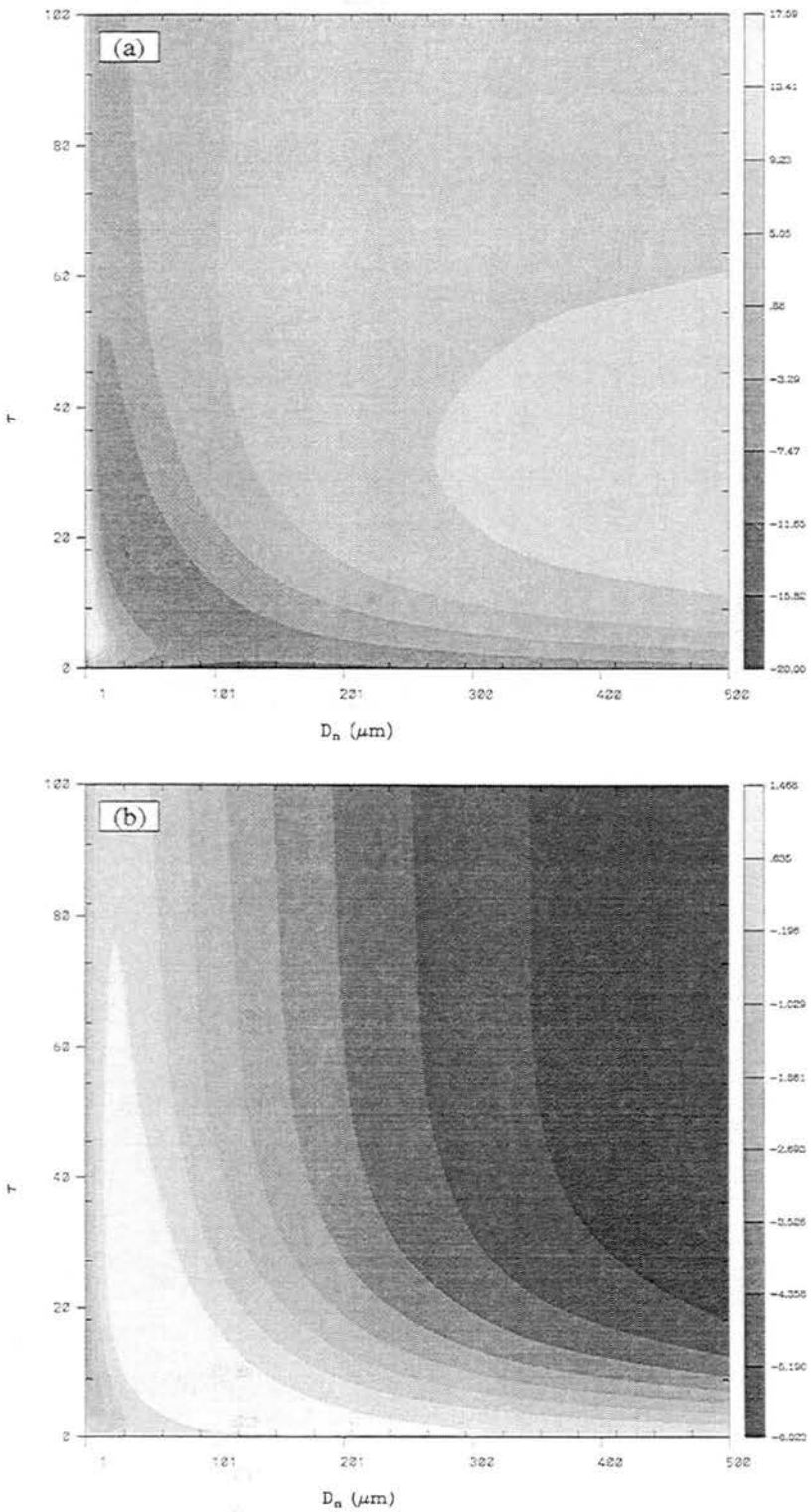

Figure 3.5: Relative error in absorption (a) and reflection (b) for water drops with c_i-limited (3-band compared to 30-band solar model).

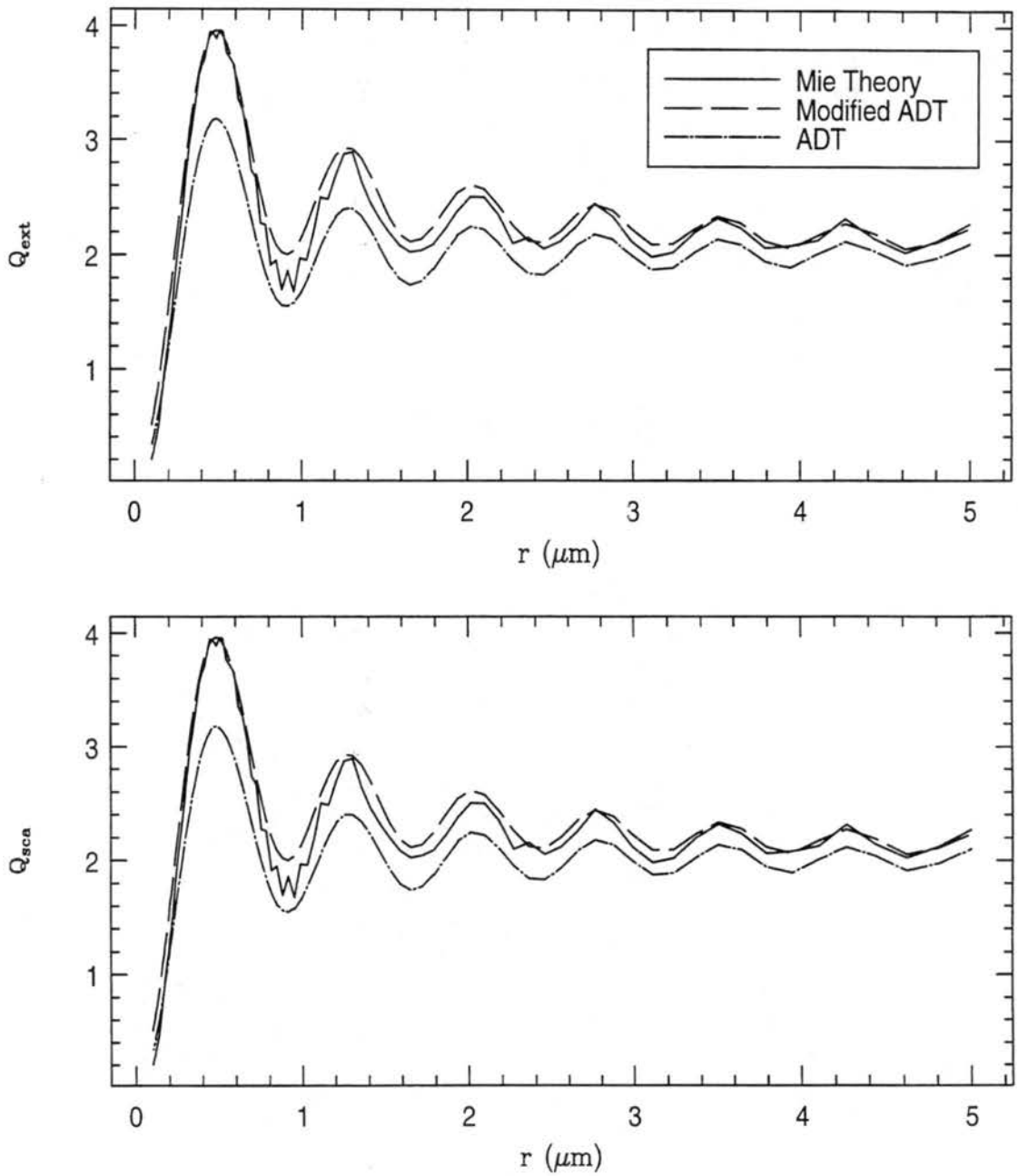

Figure 3.6: Comparison of ADT, Modified ADT, and Lorenz-Mie theory at $\lambda = 0.5\mu m$.

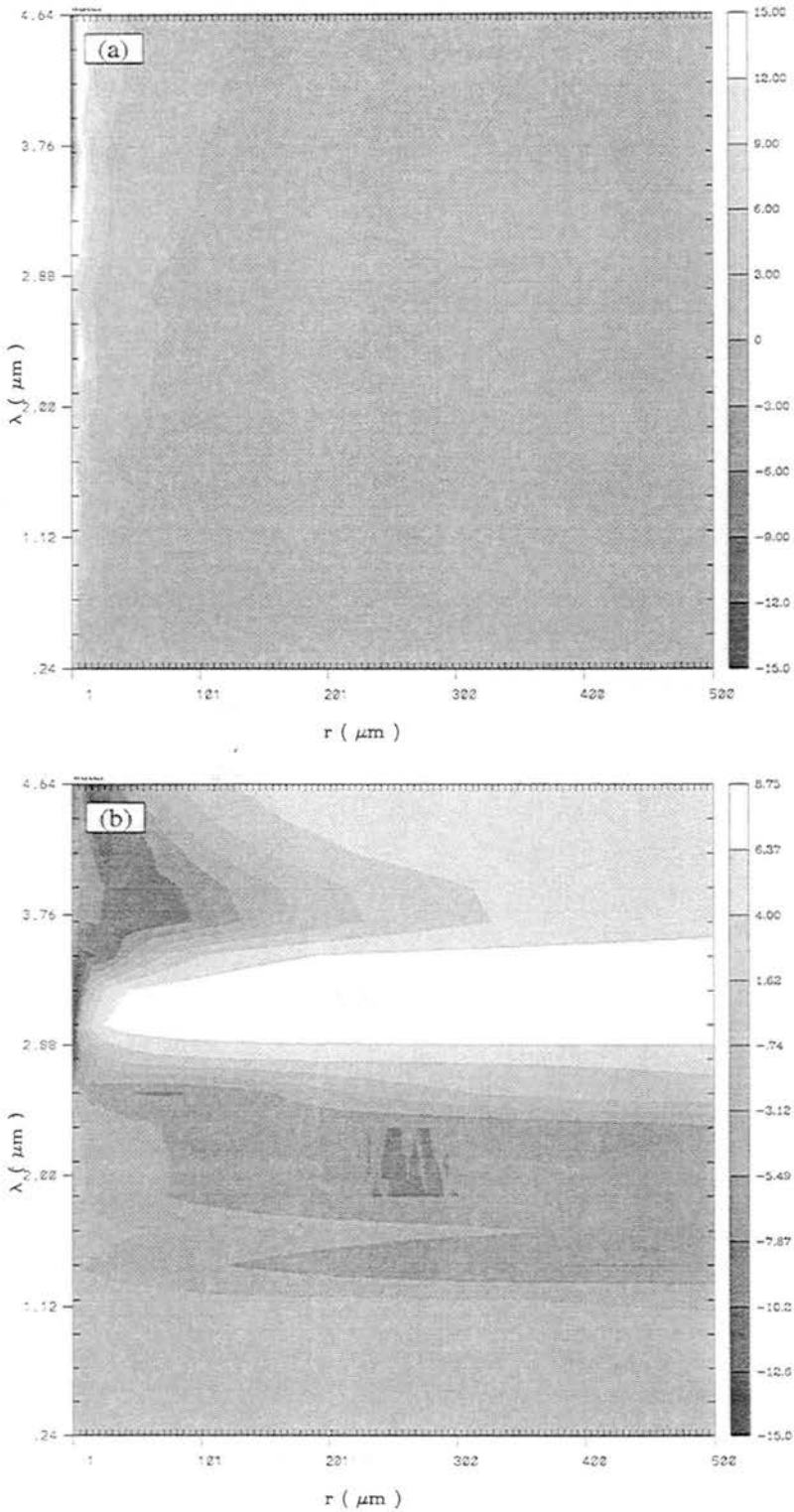

Figure 3.7: Relative error in ADT for solar wavelengths as compared to Lorenz-Mie theory with error in (a) Q_{ext} and (b) ω_p shown.

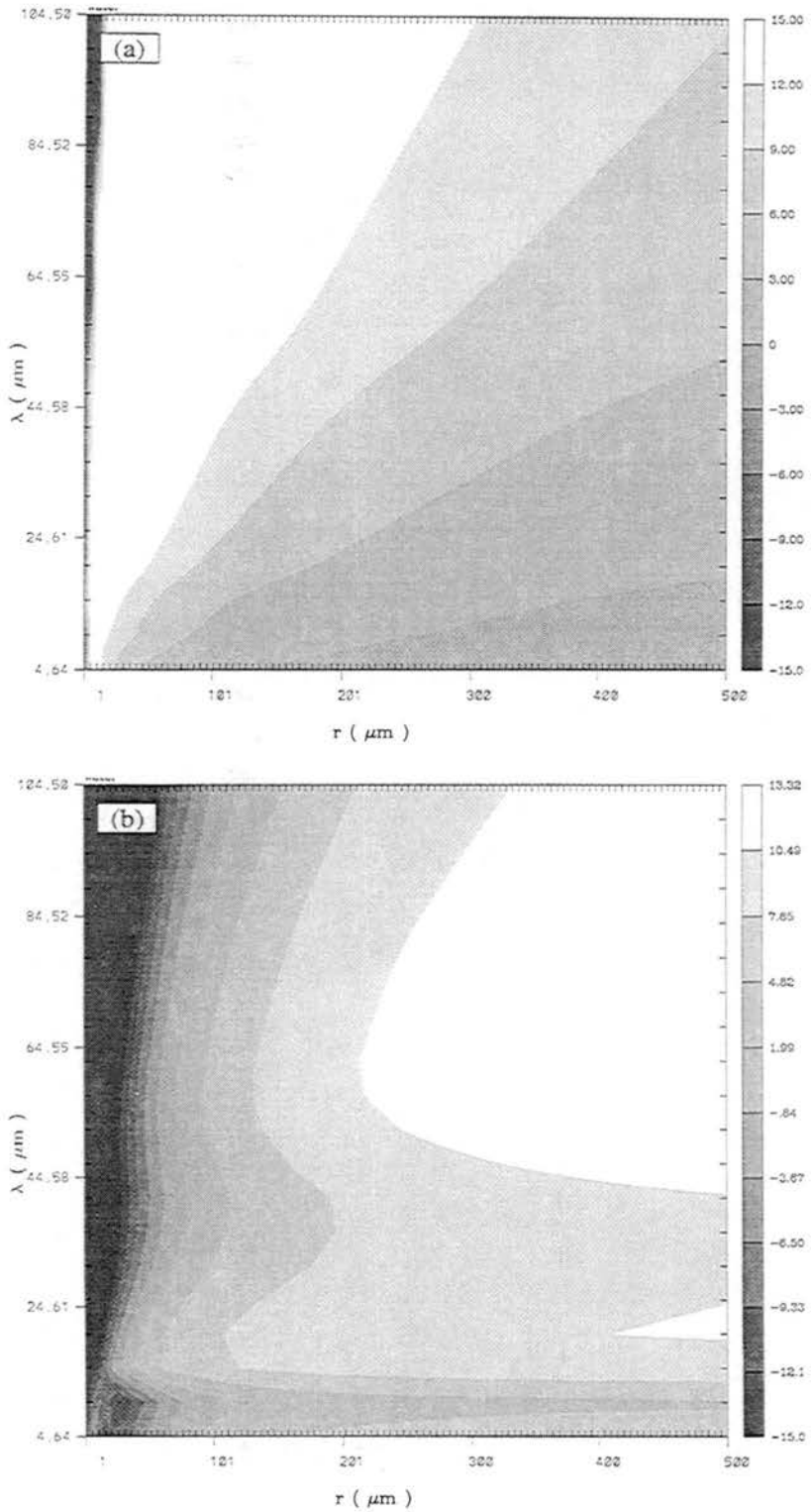

Figure 3.8: Relative error in ADT for IR wavelengths as compared to Lorenz-Mie theory with error in (a) Q_{ext} and (b) ω_p shown.

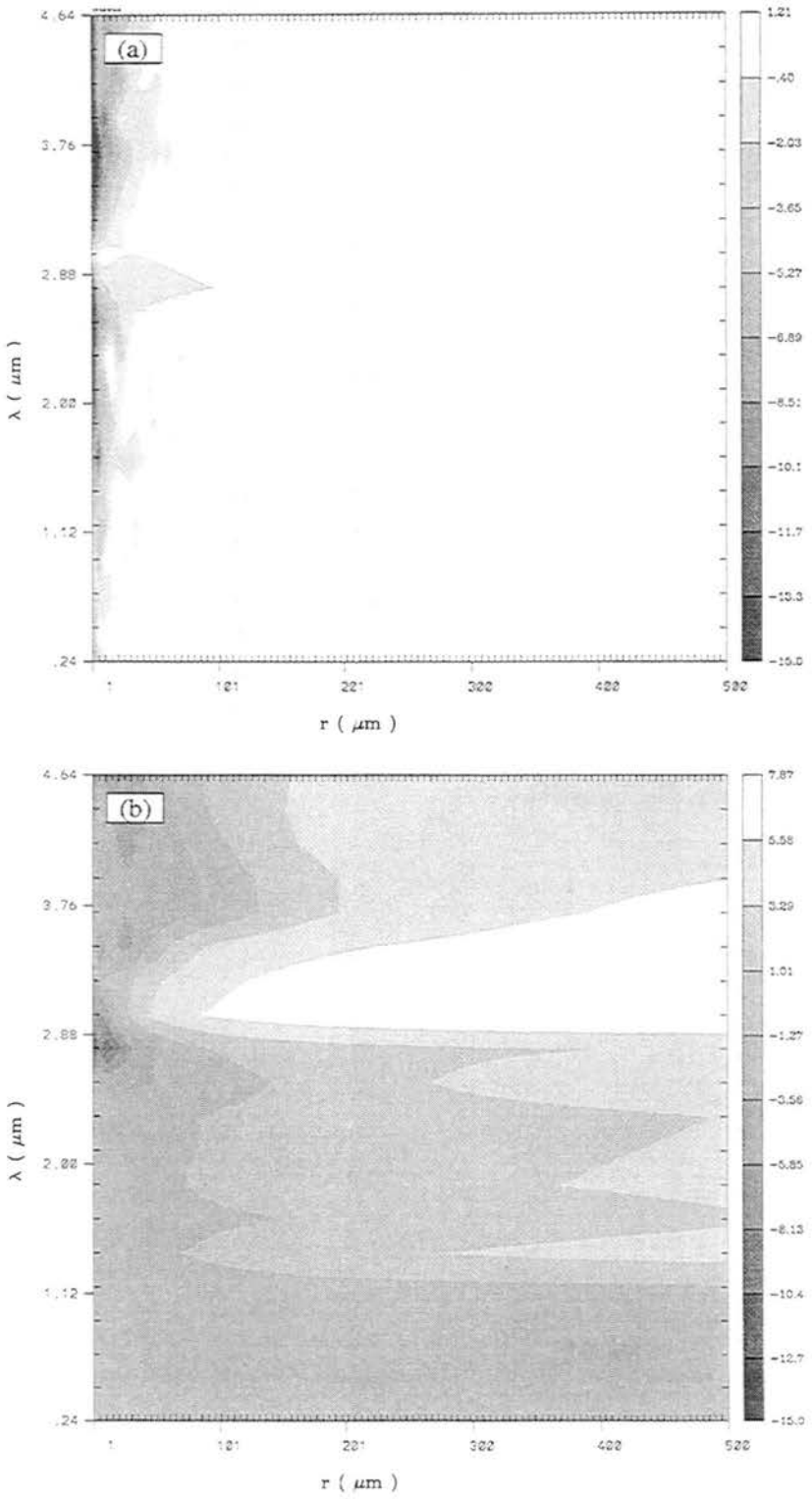

Figure 3.9: Relative error in Modified ADT for solar wavelengths as compared to Lorenz-Mie theory with error in (a) Q_{ext} and (b) ω_p shown.

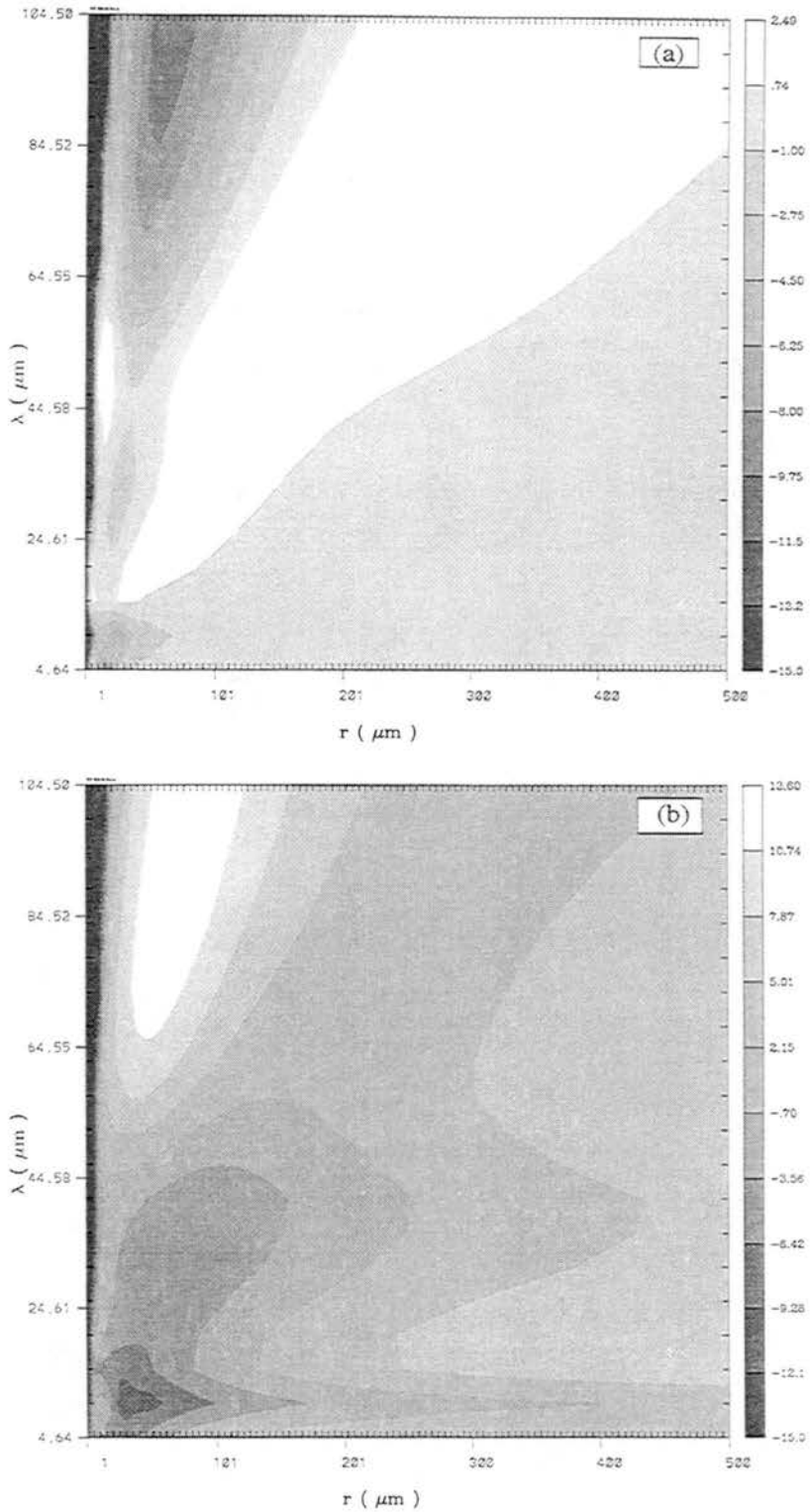

Figure 3.10: Relative error in Modified ADT for IR wavelengths as compared to Lorenz-Mie theory with error in (a) Q_{ext} and (b) ω_p shown.

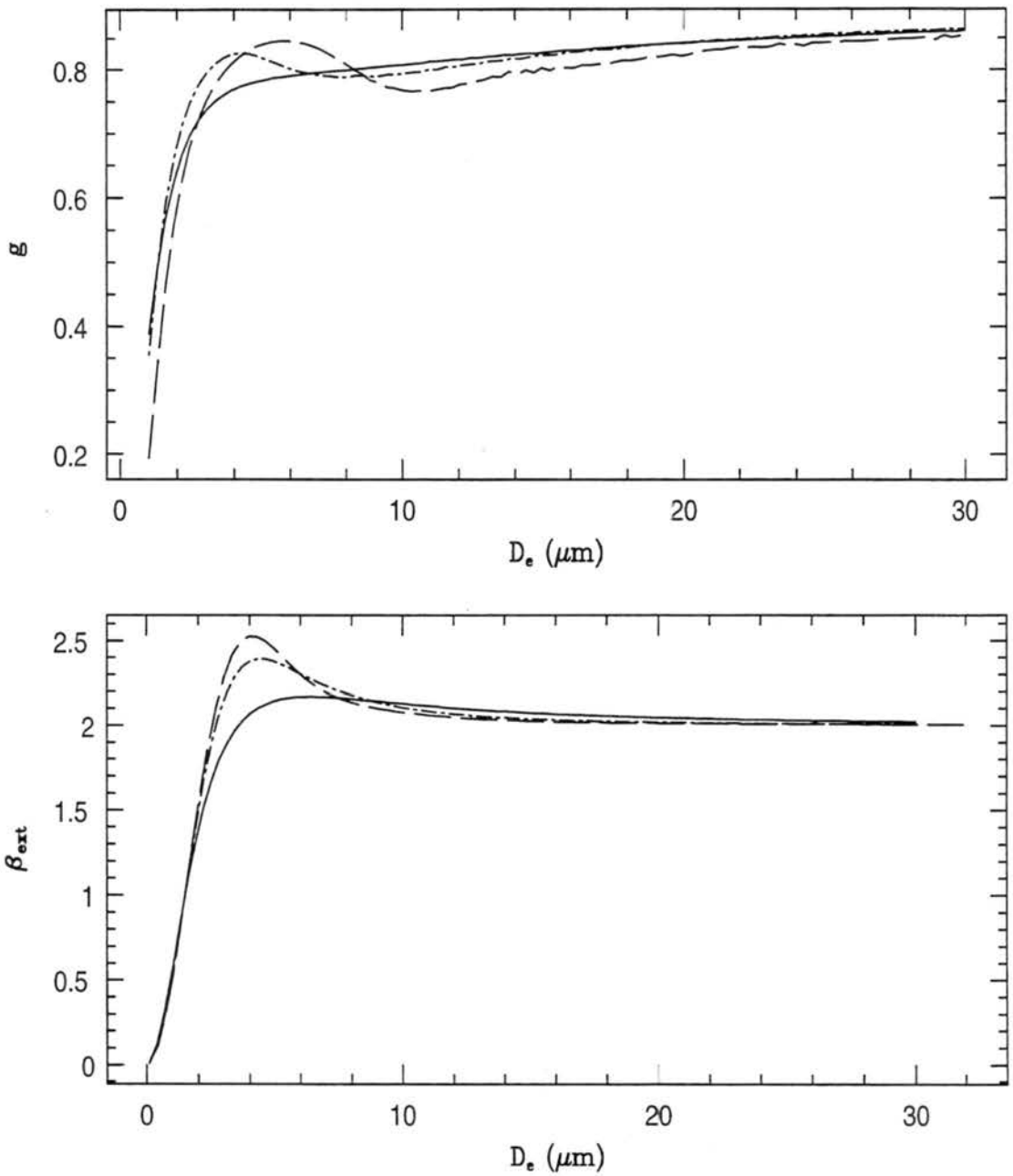

Figure 3.11: Comparison of Q_{ext} and g_p for various ν as a function of D_e. Different ν values are denoted by a solid line for $\nu = 1$, a dashed-dotted line for $\nu = 6$, and a dashed line for $\nu = 14$.

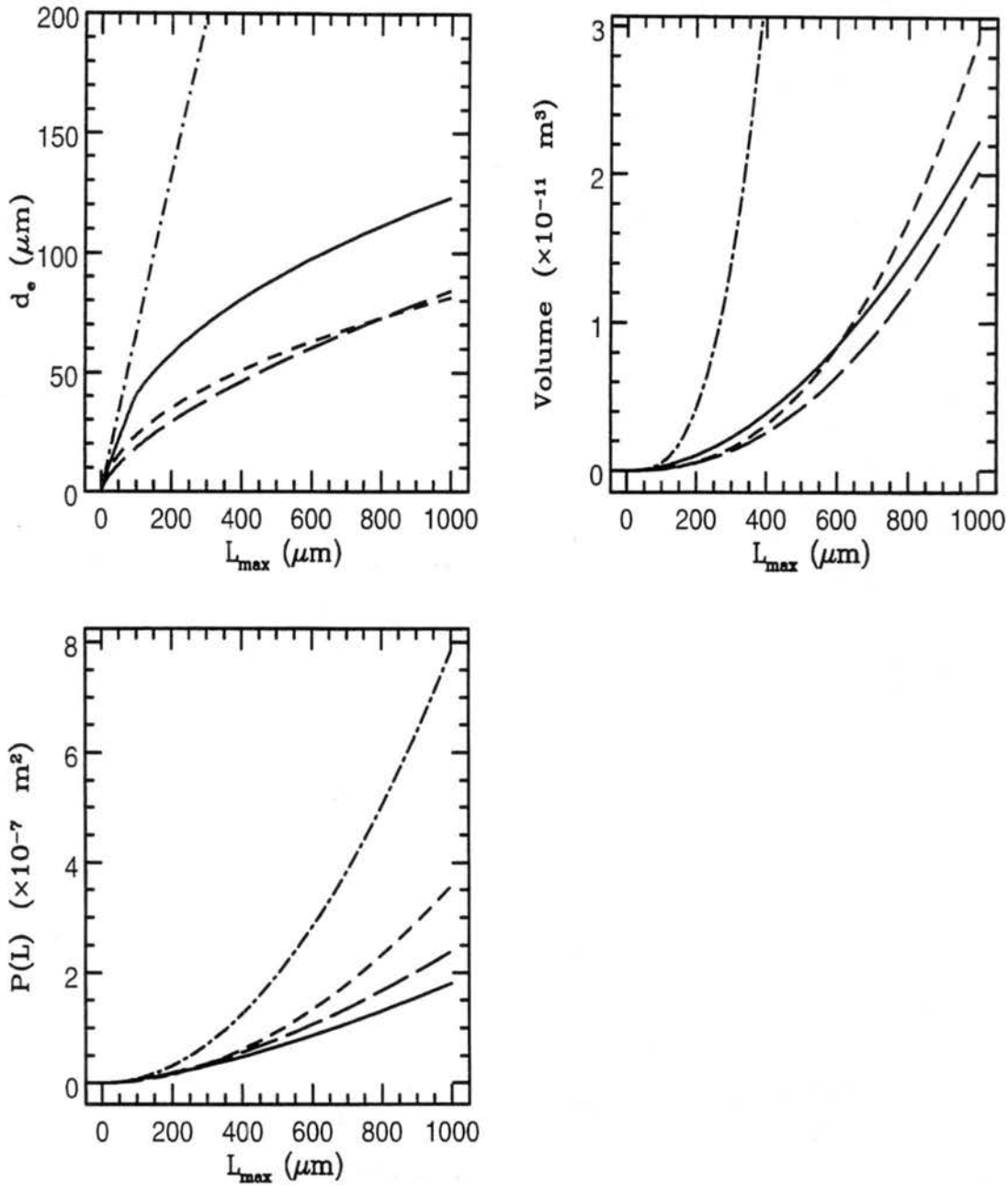

Figure 3.12: Comparison of d_e, crystal projected area, $P(L)$, and the volume for various ice habits. Included in the figures are spheres (dash-dotted line), hexagonal columns (solid line), hexagonal plates (short dashed line), and rosettes (long dashed line).

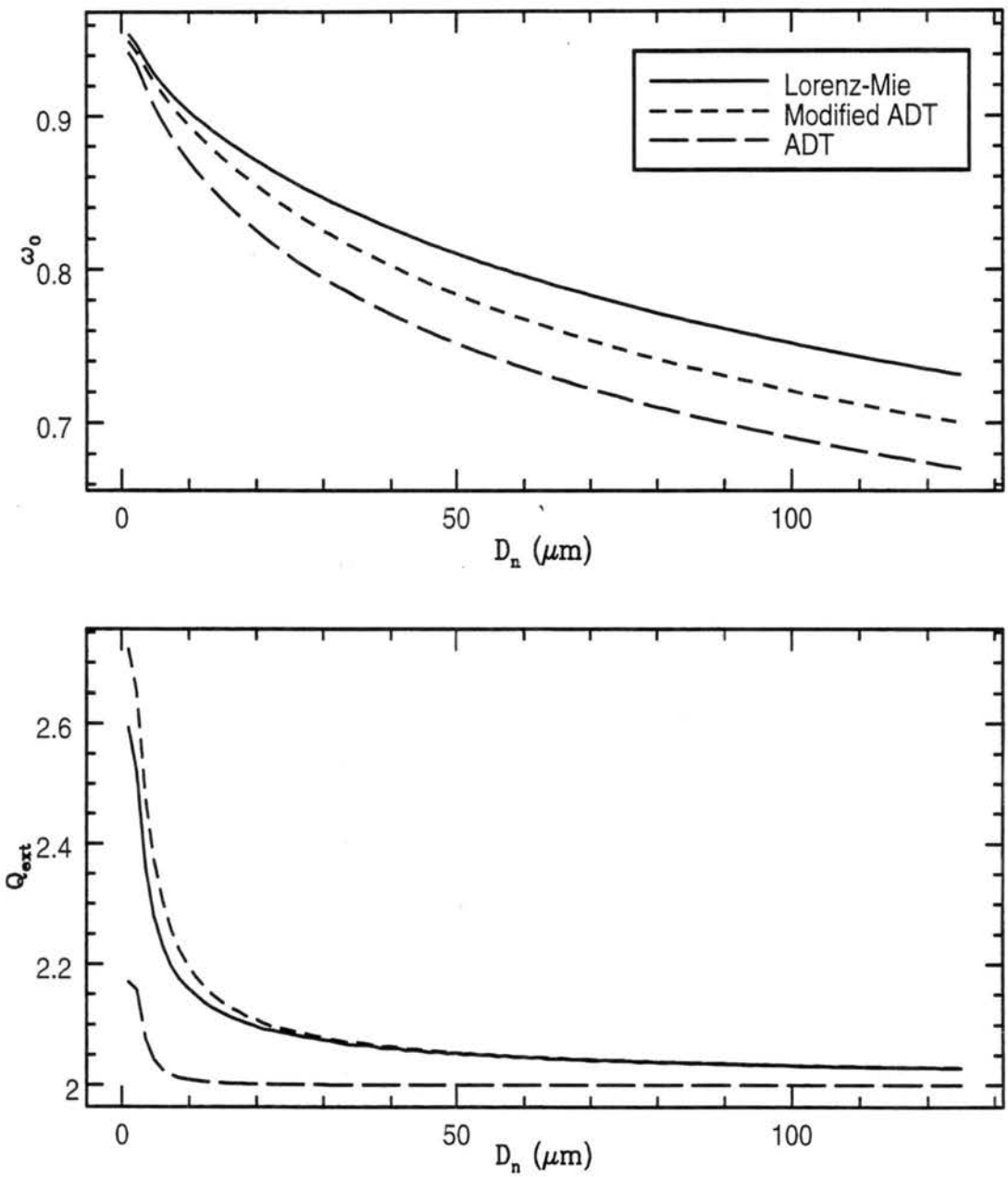

Figure 3.13: Comparison of MADT (spheres) and Lorenz-Mie theory values of Q_{ext} and ω_0 values for model band 1.

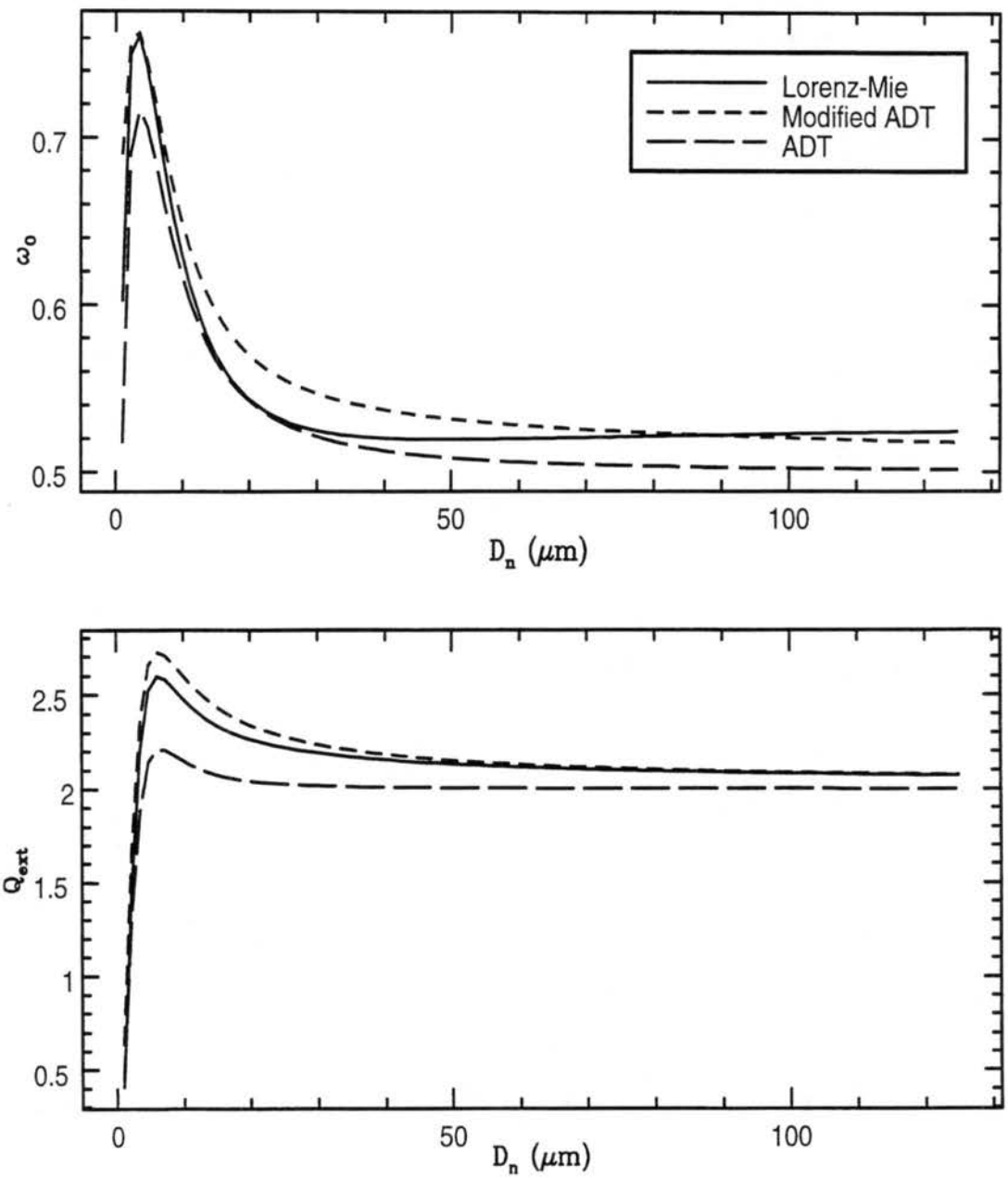

Figure 3.14: Comparison of MADT for spheres with Lorenz-Mie theory. Q_{ext} and ω are shown for model band 6.

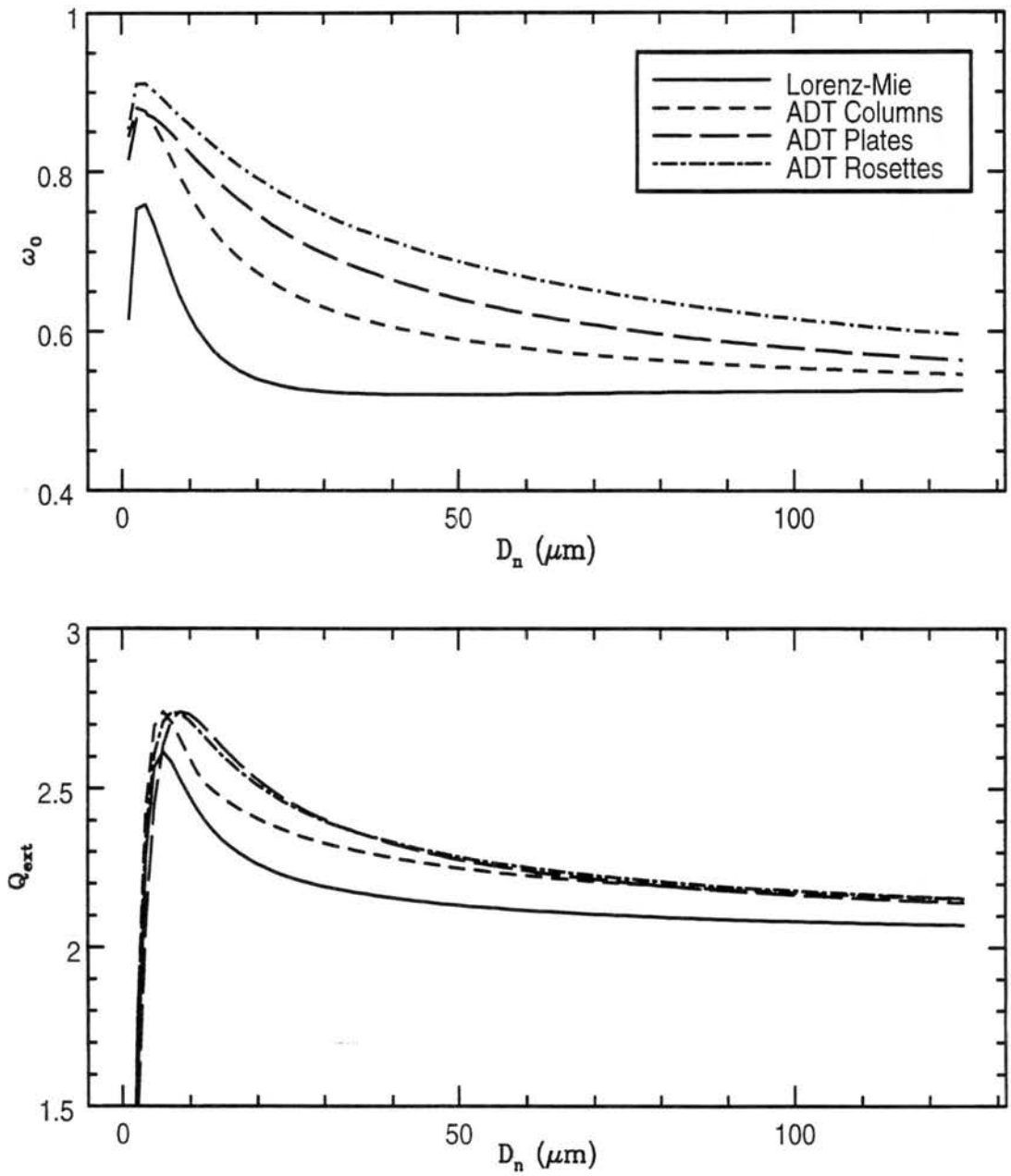

Figure 3.15: Illustration of the non-spherical ice optical properties for band 6.

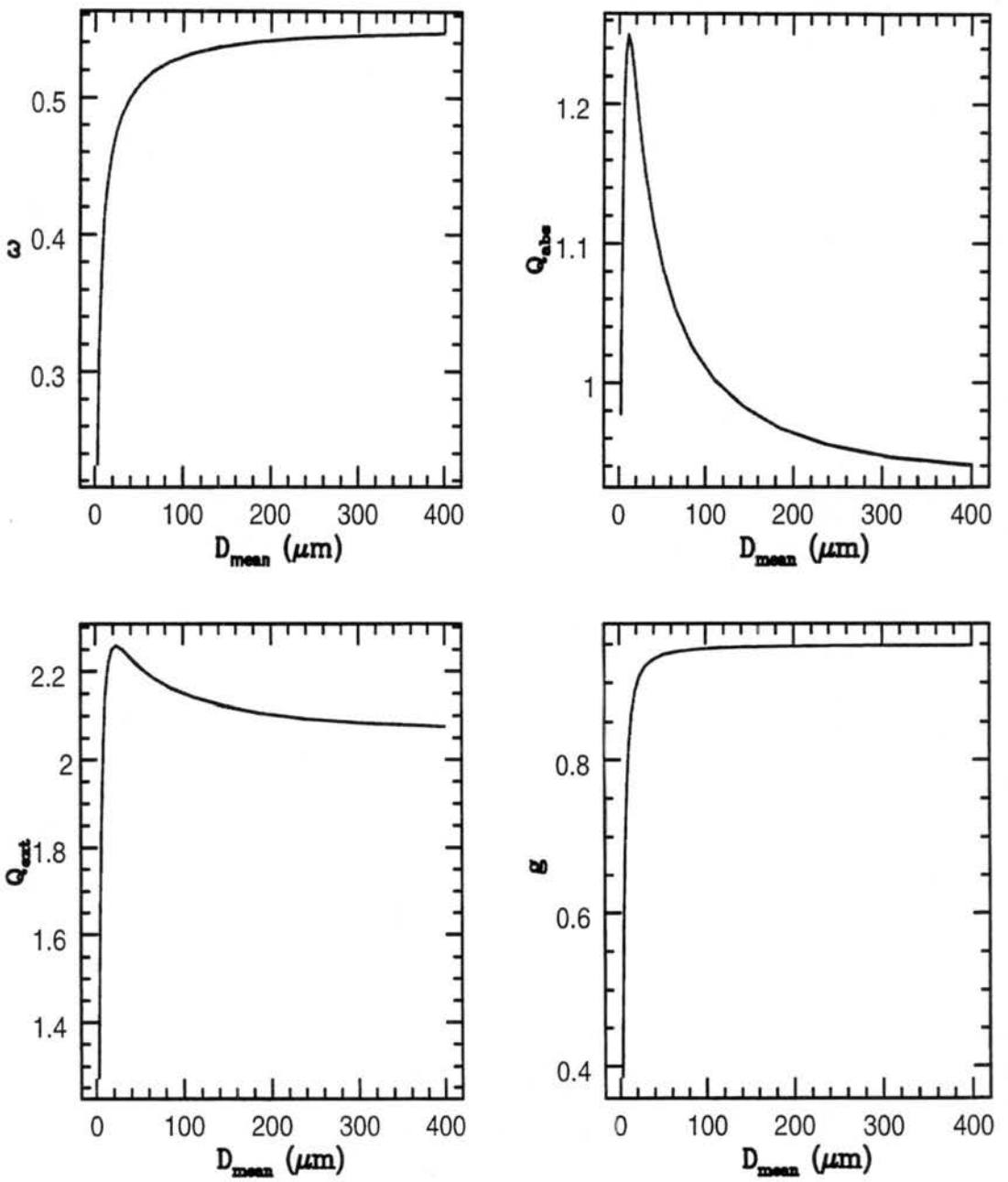

Figure 3.16: Comparison of bin mean method for spheres with exact gamma distribution solution for band 5. The solid line is the exact solution for a gamma distribution with $\nu = 2$ while the grey dashed line uses the bin mean method.

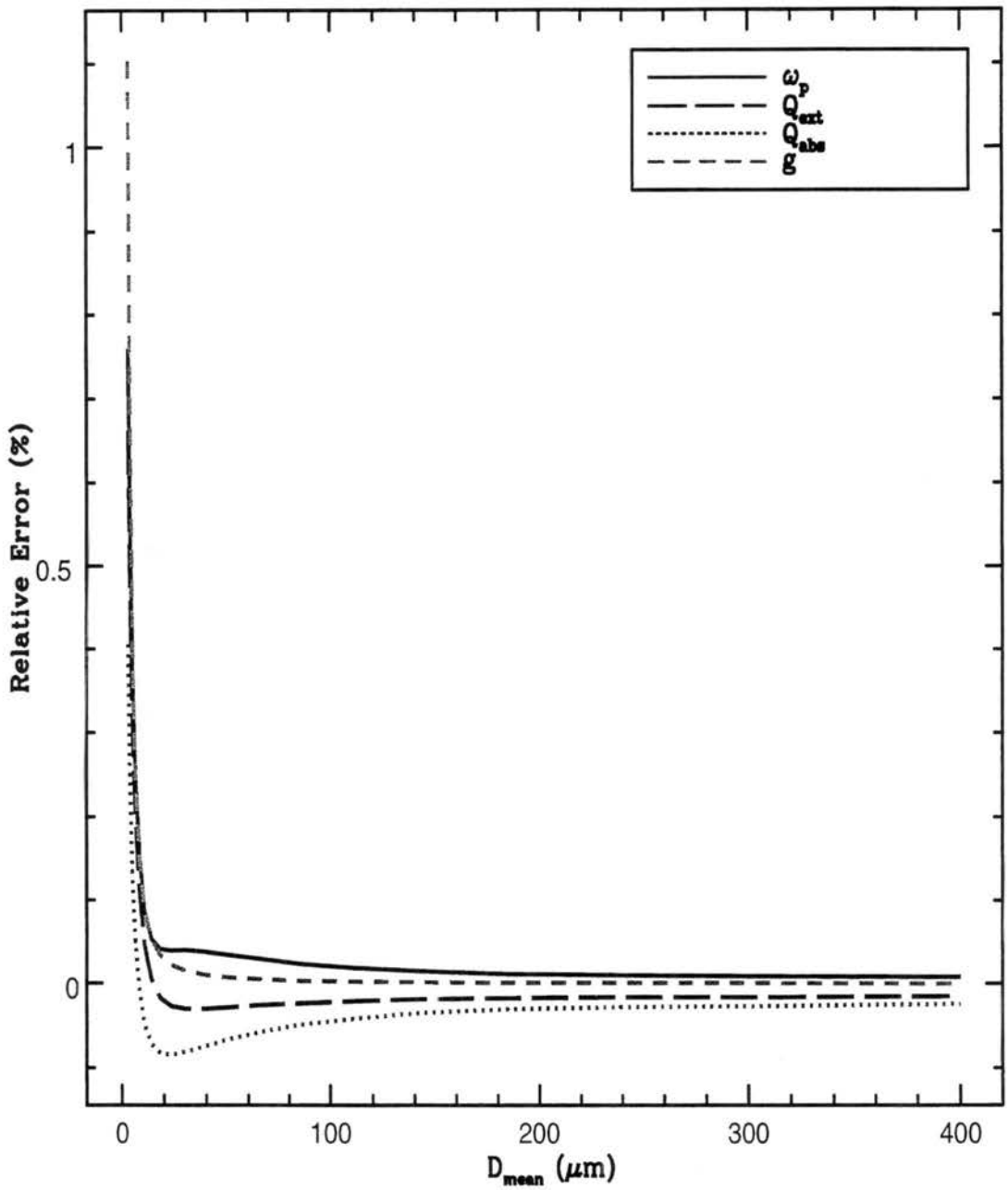

Figure 3.17: Relative errors associated with the bin mean method for band 5. Errors for the various optical properties in comparison to exact gamma distribution with $\nu = 2$ are plotted.

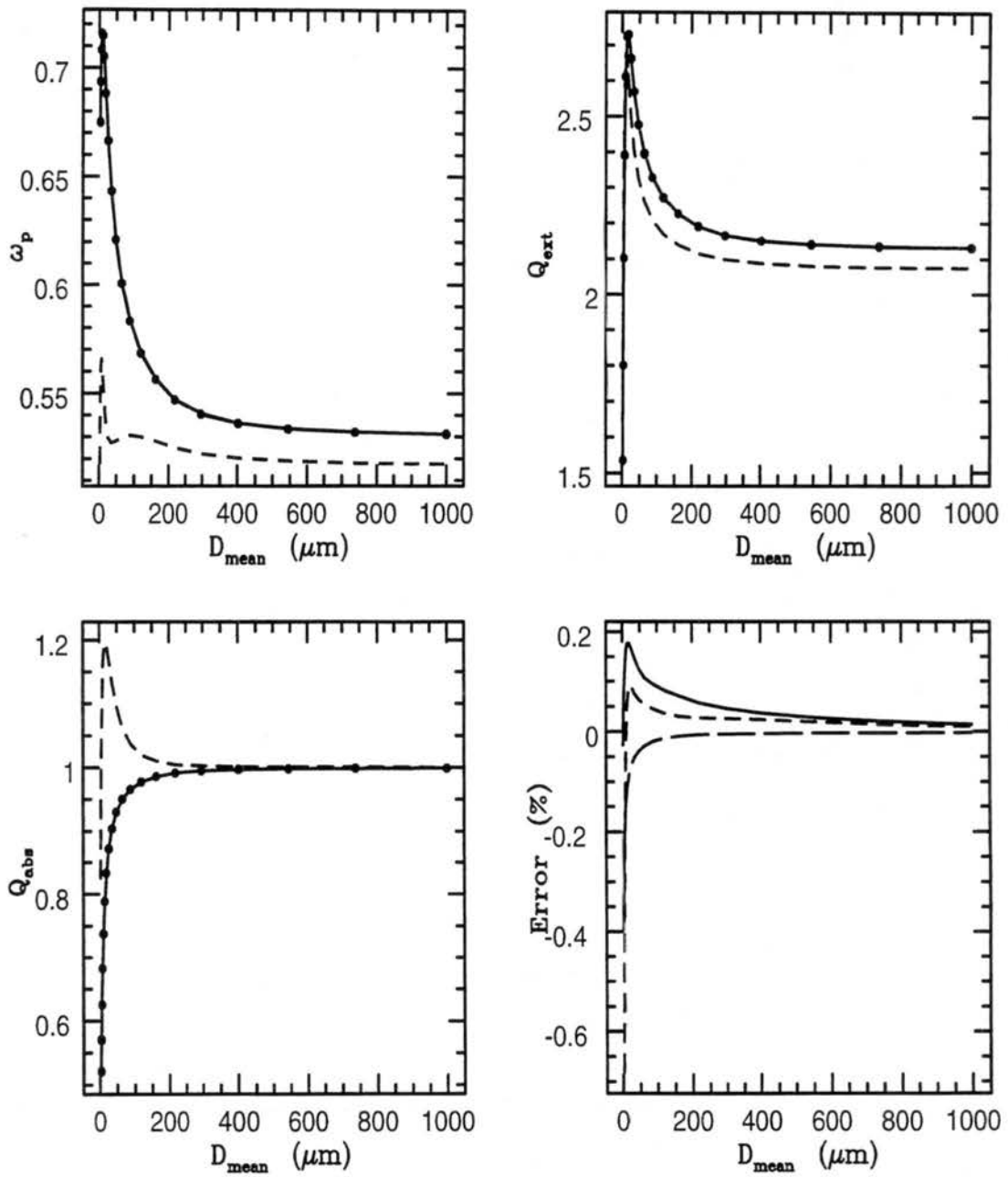

Figure 3.18: Bin mean method for ice plates using $\nu = 2$. The plots for Q_{ext}, Q_{abs} and ω_p show the analytical solution (solid line), the bin mean method solution (solid dots) and Lorenz-Mie theory for spheres as a comparison (dashed line). The plot of relative error shows the error for Q_{ext} (short-dashed line), Q_{abs} (long-dashed line), and ω_p (solid line).

Chapter 4

THE JUNE 28, 1980 ARCTIC STRATUS CASE

4.1 Introduction

The sounding used for these studies is derived from data taken during the June 28, 1980 period of the Arctic stratus experiment (ASE) over the Beaufort sea. Since spatial and temporal data sets are sparse over the Beaufort sea, a single sounding is used to initialize the model. The June 28 ASC case was characterized by two persistent cloud layers; an upper deck about 300 m thick and a lower fog layer which was about 100 m think and extended to the surface. This particular case was chosen for these studies as the upper cloud deck (upon which we focus our attention) is well mixed and can be explored in a two-dimensional modelling framework. An overview of the case is presented here along with a discussion of the microphysical and radiative properties of the cloud system. A discussion of the various aspects of the data procurement procedures may be found in Curry (1986) and Tsay and Jayaweera (1984).

A discussion of the experiment area and the attendant large scale flow patterns is presented in the next section. This is followed by a discussion of the radiative, microphysical and dynamical characteristics of this particular ASC case.

4.2 The large scale environment of the June 28 ASC case.

During the month of June in 1980, aircraft measurements of the microphysical and radiative properties of ASC were carried out over the Beaufort sea north of Barrow and Prudehoe Bay, Alaska. Figure 4.1 shows the experimental areas and dates flown by the aircraft during the experiment. The area denoted by D5 is that in which the flights for the 28 June cases were executed.

The Beaufort sea and Alaska were under high pressure throughout most of the month of June with some slight synoptic scale disturbances propagating through the area from time to time. The areas of cloudiness through out this month were predominately due to air mass modification (by advection over cool ice surfaces) with synoptic scale activity superimposed (Curry and Herman, 1985b). Formation of the lower level cloud decks, through moisture and heat budget analysis, was shown by Curry and Herman (1985b) to be due to a combination of the advection of warm, moist air over the ice pack with subsequent cooling (radiative and turbulent) causing dew point drops and subsequent condensation. Synoptic scale disturbances helped to promote or hamper cloudiness in different situations, the predominate results showing that infrequent synoptic scale features during the Arctic summer have relatively little affect on low level cloudy conditions.

It was noted by Tsay and Jayaweera (1984) that the air mass that influenced the cloudiness during the month of June over the Beaufort sea originated over northern Siberia and had sufficient time to produce elevated moisture contents by advection over the Chukchi and Bering Seas. Whether or not this same air mass was involved in forming the ASC on June 28 is somewhat uncertain. Figure 4.2 shows that the predominate 850 mb flow on the morning of 29 June was essentially out of the west and had shifted from flow that was essentially out of the southwest on 14 June. The advection of warm, moist air into the area during June is outlined in Curry and Herman (1985b) using heat and moisture budgets for 28 June to show that the formation of the low cloud cover during this period was dominated by three dimensional heat and moisture convergence in the area. Radiative and turbulent cooling of the air as it flowed over the ice pack caused reductions in dew point until condensation occurred and the low level clouds form. Vertical motions during this time period showed weak vertical ascent which produced little effect on the heat and moisture budgets of the low level clouds. Values of the large scale ascent were placed between 0.12 and 0.2 $cm\ s^{-1}$. Mid-level cloudiness was present on 28 June from 0000 to 1200 GMT, however this rapidly dissipated near 1200 GMT as a dry air intrusion caused the clouds to evaporate. Thus, our simulations were initiated well after the dissipation of the mid-level cloud cover. Low cloud amount varied from between 40 and 80% during the

period of 23 through 30 June, illustrating the persistent cloud cover over the Beaufort Sea experimental area.

Figure 4.3 shows the flight patterns taken through the 28 June ASC decks. The June 28 case consisted of two parallel decks of clouds with a clear interstice separating the decks. The thickness of the upper deck varied between about 250 and 400 m while the lower deck attained thicknesses of 100 to 200 m. Vertical and horizontal legs were flown during the experiment to produce spacial and temporal microphysics and radiation data for the cloud systems. Unfortunately, cloud microphysics and concomitant radiation measurements were not taken.

4.3 Properties of the June 28, 1980 ASC case

Aircraft data for the various flight legs during the June 28 ASC case are shown in Figs. 4.4 and 4.5 (Curry, 1986) with each data point indicating a measurement taken during the flight. Cloud liquid water contents (LWC) reach a maximum of about 0.5 $g\ m^{-3}$ for the upper cloud deck with the LWC of lower portions of the cloud following that of the adiabatic LWC (straight line). This illustrates the well mixed layer associated with the upper deck. The top of the upper cloud shows plenty of scatter with respect to the LWC showing that variations in cloud depth are due to an undulating cloud top. Values of the liquid water path (LWP) for this case range from 61 to 117 $g\ m^{-2}$. Wind shear was weak throughout the region of the upper cloud deck; in fact Curry *et al.* (1988) showed that buoyancy production is the dominate process whereby cloud-scale TKE is produced. The lower fog layer (situated in an extremely stable environment with a lapse rate of about 30 $K\ km^{-1}$) is quite tenuous with LWC maxima of just around 0.1 $g\ m^{-3}$. This layer is situated in a region of larger wind shear (see Chapter 5) which is its predominate forcing mechanism. Drop concentrations in the upper deck approach values as large as 500 cm^{-3} (illustrating the effects of large number of CCN) thus producing small cloud mean radii. Drop dispersions for the upper cloud deck can be quite large (up to about 0.9 in some locations) and show possibilities of drizzle. It should be noted, however, that an examination of the drop data presented in Herman and Curry (1984) shows that most of

the dispersion is due to a relatively flat spectra within the small drop size range (out to about $r = 10\ \mu m$) with very few drops in the range of 10 to 20 μm (this is also true of the lower cloud deck). Thus, the large dispersions for these distributions are probably not due to a drizzling mode. However, it was mentioned by Tsay and Jayaweera (1984) that periods of sporadic drizzle did occur from the cloud deck. The lower fog layer contains smaller concentrations of drops (on the order of 150 cm^{-3}), presumably due to the weak to non-existent vertical motions and associated low supersaturations. Drop mean radii and distribution dispersions are similar to the upper deck with the breadth being mostly due to drops in the 1 to 10 μm radii range. The fact that the distributions for this cloud systems were predominately narrow may be seen in Fig. 4.6 from Tsay and Jayaweera (1984). The distribution covers the diameter range of 3.1 to 47 μm with concentrations approaching zero beyond the 10 μm radius size. The distributions at cloud top and about 40 m below cloud top show a bi-modal structure with a predominant second mode; this being especially true at cloud top. The distribution at cloud base is mono-modal with a similar distribution shape as cloud top at the smaller drop sizes. Tsay and Jayaweera (1984) suggest that the bi-modal distributions in the upper half of the cloud may be due to inhomogeneous mixing. They base this hypothesis on the fact that drop concentrations decrease systematically with height but fluctuate substantially in the horizontal (thus indicating mixing processes). This was not apparent, however, in the vicinity of cloud base.

As microphysical and radiative data were not obtained simultaneously, Herman and Curry (1984) and Curry and Herman (1985a) used the microphysical data discussed above in conjunction with two-stream radiative transfer models to compute the details of the solar and infrared radiative properties of the clouds that occurred during June 1980. To obtain a better grasp of the details of the short-wave radiative properties of summertime ASC, Herman and Curry (1984) utilized the short-wave (two-stream) model of Slingo and Schrecker (1982). Computations with this model produced acceptable results as compared with observed profiles. Figure 4.7 shows the up-welling and down-welling fluxes observed with an Eppley pyranometer. Total downwelling and upwelling solar fluxes at the top of the upper cloud deck were about 600 and 400 $W\ m^{-2}$, respectively. Significant in-cloud

attenuation of the fluxes within the upper cloud deck is noted. Downwelling and upwelling fluxes in the vicinity of the lower cloud deck are quite similar to those measured at the base of the upper cloud deck, illustrating that the intervening layer and the lower deck affect the radiative fluxes weakly. Reduced reflectivity (R_0) and transmissivity (T_0)[1] values for the June 28 case range from 0.58 to 0.65 and 0.35 to 0.25, respectively. Solar radiative heating rates, as computed by Curry (1986), are quite weak with a maximum of about 1.5 $K\ h^{-1}$ (around 35 $K\ d^{-1}$) and extending throughout the cloud layer (see Fig. 4.8).

Infrared radiative measurements were also obtained during the aircraft flights. Detailed analysis of the infrared properties of the June ASE cases was undertaken by Curry and Herman (1985a) who utilized a two-stream model (without scattering, $\omega_0 = 0$) to assist with the analysis. Infrared fluxes for the June 28 case (shown in Fig. 4.9) illustrate that the cloud was close to a blackbody with derived emissivities between 0.94 and 1.0. Total downwelling and upwelling fluxes at the top of the cloud layer were measured at about 233 and 325 $W\ m^{-2}$, respectively. Fluxes at the base of the cloud layer approached 330 $W\ m^{-2}$. The fluxes illustrate that most of the divergence occurs over a layer about 100 m deep with respect to cloud top. As is shown in Fig. 4.8, for the computed heating rates, IR cooling does occur mostly over the 100 m layer with maximum cooling rates of about 7.1 $K\ h^{-1}$. The total radiative heating rate is dominated by the longwave cooling in these computations, producing cooling throughout the entire cloud layer. Since the fraction of radiative cooling that lies in the mixed layer is correlated with regions of cool air sinking in downdrafts, this amount of radiative cooling should be readily available for generating mixed-layer convection (Deardorff, 1976). Shortwave heating within up-drafts may play a similar role in updrafts, however this heating will also suppress condensational heating which could hinder buoyancy production. The *radiative extinction length*, l_r, has been used to describe the fraction of the net longwave flux that lies within the mixed layer (Brost *et al.* , 1982). This length scale is simply the depth below cloud top in which the net flux, $\bar{F}$,

---

[1] Reduced values account for the reflectivity of the layers below the upper cloud deck, effectively reducing this reflection to zero. This allows the reflection, transmission and absorption functions for the cloud layer to be specified in terms of fractions of 100% . Herman and Curry (1984) discuss this in more detail.

is reduced by the factor $(1 - e^{-1})$. For the 28 June case derived values of this parameter (Curry and Herman, 1985a) range from 32 m for the largest LWP and maximum LWC (117 $g\ m^{-2}$ and 0.5 $g\ m^{-3}$) up to 55 m for smaller values of the LWP and maximum LWC. For clouds with large LWP and cloud top LWC, the radiative extinction at cloud top is usually quite large and, thus, the net flux rapidly decreases with distance into the cloud (which is why l_r decreases). In regions of the cloud deck where the top is more tenuous (less opaque), the net IR flux is diminished over a much longer distance and l_r is larger. If this value is related to mixed-layer convection then there is necessarily a competition between increasing cloud top cooling through increasing cloud top LWC (which can decrease l_r) and increasing mixed-layer convection (something we explore in chapter 5).

Turbulence measurements were also taken during the ASE June aircraft flights. Vertical velocity variance, $< w'w' >$, for June 28 shows cloud top and base maxima in the energetics of the cloud-scale eddies (0.15 and 0.16 $m^2\ s^{-2}$, respectively) illustrating the effects of radiative and evaporative cooling and condensational heating (Curry, 1986). Values of $< w'w' >$ within the cloud layer for this case are significant showing the relatively vigorous mixing taking place within the cloud layer. Values of $< \theta'_e \theta'_e >$ (equivalent potential temperature variance) and $< r'_t r'_t >$ (total mixing ratio variance) tend to increase with height which Curry (1986) attributed to cloud top cooling and condensational growth. Large values of these variances exist at cloud top and are likely partially due to cloud top entrainment of warm, moist air from above (as water vapor increased above the inversion). Fluxes of θ_v ($< w'\theta'_v >$) increase from cloud base values of 0.001 to 0.0030 $K\ m\ s^{-1}$ just below cloud top (940 m). At cloud top, $< w'\theta'_v >$ becomes negative (-0.0013 $K\ m\ s^{-1}$) indicating increasing entrainment of less buoyant air from above the inversion. The large values of $< w'\theta'_v >$ just below cloud top show that large buoyancy production rates are occurring which is indicative of strong buoyancy produced by cloud top radiative cooling. Measured fluxes of droplets with $r < 24\ \mu m$ dominate the turbulent fluxes of liquid water, showning that most of the droplets are small. Turbulent fluxes of liquid water ($< w'r'_l >$) are negative at cloud base (-3.1$\times$ 10^{-4} $g\ m^{-3}\ m\ s^{-1}$) and increase with height in the cloud to just below cloud top where the maximum of 55.0$\times$ 10^{-4} $g\ m^{-3}\ m\ s^{-1}$ is reached.

Thus, turbulent eddies flux liquid water upward with large values at cloud top co-located with large values of LWC. The flux of water vapor, $< w'r_v' >$, is positive throughout the cloud and has a maxima at cloud top and cloud base (30.0 and 39.0$\times$ 10^{-4} $g\ m^{-3}\ m\ s^{-1}$, respectively). The fluxes decrease from cloud base to just below cloud top showing that significant fluxes of vapor are occurring from lower layers of the cloud (possibly from evaporated droplets and large values of $< w'w' >$). The cloud top maximum is most likely due to the fact that this cloud is entraining more moisture from the larger r_v values above the inversion (Curry, 1986). Curry (1986) computed the sum total of all water fluxes and showed that for the June 28 case the total fluxes are not only positive but that the net flux divergence of total water is quite small. This is indicative of a cloud that is reasonably well mixed.

By computing the total heat fluxes that balance the radiative cooling that occurs within the mixed layer (characterized by l_r), Curry (1986) postulated that only a small fraction (on the order of 10%) of the radiative cooling was available for the generation of mixed layer convection. The rest lies in the layer above cloud top, cooling air that lies within the inversion and may promote entrainment through the process of radiative encroachment (Deardorff, 1981). Indeed, Curry (1986) illustrated that between 10 and 71% of the estimated entrainment heat flux was balanced by radiative cooling lying within the inversion. This results, however, seems somewhat suspect as radiative cooling was shown to exist over a substantially deep layer while entrained air appeared to be confined to a narrow region near cloud top. The maximum in $< w'\theta_v' >$ co-located with cloud top, indicating that the largest buoyancy production is occurring there.

The information discussed above is by no means complete enough to make claims about verification of the modelling studies to come in subsequent chapters. Indeed, we have covered most of the information pertenant to the case. These data are, however, presented not only as an overview but also as a means of discussing the physical plausibility of the numerical experiments to follow.

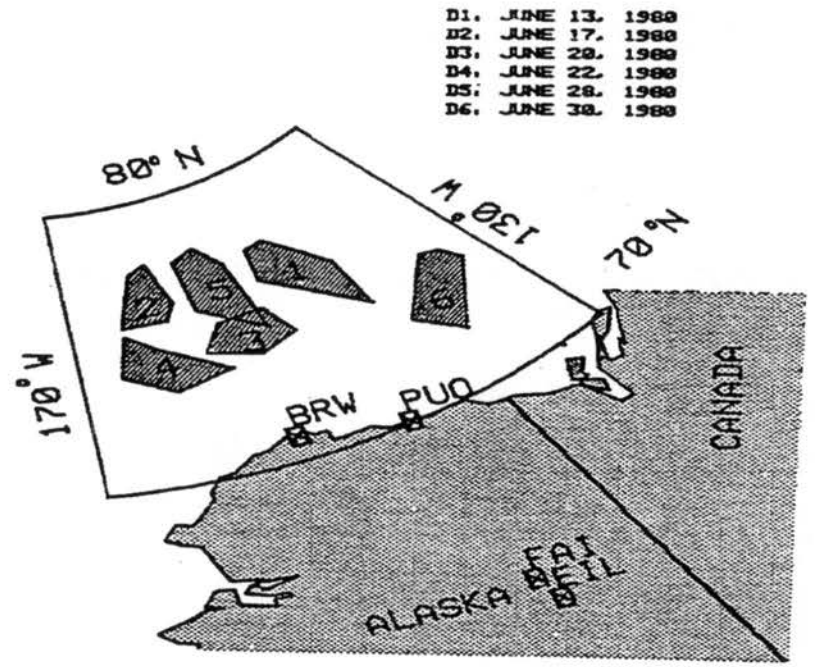

Figure 4.1: Experimental area for the Arctic Stratus Experiment of June 1980 (from Tsay and Jayaweera, 1984).

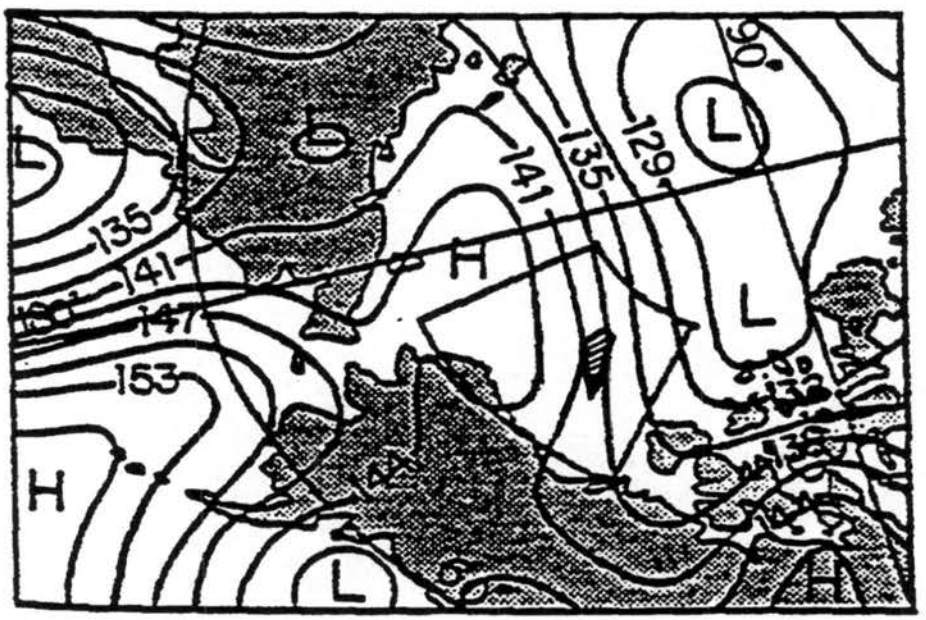

Figure 4.2: Heights for 850 *mb* on June 29, 1980 (from Tsay and Jayaweera, 1984).

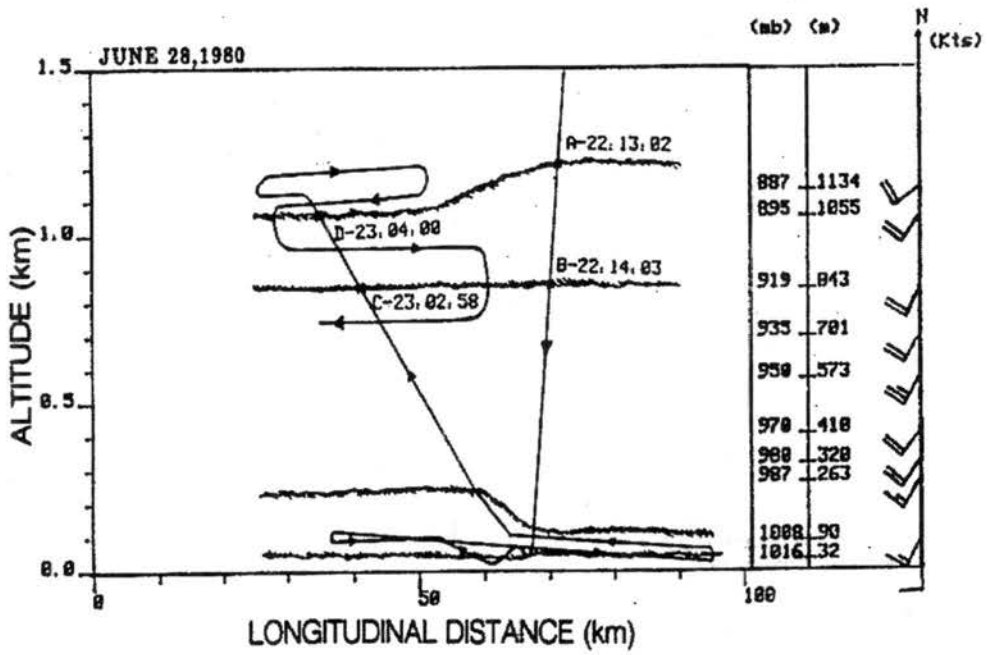

Figure 4.3: Aircraft flight pattern on June 28, 1980 (from Tsay and Jayaweera, 1984).

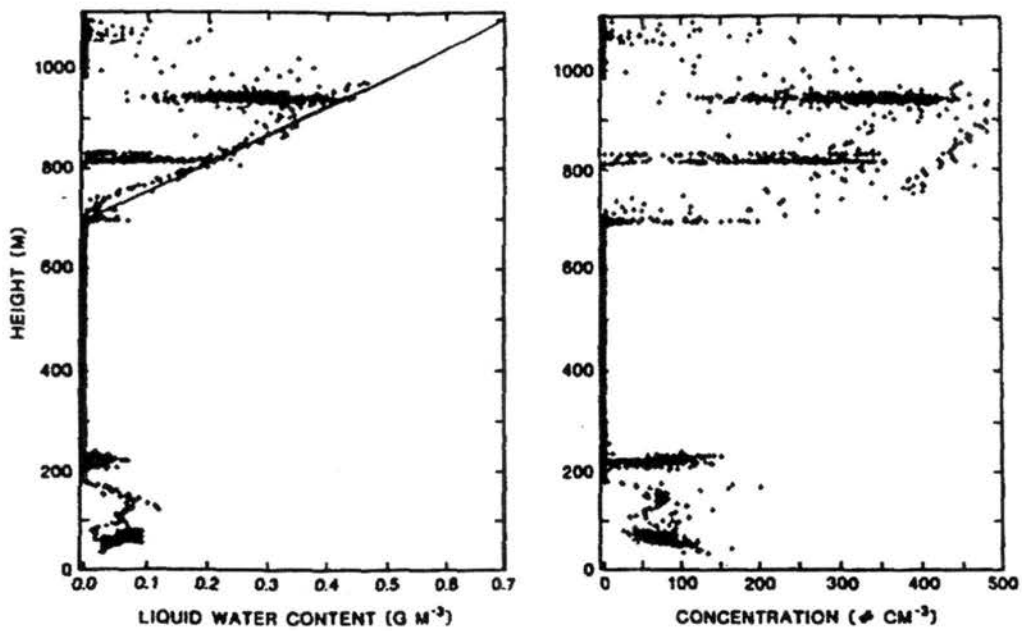

Figure 4.4: Profiles of LWC and number concentration data for the June 28, 1980 case (from Curry, 1986).

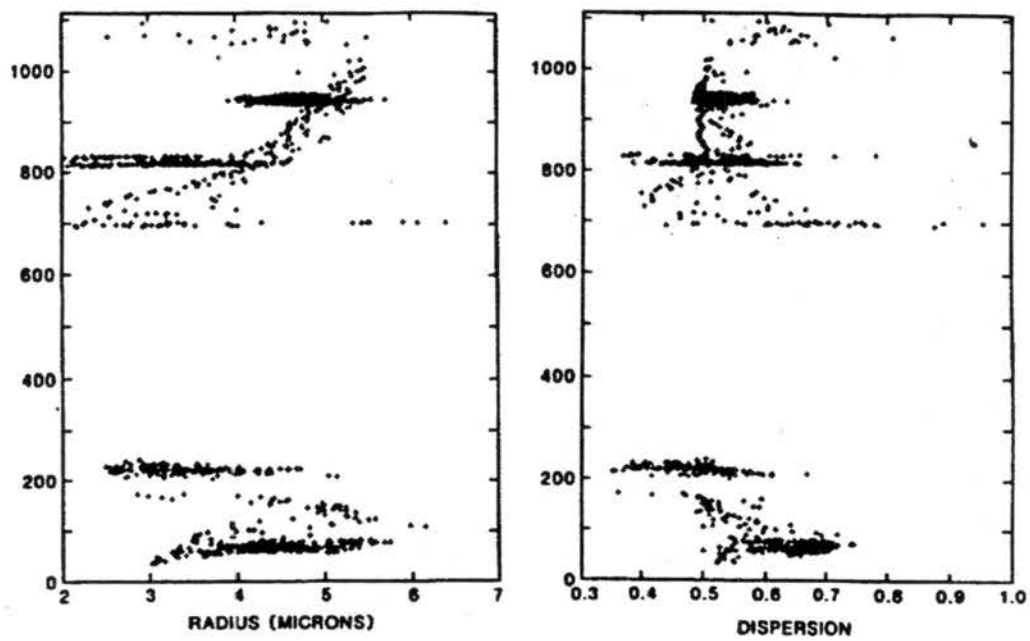

Figure 4.5: Profiles of mean radius and distribution dispersion data for the June 28, 1980 case (from Curry, 1986).

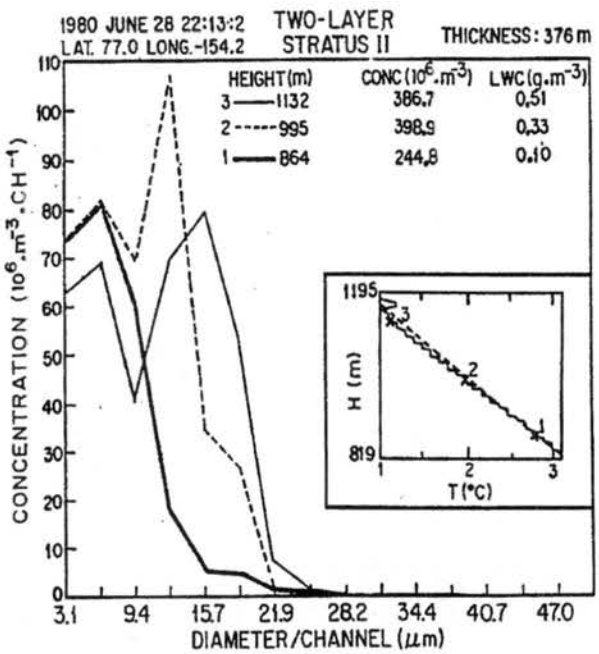

Figure 4.6: Observed drop size distributions for the June 28, 1980 ASC case (from Tsay and Jayaweera, 1984).

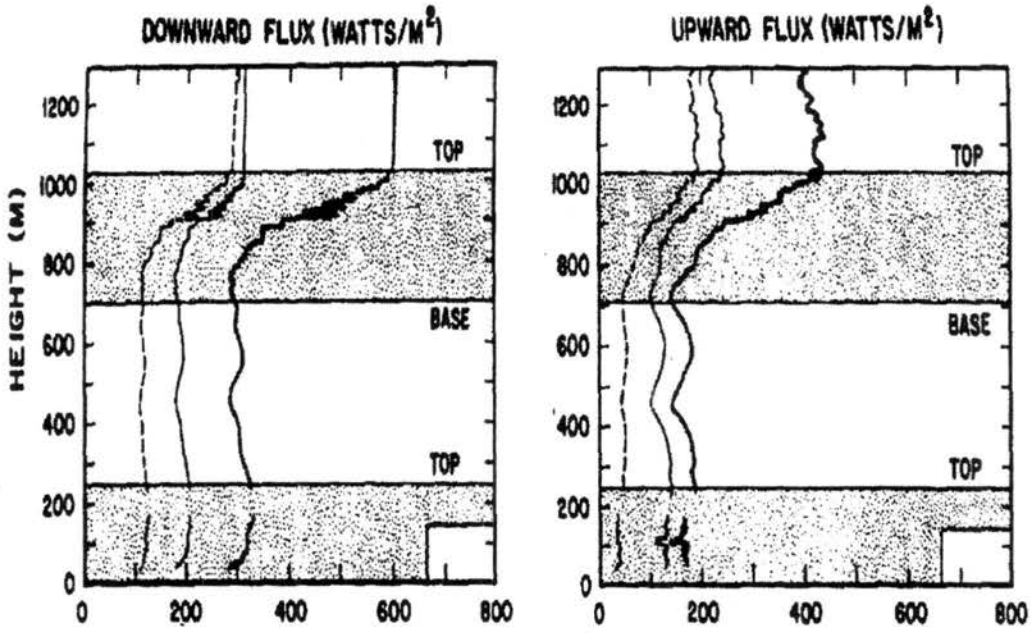

Figure 4.7: Observed solar fluxes for the June 28, 1980 ASC case (from Herman and Curry, 1984). Plotted is the total solar (heavy solid line), the visible (thin solid line) and the near infrared (dashed line) fluxes.

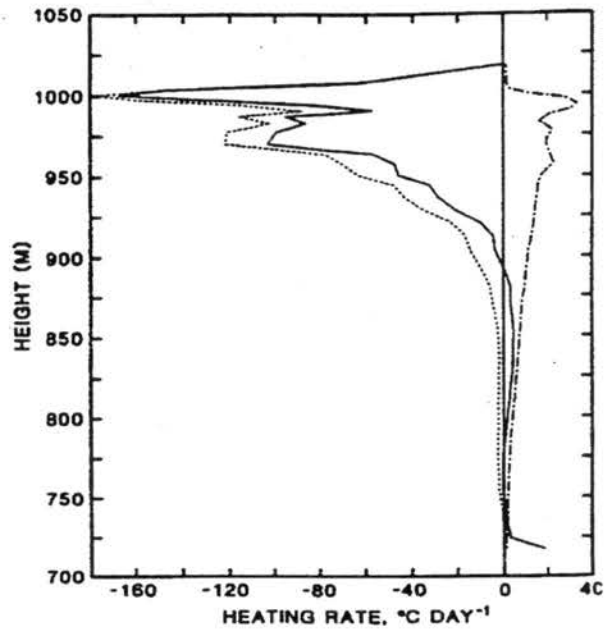

Figure 4.8: Modelled radiative heating rate for the June 28, 1980 ASC case (from Curry, 1986). Plotted is the shortwave (dot-dashed line), longwave (dotted line) and total (solid line) heating rates.

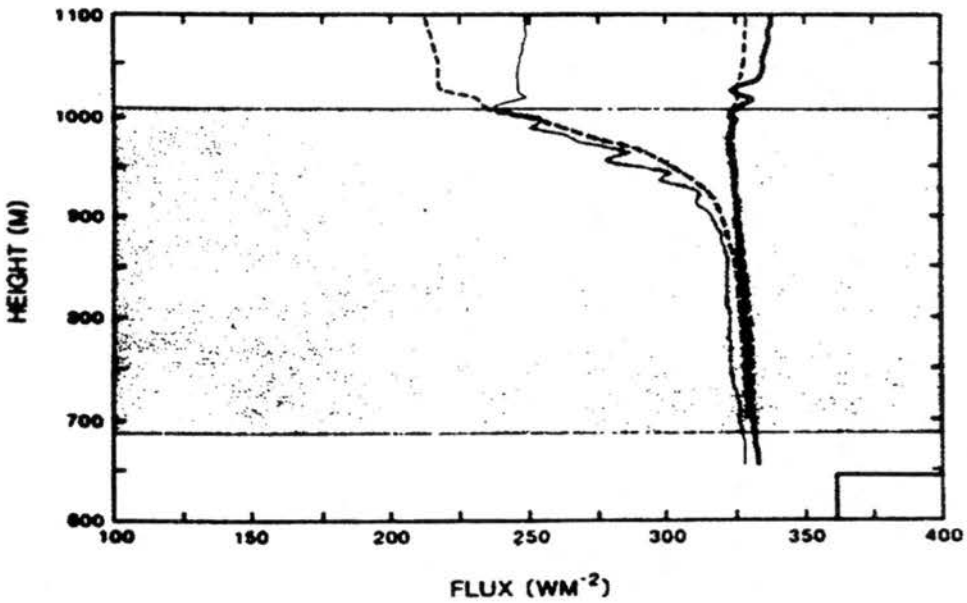

Figure 4.9: Observed infrared fluxes for the June 28, 1980 ASC case (from Curry and Herman, 1985a). Plotted are the observed upwelling (heavy solid line) and downwelling (thin solid line) fluxes along with model computed upwelling (heavy dashed line) and downwelling (thin dashed line) fluxes.

Chapter 5

SUMMER-SEASON SIMULATIONS OF ARCTIC STRATUS

In this chapter, we use the CRM described by Stevens (1996) coupled to the radiative transfer model described in Chapter 3 to examine the effects of microphysics and radiation couplings on simulated ASC. Preliminary studies with the CRM coupled to the the bulk microphysical model of Walko *et al.* (1995) failed to reproduce the drizzle process using the mean radii quoted in Curry (1986), thus we use the the CRM with the explicit, bin resolving microphysical model of Feingold *et al.* (1994) and Stevens *et al.* (1996). The goals of this chapter include the simulation of ASC which were observed during June 28, 1980 as described in Chapter 4. This case was characterized by a cloud-topped boundary layer driven by radiatively produced instability (Curry *et al.* , 1988). The strong mixed-layer which occurred on that day makes this case amiable to CRM simulation. The ability of the CRM to reproduce the mean characteristics of the June 28, 1980 case is explored by comparison to the data of Curry *et al.* (1988) and Curry (1986). Because of the lack of data that plagues ASC analysis, these simulations are not considered to be a case study but simply a physically plausible arena through which various sensitivities may be explored. As has been hypothesized by many authors (*e.g.* Hegg *et al.* , 1995; Shaw, 1986), alteration of CCN concentrations (N_{ccn}) may have a strong impact on the radiative, dynamical and, hence, the microphysical structure of ASC. In conjunction with this, it has been postulated by Albrecht (1989) along with Ackermann *et al.* (1993) that N_{ccn} may also modulate the stability of a stratus cloud layer through the drizzle process. Strong pollution events occur within the Arctic basin (Shaw, 1986) which may, thus, affect the cloud structure dramatically. Because of this, all studies conducted herein utilize $N_{ccn} = 100cm^{-3}$ and $500cm^{-3}$, following the concentration observations of Curry (1986). Activation of drops follows an assumed log-normal distribution function as discussed in Stevens (1996). Since

ASC are continually affected by solar radiation, an examination of SW effects and optical property representations are also undertaken.

5.1 Description of the simulations

In order to produce an initial cloud rapidly without the complicating effects and computational costs of the bin microphysical model, an initial cloud field is produced by using the CRM-NM (supersaturation condensed) model discussed in Chapter 2. This model is run for 4 hours at which time the cloud-dynamical fields have reached a quasi steady-state. This simulation is then used as a common point of departure for studies with the CRM-LBM (Liquid phase Bin Microphysics) simulations. Table 5.1 lists the sets of simulations undertaken in this chapter. In order to explore the effects of radiative and microphysical properties on the simulated cloud layers, two experiments are undertaken (100A and 500A) which use different N_{ccn} and illustrates the effects of drizzling and non-drizzling clouds on the simulated boundary layer. These simulations are treated as control cases as all physical processes are included in the simulation. Comparisons with observational results for these cases illustrate the physical plausibility of the simulations. Since the drizzle process appears to be important for the cloud microstructure, boundary layer evolution and radiative feedbacks, simulations with sedimentation and collection processes (ND simulations) deactivated are undertaken. Comparisons with the A simulations illustrates the importance of precipitation processes on cloud microstructure. As solar radiation is a constant effect in the summertime Arctic, model integrations without the effects of SW radiation (NS) are undertaken in order to ascertain its importance. For all of these simulations drop optical properties are treated by utilizing a fixed gamma distribution function with $\nu = 6$. This value was chosen by comparisons with ASC drop distributions (*e.g.* Tsay and Jayaweera, 1984; Herman and Curry, 1984). As will be shown further in the text, there is evidence from the simulations that this choice is appropriate. Distribution r_e values computed from a gamma distribution with $\nu = 6$ and from the bin model spectral information are in excellent agreement, suggesting that optical properties derived from the gamma distribution are appropriate (Hu and Stamnes, 1993). In addition, the use of a gamma function

Simulation	N_{ccn} cm^{-3}	Microphysics	Radiation	Opt. Properties	Time
NM		$\tau_{cond} \rightarrow 0$	All	Gamma	0 to 4 h
100A	100	All	All	Gamma	4 to 6 h
500A	500	All	All	Gamma	4 to 6 h
100ND	100	No Collection or Sedim.	All	Gamma	4 to 6 h
500ND	500	No Collection or Sedim.	All	Gamma	4 to 6 h
100NS	100	All	No SW	Gamma	4 to 6 h
500NS	500	All	No SW	Gamma	4 to 6 h
100BA	100	All	All	Bin	4 to 6 h
500BA	500	All	All	Bin	4 to 6 h
100HS	100	All	All	Hu & Stamnes	4 to 6 h
500HS	500	All	All	Hu & Stamnes	4 to 6 h

Table 5.1: Warm-cloud simulations. Simulation title and physical processes utilized during the simulations are listed. $\tau_{cond} \rightarrow 0$ means that condensation occurs over a zero time-period in the CRM-NM, therefore all water above 100% RH is immediately condensed.

optical properties reduced one particular degree of freedom, that of alterations in distribution shape affecting the cloud microphysics and dynamics. This constraint is relaxed in the BA simulations which utilizes the accurate bin representation of the optical properties discussed in Chapter (3). The differences with the gamma simulations are shown to be dramatic, thus leading to the question of whether r_e alone is a good characterization of radiative properties in terms of cloud process interactions. To answer this, the optical property computation method of Hu and Stamnes (1993), HS, is utilized. These simulations give circumstantial evidence that distribution shape, as regards optical property computations, is important for the structural evolution of the cloud layer. The final section of this chapter provides some evidence as to this dependence which is consistent with the behavior shown in the other simulations.

In the next section, we discuss the production of the initial fields with the CRM-NM model. The sections that follow address specific issues related to microphysical and radiative interactions and the effects produced.

5.2 Production of the initial field and CRM-NM results

The initial mean fields used in the CRM-NM to produce a steady cloud field were derived from aircraft data taken during the June 28, 1980 ASE (as discussed in Chapter 4) and are shown in Fig. 5.1. The initialized water vapor amounts are large enough so that two quasi-parallel cloud layers are produced. The upper cloud deck is about 300 m thick with 0.38 $g\ m^{-3}$ LWC[1] while the lower fog layer is about 270 m thick and extends completely to the ice surface. Maximum LWC for the lower fog layer is about 0.16 $g\ m^{-3}$, which is consistent with the results of shown in Chapter 4. The upper cloud layer is capped by a strong inversion with a nearly moist-adiabatic layer existing down to the top of the fog layer. The lower fog layer, by contrast, exists in an extremely stable environment (lapse rate of almost 30 $K\ km^{-1}$) with strong shear of the horizontal winds. The nature of the profiles of θ and the horizontal winds suggests that the layer from about 1100 m down to about 600 m is relatively well-mixed, as is expected for a cloud-topped boundary layer which is driven by radiative cooling. The lower fog layer appears to be decoupled from the upper cloud deck and is not driven by any sort of radiatively forced eddies.

An initial inhomogeneity is introduced through a random perturbation of $\delta = \pm 0.1\ K$ applied to the model θ-fields; the perturbation satisfies, $\int \delta(x,z)dx = 0$ so that increases or reductions in the integrated heat content do not occur. Simulations with the CRM-NM were conducted for a 4 hour time period to produce an initial cloud layer. A constant cloud drop number concentration of 100 cm^{-3} is used for interactions with the radiation, leading to droplets distributions with mean radii of about 10 μm, which is close to the observed value (6 to 12μm; Curry, 1986). Throughout the simulation horizontally averaged statistics are compiled after every 20 seconds of model time. These horizontal averages are accumulated and then averaged over a temporal period of 15 minutes. Longer temporal averages are generally needed in order to discuss average system behavior, so fields will be plotted as 1 hour averages unless otherwise stated.

---

[1]Liquid water content (LWC) is defined by the integral, $\int m(r)n(r)dr$, where $m(r)$ is the mass of a drop with radius r.

After 4 hours of simulation, the CRM-produced cloud layers show many features which are in accord with observations (Fig. 5.2). Liquid water contents of the upper cloud layer have a similar depth and maximum (0.46 $g\ m^{-3}$) as those presented in Curry (1986). The lower cloud deck is slightly thicker than Curry's (1986) results ($200m$), but LWCs are similar (about 0.1 $g\ m^{-3}$). Longwave (LW) and shortwave (SW) heating rates have greater maxima (by about 1 $K\ h^{-1}$) and somewhat smaller depths than Curry's results and are apparently due to the simplified microphysics. Without drizzle and with constant cloud top drop concentrations radiative flux divergence occurs over a very shallow layer. In addition to this, the microphysical information actually used in the radiative computations of Curry (1986) is not stated. If microphysical data points associated with cloud top turrets are included, then the cloud top region will appear more diffuse to the plane-parallel radiative transfer code. Thus, the flux divergence produced would occur over a deeper layer with a smaller maximum and is a possible source of the discrepancy between our results. The destabilization of cloud-top caused by the strong radiative cooling in the model produces coherent eddy structures whose vertical component of TKE ($1/2\ < w'w' >$) is peaked below the mid-cloud level. The results of Curry (1986) shows $< w'w' >$ maxima at both cloud top and cloud base, which contrasts the results presented here. The $< w'w' >$ maximum of 0.18 $m^2\ s^{-2}$ is close to the observed range of 0.08 to 0.16 $m^2\ s^{-2}$ (Curry, 1986).

As the lower cloud layer exists in a strongly sheared environment which is not well represented in the 2-D framework (Stevens, 1996), and since the lower cloud layer is decoupled from the upper cloud[2], we focus attention on the upper cloud deck throughout the remainder of this chapter.

---

[2]The lower cloud deck has a similar reflectivity as the ice surface and, thus, its radiative influence on the upper deck should be small. In addition, the strong, stable lapse rate near the surface prevents lower cloud fluxes from penetrating to the upper deck. Trajectories used in Chapter 6 showed that parcels initiated in the lower layers never make it to the upper deck.

5.3 Simulations with the CRM-LBM

The general order in which simulation results are discussed throughout the remainder of this chapter is as follows. First, the control (A) simulations are discussed in terms of the differences between the N_{ccn} cases. Sensitivities which use the fixed gamma distribution optical properties (ND and NS) are then discussed in comparison to the control simulation. Following these discussions is a section that examines the effects of radiation on the cloud structure when the constraint of fixed distribution optical properties is relaxed (BA). In the final sections, the effects of using optical properties derived from r_e values on the cloud structure is examined (HS) along with a short exposition on the effects of distribution shape on cloud evolution.

5.3.1 Properties of the simulations with all microphysics (A).

One expects, that for a given LWC, a cloud with larger drops concentrations would be expected to produce less drizzle and, therefore, larger cloud top reflectivities than clouds with smaller drop concentrations. The effects of differing CCN concentrations (N_{ccn}) on the mean structure of the simulated ASC layer is shown in Fig. 5.3 for 100A, 500A and the NM simulation for comparison. As is shown in Fig. 5.3, larger values of N_{ccn} lead to larger cloud top LWC values (0.47 $g\ m^{-3}$ vs. 0.38 $g\ m^{-3}$) and much larger cloud drop concentrations (180 cm^{-3} vs. 50 cm^{-3}) which translates into more numerous small droplets for 500A (r_e profiles). The concentrations produced by the model are lower than those presented by Curry (1986) for this case (Fig. 4.4) and is most likely due our choice of $N_{ccn} = 500cm^{-3}$, of which a fraction, but not all, will be activated by the numerical routine. The effective radius (r_e) is about 5 μm smaller throughout the cloud than 100A, since the available water vapor must be distributed over more CCN through condensation in 500A. Profiles of number concentration for all cases illustrate the nearly constant with height concentration profiles that are observed in stratocumulus, which compares well with observations of the June 28, 1980 case study (see Chapter 4). Profiles of concentrations for droplets larger than $D = 50\ \mu m$ (N_r) illustrate that the lower CCN concentrations

produce more drops within the *drizzle*[3] portion of the spectrum. Note that the profile is preferentially skew to the top portion of the cloud with drizzle drop concentrations of 0.085 cm^{-3} for 100A and 0.00015 cm^{-3} for 500A. The reason for this profile seems somewhat straight-forward, as droplets growing within supersaturated updrafts spend enough time at cloud top to produce significant numbers of drizzle drops (a point that will be elucidated further in Chapter 6). This is corroborated by the reduction of the cloud top LWC and the increase of lower cloud LWC in 100A as compared to the 4 hour NM profiles. This along with the larger r_e values and cloud base peak indicates an active drizzle process in 100A, however, not in 500A. Even though larger concentrations were observed for this case, observations showed periods of sporadic precipitation from the cloud layer (Tsay and Jayaweera, 1984). The $500cm^{-3}$ cases can produce precipitation, however the reader is differed to Chapter 6 for this discussion.

Values of r_e derived with the gamma distribution used to compute the optical properties,

$$\begin{aligned} r_e &= \frac{\int_0^\infty D^3 n(D) dD}{\int_0^\infty D^2 n(D) dD}, \\ r_e &= \frac{(\nu+2)}{2}\left[\frac{N_t}{LWC}\frac{6\rho_a}{\pi\rho_l}\frac{\Gamma(\nu)}{\Gamma(\nu+3)}\right]^{1/3}, \end{aligned} \tag{5.1}$$

compare well with the bin computed profiles (Fig. 5.3) throughout the upper most 150 m of the cloud in 100A and throughout the entire cloud in 500A. These results suggest that optical properties computed with the gamma distribution function should well represent those of the bin microphysics (see Chapter 3 or Hu and Stamnes, 1993).

Radiatively, the 500A case compares best to the observations of Curry (1986); most likely because of the fact that drop concentrations in 500A are closer to observed values. Infrared fluxes computed by the model (Fig. 5.4) compare well to those presented in Curry and Herman (1985a) (Fig. 4.9) with upwelling and downwelling LW fluxes near cloud top of 325 $W\ m^{-2}$ and 215 $W\ m^{-2}$, respectively while LW fluxes at cloud base are about

---

[3]We will delineate *drizzle droplets* as those with diameters greater than 50 μm as these drops have significant collection efficiencies (greater than 0.2) and may have a sizeable impact on the drizzle process.

	100A	500A	100ND	500ND	100BA	500BA
R_0	0.495	0.544	0.526	0.586	0.590	0.682
T_0	0.390	0.340	0.363	0.298	0.335	0.246
A_0	0.115	0.116	0.111	0.116	0.075	0.072

Table 5.2: Reflection (R_0), transmission (T_0) and absorption (A_0) functions for the simulated clouds derived as per Herman and Curry (1984).

327 $W\ m^{-2}$. The simulated ASC has a flux emissivity of 0.965 which is well within the observed range of 0.95 to 1.0 (Curry and Herman, 1985a). Comparison of the solar fluxes to the observed values (Fig. 4.7) shows that downwelling and upwelling solar fluxes are a few $W\ m^{-2}$ greater at the top of the simulated cloud. Fluxes near cloud base are somewhat smaller indicating that stronger attenuation is occurring within the simulated system. Overall, however, the radiative fluxes compare well with those observed during this case.

The larger cloud top cooling rates in 500A as compared to 100A can be attributed to the following factors. Plotted in Fig. 5.5 are the layer optical depth, τ, and the net flux, $\Delta F = F^- - F^+$, for both shortwave and longwave radiation. Because 500A contains much larger drop concentrations and larger LWC as compared to 100A, the 500A simulation necessarily produces greater solar and infrared optical depths. Gradients of τ near cloud top are much larger in 500A, however the net flux profiles are not exceedingly different between the cases. The largest difference occurs in the SW where much more radiation is reflected by the cloud layer in 500A. Table 5.3.1 shows that cloud reflectivities are much lower in 100A (0.495) than in 500A (0.544). Even though the 500A cloud layer reflects more radiation, the increased optical paths due to scattering allows for slightly more overall absorption in this case (0.116 as compared to 0.115 in 100A). Most of this absorption occurs near cloud top through the larger net flux divergence in 500A. Measured reflectivities (~ 0.6) and absorptivities (~ 0.06) shown in Herman and Curry (1984) illustrate that the observed cloud was more reflective and less absorptive than the simulated ASC.

In conjunction with these results, radiative heating and cooling rates attain greater maxima and are more concentrated near cloud top in 500A as is shown in the θ_l -tendency

panels of Fig. 5.6. Cloud top cooling rate maxima, between -4 and -5.5 $K\ h^{-1}$, are lower and heating rate maxima, between 0.6 and 1.1 $K\ h^{-1}$, are greater than the modelling results presented in Curry (1986) (see Chapter 4). The biggest difference appears to be the stronger SW heating rates that occur in these cases. This, as it turns out, is due to the gamma distribution optical properties which increase SW absorption because of its anomalous breadth. Evidence to corroborate this will be given in §5.3.4.

The radiative cooling and heating strongly affect the total heat budget of the cloud layer given by the total θ tendency ($d\theta/dt$ in Fig. 5.6). The 100A case shows much stronger cooling ($d\theta/dt$) of the entire layer than 500A; the causes of which may be ascertained from the plots of the liquid water potential temperature (θ_l) tendency components in Fig. 5.6. These tendencies illustrate the potential for a given process to heat/cool the local environment and, thus, gives information about the importance of that process in the overall cooling (called equivalent heating in Frisch *et al.* , 1995 and Feingold *et al.* , 1996a). The effects of cloud top radiative cooling are largely offset by microphysical processes in 100A, but through microphysics and diffusion in 500A. Overall, cloud top is cooled much more strongly in 500A as shown in both the $d\theta/dt$ and $d\theta_l/dt$ profiles for that case. Larger drizzle rates in 100A increases the evaporative cooling of drops beneath cloud base, thus leading to stabilization of the layer. The cooling of the lower portions of the cloud must be maintained against the SW radiative heating which helps to stabilize the cloud. In 100A, microphysical, advective and diffusive processes substantially offset this heating whereas in 500A, even though diffusive cooling is much larger, the effect is less pronounced (compare $d\theta_l/dt$ for each case) causing much stronger overall heating in this case.

Since cooling of the cloudy layer is indicative of eddies mixing-down air cooled radiatively at cloud top, the radiative heating and cooling profiles are integrated in order to ascertain the total radiative effect. Radiative cooling that occurs within the mixed-layer is immediately available for TKE generation (Deardorff, 1981) and, therefore, any cooling that occurs in this region should be readily mixed throughout the cloudy layer. In order to ascertain the strength of this in each case, the radiative cooling is integrated within the

mixed layer (C_M), within the inversion zone (C_I) and throughout the entire cloud for radiative heating (H). The results have been accumulated in Table 5.3.1. Much more of the

	100A	500A	100ND	500ND	100BA	500BA
C_I ($K\ h^{-1}\ m^{-1}$)	-67.3	-90.0	-73.2	-87.7	-58.2	-62.08
C_M ($K\ h^{-1}\ m^{-1}$)	-66.3	-56.7	-60.3	-60.2	-114.3	-120.3
H ($K\ h^{-1}\ m^{-1}$)	77.0	118.3	80.35	119.0	39.0	60.49
Total ($K\ h^{-1}\ m^{-1}$)	-56.6	-28.4	-53.15	-28.9	-133.5	-122.61

Table 5.3: Radiative cooling rates integrated within the mixed-layer (C_M), the inversion (C_I) and the total integrated radiative heating (H).

radiative cooling is partitioned to the inversion layer in 500A because the radiative cooling occurs over a more shallow depth in that case. Thus, more cooling is readily available for negative buoyancy generation in 100A. In conjunction with the greater in-cloud cooling, 100A also has smaller integrated heating rates. Radiative effects, therefore, cool the cloud layer more in 100A than in 500A which accounts for the differences in total cooling rates ($d\theta/dt$). This compares well with the analysis of Nicholls (1988) who showed, for subtropical stratocumulus, that the incorporation of radiatively cooled air into downdrafts is the primary mechanism for cooling and negative buoyancy production.

The total cooling of the layer in 100A (Fig. 5.7) is great enough to cause significant decreases in θ_v[4] with time while in 500A, θ_v has increased in comparison to the 4 hour CRM-NM profile. The larger cooling rates in 100A allows for further condensation and, hence, larger reductions in r_v during the model integration. The reduction in θ_v, θ and r_v in 100A through microphysical and radiative effects causes greater buoyancy production of $< w'w' >$ in 100A and, thus, stronger circulations (Fig. 5.2) in that case. Since θ_v and r_v are increased throughout the 500A cloud layer as compared to the 4 hour values, buoyancy is suppressed in comparison to 100A which reduces the eddy strength. Circulation strengths in both 100A and 500A are reduced in comparison to the 4 hour CRM-NM profiles (Fig. 5.2)

[4]We use the θ_v variable here as it is related to the buoyancy production of $< w'w' >$ within the cloud layer. This is defined as $\theta_v = \theta(1 + 0.61 r_v)$.

because drizzle, as shown in Fig. 5.6, tends to stabilize the cloud layer (similar to the results of Stevens, 1996).

The model generated buoyancy production maxima between 2 and $3\times\ 10^{-4}\ \ m^2s^{-3}$ are somewhat greater than aircraft derived values near $1.6\times\ 10^{-4}\ \ m^2s^{-3}$ (Curry *et al.* , 1988) but is definitely within reasonable limits. In addition, buoyancy production of $< w'w' >$ in the model is the dominate term, which is consistent with the results of Curry *et al.* (1988).

5.3.2 Properties of the simulations without sedimentation (ND)

The effects of drizzle on the cloud structure in the $100cm^{-3}$ and $500cm^{-3}$ cases is weak as a comparison of the microphysical profiles for ND (Fig. 5.8) and A (Fig. 5.3) shows. Liquid water contents are similar between the cases and only the drizzle characteristics of 100A stand apart. Much fewer drizzle droplets are produced in these cases (N_r) with the largest amounts occurring at cloud top. The effective radius profiles are surprisingly similar to the A cases with the largest difference being the lack of a cloud base peak in r_e due to drizzle in 100ND. Values of r_e derived with the gamma distribution function used in the radiative calculations again shows good agreement with the bin-derived values, suggesting the appropriateness of the optical property calculations.

Without the effects of drizzle, both cloud layers become more reflective, and less transmissive (Table 5.3.1) as few drizzle-sized drops are produced. Total solar absorption is reduced in the 100ND case, while it is not affected at all in 500ND. The latter result can be traced to the fact that the 500ND and 500A cases are almost microphysically identical since little drizzle is produced in 500A. The drizzle effects on the radiative properties, however, produce only a small effect on the radiative heat budget. Radiative heating rates (Fig. 5.9) are similar to those produced in the A cases (Fig. 5.6). In addition to this, Table 5.3.1 shows similar integrated heating and cooling is occurring in the ND as in the A cases. The greater SW heating in 500ND, as in 500A, leads to smaller in-cloud cooling rates ($d\theta/dt$, Fig. 5.9) and, therefore, similar stabilizing effect in 500ND as in 500A. Thus, differences in the θ_v and r_v profiles (Fig. 5.9) along with buoyancy production of $< w'w' >$ are similar to the A cases. Without the stabilizing effects of drizzle, however, buoyancy

production rates become larger as do the circulation strengths ($< w'w' >$) than those in the respective A cases. The difference between the strength of the circulating eddies in $100cm^{-3}$ and $500cm^{-3}$ remains because of the stronger SW heating in 500ND.

Thus, the main effect of drizzle on the simulated ASC appears to be the stabilization of the cloud layer (for an in depth discussion of this see Stevens, 1996). Even in cases with large CCN concentrations (such as 500A and 500ND) which produce very low drizzle amounts, the effects of this stabilization are noticeable.

5.3.3 Properties of the simulations without shortwave radiation (NS).

Since the SW radiative properties appear to have a strong stabilizing effect on the ASC layer, simulations with solar radiation deactivated gives an indication of just how strong this affect is. The deactivation of SW heating has a dramatic effect on the microphysical structure of the cloud layer, as a cursory comparison of Figs. 5.10 and 5.3 shows. The depths and LWCs of the clouds are significantly increased in these cases, with 500NS producing a higher cloud top through radiative encroachment (Deardorff, 1981). Concentrations of drops have increased in both 100NS and 500NS cases due to increased mixing and cooling (see below) which allows for further drop activation. Drizzle drop concentrations are reduced in comparison to the A cases and appears to be due to enhanced collection processes as r_e values near cloud base have been substantially increased. The 500NS case, however, produces little difference in r_e profiles in comparison to 500A, indicating that even though greater condensation is obviously occurring in 500NS, it is not enough to initiate the drizzle process.

Cloud top radiative cooling rates have been increased in both maxima and depth (Fig. 5.11) as compared to the A simulations since no SW heating occurs and LWCs have increased. Further condensation above the initial cloud top in 500NS occurs because a large portion of the LW cooling occurs here (-237 $K\ h^{-1}\ m^{-1}$ as compared to -165 $K\ h^{-1}\ m^{-1}$ for 100NS). Mixed-layer radiative cooling is, again, much greater in 100NS with values of -136.3 $K\ h^{-1}\ m^{-1}$ compared to -66.5 $K\ h^{-1}\ m^{-1}$ in 500NS. A small amount of LW heating within the lower portions of the cloud occurs in both cases and is barely discernable in (Fig. 5.11, Table 5.3.1).

Greater radiative cooling of the mixed-layer in the NS simulations produces larger total cooling ($d\theta/dt$) of the cloudy layer in time as compared to the A simulations. The larger mixed-layer radiative cooling in 100NS contributes to the greater $d\theta/dt$ values. This larger cooling reduces θ_v and r_v (Fig. 5.12) by a much larger amount than the A simulations. Overall, the differences in thermodynamic structure between the 500NS and 100NS cases are minimal, suggesting that SW heating plays a dominate role in the thermodynamic differences portrayed in the A simulations.

Since radiative destabilization of the cloud layer is not offset through the stabilizing effects of SW heating, buoyancy production of $< w'w' >$ increases by over a factor of 2 in the NS as compared to the A cases. This produces stronger circulating eddies ($< w'w' >$) that penetrate deeper into the boundary layer, thus enacting a stronger effect on the microphysical fields presented above. Buoyancy production is reduced in 100NS over 500NS and, as all other thermodynamic tendencies are similar, must be due to the stabilizing effects of stronger drizzle production in this case (Fig. 5.11)

It becomes apparent thorough a comparison of the NS and A simulations that the stabilizing effects of SW radiation can dominate the stabilizing effects of drizzle in weakly drizzling situations. Indeed, the stronger SW heating in 500A caused weaker circulations than 100A even though drizzle was produced. Because SW stabilization occurs in the vicinity of the buoyancy production maximum, circulations also tend to become more shallow (as downdrafts are the primary driving mechanism; Nicholls, 1984). The effects are not as pronounced in the ASC as they are in simulated subtropical stratocumulus (Bougeault, 1985) because of the strong stabilization of the lower layers in ASC. These effects, of course, are noticed in simulations which fix the distribution shape dependence of the optical properties. Even though derived r_e values match well, we would like to know, "*how well does r_e characterize radiative properties that feedback into a dynamical/microphysical system?*" This is examined in the next section.

5.3.4 Properties of the simulations with bin optical properties (BA)

The utilization of the bin optical property method described in Chapter 3, allows for the most accurate computation of the microphysical/radiative coupling possible. One

would think that, since mean r_e values match well for the previous simulations, model integrations utilizing the bin optical properties should produce similar microphysical and dynamical fields. A quick perusal of the microphysical profiles (Fig. 5.13) produced shows that this is not the case. Profiles of the mean LWC for the BA-simulated clouds in comparison to the A simulations (Fig. 5.3) show that not only is more liquid water condensed in the BA cases, but that more drizzle is produced. Cloud top LWC in the 500BA case more closely compares with the 500NS simulation than 500A. Larger numbers of drops (N_t) are produced in 500BA than 500A, while in 100BA larger number concentrations occur in the lower portions of the cloud than 100A. In addition to this, greater numbers of drizzle drops (N_r) are produced along with a much more prominent cloud base drizzle mode in the r_e profile of 100BA. The large effective radius values in the vicinity of cloud base are even greater than those produced in 100NS, indicating that accurate computations of distribution optical properties are important for the determination of the microphysical structure of the cloud, especially in weakly drizzling cases such as the $100cm^{-3}$ cases. The 500BA profile of r_e shows that, even though drizzle is enhanced further in 100BA, little effect on distribution breadth occurs in 500BA.

Cloud top radiative cooling maxima (Fig. 5.14) are increased by about 17% while in-cloud heating maxima are reduced by as much as 46% . Since the explicit distribution function does not necessarily have a tail, as does the gamma distribution used to derive optical properties in the last section, the artificial influence of large drops on optical properties does not occur. Thus, cloud reflectivities and absorptivities (Table 5.3.1) are much more representative of a cloud whose top region is characterized by small droplets; the values produced (0.682 for 500BA and 0.590 for 100BA) are more in accord with measured ranges of Herman and Curry (1984) than the A cases discussed above. Total integrated cooling rates have increased (Table 5.3.1) and SW heating of the layer is reduced in both cases (the greatest reduction occurs in 500BA). This leads to a substantial increase in the overall cooling of the layer in the BA simulations ($d\theta/dt$ in Fig. 5.14). Total cooling of the layer lies between that produced in the A and NS cases, as reason would contend.

The similarity in the overall cooling rates in the BA cases produces θ_v and r_v profiles (Fig. 5.15) that are similar throughout the cloud layer. Below cloud base, however, the

greater drizzle rates in 100BA causes much more significant cooling and moistening of the sub-cloud layer. Thus, as the microphysical components to the $d\theta_l/dt$ equation show, the layer is much more strongly stabilized in the 100BA case. The greater drizzle stabilization causes reductions in buoyancy production and larger stabilizations of the sub-cloud layer. This, in turn, reduces the depth and strength of the circulating eddies, as characterized by $< w'w' >$, in 100BA as compared to 500BA. The reduction in SW heating through the accurate computation of drop optical properties produces eddies that are stronger than the respective A cases. The penetration depth of the eddies in 100BA is, however, not increased as compared to 100A since the greater drizzle rates substantially stabilize the lower layers. In 500BA, where drizzle production is still weak, the eddies not only grow stronger but increase their depth as little stabilization though drizzle occurs. The strong increase in eddy strength in these cases is in-line with the results of Deardorff (1981), in which he showed that if the ratio of radiative cooling in the inversion zone is about 30% that of the total, then buoyancy production of $< w'w' >$ would be maximized. This ratio, from Table 5.3.1, is about 33% for the BA simulations while for the A simulations it is closer to 55%.

The results of this section leads to the question, "*if the r_e derived from the gamma distribution gives similar values as compared to bin derived values in the mean, then why are the radiative and, hence, the microphysical and dynamical properties so different for the simulations using accurate bin representation of the optical properties*?" This points to the fact that even though the r_e values agree in the mean, shorter temporal variations in the distribution shape can have a large effect. If this is true, then using mean r_e values for optical property computation can lead to large errors in terms of the microphysical and dynamical evolution of the cloud layer. To test this further, we use the method described in Hu and Stamnes (1993) (see Chapter 3) for the computation of the optical properties. This method assumes that r_e is the fundamental quantity in the computation of the hydrometeor optical properties, whereas the A, ND and NS simulations assumed a fixed distribution shape of $\nu = 6$.

5.3.5 Properties of the simulations using the method of Hu and Stamnes (HS)

In this subsection we compare simulated ASC using the Hu and Stamnes (1993) method of computing drop distribution optical properties to those presented in the previous sections. To utilize this method, we derive optical properties from a gamma distribution function with $\nu = 6$, however, instead of conserving the LWC and concentration (N_t) of the bin distribution (as in the A cases), we now conserve r_e and N_t of the bin distribution and use these in the gamma distribution. If r_e is a good characterization of the radiative properties, the simulation results should match those of BA above.

As a comparison of Figs. 5.16 and 5.13 shows, the microphysics of the cloud layer are in close agreement with that produced by the bin optical property method (BA), including the prominent drizzle at cloud base shown in the r_e plots. Profiles of LWC and drop concentrations (N_t) show similar characteristics as those computed with the more accurate model. Radiative heating of the layer appears, through a qualitative analysis of Figs. 5.17 and 5.14, to have similar characteristics as BA. Comparisons of cloud reflectivity

	R_0	T_0	A_0	C_I ($K\ h^{-1}\ m^{-1}$)	C_M ($K\ h^{-1}\ m^{-1}$)	H ($K\ h^{-1}\ m^{-1}$)
500HS	0.646	0.298	0.055	-65.4	-122.2	48.5
100HS	0.591	0.349	0.059	-65.0	-116.8	30.1

Table 5.4: Radiative properties of the HS simulations. Cloud layer reflection (R_0), transmission (T_0), and absorption (A_0) are computed following Herman and Curry (1984). Integrated radiative cooling is computed in the inversion (C_I), the mixed-layer (C_M) while radiative heating is integrated throughout the cloud layer (H).

and absorptivity between the NS (Table 5.3.5), A and BA (Table 5.3.1) shows that the HS simulation produces a more reflective cloud with lower absorptivity than the A simulation and in close agreement with BA, however the absorptivity is somewhat lower. Because of this, the integrated radiative cooling rates are somewhat greater and the integrated heating rates somewhat smaller (Table 5.3.5) than those in the BA simulations. Even though this is the case, thermodynamic tendencies (Fig. 5.17) computed for the HS simulations show strong similarities to those produced in the BA simulations (Fig. 5.14). Microphysical, diffusive and advective tendencies all show qualitatively the same features leading to total

cooling rates ($d\theta/dt$) which are similar to the BA simulations. The eddy circulation strengths ($< w'w' >$), however, are somewhat stronger than the respective BA cases while the circulation depth is similar. The stronger circulations are possibly due to the stronger radiative cooling and weaker SW heating that occurs in this case.

The reason for the differences between the A and HS simulations, even though the same distribution function was used, is due to the bulk microphysical properties that one conserves in deriving the optical properties. In the case of the A simulations, because LWC and N_t are conserved the mean drop sizes produced by the gamma function are larger than those produced by conserving r_e and N_t. Thus, the A cases produce a more absorbing, less reflecting cloud layer. The results of this section shows that conserving r_e and N_t, as implied by the method of Hu and Stamnes (1993), can accurately capture the microphysical evolution of the system in comparison to the bin optical property method; the dynamics of the system, however, were artificially strengthened.

Taken together, the A, ND, NS, BA and HS simulations point to the fact that SW heating of the cloud layer can have a stronger stabilizing effect on the cloud dynamics than drizzle in weakly drizzling situations. And, as the A cases have shown, this can lead to stronger circulations in the drizzling case. This affect appears to have a distribution shape dependence as the A case optical properties were computed for a much broader drop distribution function than BA (which showed the opposite dynamical effects). Whether or not this is the case is explored briefly in the final section of this chapter.

5.3.6 CRM-NM simulations with fixed distributions

In order to test how strongly cloud top distribution shapes may affect the dynamics of the simulated eddies, 8 hours of simulation were performed with the CRM-NM with optical properties derived for gamma distributions with shapes $\nu = 6$, 14, and 30, as shown in Fig. 5.18. As the value of ν increases, the distributions become more narrow and, thus, should affect the radiative properties in a similar manner to that which occurs in the A (broad distributions) and BA (narrow distributions) simulations. For consistency, we utilize drop concentrations of $100cm^{-3}$ and $500cm^{-3}$ as in the other simulations. The following simulations are by no means considered to be all inclusive, but simply corroborating evidence for the discussions presented in the sections above.

For the broader distributions ($\nu = 6$), such as those utilized in the A and ND simulations, buoyancy production rates are larger for the $100cm^{-3}$ simulations as are the circulation strengths ($< w'w' >$ in Fig. 5.19). This is expected as similar results are obtained for the A and ND simulations. As the distributions become progressively more narrow, buoyancy production rates increase for the $500cm^{-3}$ simulations and, thus circulations increase and deepen as the SW absorption of the layer is reduced. Total layer absorption drops in the $500cm^{-3}$ simulation from 0.1 to 0.05 while layer reflectivity increases from 0.77 to 0.9 as the distribution shape is narrowed. For the $100cm^{-3}$ case, the absorption drops from 0.083 to 0.059 while the reflection increases from 0.64 to 0.8 as the distribution shape becomes more narrow. This suggests that clouds with narrow cloud top drop distributions should produce stronger, deeper circulations which feedback into the cloud microphysics enhancing LWC and drizzle rates as in BA. Since this effect differs depending upon the CCN concentrations, stronger circulations are not necessarily monotonic with increases in drop concentrations. These results are consistent with the differences between the respective A and BA cases presented above.

5.4 Summary

The modeled ASC showed reasonably good agreement with observations for the June 28, 1980 ASC case. Simulations with larger CCN concentrations compared the best, however no drizzle was ever produced in that case while the true cloud system showed periods of intermittent drizzle production (Tsay and Jayaweera, 1984).[5] All simulations produced reasonable microphysical and thermodynamic cloud structures with the detailed optical property simulations (BA) producing the best agreement in terms of radiative properties. Circulation strengths were much greater than observed but did produce a cloud base maximum in $< w'w' >$ as noted in Curry (1986). The larger circulation strengths being due to the 2-D representation (Stevens, 1996). Sensitivities conducted showed the importance of radiative-microphysical-dynamical interactions in ASC, highlighted below.

---

[5]See Chapter 6 for further discussion of drizzle production in the N_{ccn} =$500cm^{-3}$ cases.

Increases in CCN concentrations affect eddy strengths, however distribution shape is an equally important factor for deciding how buoyancy generated at cloud top is distributed. Drop distributions with broad tails (such as those of the gamma distribution with $\nu = 6$) absorb more solar radiation and this puts constraints on not only the strength but the depth of the circulations. Drizzle reduces eddy strength as shown in the comparison of the A and ND simulations, however SW heating can have a stronger stabilizing effect (*i.e.* 100A vs. 500A). Solar radiation appears to feedback into the dynamics and, hence, the microphysics and thermodynamics in two specific manners. The first is through control of the strength of the destabilization of the cloud top while the second is through controls on the depth of the cloud scale mixing (and, thus on the location of the $< w'w' >$ maximum). Clouds with larger solar heating rates (broad distributions) reduce the buoyancy production and, thus, constrain the depth of the circulations. Clouds with weaker solar heating rates (narrow distributions) affect buoyancy production maxima and depths less thus creating deeper, stronger circulations. Partitioning of radiant energy between the inversion zone and the mixed-layer is affected by the gradient in extinction at cloud top; this partitioning is dependent upon distribution shape which helps determine the amount of buoyancy generated.

Even though mean values of r_e from the gamma optical property simulations compared well with the bin derived values, significant differences in the microphysical and dynamical fields are produced in comparisons with simulations which compute the optical properties accurately (BA). The reduced SW heating of the layer allowed for stronger circulations, a cooler cloud layer and greater drizzle production. Computations of the optical properties using the method of Hu and Stamnes (1993), showed that the microphysical and radiative characteristics were well reproduced by the method. The dynamic structure, however, shows that eddy strengths and fluxes were over-predicted by the method. In any event, it appears that conserving r_e and N_t of the distribution provides an accurate representation of the radiative, microphysical and dynamical feedbacks. Although, as the Hu and Stamnes (1993) method offers no computational advantage over the bin optical property method, the latter method is a better choice for representing optical properties in an explicit cloud microphysical model.

The results of this chapter point to the following caveats as concerns radiative interactions in evolving cloud systems. First, using mean r_e values to drive circulations (such as might be approximated in a simple model) will likely produce inaccurate results. Simple radiative-microphysical couplings in models of ASC (and stratocumulus), particularly as regards SW heating, can produce erroneous results. This is particularly important for ASC which are affected by continual daylight. Using single gamma distribution representations of the drop spectrum not only drastically simplifies microphysics, but also affects the strengths of the cloud circulations through radiative interactions. Thus, not only is appropriate drizzle representation important for cloud evolution, but so are the radiative interactions.

One factor not considered in these simulations is the effect of radiative heating/cooling on the heat budget of the drops as concerns drop growth from the vapor. The bin-dependent optical properties used above (BA) are advantageous here as the effect is drop size dependent. This factor is considered in the next chapter.

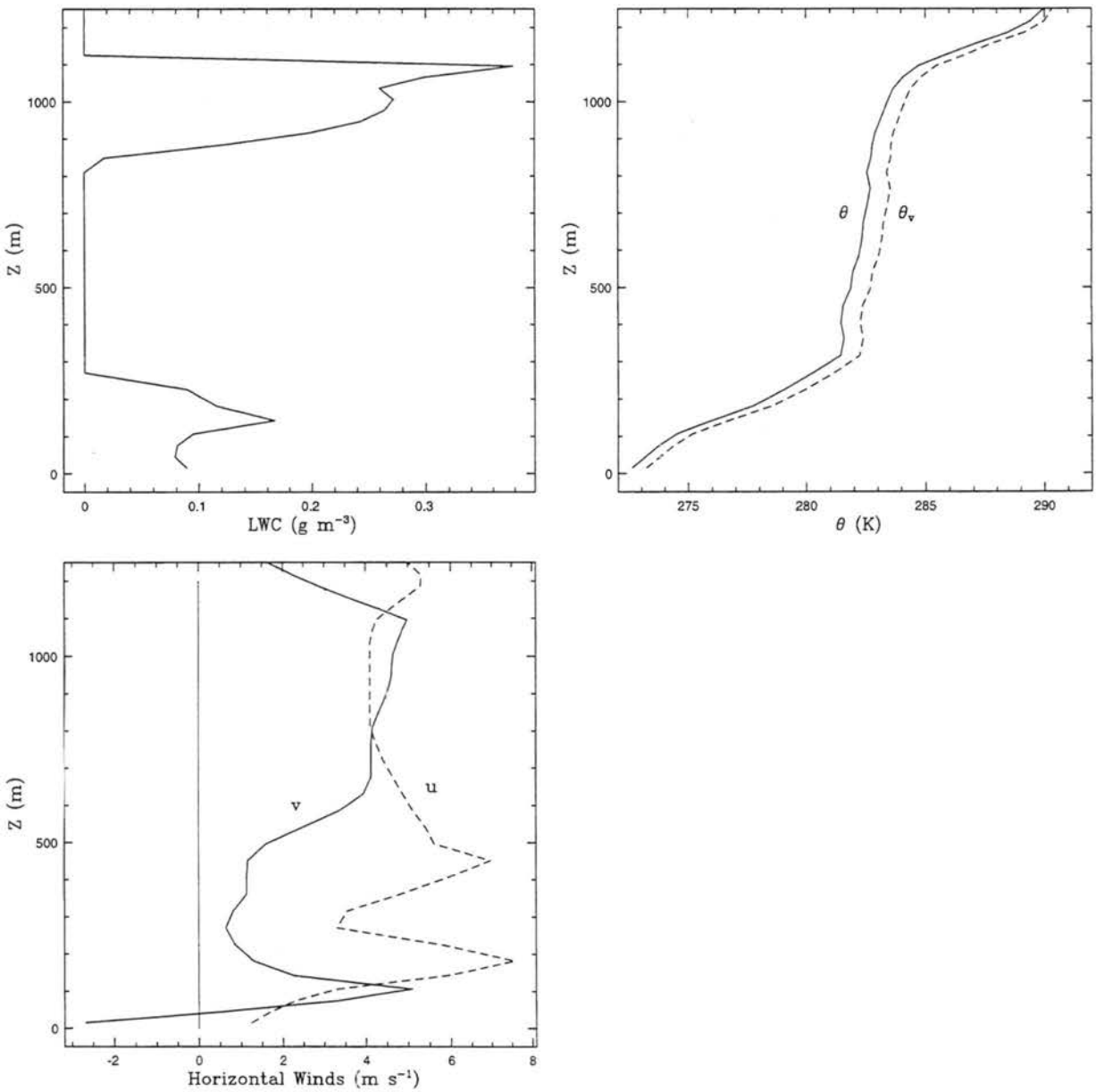

Figure 5.1: Mean fields used to produce the initial cloud field. Plotted are the liquid water content (LWC), θ and θ_v, and the u and v winds.

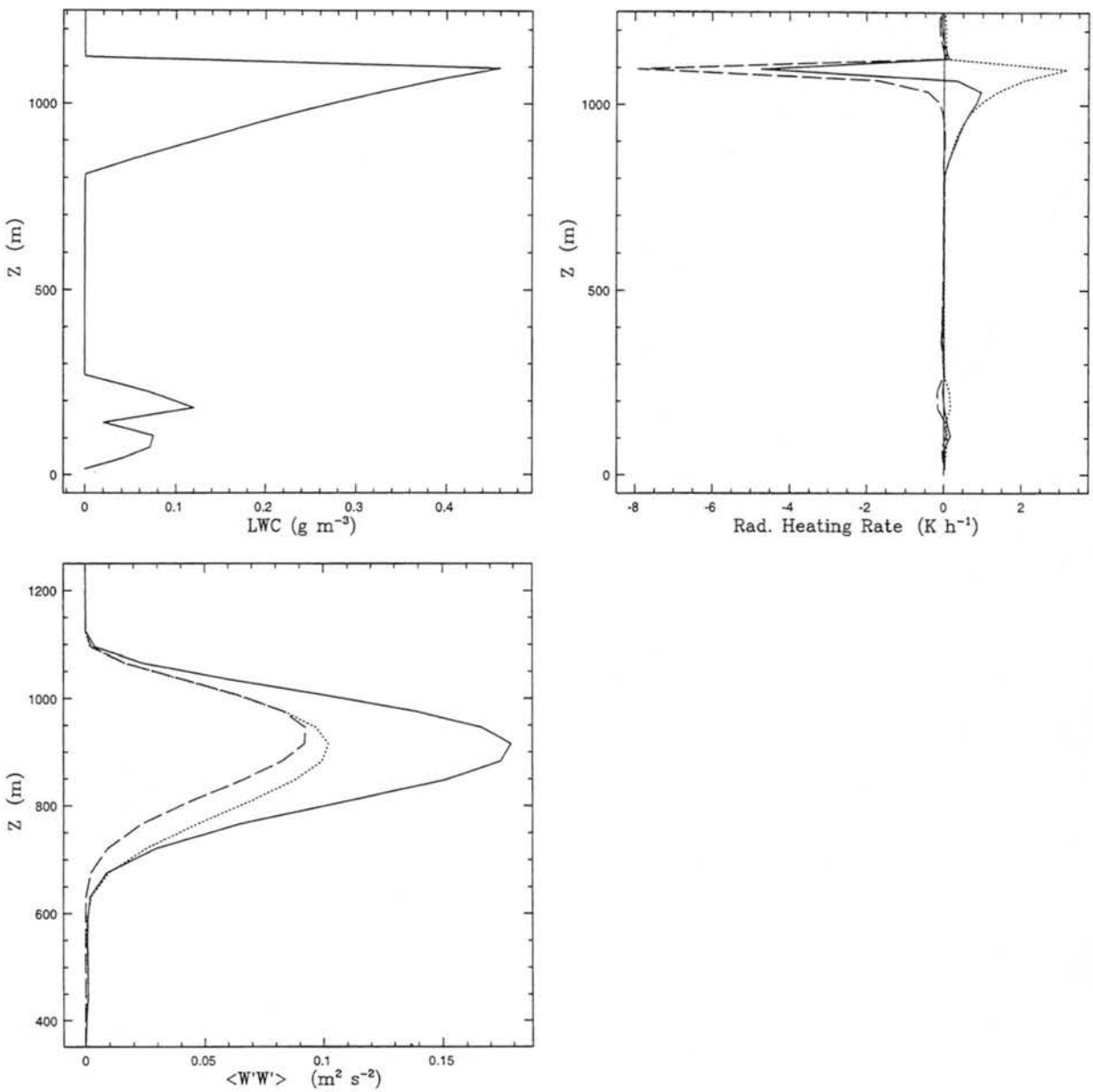

Figure 5.2: CRM-NM four hour fields. Total heating rate is given by the solid line, longwave cooling by the dashed line and shortwave heating by the dotted line. $< w'w' >$ is plotted for CRM-NM (solid line), CRM-LBM cases 100A (dotted-line) and 500A (dashed line).

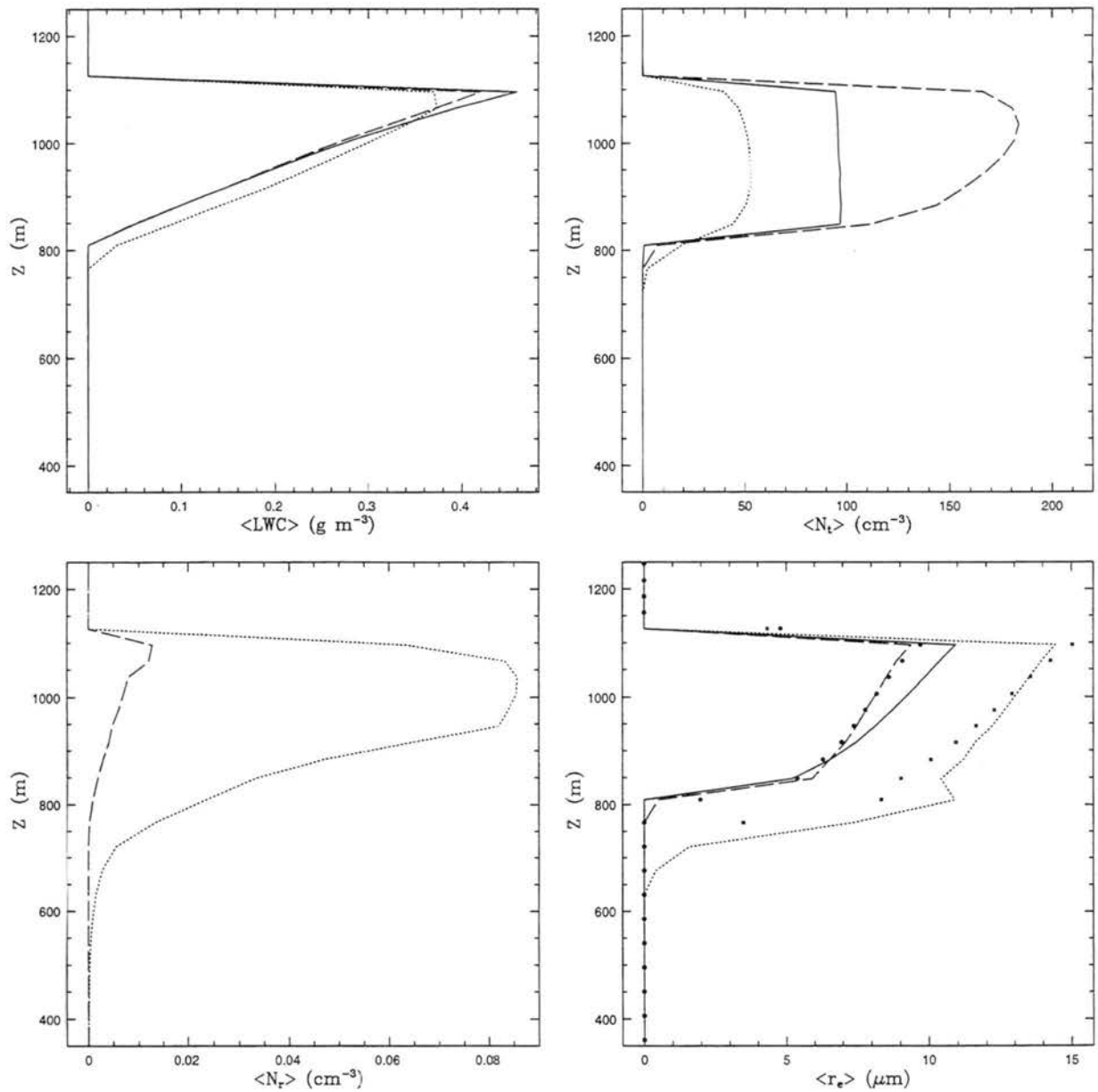

Figure 5.3: Microphysical profiles for A and NM simulations. Panels show profiles of LWC, total concentration (N_t), drizzle concentration (N_r), and effective radius (r_e) for simulations NM (solid line), 100A (dotted line) and 500A (dashed line). Points plotted in the r_e profile are derived from assumed gamma ($\nu = 6$) for 100A (squares) and 500A (spheres). Values of N_r for 500A have been multiplied by 1×10^2 to facilitate comparison.

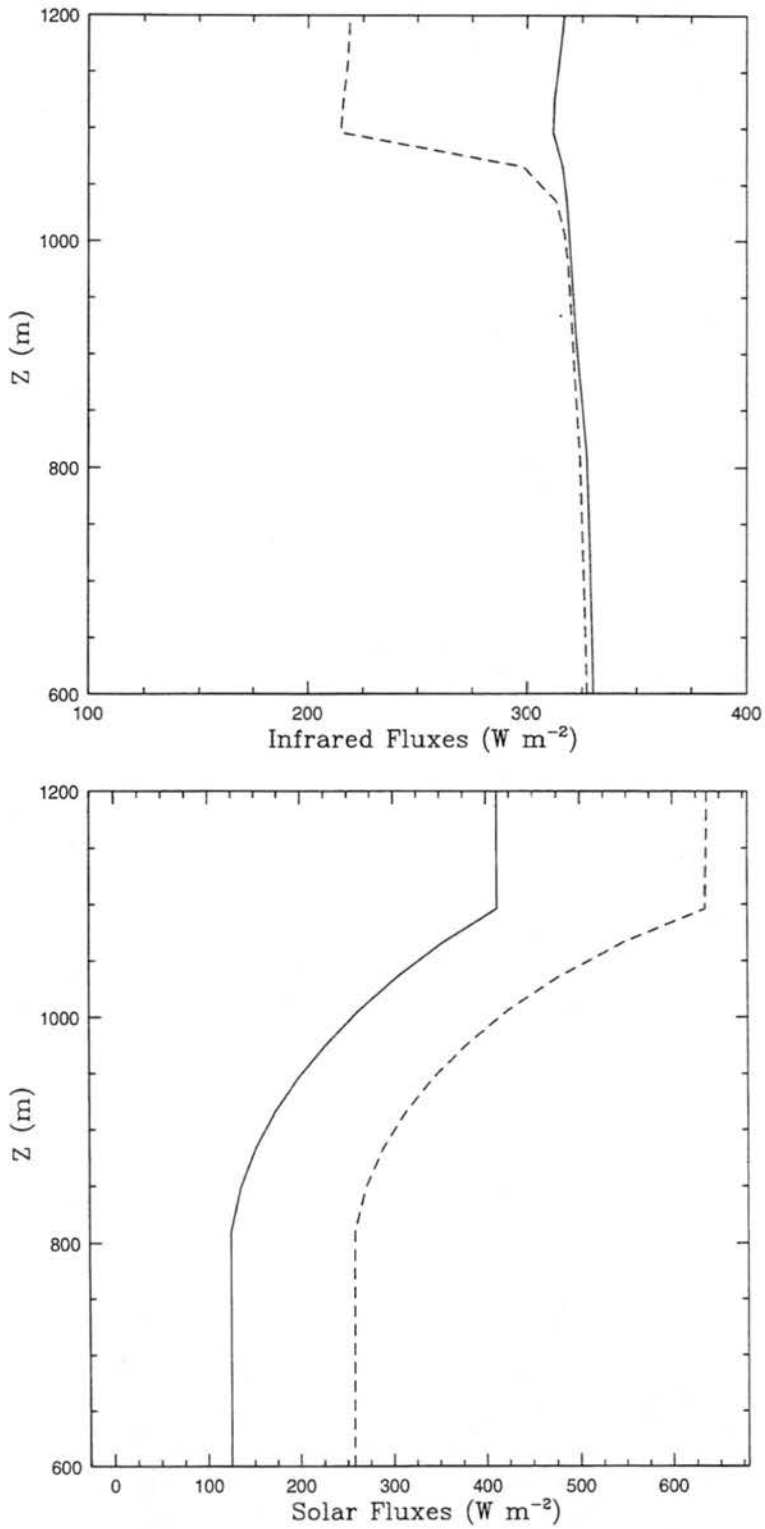

Figure 5.4: Radiative fluxes for 500A. Downwelling fluxes are denoted with the dashed line while upwelling fluxes are denoted with the solid line.

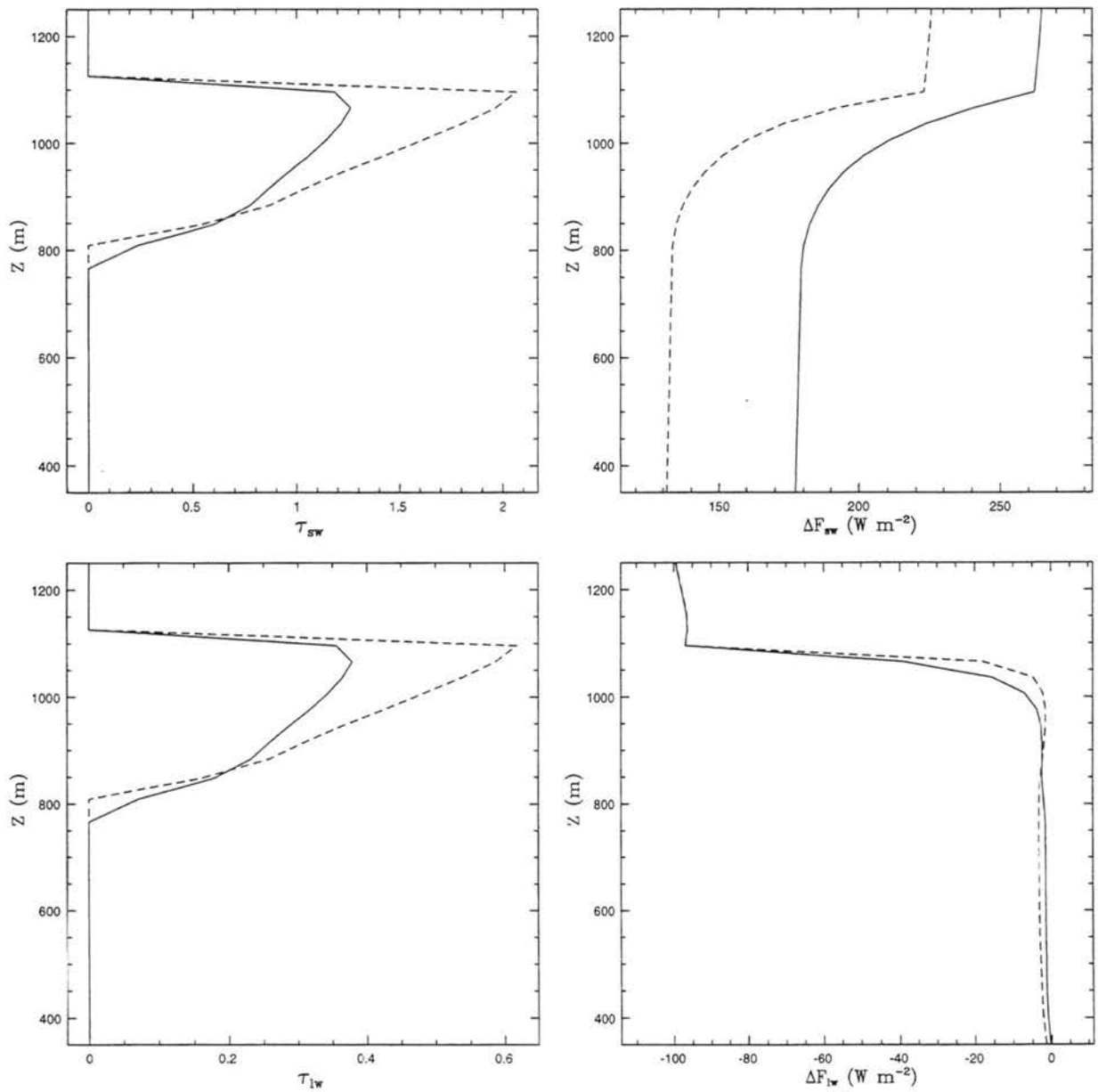

Figure 5.5: Radiative profiles for the A simulations. Panels show profiles of the net flux (ΔF) and layer optical depth (τ) for SW and LW radiation. Case 100A is denoted by a solid line and 500A by a dashed line.

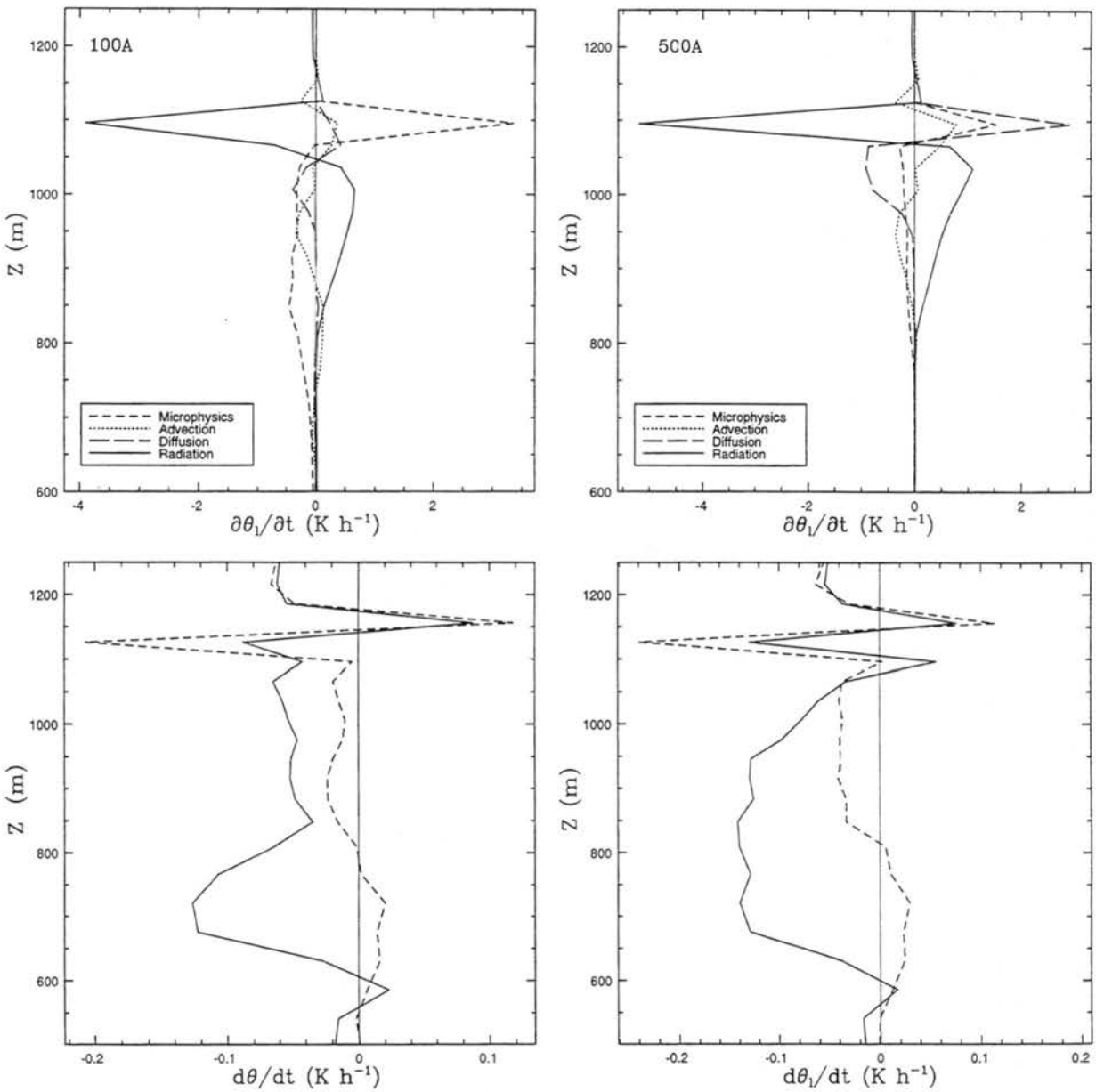

Figure 5.6: θ and θ_l -tendencies for the A simulations. Panels show profiles of the total θ tendency ($d\theta/dt$), total θ_l - tendency ($d\theta_l/dt$) and the contributions from various model components to θ_l for 100A and 500A. Solid and dashed lines represent 100A and 500A, respectively in the total tendency frames.

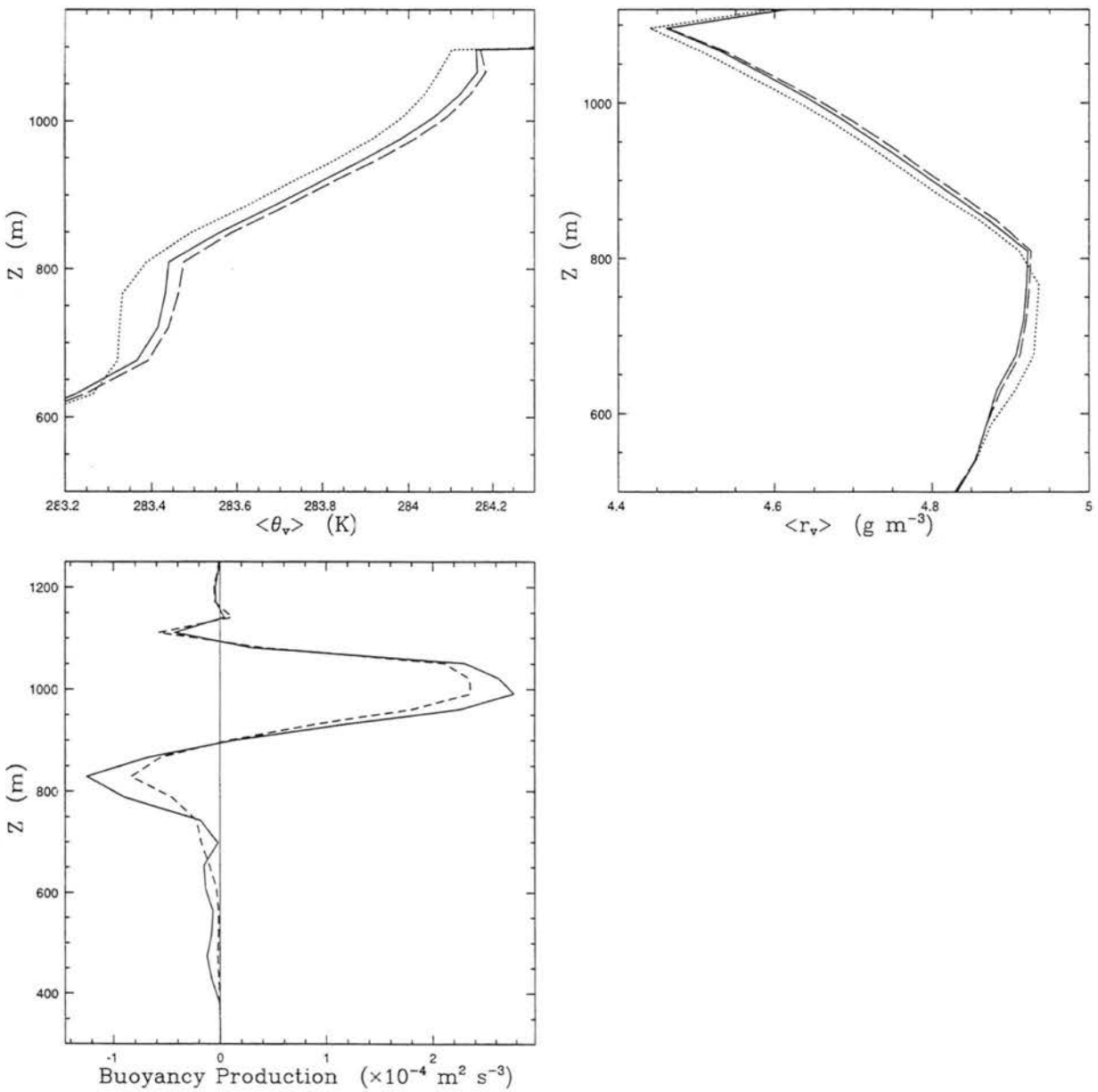

Figure 5.7: Profiles of θ_v, r_v (solid line for CRM-NM, dotted line for 100A, dashed line for 500A) and buoyancy production (solid line for 100A and dashed line for 500A) for the A simulations.

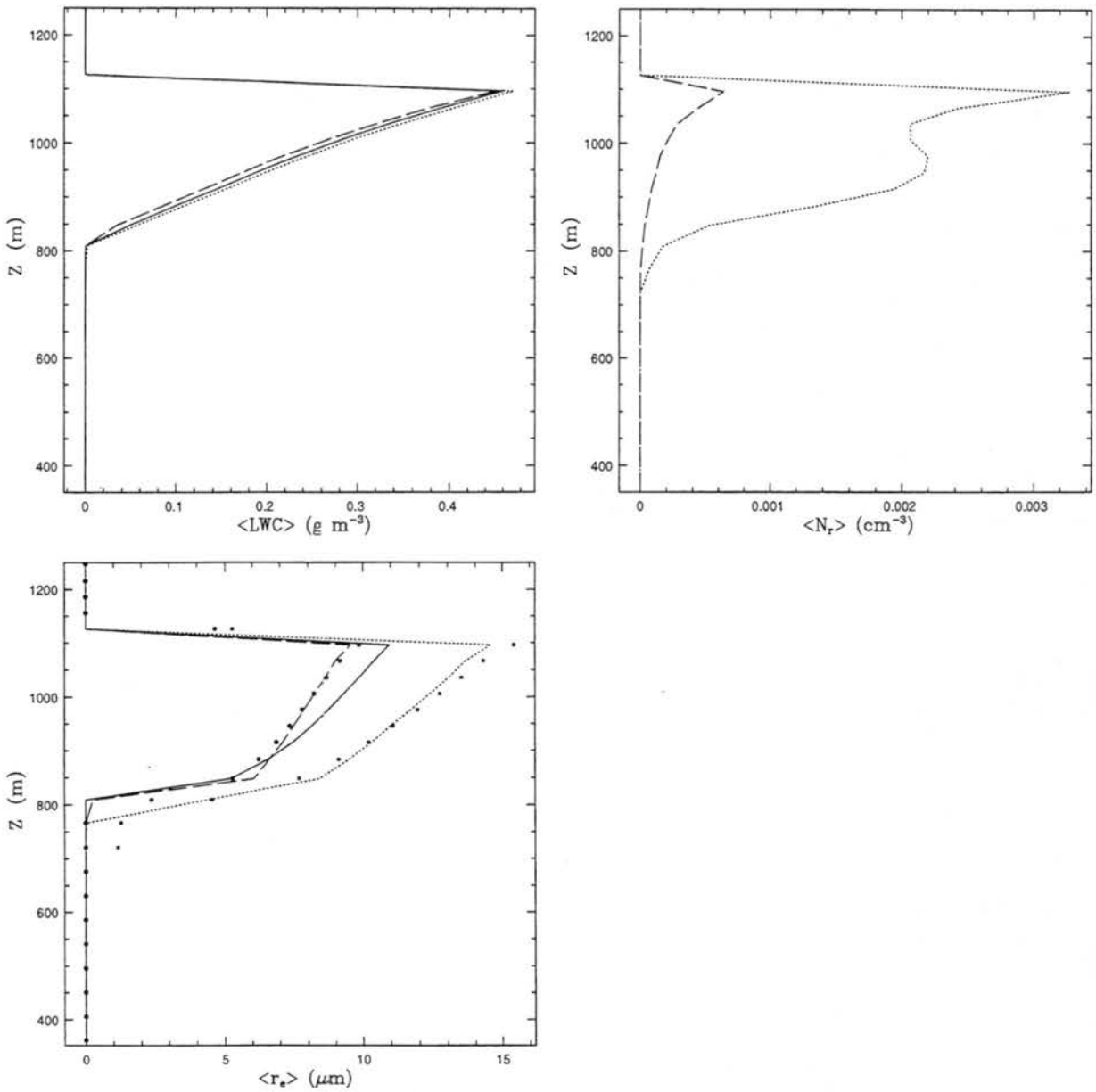

Figure 5.8: Microphysical profiles for ND simulations. Panels show profiles of LWC, drizzle concentration (N_r), and effective radius (r_e) for simulations NM (solid line), 100ND (dotted line) and 500ND (dashed line). Points plotted in the r_e profile are derived from an assumed gamma ($\nu = 6$) for 100ND (squares) and 500ND (spheres).

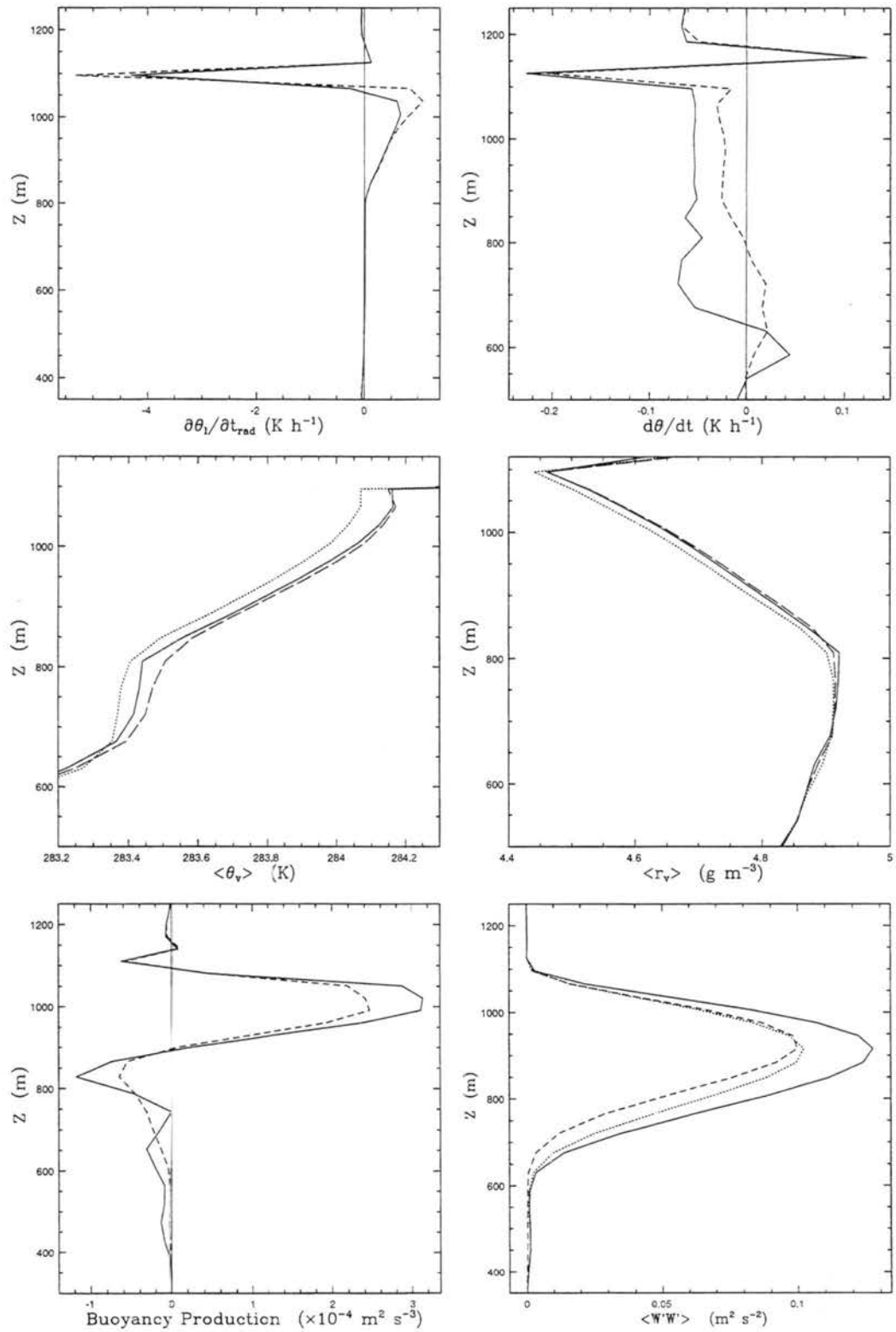

Figure 5.9: Thermodynamic and dynamic profiles for ND simulations. Panels show profiles of total θ tendency ($d\theta/dt$), radiative heating rate ($\partial\theta_l/\partial t_{rad}$) and buoyancy production (solid for 100ND, dashed for 500ND); θ_v and r_v (solid line for NM, dashed line for 500ND, dotted line for 100ND), and $< w'w' >$ (solid line for 100ND, dashed line for 500ND, dotted line for 100A).

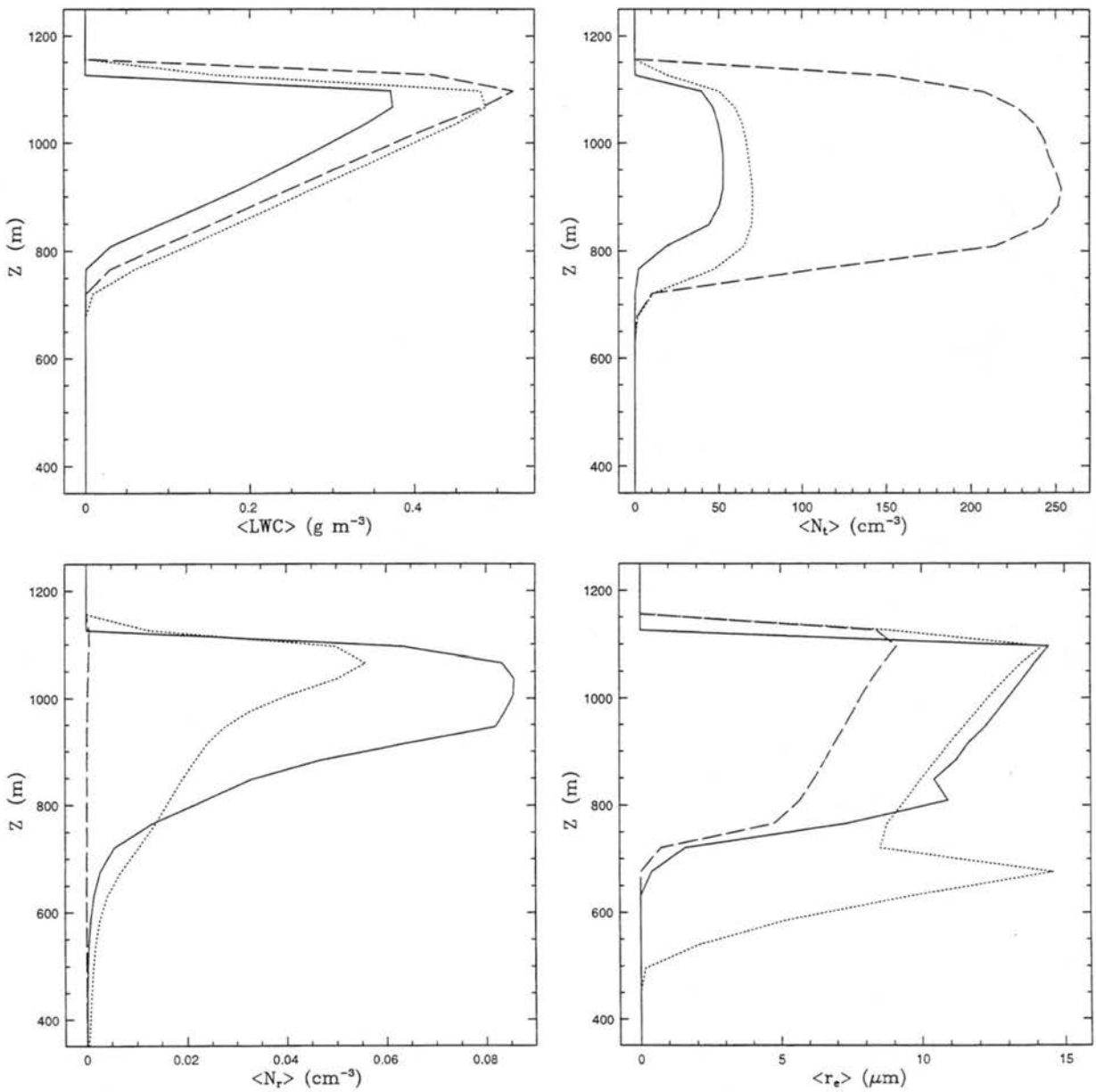

Figure 5.10: Microphysical profiles for NS simulations. Panels show profiles of LWC, total concentration (N_t), drizzle concentration (N_r), and effective radius (r_e) for simulations 100A (solid line), 100NS (dotted line) and 500NS (dashed line).

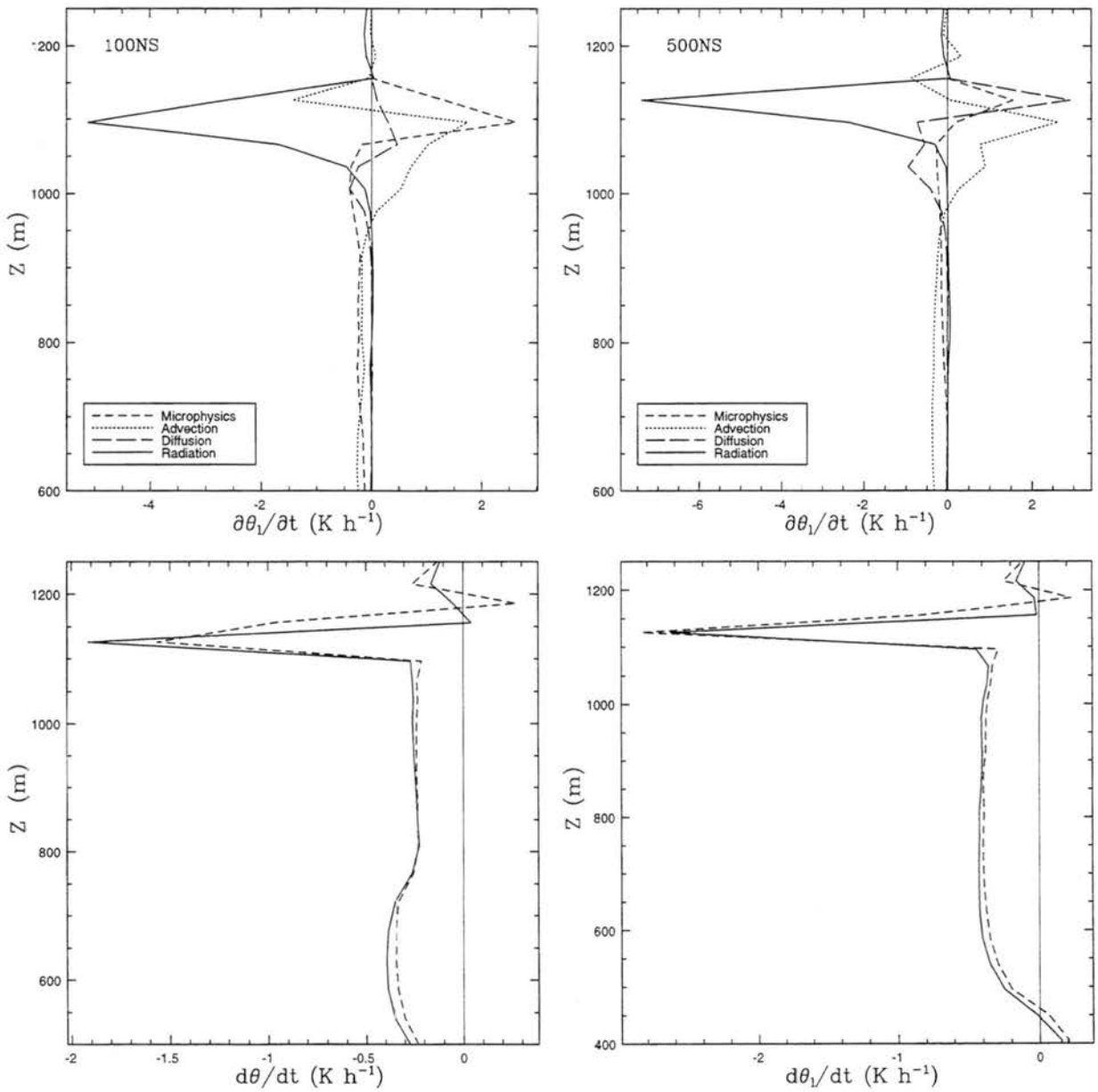

Figure 5.11: θ and θ_l -tendencies for the NS simulations. Panels show profiles of the total θ tendency ($d\theta/dt$), total θ_l tendency ($d\theta_l/dt$) and the contributions from various model components to θ_l for 100NS and 500NS. Solid and dashed lines represent 100NS and 500NS, respectively in the total tendency frames.

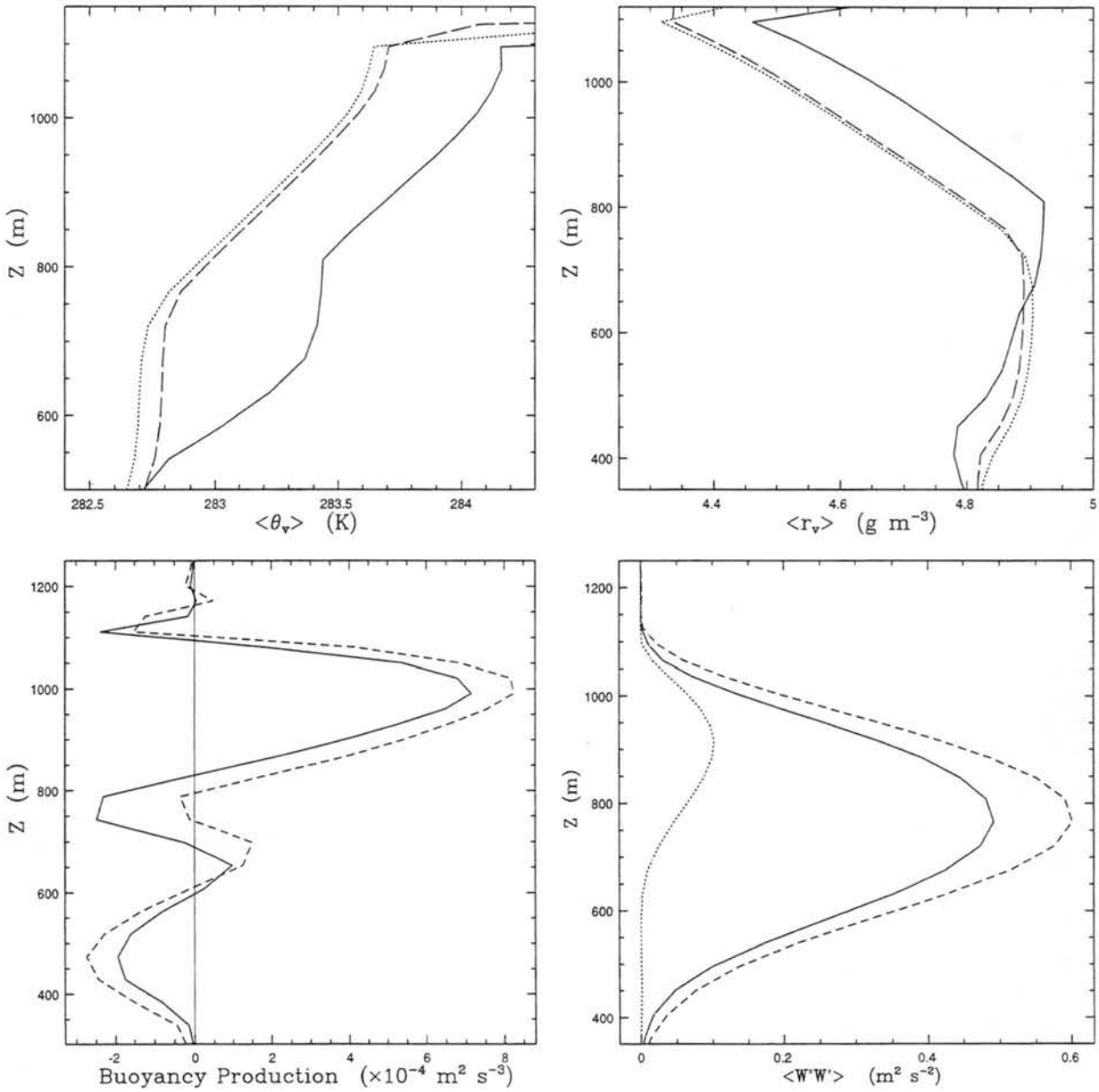

Figure 5.12: Profiles of θ_v, r_v (solid line for CRM-NM at 4 hours, dotted line 100NS and dashed line 500NS), buoyancy production and $< w'w' >$ (solid line for 100NS and dashed line for 500NS). The dotted line representing 100A in the $< w'w' >$ panel is for comparison.

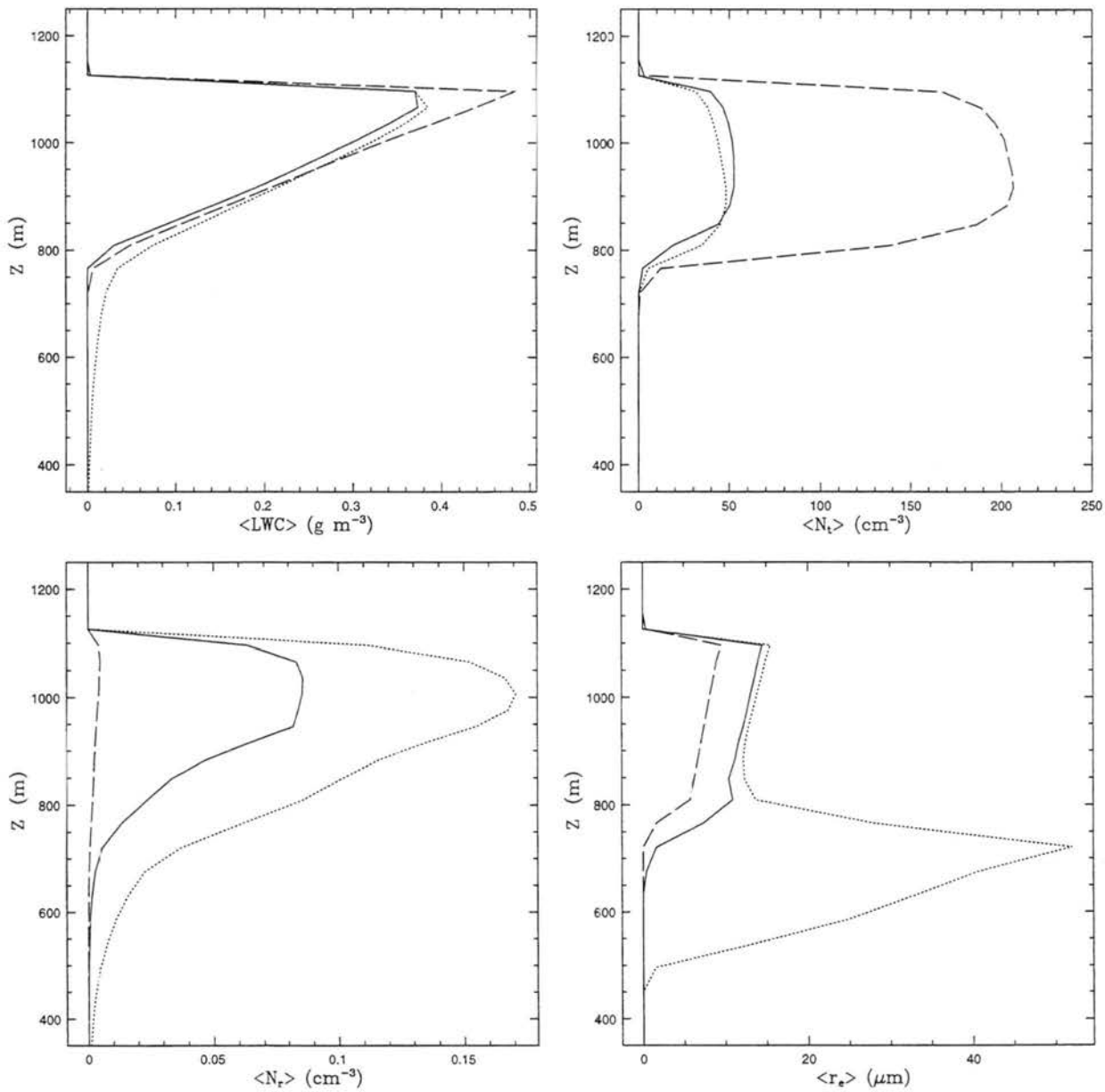

Figure 5.13: Microphysical profiles for BA simulations. Panels show profiles of LWC, total concentration (N_t), drizzle concentration (N_r), and effective radius (r_e) for simulations 100A (solid line), 100BA (dotted line) and 500BA (dashed line).

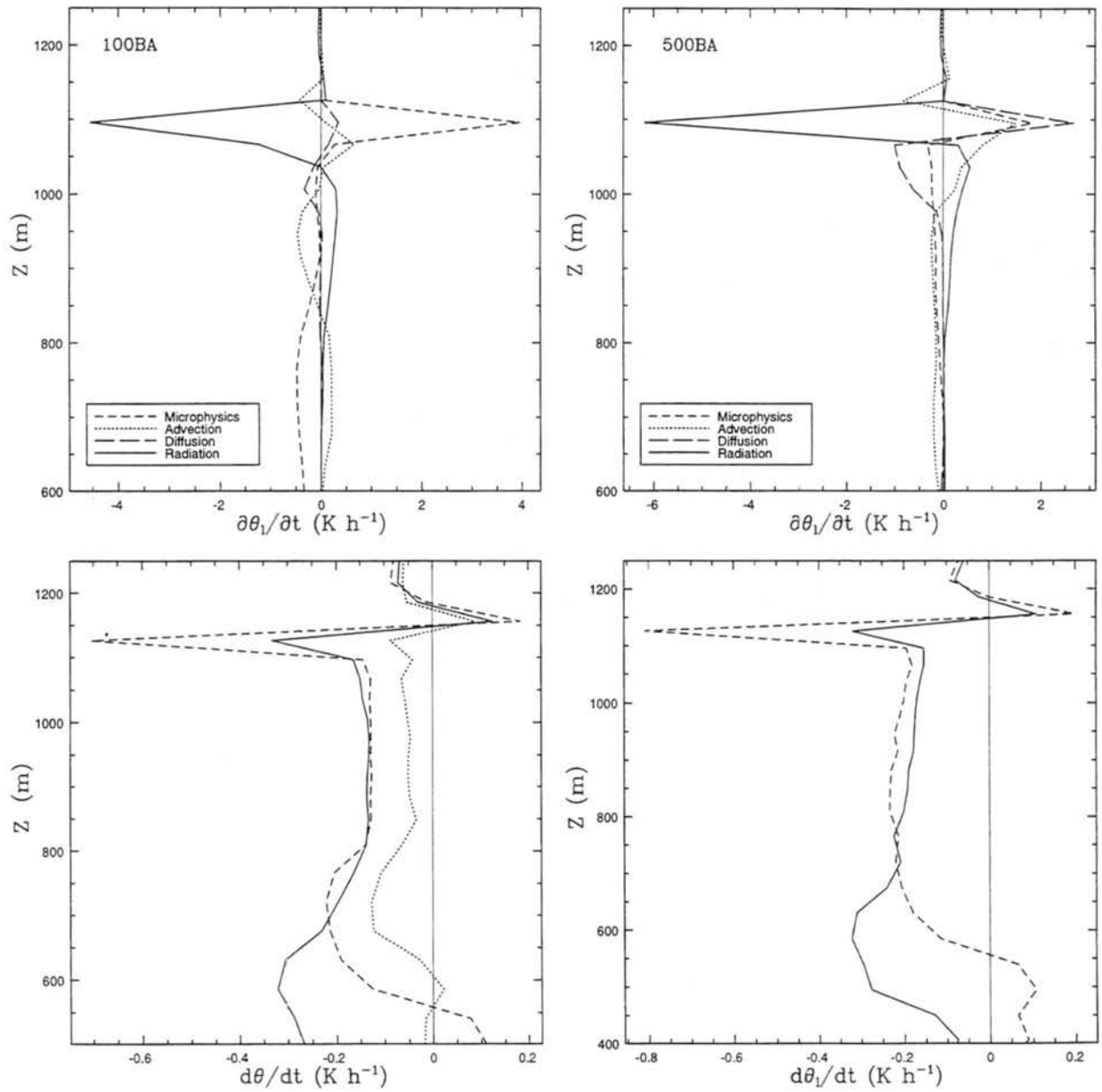

Figure 5.14: θ and θ_l -tendencies for the BA simulations. Panels show profiles of the total θ tendency ($d\theta/dt$), total θ_l tendency ($d\theta_l/dt$) and the contributions from various model components to θ_l for 100BA and 500BA. Solid and dashed lines represent 100BA and 500BA, respectively in the total tendency frames. The dotted line in $d\theta/dt$ is for 100A as reference.

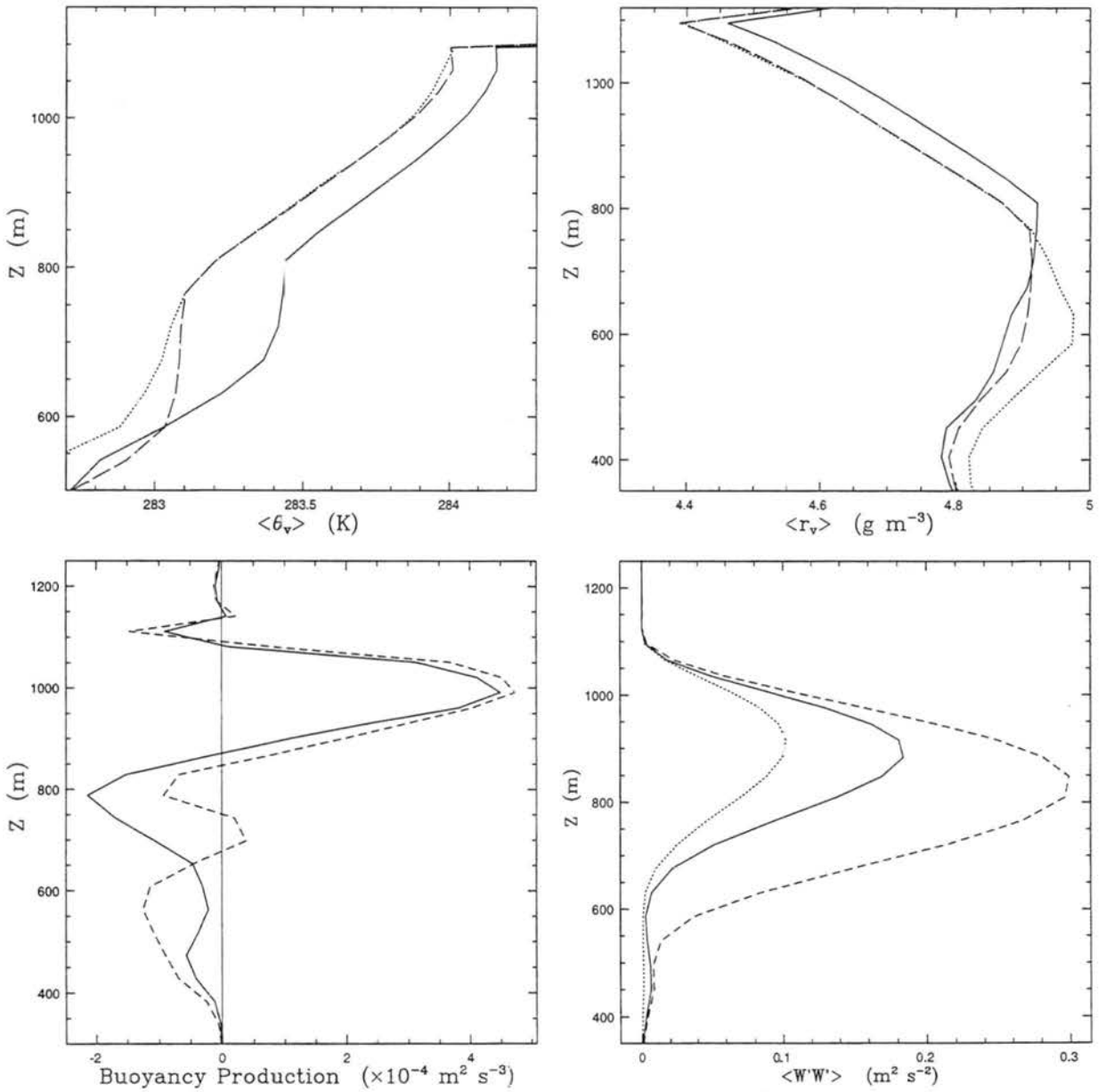

Figure 5.15: Profiles of θ_v, r_v (solid line for CRM-NM at 4 hours, dotted line 100BA and dashed line 500BA), buoyancy production and $< w'w' >$ (solid line for 100BA and dashed line for 500BA). The dotted line representing 100A in the $< w'w' >$ panel is for comparison.

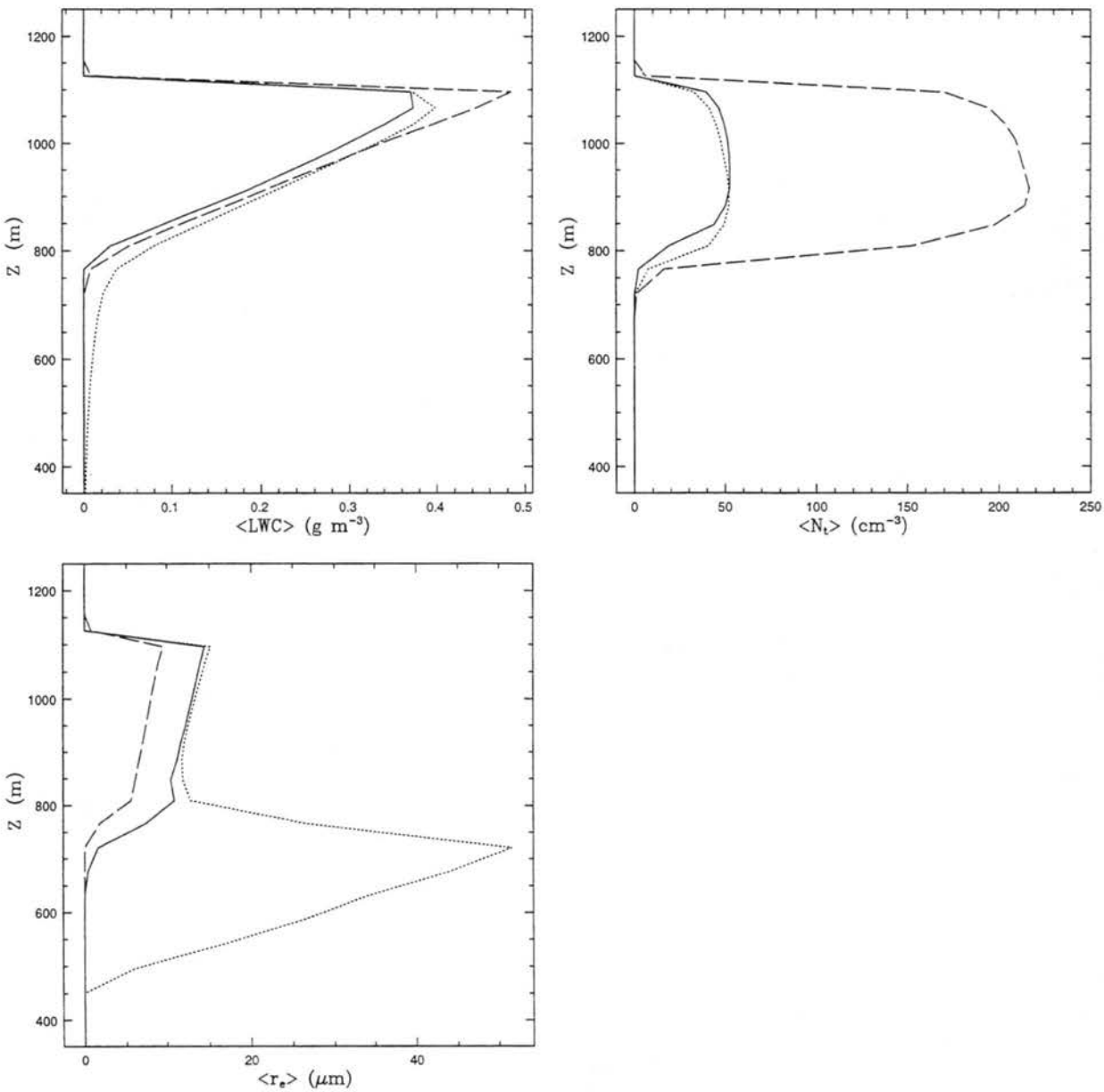

Figure 5.16: Microphysical profiles for HS simulations. Panels show profiles of LWC, total concentration (N_t), and effective radius (r_e) for simulations 100A (solid line), 100HS (dotted line) and 500HS (dashed line).

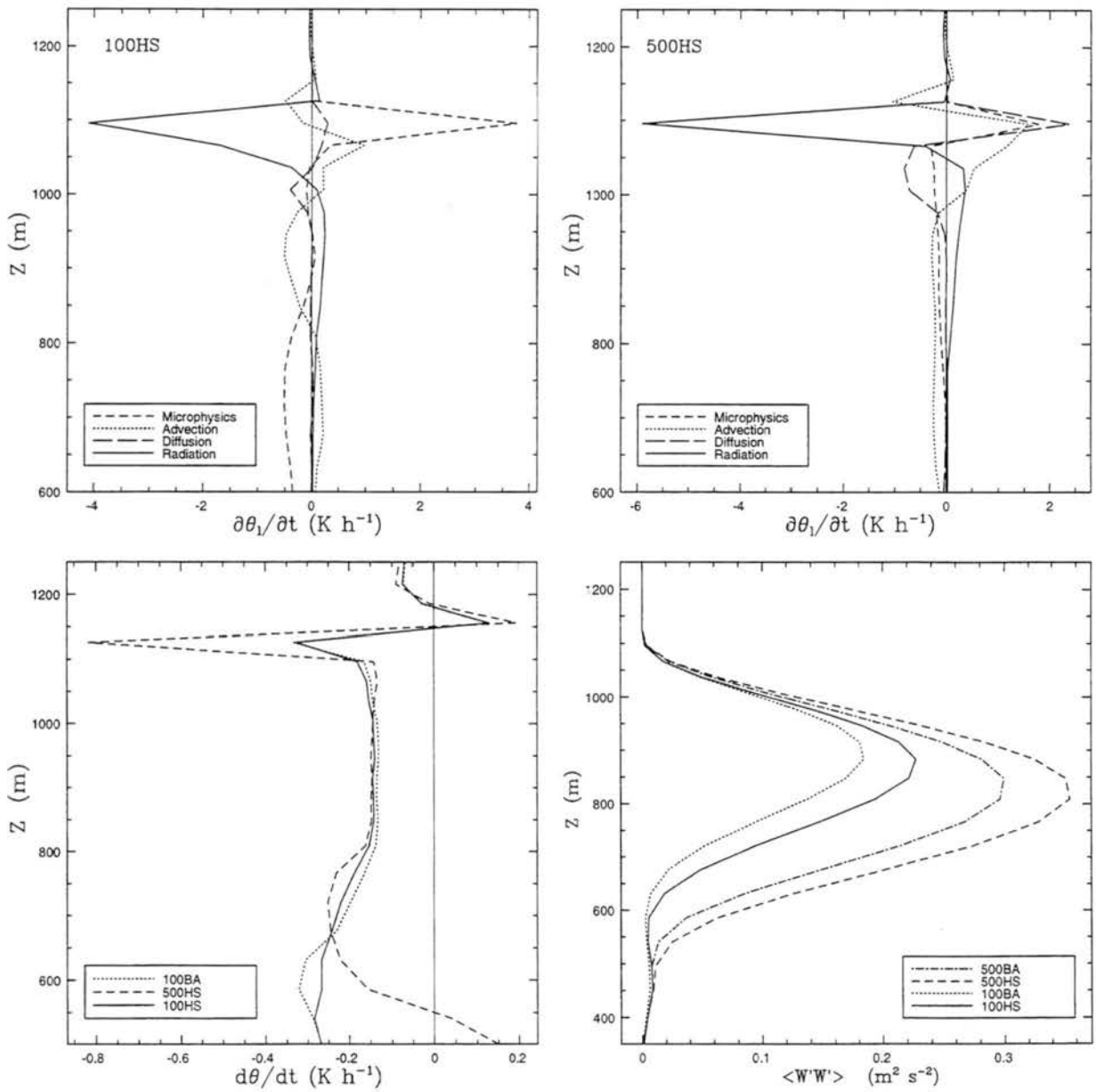

Figure 5.17: θ-tendencies and $< w'w' >$ for the HS simulations. Lines are labeled in the individual panels.

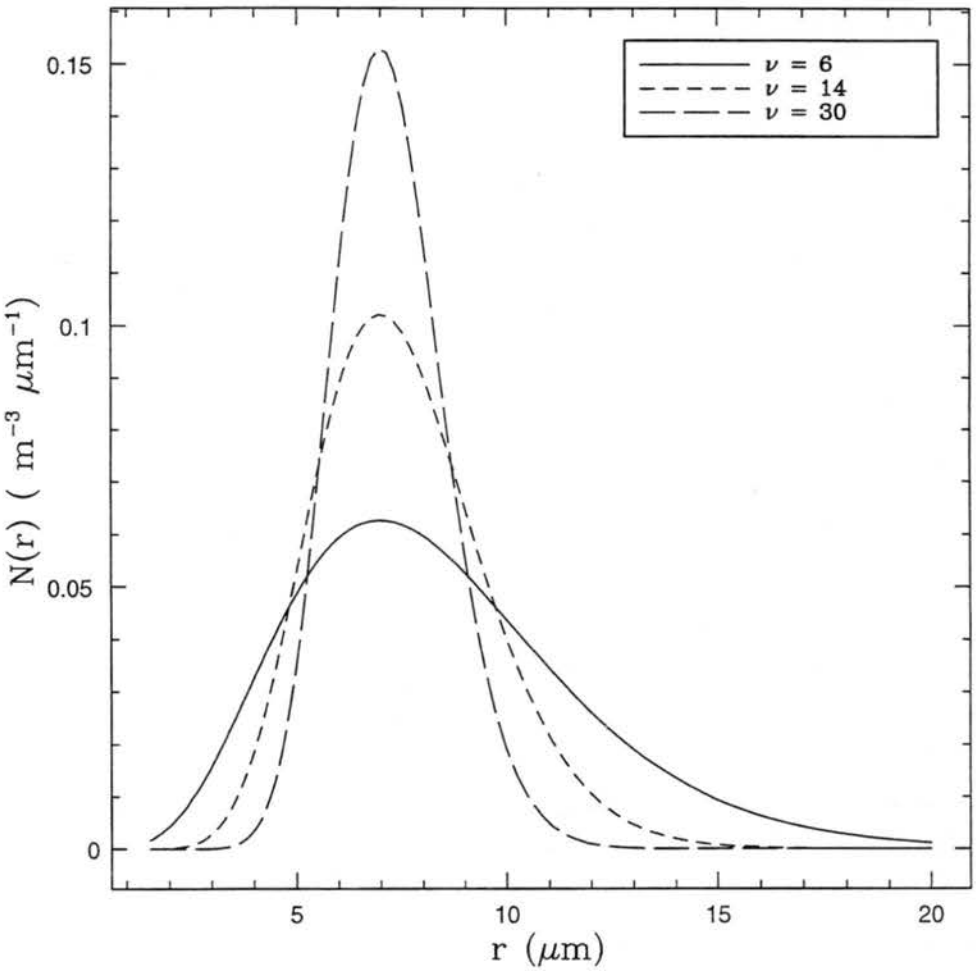

Figure 5.18: Gamma distributions for $\nu = 6$, 14, and 30.

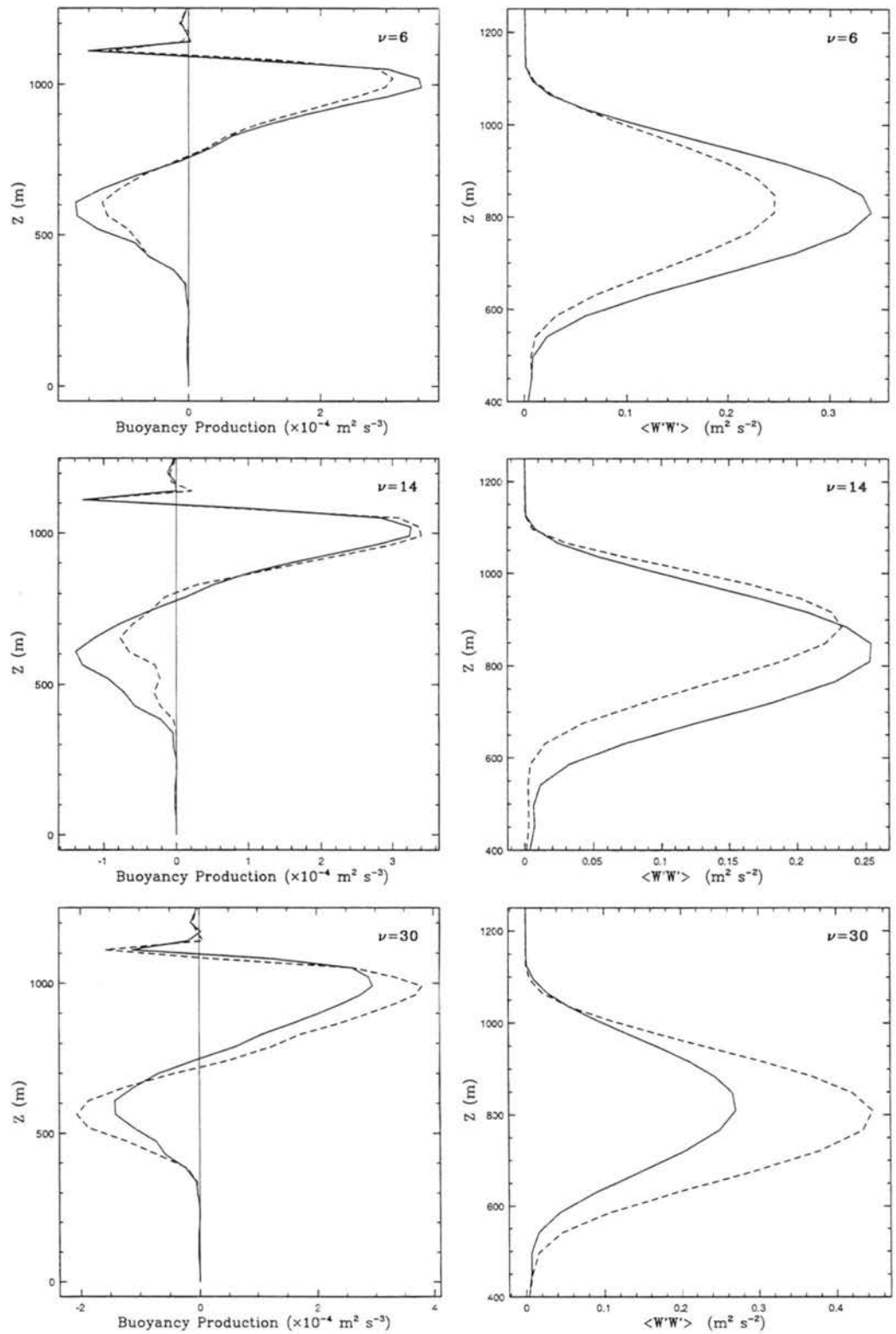

Figure 5.19: Buoyancy production and $< w'w' >$ for various gamma distributions (labeled within individual panels). Solid line denotes $100cm^{-3}$ while dashed line denotes $500cm^{-3}$ simulations.

Chapter 6

RADIATIVE EFFECTS ON THE VAPOR GROWTH OF DROPLETS IN ARCTIC STRATUS

In this chapter we focus on the effect that radiative transfer has on the production of drizzle-sized droplets and on the growth of small droplets. The effects are examined for simulated Arctic stratus within two numerical frameworks in order to build a hierarchy with which to understand the phenomenon. The first framework is that of a Lagrangian parcel model driven with information produced by a cloud-resolving model (CRM, *e.g.* Stevens *et al.* , 1996) simulation of Arctic stratus clouds (ASC). Here we wish to elucidate some of the processes that may be obscured in a full simulation with a CRM. We should note at this point that the issues discussed in the trajectory model are not meant as surrogates for the drizzle process in real clouds. The value of the trajectory model lies in the ability to accurately discuss microphysical effects without the attendant difficulties related to cloud dynamical feedbacks. The second framework is that of a full simulation within the CRM itself; the focus being on the production of drizzle in the CRM and its subsequent effects on liquid water redistribution.

This chapter is organized in the following manner. In the first section we discuss how the radiative information is coupled to the microphysical vapor growth equations. The results from a simulation of ASC with a CRM are discussed in the next section along with a discussion of the information written out for use in the trajectory parcel model (TPM). The TPM is then used to examine the radiative effect on the growth of a distribution of droplets along with how collection, shortwave (SW) radiation, and activation of aerosols affect the results for a single parcel. Once an understanding of the results for a single parcel is obtained we then discuss results from simulations with an ensemble of parcels.

The final section of this chapter includes a set of simulations from a CRM and a discussion of the radiation-vapor growth effects on the cloud properties.

6.1 Radiative and Microphysical Connections

The microphysical growth of droplets is usually discussed in terms of solutions to a coupled set of ordinary differential equations that describe a balance between the condensation (evaporation) of water vapor and heat diffusion. Radiative heating (cooling) affects this balance through the coupling between heat equation of the drop (Roach, 1976),

$$L_c \frac{dm}{dt} - R = 4\pi r K (T_r - T_\infty) \tag{6.1}$$

and the mass growth equation,

$$\frac{dm}{dt} = 4\pi r D_v (\rho_{v,\infty} - \rho_{v,r}) \tag{6.2}$$

where L_c is the latent heat of condensation, m is the mass of the drop, r is the radius of the drop, K is the coefficient of heat diffusion, T_r is the temperature at the surface of the drop, T_∞ is the temperature of the environment a large distance from the drop, D_v is the vapor diffusivity, $\rho_{v,\infty}$ is the water vapor density a large distance from the drop, $\rho_{v,r}$ is the water vapor density near the surface of the drop and R is a term that describes the addition/removal of heat from the drop by radiant energy (units of W). We have written the above equation with the R-term on the left hand side to stress its connections to the growth equation (dm/dt). Thus, the balance between condensation which produces heat and the dissipation of this heat through diffusion is affected by the fact that radiative cooling removes some of the heat caused by condensation. In the form of the equation given above, a positive (negative) value of R constitutes radiative cooling (warming) since the heat generated by condensation is reduced (increased).

The term for the radiative effect, R, is derived from considering the radiant energy budget of a given droplet. Since R is related to the net energy budget of the drop, Roach (1976) showed,

$$R = P_e - P_a \tag{6.3}$$

where P_e and P_a describe the total radiative power emitted and absorbed, respectively, by the drop. These terms are given by the integrals,

$$\begin{aligned} P_e &= 4\pi r^2 \int Q_a(r,c,\lambda)\pi B(T_d,\lambda)d\lambda \\ P_a &= \pi r^2 \int Q_a(r,c,\lambda) I(\underset{\sim}{s},\lambda)d\lambda d\underset{\sim}{\Omega} \end{aligned} \tag{6.4}$$

where Q_a[1] is the absorption coefficient, $\underset{\sim}{s}$ is the direction vector for the radiance I, $\underset{\sim}{\Omega}$ is the differential for the direction and T_d is the temperature of the droplet. Utilizing the two-stream approximation in the above integrals one gets R for a droplet of radius, r, as

$$R = \int_\lambda 4\pi r^2 Q_a(r,c,\lambda)\left[\pi B(T_d,\lambda) - \frac{1}{2}(F^+ + F^-)\right] d\lambda. \tag{6.5}$$

For consistency with the two-stream model, we use an average value of Q_a for a given spectral band, i, and the above equation becomes,

$$\begin{aligned} R_i &= 4\pi r^2 \bar{Q}_{a,i}(\bar{r}_k) E_{d,i} \\ E_{d,i} &= \left[\pi B_i(T_d) - \frac{1}{2}(F_i^+ + F_i^-)\right] \end{aligned} \tag{6.6}$$

where $\bar{Q}_{a,i}(\bar{r}_k)$ is the absorption coefficient averaged over spectral band i and computed at the mean size of microphysical bin k as discussed in the section on bin optical properties in Chapter 3, F_i^+ and F_i^- are the values of the fluxes for band i, $B_i(T_d)$ is the band integrated Planck function evaluated at the drop temperature. We have defined $E_{d,i}$ as a radiative "effect" that includes all of the flux terms. Utilizing R_i in the heat diffusion equation given above and following the nomenclature of Tzivion *et al.* (1989) one finds for the vapor growth equation,

$$\begin{aligned} \frac{dm}{dt} &= C(P,T)\frac{m^{2/3}}{m^{1/3}+l_0}\left[\eta(t) + \frac{r_s L_c \alpha_c m^{1/3} E_d(r)}{K R_v T^2}\right] \\ &= \frac{m^{2/3}}{m^{1/3}+l_0} C(P,T)\left[\eta(t) + J(P,T) m^{1/3} E_d(r)\right] \end{aligned} \tag{6.7}$$

where $\eta(t)$ is the excess specific humidity ($= r_v - r_s(t)$), r_s is the saturation mixing-ratio, and R_v is the gas constant for moist air, l_0 is a length-scale representing the gas-kinetic

---

[1]Since we will extensively utilize the symbols m for drop mass and n for the drop distribution throughout this chapter, we adopt the symbol c for the index of refraction of water so as to reduce any confusion.

effects (*e.g.* Clarke, 1973), and the function $C(P,T)$ is defined in Tzivion *et al.* (1989). The other terms in the growth equation are defined as,

$$\begin{aligned} E_d(m) &= \sum_{i}^{N_{bands}} Q_{a,i}(m)E_{d,i} \\ &= E_d(\bar{m}_k) = \sum_{i}^{N_{bands}} \bar{Q}_{a,i}(\bar{m}_k)E_{d,i} \\ \alpha_c &= \left[\frac{3}{4\pi\rho_l}\right]^{1/3}. \end{aligned} \tag{6.8}$$

In order to utilize this equation in the explicit microphysical model we must include the above radiative term in the equation for supersaturation and for the growth of droplets. These equations must be solved in a manner that ensures self-consistency. The equation for the supersaturation is given as (similar to Tzivion *et al.* , 1989 without the dynamic term),

$$\frac{d\eta}{dt} = D - A(P,T)\frac{dM}{dt} \tag{6.9}$$

where the term D represents the increase/decrease in η due to vertical motions and $A(P,T)$ is a function associating the total mass growth rate, dM/dt to the change in η (these functions are given in Tzivion *et al.* , 1989). Adding the equation for dM/dt gives,

$$\begin{aligned} \frac{d\eta(t)}{dt} &= D - A(P,T)C(P,T)\eta(t)\int \frac{m^{2/3}}{m^{1/3}+l_0}n(m)dm \\ &\quad -A(P,T)C(P,T)J(T,P)\int \frac{m}{m^{1/3}+l_0}E_d(m)n(m)dm. \end{aligned} \tag{6.10}$$

The integrals on the right hand side of Eq. 6.10 are evaluated as discrete sums over the bins k at the bin mean mass ($\bar{m}_k$). The radiative term is combined with the dynamic term (as η does not appear in the radiative term) and the equation for the vapor excess becomes,

$$\frac{d\eta(t)}{dt} = D' - G\eta(t), \tag{6.11}$$

where G includes all of the extra terms shown above. The solution to this equation is straight-forward as long as the terms D' and G can be assumed to vary slowly over a time-step (in our case 2 seconds, see Tzivion *et al.* , 1989 for a full discussion); we find upon solving the differential equation,

$$\eta(t) = \left[\eta(t_0) - \frac{D'}{G}\right]e^{-G(t-t_0)} + \frac{D'}{G} \tag{6.12}$$

By separating out the radiative term ($D' = D - Rad$),

$$\eta(t) = \underbrace{\left\{\left[\eta(t_0) - \frac{D}{G}\right] e^{-G(t-t_0)} + \frac{D}{G}\right\}}_{\text{Standard equation}} - \frac{Rad}{G}\left[1 - e^{-G(t-t_0)}\right], \tag{6.13}$$

one may note that the radiative effect on η is to reduce (increase) η more quickly than the standard equation (no radiation) under radiative cooling (heating). Under standard forcings, drops that reside for a considerable amount of time near cloud top will drive the supersaturation to values near 1.0. Under radiative forcing, since $\frac{Rad}{G}$ is positive for cloud top cooling η can attain equilibrium at a subsaturated value.

In order to deduce how number and mass within each bin is redistributed by the vapor growth process we must integrate Eq. 6.7 in time. Note that when the radiative term is not included this integration is straight-forward as long as P, T, and $n(m)$ may be considered constant over a time-step (Tzivion *et al.* , 1989). With the radiative term included, however, this integral is no longer easily solved since an $m^{2/3}$ term multiplies the radiative effect and the equation must be solved iteratively. To simplify this calculation, we follow the method described in Stevens (1997) for the effects of ventilation. The hypothesis being that since Eq. 6.7 is solved locally for each bin, using a mean value of the radiative term for each bin may produce acceptable accuracy. Upon applying this method to the radiative term Eq. 6.10 becomes,

$$\begin{aligned}
\int_{m_i}^{m_f} \frac{m^{1/3} + l_0}{m^{2/3}} dm &= C(P,T) \int_{t_i}^{t_f} \eta(t) dt + \bar{m}_k^{1/3} C(P,T) J(P,T) E_d(\bar{m}_k) \Delta t \\
&= \tau_r = \tau + \tau_k \\
m_f &= \left\{\left[(m_i^{1/3} + l_0)^2 + \frac{2}{3}\tau_r\right]^{1/2} - l_0\right\}^3
\end{aligned} \tag{6.14}$$

where m_k is the mass of the lower bin edge, τ is the standard forcing not including the radiative effect and is found by integrating Eq. 6.12 over a time-step using D instead of D' (see Tzivion *et al.* ,1989), τ_k is the bin-dependent radiative forcing term, τ_r is the total effect on the mass in bin k, m_f is the final mass after condensation/evaporation and m_i is the initial mass of the droplet.

In order to examine the accuracy of using Eq. 6.14 we solve Eq. 6.7 iteratively using a 2 second time-step and then compare the results. The computations use E_d values of

10, 20, and 60 Wm^{-2}, a drop radius range of 1.6 to 500 μm, and a supersaturation range of 0.01 to 10% . Errors plotted in Fig. 6.1 are for $E_d = 60\ W\ m^{-2}$, as this greater than the largest values encounter in our stratus simulations, and since errors increase with increasing E_d. The largest errors never exceed 1.5% , illustrating the practicality of the approximation in Eq. 6.14.

This approximation is thus included in the explicit microphysical model described in Feingold *et al.* (1994) and Stevens *et al.* (1996).

6.2 Arctic stratus as a test case

We utilize the information discussed in Chapter 5 on the summertime liquid phase ASC cases to examine the radiative effects on the growth of droplets. In Chapter 5, §5.3.4 we discussed a CRM simulation of ASC that included the use of an explicit method of dealing with the optical properties of the droplets which is coupled to the explicit microphysical model. During the simulations 500 parcels are placed throughout the dynamic layer associated with the ASC in various vertical and horizontal locations. As the simulation proceeds, sets of information are written out that can be used by a trajectory parcel model (TPM) to do off-line tests of the radiative effects on drop growth. The information written out for each of the 500 parcels includes:

- x and z positions,
- θ_l, P and r_t,
- w, u, and v wind components,
- the $E_{d,i}$ radiative terms for each band.

The TPM is then driven with these data that are derived from the explicit, cloud resolving simulations. Details of the method can be found in Stevens *et al.* (1996). The TPM takes this information and drives either an individual parcel or the whole ensemble of parcels using the prescribed motion fields. Microphysical effects are computed by using the same liquid phase model as in the CRM run except that the microphysics are driven

by the dynamics and thermodynamics as prescribed by the parcel information. Droplet activation, condensation, and collection follow the same mechanisms as in the CRM with the exception being that all condensate follows a given parcel (*i.e.* drop sedimentation is neglected). Activation of droplets takes two possible forms. The first is what we will term *single bin* activation; in this scheme all of the activated drops are placed within the first bin of the explicit drop representation. This places an upper limit on the time required for the process to act as activated drops have the smallest possible size. The second method, termed the *distribution* activation, activates the droplets in accord with a prescribed gamma distribution function. We choose a gamma function with $\nu = 2$ for the activation with three different values of D_n as shown in Fig 6.2. This distribution function is chosen to represent activation from a CCN spectrum with a relative abundance of small particles.

The study of the radiation-drop growth phenomenon within the TPM framework has some decided advantages over studying these effects within the CRM. First, the TPM allows for the examination of microphysical effects without complicating feedbacks associated with dynamics. Thus, we can study a variety of processes, essentially isolated from other effects. The TPM also allows for accurate solution of droplet growth without spurious spectral broadening due to advection errors that occur in the CRM (Clark, 1974; Stevens *et al.* , 1996). Since drop growth occurs on an Eulerian grid, drop distributions are still subject to diffusive broadening (Clark, 1974), however the top-hat condensation method of Stevens *et al.* (1996) mitigates this somewhat. The method, however, has its drawbacks (see Stevens *et al.* , 1996 for a complete discussion), the most important of which for this study are the following. The parcels used in the TPM are advected by the grid-point mean wind in the CRM. This can lead to extended cloud top residence times that may affect the results (Stevens *et al.* , 1996). Since mixing across interfacial boundaries are not well represented (Stevens *et al.* , 1996), affects near cloud top may not be accurately represented (although this is also a problem in the CRM). Finally, since they are prescribed along the trajectory, the radiative fluxes cannot vary as the drop distribution varies in the TPM (even though the amount of absorption can). These limitations must be borne in mind throughout the subsequent discussion.

The breadth of the distribution functions produced by the microphysical model will be discussed in terms of the total number and mass of droplets with $r > 20\ \mu m$, the effective drizzle rate, and the "predominant" radius, r_p, defined as in Berry and Reinhardt (1974). Since drops with radii greater than 20 μm have significant collision-coalescence efficiencies, we use this size to delineate between larger drops (what we will term *drizzle*) and small drops (what we will term *cloud drops*). The predominant radius, which is defined as

$$r_p = \left[\frac{3}{4\pi\rho_l}\right]^{1/3} \left\{\frac{\int_0^\infty m^2 n(m)dm}{\int_0^\infty mn(m)dm}\right\}^{1/3}, \tag{6.15}$$

can be used as a measure of the potential for a stratus cloud to precipitate as r_p values between 45 and 75 μm are representative of precipitating stratocumulus (Austin *et al.* , 1995). This definition strongly weights the drops with the greatest mass, thus r_p is highly sensitive to changes in the numbers of drizzle sized drops.

In the next section we give details as to how radiation affects the growth of droplets by condensation and collection for two particular parcels. In the section following §6.3, we examine the results from statistics associated with the ensemble of 500 parcels.

6.3 Trajectory parcel model results: single parcels

Examination of the radiative effects on drop growth with individual parcels allows details to be elucidated without other complicating feedbacks. In particular, we pick a single parcel that follows cloud top for the better part of the first hour of the CRM simulation, allowing us to take advantage of the strong radiative cooling. We do computations over only the first hour of the CRM simulation as we are interested primarily in the initiation of some large drops through enhanced condensation. In addition, runs beyond this time can produce large numbers of drizzle-sized droplets and, as sedimentation becomes important at this time, the results of the parcel model are no longer valid. Since this particular parcel is not representative of most parcels in the simulation (most parcels frequently cycle through cloud updrafts and downdrafts, Stevens *et al.* , 1996), we present results for a second parcel which has a more characteristic evolution. A list of simulations for the single parcels is given in Table 6.1. The first 4 simulations in Table 6.1 are for the parcel that

Simulation	Collection	Shortwave	Single bin act.	Distribution act.	Parcel
TAP	Yes	Yes	Yes	No	Top
TNS	Yes	No	Yes	No	Top
TNC	No	Yes	Yes	No	Top
TDA1& TDA2	Yes	Yes	No	Yes	Top
CAP	Yes	Yes	Yes	No	Cyclic
CDA1 & CDA2	Yes	Yes	No	Yes	Cyclic

Table 6.1: Simulations with individual parcels.

skims the top of the cloud (T = Top). The control simulation, TAP (Top, All Physics), includes all relevant physics with activated drops placed in the first drop bin. A similar simulation, TNR (not shown in table), which computes condensation without the radiative effect is used as a basis of comparison with TAP and, together, are considered the *control simulations*. Sensitivities based on the control case, TAP, are done in order to examine the magnitude of each effect. Simulations which do not include shortwave radiation (NS) or collection (NC) illustrate the magnitude of these effects. The importance of drop activation (either distribution or single bin) is explored by activating drops with the gamma function shown in Fig. 6.2 for $D_n = 2\mu m$ (TDA1) and $D_n = 3\mu m$ (TDA2). The last two simulations in Table 6.1 are for a parcel that cycles through the cloud (C = Cyclic) and are done as an example of the effect in a more characteristic cloud parcel. We examine only no radiation (CNR), radiation (CAP), and distribution activation (CDA1 and CDA2) simulations. The results are discussed in the subsections below.

6.3.1 Control simulation

In this subsection, we discuss the results of the control simulations for the two parcels, TAP and CAP, each of which utilizes the simple activation scheme. The control case is run with this activation scheme for two reasons. The first is that since all of the droplets are activated at the smallest size possible, runs with the single bin activation should put an upper limit on the time for the radiative effect to operate. The second is that using the

single bin activation method reduces the number of degrees of freedom (in terms of aerosol distribution parameters) that must be explored.

Cloud top parcel: TAP

A time series of the general microphysical results from the control runs (TAP and TNR) are shown in Fig. 6.3. The parcel's position with height shows that, once initiated, it reaches cloud top within 20 minutes and remains at cloud top throughout the rest of the hour.[2] The liquid water content of the parcel increases continuously as the parcel is advected upward in a supersaturated $(S-1)$ updraft. Once at cloud top, the parcel without radiative effects on the growth of droplets maintains a relatively constant mixing-ratio (around 0.4 $g\ kg^{-1}$) consistent with the cloud top values produced by the CRM in Chapter 5. Number concentrations remain near 90 cm^{-3} with a slight decrease in time due to collection. Supersaturations oscillate around $S-1=0$ as condensed water remains in the parcel and, since the dynamics are weak ($w \sim 0$), supersaturations cannot be continually produced.

For the case with the radiative effects turned on (TAP), r_l increases above that of the standard case and remains constant around 0.55 $g\ kg^{-1}$ for the last 25 minutes of the simulation. Concentrations are similar to the no-radiation (TNR) run until 4.55 h when the drop concentration begins to decrease. Supersaturations drop below zero and attain equilibrium at a slightly negative value (see Eq. 6.12). The radiative term, E_d, rapidly increases as the parcel moves toward cloud top reaching a mean value of about 40 $W\ m^{-2}$ (not shown), which is at the upper end of the range discussed by Austin *et al.* (1995).

Figure 6.4 shows the mixing-ratio and concentration for cloud droplets ($r_{l,s}$ and N_s respectively) and for drizzle droplets ($r_{l,r}$ and N_r respectively). One can see from the figure that most of the mass and concentration for both the no radiation and radiation runs is contained in the $r < 25\mu m$ portion of the drop spectrum. The concentration of cloud droplets decreases over the last 18 minutes from about 90 cm^{-3} to around 70 cm^{-3} while

---

[2]This parcel had the longest cloud top transect of any parcel in the trajectory set.

TNR shows almost no change in concentration. The TNR simulation shows no significant mass or number concentration within the drizzle sizes while TAP produces an increase in the number and mass of drizzle drops over the last 18 minutes of the simulation. Even though the amounts are not large, they do have a substantial impact on drizzle formation (Fig. 6.5) since r_p increases rapidly in TAP after about 4.7 h reaching 45 μm (drizzle size, according to Austin *et al.* (1995)) in only 12 minutes. This rapid increase in drop sizes increases drizzle rates from about 0.75 $mm\ d^{-1}$ to 3 $mm\ d^{-1}$ within this 12 minute period (see inset).[3]

The physical differences between the runs with (TAP) and without (TNR) radiation may be understood by examining Figs. 6.6 and 6.7. Figure 6.6 shows τ (proportional to the time integrated supersaturation, Eq. 6.14) for TAP (panel a) and TNR (panel b). Drops in TNR and TAP experience similar, initially large growth rates as supersaturations are produced primarily by updraft motion. Once cloud top is reached, τ approaches an equilibrium value since dynamic effects are small. With radiative effects included, droplets with $r > 10\ \mu m$ grow rapidly due to radiative cooling at cloud top as the radiative effect, E_d, increases with drop size. The larger droplets take up vapor faster than the smaller droplets (as τ_r is larger), reducing water vapor amounts until subsaturation occurs. In addition, the radiative effect on drops with $r > 10\ \mu m$ is large enough to support subsaturated growth (see $S - 1$, Fig. 6.3). Smaller drops ($r < 10\ \mu m$), however, evaporate (Fig. 6.6a) since the radiative effect is not as strong. This constitutes a differential size-sorting effect due to cloud top radiative cooling on the growth of the drop distribution and will alter the distribution shape with time. This effect has been briefly hinted at in the paper by Guzzi and Rizzi (1980) for a population of drops. Unfortunately, since their drop size distributions did not include collection effects few drops with radii greater than 10 μm were produced and, therefore only a few small drops were affected.

The production of drizzle drops, and the evaporation of small drops, is illustrated quantitatively in Fig. 6.7. The number of drops evaporated (ΔN_{evap}), number of drops

---

[3]These "effective" drizzle rates are shown simply as an illustration of the fact that drizzle formation is occurring, since large drops would quickly sediment out of the parcel in a real cloud.

collected (ΔN_{col}) and the number of drops transferred across $r = 20\mu m$ (ΔN_{trans}) by condensation during a model time-step are plotted in this figure. In order for collision-coalescence to be initiated, drops with $r > 20$ μm must be produced. In the TAP case, the number of droplets transferred by condensation to $r > 20$ μm occurs during two periods while number transfer to larger sizes in TNR is almost zero. This transfer enhancement through radiation near $r = 20$ μm, produces more drizzle droplets which increases the collection process in TAP (ΔN_{col}). Once collection begins to produce drizzle drops in TAP, the number of cloud drops lost through evaporation in a time-step (ΔN_{evap}) increases because the larger drizzle drops rapidly take up the available vapor. Interestingly, the decrease in N through evaporation assists the growth of larger drops, in a fashion similar to the Bergeron-Findeisen process.

The drop distribution shape is altered through these processes as compared to TNR (Fig. 6.8). During the first 0.2 hours of the simulation, the drop distributions for TAP and TNR are quite similar. As large drops are produced, between 4.2 and 4.4 hours, a bimodal spectrum is produced through the combined effects of condensation for $r > 10$ μm drops and the evaporation of $r < 10$ μm drops. This effect continues in time as drizzle drops grow through condensation and collection, reducing water vapor contents which causes further evaporation of small drops. The minimum between the two drop modes occurs right at the $r = 9\mu m$ size which delineates growing and evaporating drops. These results suggest that parcels which spend at least 0.2 hours (12 minutes) at cloud top can initiate a bimodal spectrum through the differential effects of radiation on drop growth, thus constituting a method of spectral broadening.

Cyclic parcel: CAP

Figures 6.9 and 6.10 illustrate the effects of radiation on drop growth for a parcel that is more representative of the ASC (the Cyclic parcel). The differences between the radiation (CAP) and no-radiation (CNR) simulations are much smaller in this case as the cloud-top residence time of the parcel is much less than in TAP. The mixing-ratio (r_l) is slightly larger for the radiation case and appears to be created during the short time that the parcels spend at cloud-top. Drop concentrations (N) are only slightly affected by the

radiative effects with a noticeable drop in concentration occurring towards the end of the simulation. Water supersaturations ($S-1$) show the same decrease during the cloud top traverses as in TAP; drops with $r > 10\ \mu m$ grow quickly producing slightly subsaturated environments. Figure 6.10 shows that most of the mass and number is contained in cloud drops for both the CAP and CNR simulations. The run with radiation, however, is evidently producing enough large droplets through enhanced condensation to initiate greater collision-coalescence rates as $r_{l,r}$ and N_r increase over the last 0.5 hours of the simulation.

As these results show, parcels that spend large amounts of time at cloud top appear the be the most likely to initiate drizzle. This is consistent with the results of Feingold *et al.* (1996b), in which relations between cloud top residence times and drizzle production were discussed (Stevens *et al.* , 1996 also discussed this connection). This dependence will be explored in the section on ensemble results.

6.3.2 Results of other sensitivities

In order to examine the importance of various processes on the results discussed in §6.3.1, a set of sensitivity studies are performed and are listed in Table 6.1. In order to refrain from producing an inordinate number of figures, selected bulk information that captures the essence of the sensitivities is collected and presented in Table 6.2. As was shown above, the variation of the distribution characteristics due to radiative effects on drop growth is well represented by r_p, the drizzle flux (F_{driz}), the fraction of the total mass in drizzle drops (M_f) and concentration tendencies. Here, the distribution characteristics (such as r_p) are averaged over the hour simulation period. Instead of r_p itself, we find the time (T_p) that it takes for r_p to reach 45 μm (the lowest size of the predominate radius for which drizzle was observed to occur, Austin *et al.* , 1995). For some parcels, r_p never reaches $45\mu m$ so we extend the simulation until this value is reached.[4] Effects on drop concentration are computed as a sum of the effect over the one hour period. Collection (N_{col}), number of drops transferred across $r = 20\ \mu m$ (N_{trans}), and number of drops

[4]This can easily be done as parcel data was written out for two hours of the CRM simulation.

that completely evaporate (N_{evap}) are included in this manner. Intercomparisons amongst simulations is possible as approximately the same number of drops are activated in each simulation.

Simulation	T_p	F_{driz}	M_f	ΔN_{trans}	ΔN_{col}	ΔN_{evap}
TNR	57.3	1.0	0.039	$9. \times 10^{-5}$	2.39	1.846
TAP	36.0	2.06	9.58	0.33	10.94	8.62
TNS	33.6	2.31	23.4	0.376	20.14	10.66
TNC	***	***	0.005	0.17	0.0	8.94
TDA1	32.0	1.95	20.0	0.438	19.11	8.58
TDA2	18.7	1.90	83.22	1.77	63.33	8.22
CNR	80.7	0.42	0.165	2.5×10^{-9}	2.66	0.138
CAP	72.8	0.85	0.67	1.1×10^{-7}	2.89	0.94
CDA1	50.1	1.20	8.74	1.4×10^{-4}	5.60	1.11
CDA2	31.3	0.94	99.9	0.16	47.9	59.0

Table 6.2: Sensitivity results for single parcel. T_p in minutes, F_{driz} in $mm\ d^{-1}$, M_f in % , ΔN_{trans} , ΔN_{col}, and ΔN_{evap} in cm^{-3} . The *** mean that $r_p = 45\ \mu m$ was never reached during the simulation time.

The results from the control runs (TAP and CAP) and the corresponding no-radiation runs (TNR and CNR) are included as a basis of comparison. The time required for the production of significant drizzle is reduced by about 21 minutes in TAP and is related to larger cloud drop transfer rates (ΔN_{trans}) which enhances collection (ΔN_{col}) effects as compared to TNR. These times are different from Austin *et al.* 's (1995) results which showed a reduction in T_p from 80 to 20 minutes due to radiation. In their computations, the drops remain at cloud top throughout the computations warranting comparison with the cloud top parcel. In addition, their results are produced with an initial drop size distribution (broad and narrow) whereas drops in our case drops are activated from an assumed aerosol size distribution. Concentrations used in Austin *et al.* (1995) range between 30 and 120 cm^{-3} which is similar to the concentrations used here. Thus, the longer time-scales in our case and are likely due to the fact that we do not begin with some large drops already in existence. The cyclic parcel shows smaller effects as compared to the cloud top parcel with reductions in T_p that are much less in CAP (only 8 minutes) as the transfer of drops and collection effects are only slightly enhanced. Other bulk numbers in

the table show the important features between the TAP, TNR, CAP and CNR simulations discussed in the last section.

The removal of shortwave absorption (TNS) allows for larger cooling rates and, hence, greater condensational growth, which significantly increases M_f but not T_p. Significant drizzle production, as characterized by T_p, occurs only three minutes earlier in TNS as compared to TAP. Transfer rates are slightly greater than TAP and, therefore, not the reason for the larger drizzle drop mass fractions (M_f) in this case. Since similar drop concentrations are transferred to larger sizes (ΔN_{trans}) as in TAP, increased condensational growth rates of large sized drops must be producing the greater drizzle mass amounts. This produces larger collection rates, larger drops and, hence, increased cloud drop evaporation. Removal of shortwave heating at cloud top, therefore, not only increases drizzle drop masses through enhanced condensation but also effectively redistributes drop mass in the small sizes ($r < 10\ \mu m$) to larger droplets.

Collision-coalescence , of course, greatly affects the mass partitioning within the drop distribution. Condensation by itself, along with long and shortwave effects (TNC), never produces a significant drizzle mode. Cloud drop transfer rates (ΔN_{trans}), however, are greater than TNR showing that radiatively-enhanced condensation significantly affects the initial production of drizzle sized drops. The evaporative loss of $r < 10\ \mu m$ drops is similar to TAP and TNS showing that *it is the radiative-enhanced condensation of drops in the $r = 10$ to 20 μm range which are the dominant reason for the evaporation of small cloud drops and, hence, the spectral broadening at small sizes.*

Activating drops in the 1.56-6 μm (TDA1) and 1.56-10μm (TDA2) ranges as opposed to single bin activation (TAP) has a strong effect on drop growth. Production of significant drizzle drops, as defined by T_p, is not enhanced significantly in TDA1 but is in TDA2 (T_p of 18.7 min). These results compare more favorably with Austin *et al.* (1995) since a drop distribution is activated, thus indicating the strong effects an initial spectrum has on the results. Cloud drop transfer and collection rates increase in both cases, however, this is more rapid in TDA2 because some 10 μm drops are activated. The production of large drops is significantly altered in TDA1 as compared to TAP, but the time for drizzle

onset is not affected much. This shows that most of the increase in drizzle drop mass (M_f) occurred after $T_p = 32$ minutes. Even though more drizzle drops are produced in TDA1 and TDA2, ΔN_{evap} is similar to TAP and TNC which shows a consistent effect on $r < 10$ μm drops in each case. This supports the assertion made above that it is the drops in the $r = 10$ to 20 μm range that cause the evaporation of the smaller drops.

Sensitivities conducted with the cyclic parcel show little difference between the no-shortwave (CNS) and no-collection (CNC) simulations and, thus, are omitted. Simulations which included the activation of a few large drops (CDA1 and CDA2) show significant decreases in T_p, similar to the cloud-top parcel results. The decrease T_p is more pronounced in the CDA1 and CDA2 simulations than the corresponding TDA1 and TDA2 experiments. The results are more dramatic than in the top-tracking parcel experiments because parcels which spend a long time at cloud top will likely produce drizzle anyway (since the environment is more favorable). In the cyclic parcel case, radiative enhancement of growth does not greatly alter the time that it takes to produce large drops. Initiating a few large drops in addition to the radiative effects, however, shows a strong impact which reduces the time necessary for drizzle-size drop production. This suggests a result that will be discussed in the ensemble section; *it appears that the radiative effects may only enhance drizzle-sized drop production in parcels which produce drizzle drops anyway.* Drop evaporation also increases as the parcel tracks through the sub-cloud layer so comparisons cannot be made with the cloud-top trajectory cases.

These results are illustrative of the effects of the radiative-drop growth mechanism. The use of two parcels, one that tracks along cloud top for an extended period of time and one that has a regular cycle, produces information that will be useful in understanding the ensemble results of the next section.

6.4 Trajectory parcel model results: ensemble results

The results presented in the last section for the single parcel trajectories, while elucidating the radiative effects on the distribution function, are not representative of the cloud as a whole. Therefore, in this section we examine the effects of radiation on drop

growth for an ensemble of cloud trajectories. The TPM is run for all 500 trajectories and averaged temporally and spatially. The temporal average is computed over the entire one hour simulation period in order to ascertain the average affect of radiation on the cloud drop distribution. Profiles are produced by averaging the results into $\Delta z = 20\ m$ spacings, which is similar to that used in the CRM. Since temporal and spatial averages do not convey information concerning temporal evolution, results comparing the dependence of various processes on the cumulative cloud-top residence time (T_c) are also presented. This method produces compact results and allows for easy comparisons.

Conducted simulations include those shown in Table 6.1, except that the first letter in each acronym is removed since single parcels are not used (*i.e.* TAP, which is for Top All Physics is now simply AP). As in the above sections the total CCN concentration available for nucleation is $N_{ccn} = 100\ cm^{-3}$. In order to examine the importance of CCN concentrations, parcel trajectories from an ASC simulation with $N_{ccn} = 500\ cm^{-3}$ are also used in the TPM. Simulations conducted with the TPM are for no-radiation (500NR) and radiation (500AP) and utilize the same physics as the AP simulation. Results are presented for the AP control simulation first followed by subsections which discuss the various sensitivities.

6.4.1 Control simulation (AP): N_{ccn}= 100 cm^{-3}

An examination of the general microphysical profiles (mixing ratio, r_l, and total drop concentration, N, in Fig. 6.11) in comparison with the hour averaged profiles in Chapter 5 show that the TPM captures the microphysical structure of the ASC. Mixing ratio increases linearly with height while drop concentrations have constant-with-height characteristics (Stevens *et al.* , 1996). The major difference in the TPM simulation is that drops are not able to sediment, thus the r_l and N profiles are sharper than they would be. This, of course, is a limitation of the results presented in this section. However, one must keep in mind that we are not attempting to discuss drizzle that falls from actual clouds with the TPM as many complicating feedbacks occur in such cases (such as dynamical changes which will shift parcel trajectories). The TPM affords us the advantage of being able to describe the microphysical processes that may lead to drizzle formation within certain parcels and

within certain regions of the cloud without complicating feedbacks. In addition, the drop spectrum may be simulated without the diffusive affects of advection (*e.g.* Clark, 1973; Stevens *et al.* , 1996) that may swamp out small effects, which is a decided advantage of the TPM.

From the results presented in the last section, one would expect radiative cooling at cloud top (AP) to substantially increase the liquid water mixing-ratio (r_l) and drizzle drop mass. This is indeed the case as is shown in Fig. 6.11; cloud top mixing ratios are increased (by almost 0.1 $g\ kg^{-1}$) while concentrations are decreased. In a real cloud, one would expect cloud top r_l to decrease as large drops undergo sedimentation. The percentage of mass and number concentration (M_f and N_f, respectively) that exists in the drizzle size range ($r > 25\ \mu m$) show significant enhancement both at cloud top and cloud base in AP and NR. Cloud top enhancement of drizzle drop mass must be due to collection in NR while in AP the radiative effect and collection play a role. The cloud base maxima are due to the complete evaporation of small drops in the sub-cloud region (below about $750m$). This also occurs in AP but is enhanced because larger drops are produced in the cloud top traverses.

That this is the case is illustrated in the plot of ΔS (Fig. 6.11) which is defined as the difference between the water saturation in the radiation case (S_{AP}) and that in the no-radiation case (S_{NR}). In the region below cloud base, much more evaporation is occurring in AP as more condensation at cloud top produces greater parcel r_l which is then available for evaporation. Cloud top saturations are reduced in AP over NR as more condensation occurs in AP, which is in agreement with the discussion of §6.3. In-cloud water saturations are reduced in AP since more water vapor is removed during the cloud top traverses.

Drizzle production, as characterized by r_p and F_{driz} (the drizzle flux), are significantly enhanced through radiative effects at cloud top (Fig. 6.12) with values reaching 25 μm and 5.5 $mm\ d^{-1}$, respectively (below those quoted for precipitating stratocumulus of 45 μm, Austin *et al.* , 1995). As parcels continually cycle through the cloud, larger r_p and F_{driz} values produced at cloud top cause increases throughout the domain. A maximum in r_p also appears below cloud base in AP which is due to the evaporation of cloud drops. It may,

therefore, be the case that low-level drop size maxima in the CRM simulations (Chapter 5) are produced not only through precipitating large drops but also by the evaporation of cloud droplets.[5]

At cloud top, a comparison of the mass distribution function ($n(m)$ in Fig. 6.12) for the AP and NR simulations shows an increase in spectrum breadth for $r \leq 9\ \mu m$ and $r \geq 10\ \mu m$ regions in the AP case. The increase in small drop concentrations, the size delineation of which is similar to TAP in §6.3 , shows that this is most likely due to evaporation. This size appears to be a general delineation between drops that continue to grow through radiative effects and those that evaporate in these simulations. These results show that spectral broadening due to the simultaneous growth of large drops and evaporation of small drops also occurs for the mean, ensemble results. This effect is enhanced by the fact that large drops cannot sediment away from the cloud top region and, thus continue to grow. However, as was noted above, the 10 to $20\mu m$ drops contribute the most to this effect (and these drops have small sedimentation velocities). This, in conjunction with the result from the single parcel showing only 12 minutes near cloud top is necessary for smaller drops to evaporate, suggests that this form of broadening may be a robust feature.

The production of drizzle drops in both NR and AP is greatest in the vicinity of cloud top ($\partial N/\partial t_{col}$ Fig. 6.12) since LWCs are greatest in this region (Feingold *et al.* , 1996b). Since the production of large drops is related to parcels that spend time at cloud top, this works in unison with the radiative effect. As the results for the AP simulation illustrate, collection rates are significantly increased in the vicinity of cloud top but are similar to NR throughout the lower portions of the cloud.

Analysis of cloud top trajectories

The above results show that cloud top trajectories are important for the production of drizzle drops, therefore we compute the PDF (probability density function) for the cumulative time spent at cloud top (T_c) during the course of one hour for the entire parcel

---

[5]So that values of r_p would not become extreme, we did not compute values if $r_l < 0.01\ g\ kg^{-1}$.

set. Cloud top is defined to be, in these cases, the region in which radiative cooling is occurring. This constitutes a $100m$ depth in most cases. The PDF for the 100 cm^{-3} ASC simulation (Fig. 6.13) shows that most cloud trajectories have accumulated cloud top residence times of slightly more than 20 minutes with very few parcels spending the entire 60 minutes in the radiatively cooled region. The PDF for the 500 cm^{-3} simulation shows a maximum near 20 minutes and a broader spectrum than 100 cm^{-3} . Cumulative cloud top times are illuminating because they quantify how much total time parcels spend at cloud top and, hence, which parcels are likely to be affected by radiative cooling. These data, while illustrative, include parcels that track through the sub-cloud layer in which the distribution is affected by evaporation. Thus, it can be argued that the *continuous* time spent at cloud top may be better for discussing which parcels can contribute to drizzle production through the radiative effect. For the sake of argument, the PDF of the continuous time spent at cloud top by the ensemble of parcels is shown in Fig. 6.14. As expected, this PDF is more narrow than the PDF of cumulative time spent at cloud top, however the spectral shapes are quite similar. Mean time spent within the defined cloud top region is just under 12 minutes. It turns out that using either the cumulative or the continuous time at cloud top in the analysis below makes little difference. From these PDFs, it is immediately evident that drizzle production can be significantly enhanced if drizzle growth can be increased in the majority of parcels which have shorter cloud top residence times. Clouds in which only the trajectories with the longest cloud top times contribute to drizzle production are expected to show little drizzle production.

In order to quantify which trajectories, in terms of cloud top residence time (T_c), are likely to contribute to drizzle production in an ASC, we average the various microphysical processes over each trajectory and plot this as a function of of T_c. Computed values include the percentage of the total mass in drizzle drops (M_f), the rate of increase in drizzle drop concentrations ($r > 20\ \mu m$; N_r) due to the transfer of cloud drops by condensation ($\partial N_r/\partial t_{trans}$), and the rates of collection ($\partial N/\partial t_{col}$) (Fig. 6.15). The percentage of drizzle mass (M_f) is highly correlated with long cloud-top residence times (T_c) in both the AP and NR simulations. Indeed, in the NR simulation M_f shows a continuous increase for

trajectories with $T_c > 30$ min. The mass percentage is significantly enhanced in AP through the combination of larger condensation and collection rates. However, as comparison to the inset shows, the same subset of trajectories that potentially[6] contribute to the drizzle process in NR are affected in AP. This is corroborated by the fact that collection rates show a rapid increase after 30 minutes in AP. Thus, AP enhances drizzle within parcels that contribute to the drizzle process anyway. If the radiative effect would include a broader set of trajectories in the drizzle production process (*i.e.* include more area of the PDF), drizzle would be enhanced much more substantially.

6.4.2 Sensitivities to control simulation

In order to ascertain the importance of certain processes to the ensemble simulations, we follow a similar schedule of sensitivity tests as in the TAP simulations discussed in §6.3, however CCN concentration effects are also considered. In these sections we concentrate on physical variables that show the strongest contrasts with the control simulation and, thus, lead to quantitative information about the process. Therefore, we concentrate most of our effort on cloud top residence time profiles as these appear to illustrate the effects most strongly.

Simulation without collection (NC)

The effects of condensation on the drop spectrum may be isolated by disabling the collision-coalescence process in the TPM. The initiation of large drops through the enhanced condensation process can be seen by examining the average distribution function at cloud top ($Z = 1126m$) for the NC and NR simulations (Fig. 6.16). The "no collection" simulation shows that significant production of 25 to 40 μm radii drops occurs through radiatively enhanced condensation alone. These drops are produce only within the parcels that have the longest cloud top residence times as the condensation transfer rate, $\partial N_r / \partial t_{trans}$, shows. This shows that condensational enhancement alone may produce

---

[6] Since drizzling clouds cannot be adequately described by a TPM, we use the word *potential* to describe the production of large drops. This underscores the fact that our analysis only describes the potential for certain parcels to contribute to the drizzle process.

larger drops, however since few parcels have the required cloud top residence times, the process is expected to be slow. Collection is not required for evaporative broadening below $r = 10\ \mu m$, as condensation alone produces this effect (corroborating the results from the single parcel analysis). The transfer rates for parcels with $T_c > 50\ min$ are greater than those for AP because larger drops reduce the numbers of $r < 20\ \mu m$ drops, thus they cannot be transferred through condensation.[7]

Because large drops are readily produced in AP through collection, cloud top water saturations are reduced further than in NC (compare ΔS profiles for AP, Fig. 6.11, and NC, Fig. 6.16). This leaves more water vapor within the parcels after their cloud top treks in NC and, thus, water saturations within the mid-cloud layer are larger. Thus, parcels which undergo radiative enhanced collection can be expected to reduce water vapor amounts through the greater condensation rates of the large drops. This, of course, affects the water vapor amounts lower in the cloud layer.

Simulation without shortwave radiation (NS)

Although it is difficult to ascertain by a comparison of Figs. 6.17 and Fig. 6.12, values of r_p are increased throughout the cloud layer when SW radiation is deactivated. The primary effect is the increase in r_p at the top of the cloud layer from about 24 μm in AP to 28 μm in NS. A comparison of the cloud-top distribution functions, $n(m)$, of AP and NS shows a greater breadth in NS. Thus, the spectral broadening that occurs through the growth of large drops and the evaporation of small drops is enhanced when SW radiation is disabled. Within the mid-cloud layer, one would expect r_p values to be larger in NS as shortwave heating is removed from the drop forcing (which suppresses cloud drop growth). This is not the case, however, as r_p values are not significantly larger in NS as compared to AP. Mid-cloud portions of parcel trajectories are short-lived because vertical motions advect the parcels quickly through the regions of SW heating. Thus, the predominant effect of SW heating is the reduction of LW cooling effects on drop growth at cloud top.

---

[7] Transfer rates of drops with $r < 20\ \mu m$ due to collection are computed but are so similar to the total collection rates (such as in Fig. 6.15) that they are not plotted.

How this affects drizzle production potential within the ensemble of parcels is shown in Fig. 6.18. The reduction of LW cooling by SW heating reduces the drizzle potential as a comparison of M_f in Figs. 6.18 and 6.15 shows. Transfer rates, and thus collection rates, are increased when SW radiation is disabled. In particular, transfer rates for trajectories with long cloud top residence times ($T_c > 55\ min$) are strongly affected showing that SW radiation suppresses drop growth by the largest magnitude for these parcels. Since few parcels have these long time scales (Fig. 6.13), the overall effect on cloud structure is minimal. Parcels with smaller T_c are also strongly affected, causing substantial increases in M_f for $T_c > 30$ minutes. Drizzle enhancement is, however, still confined to the same subset of parcels as in AP (*i.e.* parcels with $T_c > 30\ min$).

Simulation with distribution activation (DA)

The effects of distributing the activated drops with a sharply decreasing function are also plotted in Figs. 6.17 and 6.18. The acronyms DA1 and DA2 have the same meanings as TDA1 and TDA2 in Table 6.1; a few 6 μm drops are activated in DA1 and a few 10 μm drops are activated in DA2.

The activation of drops over the radius range $r = 1.56$ to 6 μm (DA1) increases r_p values as compared to AP by almost the same amount as the no-shortwave simulation (NS). In fact, r_p values are increased by a larger amount throughout the cloud in DA1 with the effect being most pronounced below cloud base. Distribution breadth (shown by $n(m)$ in Fig. 6.17) is definitely increased in DA1, as the large tail end of the drop spectrum contains greater numbers of drops than either NS or AP (Fig. 6.12).

Rates of transfer for cloud drops to drizzle drops through condensation is increased by greater than 0.002 $cm^{-3}\ min^{-1}$ in DA1 (Fig. 6.18) as compared to AP (Fig. 6.15). Larger transfer rates occur for most T_c values which increases collection rates and mass fractions of drizzle drops (M_f) as compared to AP. The close match between the NS and DA1 simulations shows that the large transfer rates for parcels with large T_c ($> 55\ min$) do not significantly affect the overall microphysical structure. In addition to this DA1 shows that even if only a few small drops are initiated, the effects can effectively counteract drop growth suppression by SW heating. The activation of a few larger drops in DA1, however,

does not significantly affect parcels with $T_c < 30$ minutes as profile shapes are similar to AP.

Increasing the size of the activated drops so that a few 10 μm drops are produced drastically changes the results. Distribution breadths are increased throughout the cloud layer (Fig. 6.17) as noted by the large increase in r_p values (cloud top values reach 75 μm) and the production of significant large drops at cloud top shown by $n(m)$. The greater rapidity of the processes in DA2 is shown in Fig. 6.18. Significant transfer and collection rates occur for cloud top residence times greater than about 20 minutes, which produces larger mass fractions of drizzle sized drops (M_f). As noted above, radiative effects alone did not significantly enhance drizzle production for a broader set of parcels (*i.e.* the same subset of parcels contributes to drizzle in AP as in NR). Drizzle enhancement for a broader set of parcels (with T_c less than 30 minutes) occurs through the combination of large drop activation and radiative effects. Again, however, a comparison of the DA2 simulation conducted with and without radiation (DA2 No-Rad.) shows that the radiative effect does not drastically affect potential drizzle drop production for a broader set of parcels.

These results suggest that increasing drizzle production in parcels with shorter cloud-top residence times may be a function of the size of the activated drops and the CCN concentration. As increasing the drizzle production in short T_c parcels is important for reducing the time of drizzle onset potential (see T_p values in Table 6.2), activating a few large drops, in conjunction with enhancement through radiative effects, can significantly enhance drizzle production.

Simulation with N_{ccn}= 500 cm^{-3} (AP500)

Increases in drop concentrations are expected to produce less drizzle as the available vapor is distributed over more droplets. In order to examine this effect, the TPM was initialized with trajectories generated from an ASC simulation with 500 cm^{-3} CCN concentration. Drizzle production is suppressed as drizzle sized drops, in this case, contain a small amount of the cloud water mixing-ratio in both the radiation and no-radiation (not shown) simulations. The percentage of mass associated with drizzle drops (M_f, Fig. 6.19) is only significant for parcels with the longest cloud-top residence times (in excess of 50

min). Few parcels have such long cloud-top traverses (Fig. 6.13), thus this enhancement has little effect on the overall cloud structure. The larger M_f for parcels with $T_c \geq 55\ min$ are due to the production of few drizzle drops through radiative enhanced condensation which rapidly increases collection ($\partial N/\partial t_{col}$) because of the large drop concentrations and the high mixing-ratios at cloud top (reflected in the large transfer rates, $\partial N_r/\partial t_{trans}$).

Thus, clouds with greater CCN concentrations are adversely affected, in terms of their ability to produce drizzle, by the fact that the available vapor must be distributed over more drops. However, with or without the effects of radiation, cloud parcels must spend larger time periods within the vicinity of cloud top in order to produce drizzle than clouds with fewer CCN. Few parcels have these required cloud top residence times and fewer total parcels spend time within the region of radiative cooling.[8] Thus, longer simulations may be needed for drizzle to be produced in large CCN concentration cases. Of course, this will be true only if drops can cycle through the cloud for periods long enough so that some larger drops are produced. These larger drops could, therefore, take advantage of the cloud top trajectories.

6.5 CRM simulations of ASC with radiation-condensation coupling

The condensation coupling to radiative heating is added to the CRM used to simulate ASC in Chapter 5. Since the production of drizzle sized drops from the point of activation is important (as discussed in the sections above), simulations with the bin microphysical model are initialized and run for a six hour time period. This differs from the Chapter 5 simulations in which simulations were spun-up using a simple microphysical scheme. Simulations are conducted for 100 cm^{-3} and 500 cm^{-3} CCN concentrations with and without the radiative effect (both SW and LW) included, and are denoted 100R, 100NR, 500R and 500NR. Simulations in which collision-coalescence is deactivated are also undertaken and are denoted by adding NC to the end of the acronyms. These simulations are not intended

---

[8] An examination of the PDFs shows this. The integration of the $500cm^{-3}$ PDF has less total area than the $100cm^{-3}$ PDF, indicating that less total time is spent at cloud top in $500cm^{-3}$.

to be an all-inclusive set; they are undertaken in order to illustrate the strength of the effect in the CRM framework.

These simulations differ from the previous sections as turbulent diffusion and sedimentation are now included. This affects the cloud top residence times of parcels and the condensation and collection algorithms, as they are subjected to the physical and numerical effects of advection and diffusion (Stevens *et al.* , 1996).

Time-series plots of microphysical quantities are used as a vehicle to explore the radiative effects on the drizzle process. Model quantities included are the maximum effective radius (r_e) within the model domain and the height at which it occurs (Z_{re}), maximum LWC and LWP,[9] maximum $< w'w' >$ and updraft speed, w. Because the ASC domain is quite homogeneous, these quantities are representative of the evolution of the system. Profiles of microphysical quantities at selected times are interjected in order to elucidate the discussion where necessary.

6.5.1 Simulation with 100 cm^{-3} CCN concentration

The maximum effective radius (r_e) during the 100R and 100NR simulations is plotted in Fig. 6.20. The cases with (100R) and without (100NR) radiative effects on drop growth produce small r_e values throughout the first 1.5 hours of the simulation. These maxima are co-located with cloud top which, as discussed above, is the region of dominant collision-coalescence. The 100NR simulation undergoes a rapid change at around 2 hours, producing drop distributions with greater r_e values which, as is shown by the Z_{re} time-series, gradually sediment to lower layers of the cloud. The 100R simulation shows a similar time-series as 100NR, except that the onset of drizzle occurs 0.2 hours (12 minutes) earlier in 100R (see inset Fig. 6.20). Profiles of the microphysical results (which are averaged over the horizontal domain and over 15 minute time periods) at 2 and 3 hours into the simulation (Fig. 6.21 and 6.22, respectively) show the production of drizzle during this time. Cloud top LWCs are reduced in 100R as drizzle drops are produced (collocation with drizzle drop

[9]The liquid water path (LWP) is defined as the integral of the total condensed water (LWC) in a model column, $\int_z LWC(z)dz$.

concentration, N_r), which enhances sedimentation from cloud top. Total concentrations are reduced in 100R due to the larger collection rates which enhance the drizzle rate, as illustrated by the drizzle flux (F_{driz}). The increased drizzle produces drop size distributions with greater r_e values in the sub-cloud region.[10] It takes the 100NR simulation almost a full hour to produce the same effect (Fig. 6.22). The LWC of the cloud is now noticeably reduced in the 100R through enhanced drizzle. Comparisons of the concentration (N), the concentration of drizzle drops (N_r), the drizzle flux (F_{driz}) and the effective radius of the distribution (r_e) shows that 100NR and 100R now appear to be producing drizzle at the same rate. Even though both 100R and 100NR produce some distributions with large r_e values only about 12 minutes apart, 100R produces drizzle *in the average* about one hour earlier than 100NR.

The time-series of maximum LWC and LWP illustrates the overall effect of radiation on the cloud during the six hour integration (Fig. 6.23). The LWCs increase rapidly for both simulations during the first hour of the simulation and each tracks the other quite closely. After about one hour, however, the LWC maximum (which is synonymous with the cloud top LWC) begins to fall in comparison to 100NR. At the same time, LWPs begin to increase in 100R above those in 100NR. This shows the onset of the drizzle process, larger drops are being produced at cloud top in 100R than in 100NR which sediment out of the cloud top region. These drops, however, have not reached cloud base and, therefore, cloud top radiative cooling continues to enhance water mixing-ratios in 100R as the larger LWPs show. The LWC maximum continues to remain below that of 100NR throughout a large part of the six hour integration, showing that large drops are continually produced and removed from cloud top through drizzle production. These microphysical differences are not great enough, however, to produce a bifurcation in the respective solutions as 100R and 100NR track one another closely. This is apparently due to the fact that the inclusion of the radiative effect does relatively little to the dynamics of the cloud layer, as characterized by the similar maximum $< w'w' >$ time-series.

---

[10] In the previous sections we noted that this is probably also enhanced by the evaporation of cloud droplets.

Removal of the effects of collection from the integrations produces narrow distributions in both the 100RNC (no collection, radiation included in drop growth) and 100NRNC (no collection, radiation not included in drop growth) simulations, as shown by the small r_e values in Fig. 6.24. The effective radii for both cases follow one another closely until hour 3 at which time the radiative case (100RNC) begins to produce a distribution function with more breadth. The LWC for each case shows an increasing trend throughout the simulation with slightly greater values in the 100RNC simulation. Without drizzle production, the cloud may retain more liquid water, thus the higher LWC amounts than the 100R and 100NR simulations. In a similar manner, the dynamics of the cloud layer are weakly altered by the inclusion of the radiative term in the drop growth equation (see $< w'w' >$ panel in Fig. 6.24).

These sets of simulations show that the radiative effect, which changes some of the microphysical characteristics of the cloud layer, does not significantly alter the course of the simulation. The time of drizzle onset is noticeably reduced, especially in the average profiles and may be important for detailed case studies. The reason for the similar time-series (offset in time) for the simulations is likely related to the fact that radiation affects the same subset of parcels that produce drizzle anyway in the no-radiation run (see TPM results). From this result, it would seem that drizzle will be produced in each case with radiation simply shifting the time of drizzle onset. There is, however, another factor that confuses the issue. Spurious production of cloud top supersaturations (Stevens *et al.* , 1996) occur right within the region where radiative cooling affects drop growth in the CRM. In the TPM, cloud supersaturations drop off more realistically with increasing height and, trajectories with cloud top tracks reach and equilibrium value (Fig. 6.3). Thus, the cases with the radiative feedback may actually grow while the no-radiative cases show the small effects of very little supersaturation.

In the CRM, as Fig. 6.25 shows, the condensational growth rate at cloud top can be large in both the radiative and no-radiation cases. Condensation is confined to cloud top and cloud base until the second hour of the simulation (at which point significant broadening has occurred), however the cloud-top condensation rate is still quite large.

Thus, the effects of radiation on drop growth are felt much less strongly as compared to the TPM. This difference between the TPM and the CRM is strongly illustrated in comparison to the τ values used in the condensation forcing equation (Eq. 6.14); note that for the cloud top tracking parcel (Fig. 6.6b) condensation in the absence of radiation is very small. This is also true of the ensemble averages.

Simulation with sedimentation disabled

In order to illustrate the extent of the differences between the CRM and the TPM, we undertake a simulation in which sedimentation is disabled. Except for the effects of turbulent diffusion, all drops now follow the grid-point mean air motions, so a more direct comparison to the TPM is possible. It is immediately noted in the time-series of the effective radius (r_e, Fig. 6.26) that large drop production occurs on about the same time-scale as in the 100R and 100NR simulations. That this is the case is not surprising as the initiation of collision-coalescence should occur on a similar time-scale without sedimentation. Large drop production in the no-radiation case is much greater in the CRM than the TPM over the course of the first hour of the simulation (Fig. 6.26). Note that both the radiation and no-radiation cases produce distribution broadening at cloud top by the end of the first hour (with r_p values of $80\mu m$ and $42\mu m$, respectively). In addition, concentrations at the small end of the spectrum increase in both cases. These results are at odds with the TPM case (Fig. 6.12) in which the cloud top distribution for the no-radiation case remained narrow for the 1 hour simulation. One explanation for the differences is that numerically-induced cloud top supersaturations produce the large growth rates shown in Fig. 6.25. Because of these spurious supersaturations, the no-radiation simulations grow larger drops than would normally occur. This also biases the radiation runs, however, because the drops in the CRM experience large growth rates in either case, the differences between radiation and no-radiation cases is obscured. In addition, the broadening due to small drop evaporation does not occur and can be attributed to spurious cloud top nucleation of drops that occur within the region of high supersaturations.

Besides the purely numerical effects that produce the spurious cloud top supersaturations, subgrid scale diffusion will alter the cloud top residence times of the drops. In

addition to this, subgrid scale mixing of drops (which is not included in the TPM) will cause broadening of the drop size spectrum. This effect quite possibly plays a significant role in the number concentration increase at both small and large drop ends of the distribution functions. Due to the difficulties associated with separating effects in the model, however, it is difficult to tell exactly how important each of these effects is.

6.5.2 Simulation with 500 cm^{-3} CCN concentration

As would be expected from the discussion in §6.4, the radiative effect takes an extremely long time to act in the simulations with 500 cm^{-3} CCN concentrations. The time-series of r_e (Fig. 6.27) shows that both 500R and 500NR begin to produce drizzle by the end of the six hour integration, as r_e reaches values as large as 100 μm. The inset shows that this occurs in 500R about 0.2 hours (12 minutes) earlier than in 500NR which is almost exactly the same difference noted in the $100cm^{-3}$ simulations. Comparisons of microphysical profiles (not shown), as was done for 100R and 100NR, show the same effects in 500 cm^{-3} CCN concentration simulations with 500R producing drizzle about one hour earlier than 500NR. The similarities between the $100cm^{-3}$ and $500cm^{-3}$ simulations are striking but, perhaps, should not surprise us. The time for the onset of drizzle is increased greatly in the $500cm^{-3}$ simulation, as predicted by the analysis of §6.4, but the effect in the end is the same as in 100R. Section 6.4 suggested that drizzle drops could be produced in a simulation with $500cm^{-3}$ CCN concentration if we waited long enough for the few parcels that have long cloud top trajectories to be positively affected by the cloud top radiative cooling. It also showed that drizzle production in both the radiative and non-radiative cases was confined to parcels which had similar cloud top residence times. Since the same subset of parcels contribute to drizzle production in the radiation and no-radiation simulations, it appears that radiation should simply speed-up the process. In addition to this, if the radiative effect acts in the same manner between the $100cm^{-3}$ and $500cm^{-3}$ simulations, then the reduced time for drizzle production should be similar between the cases. This appears to be the case here. Of course, it must be kept in mind that, since all CRM simulations suffer the spurious production of cloud top supersaturations, the differences between the radiation and no-radiation cases may not be as pronounced as they were in

the TPM. In addition, advective broadening takes place in the CRM which can further reduce the differences.

Since this case produces essentially no drizzle during the first 5.5 hours of the simulation, the time-series of LWC and $< w'w' >$ (Fig. 6.28) are quite similar to those produced by the $100cm^{-3}$ simulation without collection. Alterations begin to occur at the end of the simulation when drizzle is beginning to be produce.

6.6 Summary of results

In this chapter the effects of radiative heating (cooling) on the heat budget, and therefore on the condensational growth, of a population of drops within two modeling frameworks has been discussed. Optical properties derived for the explicit microphysical framework of Feingold *et al.* (1988), described in Chapter 3, are used in a consistent fashion within the bin condensational growth framework. The CRM simulations of ASC described in Chapter 5 are used as a test-bed for the radiative effect. In order to separate the effects from complications associated with the various feedbacks that are inevitable in the CRM framework, we use an off-line trajectory parcel model (TPM) which has been successfully used in the study of stratocumulus clouds (Stevens *et al.* , 1996).

The TPM model analysis showed that the radiative effect reduced the time required for the onset of drizzle by up to 30 minutes in some cases, depending upon the cloud-top residence time of the parcels. This was also shown to depend weakly on the inclusion of SW heating but more strongly on the size of the activated drops. Distribution bimodality (spectral broadening) was a consequence for parcels that spent at least 12 minutes at cloud top and was shown to be due to the fact that drops with $r < 10\ \mu m$ evaporate. Thus the drop distribution experiences size-differential growth characteristics. Ensemble TMP simulations corroborated this as significant spectral broadening occurs in the radiative cases below $r = 10\ \mu m$. The CRM did not show this pronounced broadening even in the simulation with sedimentation disabled. This was shown to be strongly dependent on the spurious cloud top supersaturation field. Shortwave radiation does not have a strong effect within the mid-cloud as drops are advected quickly through this region. The dominant

effect of SW heating is the suppression of drop growth at cloud top. The production of drizzle drops is strongly correlated with cumulative cloud top residence time and is highly dependent upon the number of CCN. In both the radiative and non-radiative cases, the parcels which contribute to drizzle production are about the same. For the radiative, non-radiative, no-shortwave and activation of drops at $6\mu m$, parcels with cumulative cloud top residence times (T_c) larger than 30 min per hour of simulation have a significant potential for drizzle production. Since the number of parcels with a given T_c increases with decreasing time, significantly enhancing drizzle production in shorter T_c parcels can greatly enhance the potential to produce drizzle. From the TPM results, it appears that the size of the activated drops affects this the most as activating $10\mu m$ drops significantly increases drizzle production potential in parcels with T_c as low as 20 min per hour of simulation.

The simulations using $500cm^{-3}$ CCN concentrations produced the expected effect of reducing potential drizzle production. This was shown to be due to two factors. It is well known that drop distributions with larger concentrations produce drizzle more slowly as the available water vapor must be distributed over a greater number of drops. Thus, the time required to produce drizzle sized drops increases over that of lower CCN concentration cases. As was shown by the TPM analysis, cloud top residence times of greater than 55 minutes per simulation hour are required for significant drizzle production when CCN concentrations are as large as $500cm^{-3}$. Since few parcels have this required T_c, the production of drizzle in the larger CCN concentration simulation is significantly hampered.

The CRM simulations corroborated some of the TPM results. The $100cm^{-3}$ CCN concentration simulations produced greater numbers of larger drops at cloud top through enhanced condensation. However, this took almost 2 hours of simulation time to occur, which is in marked contrast to the TPM simulation in which drizzle was initiated in less than 30 minutes. A direct comparison between the two modeling frameworks is, of course, difficult as a number of problems cloud these issues. Part of the problem with a direct comparison lies in the fact that a time-period is needed to spin up coherent circulations in

the CRM (the PDF analysis with the TPM used trajectories from a steady simulation). In addition to this, cloud top residence times are likely reduced in the CRM as drizzle removes drops from the parcels. However, other issues confound comparisons on a more fundamental level and are discussed below.

Distributions with large r_e values were produced in both the radiation and no-radiation simulations differing in timing by only 12 minutes. Even though this was the case, the temporal and spatially averaged profiles showed that drizzle onset in the average was reduced by almost one hour in the simulation that included the radiative effect. This compares somewhat favorably to Austin *et al.* 's (1995) results showing a possible reduction in drizzle onset time of up to a factor of four (here a factor of three). That the result is not as striking as Austin *et al.* 's (1995) is due to the simplification of drops residing at cloud top in that study. Overall, however, the solutions tracked each other closely with the predominant differences being the quicker production of drizzle and the lower cloud top LWC in the radiation case. This seems to corroborate the TPM results in which it was shown that the same subset of parcels has the potential for drizzle production in the radiation and no-radiation cases. This indicates that, since drizzle will be produced by these parcels anyway, radiative effects may just speed up the process. If drizzle does not occur much in advance of the no-radiation simulation then it seems likely that similar cloud structures should occur with different temporal scales. The CRM cloud-scale dynamics, which were only weakly affected by the inclusion of the radiative effect in these cases, seem to corroborate this. Although, if significant drizzle can be triggered much earlier, feedbacks into the dynamics would be significant.

The $500cm^{-3}$ simulation show differences between the radiation and no-radiation cases that are similar to the $100cm^{-3}$ cases. The main difference, however, is that the time for the onset of drizzle was increased by almost 3 hours in the $500cm^{-3}$ as compared to the $100cm^{-3}$ CCN concentration simulations. These results compare well with those of the TPM analysis. The $500cm^{-3}$ simulation time-series were similar to those for the $100cm^{-3}$ simulation without collection, thus punctuating the slow drizzle production mechanism in the larger CCN concentration case.

Care must be taken in comparing the TPM and CRM results. The TPM has the advantage of computing these effects in a framework free of spurious broadening due to advection which will plague the results. In addition, the CRM produces significantly large spurious cloud-top supersaturation peaks. These cause the distribution functions in the no-radiation cases to attain broader spectra through condensation alone than they otherwise would. In addition to this, the spectra in the CRM experience the effects of mixing due to subgrid scale turbulence which will enhance the distribution broadening. Of course, it is difficult to separate the physical and artificial broadening that occurs within the CRM because of the non-linear nature of the system. In the TPM, cloud supersaturations are reduced more realistically with height, however broadening due to diffusive mixing are not included. Thus, it is difficult to do an accurate comparison of the results between the CRM and the TPM.

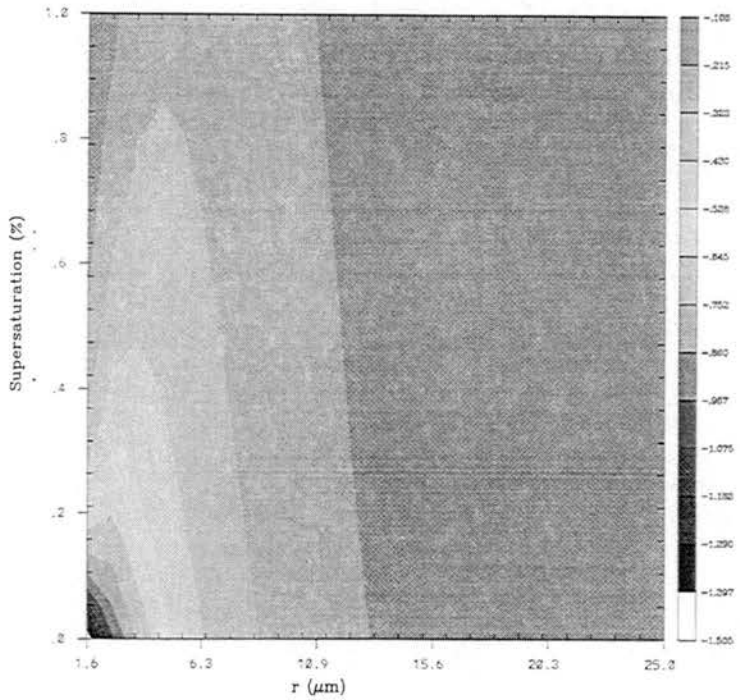

Figure 6.1: Illustration of the relative error associated with using Eq. 6.14.

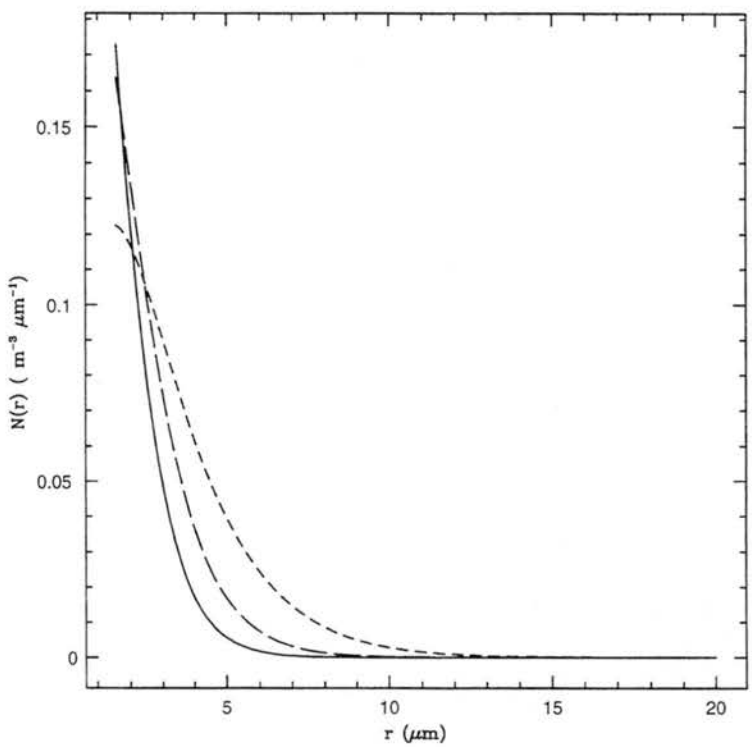

Figure 6.2: Distributions used for the activation of new drops. In each case $\nu = 2$. The solid line is for $D_n = 1.5\ \mu m$, the long-dashed line is for $D_n = 2\ \mu m$ and the short-dashed line is for $D_n = 3\ \mu m$.

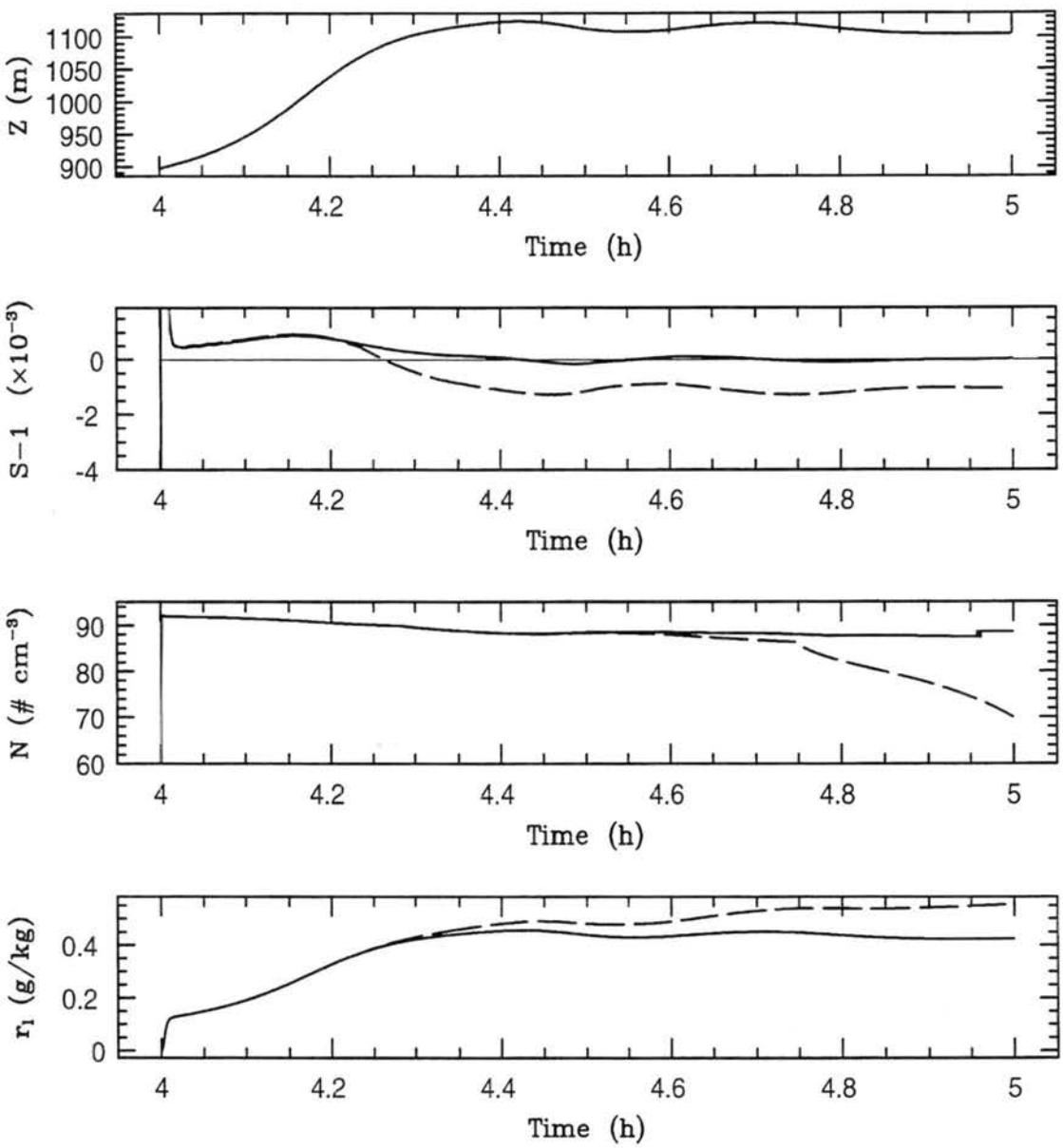

Figure 6.3: Time-series of the microphysical results for the control run (TAP). The vertical location, Z, in m, supersaturation (S), concentration of drops (N) and water mixing ratio (r_l) are shown for the case without radiation (TNR, solid line) and with radiation (TAP, dashed line).

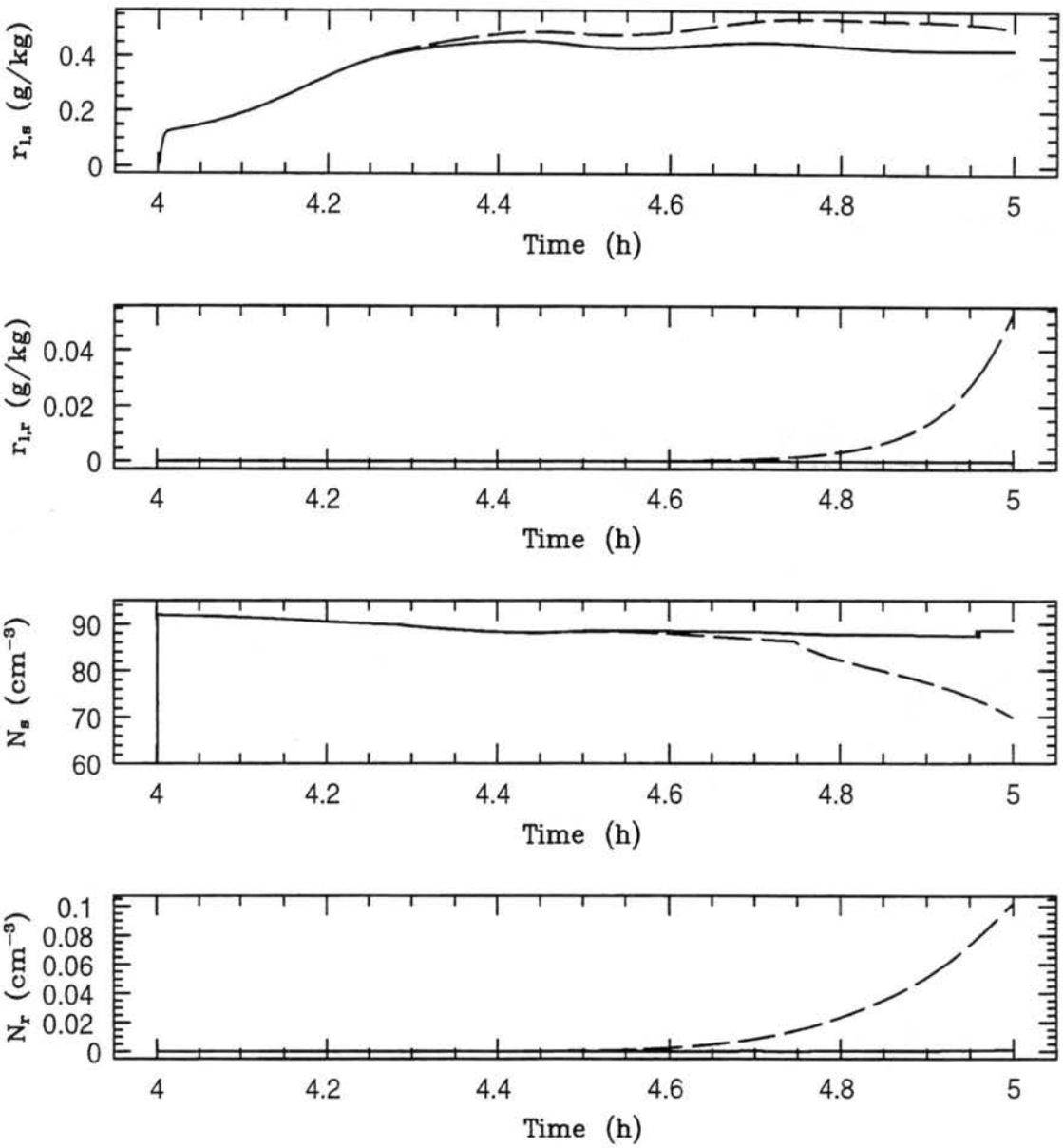

Figure 6.4: Time-series of the results for drizzle and cloud droplet number concentration and mixing ratio for control run (TAP). Results for $r \geq 25$ μm drops ($r_{l,r}$ and N_r) and for $r < 25$ μm drops ($r_{l,s}$ and N_s) are shown. The solid line and dashed line are for runs without (TNR) and with (TAP) radiation, respectively.

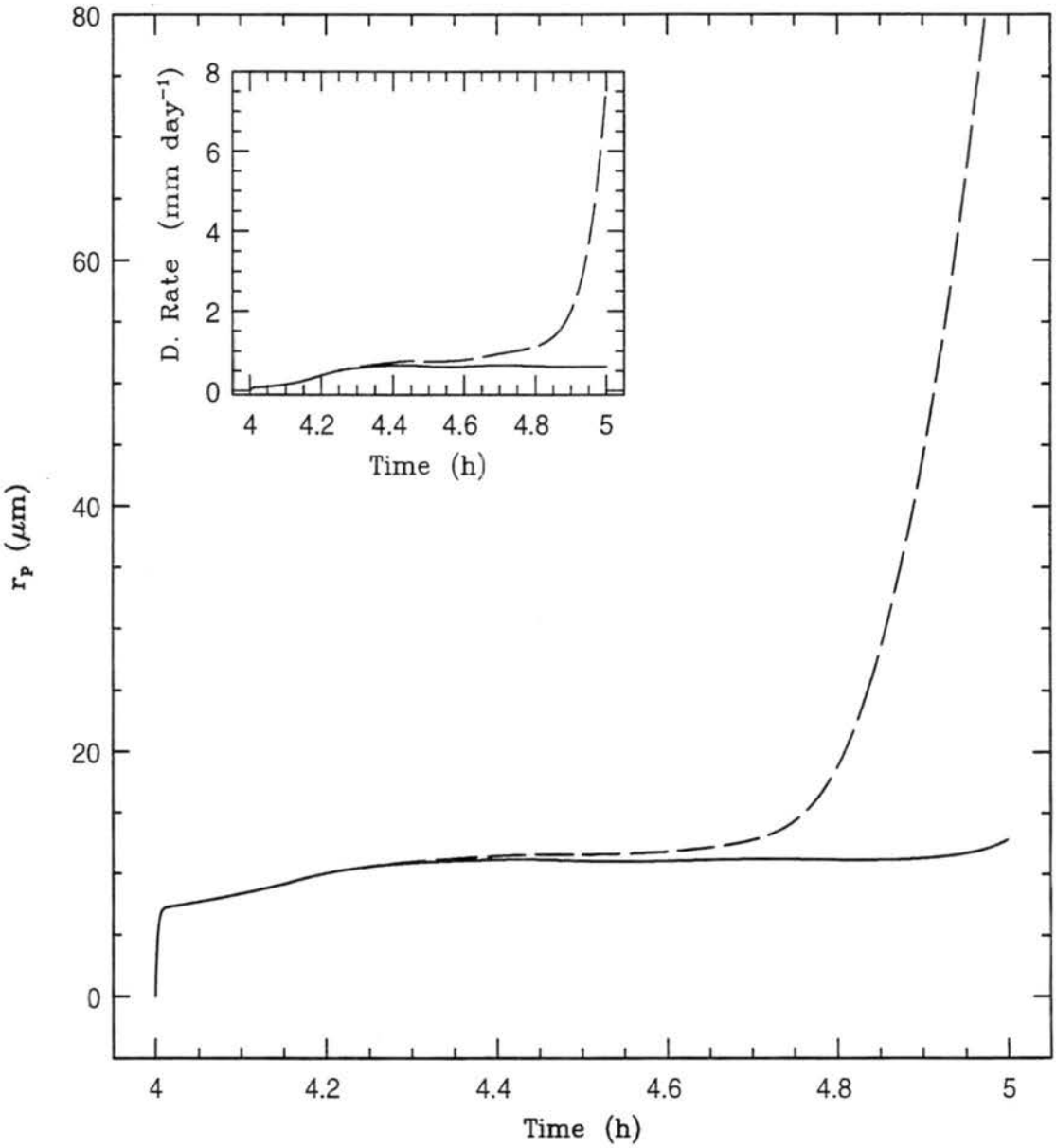

Figure 6.5: Time-series of the results for r_p and drizzle rate for the control run (TAP, dashed line) and for no-radiation (TNR, solid line).

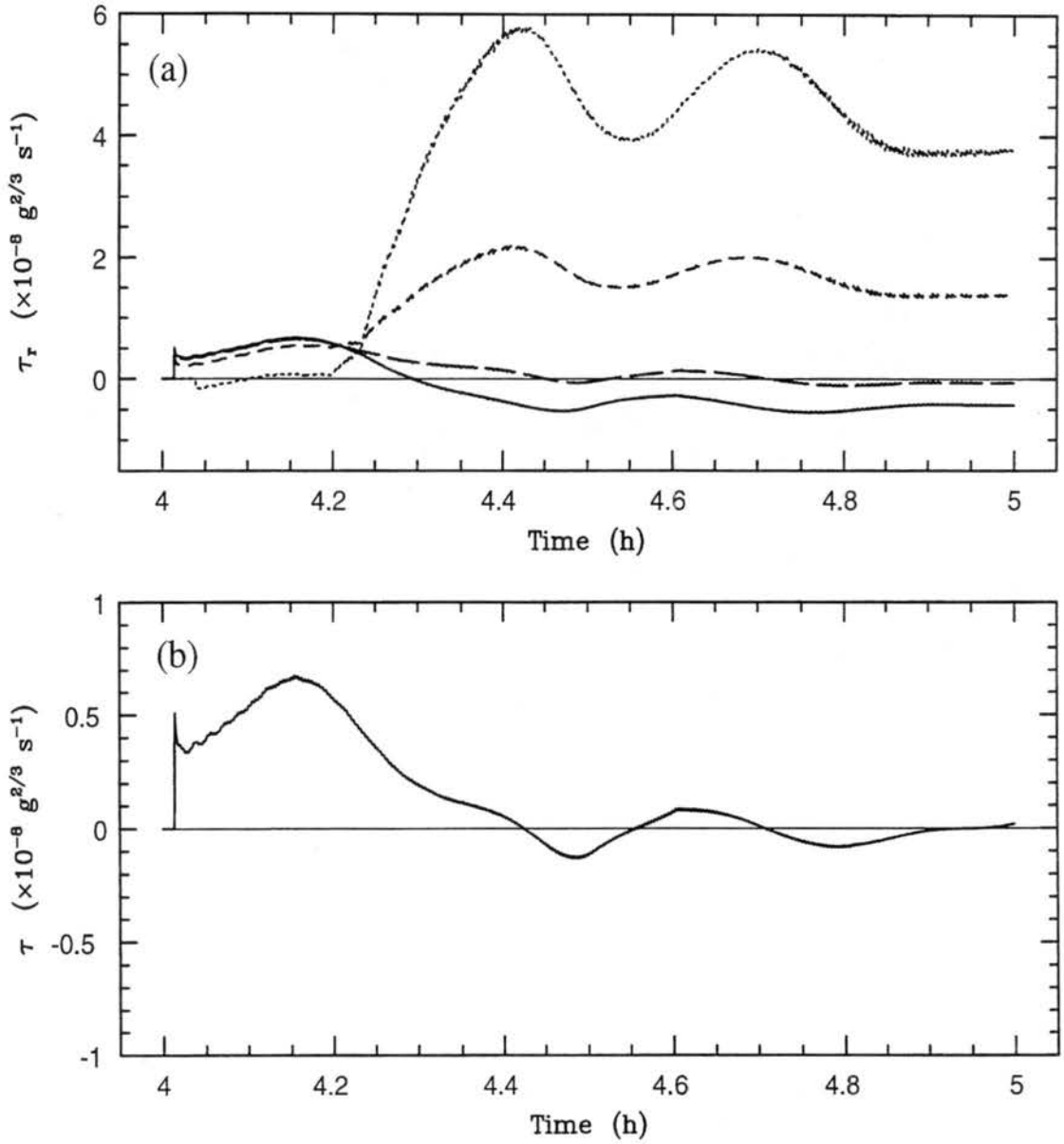

Figure 6.6: Time-series of τ from Eq. 6.14 for control run (TAP). Results including radiation, TAP (a), τ_r, are for mean bin sizes of 6 μm (solid line), 10 μm (long-dashed line), 22 μm (short-dashed line), and 60 μm (dotted line). Results without radiation (TNR) are shown in (b).

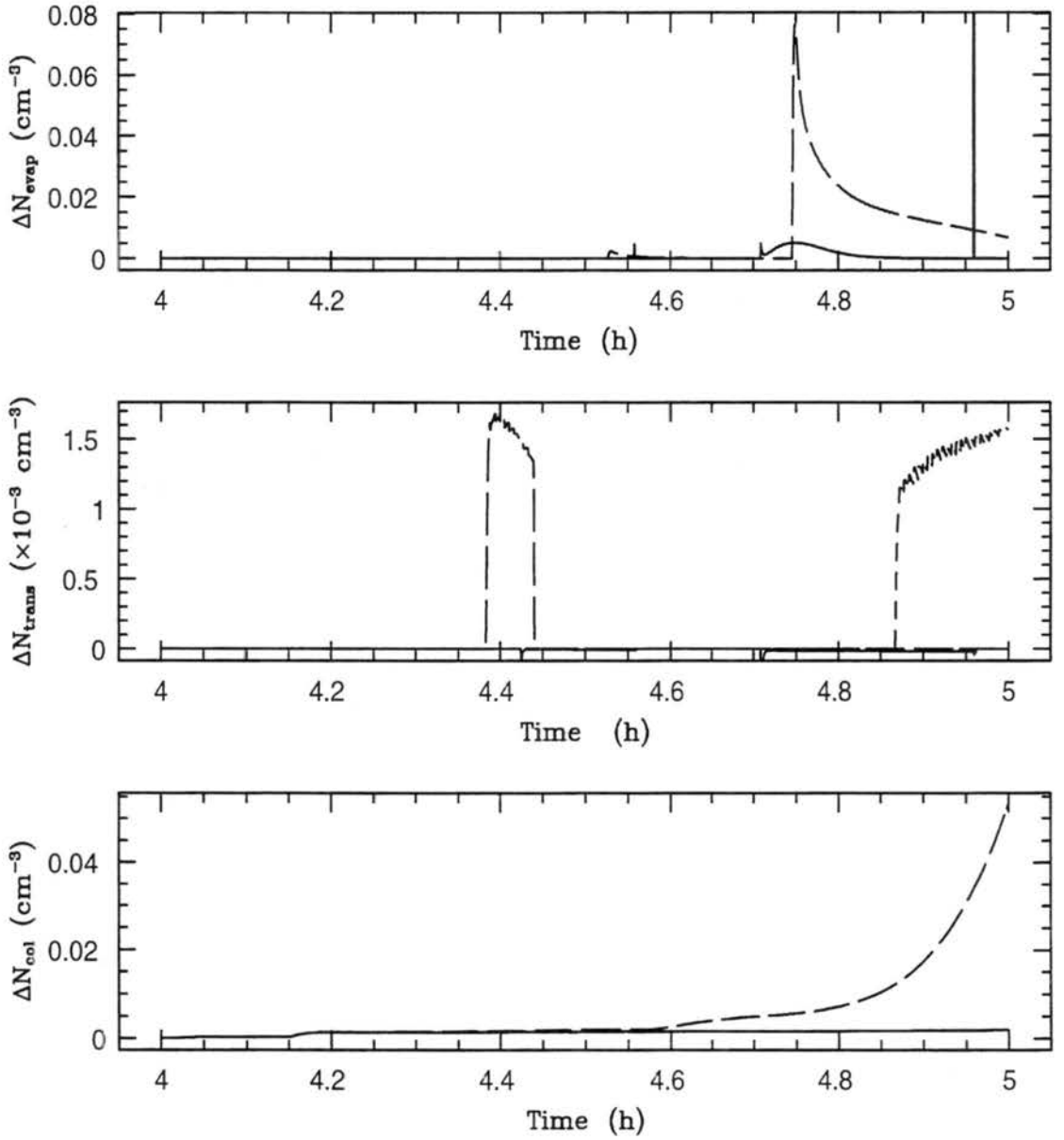

Figure 6.7: Time-series of ΔN over a time-step for various processes of the control run (TAP). Results include the loss in number concentration due to complete evaporation (ΔN_{evap}) and collection (ΔN_{col}) and the number of drops transferred by vapor growth from $r < 20$ to $r > 20$ μm by vapor growth (ΔN_{trans}). The solid line and dashed line are for runs without (TNR) and with (TAP) radiation, respectively.

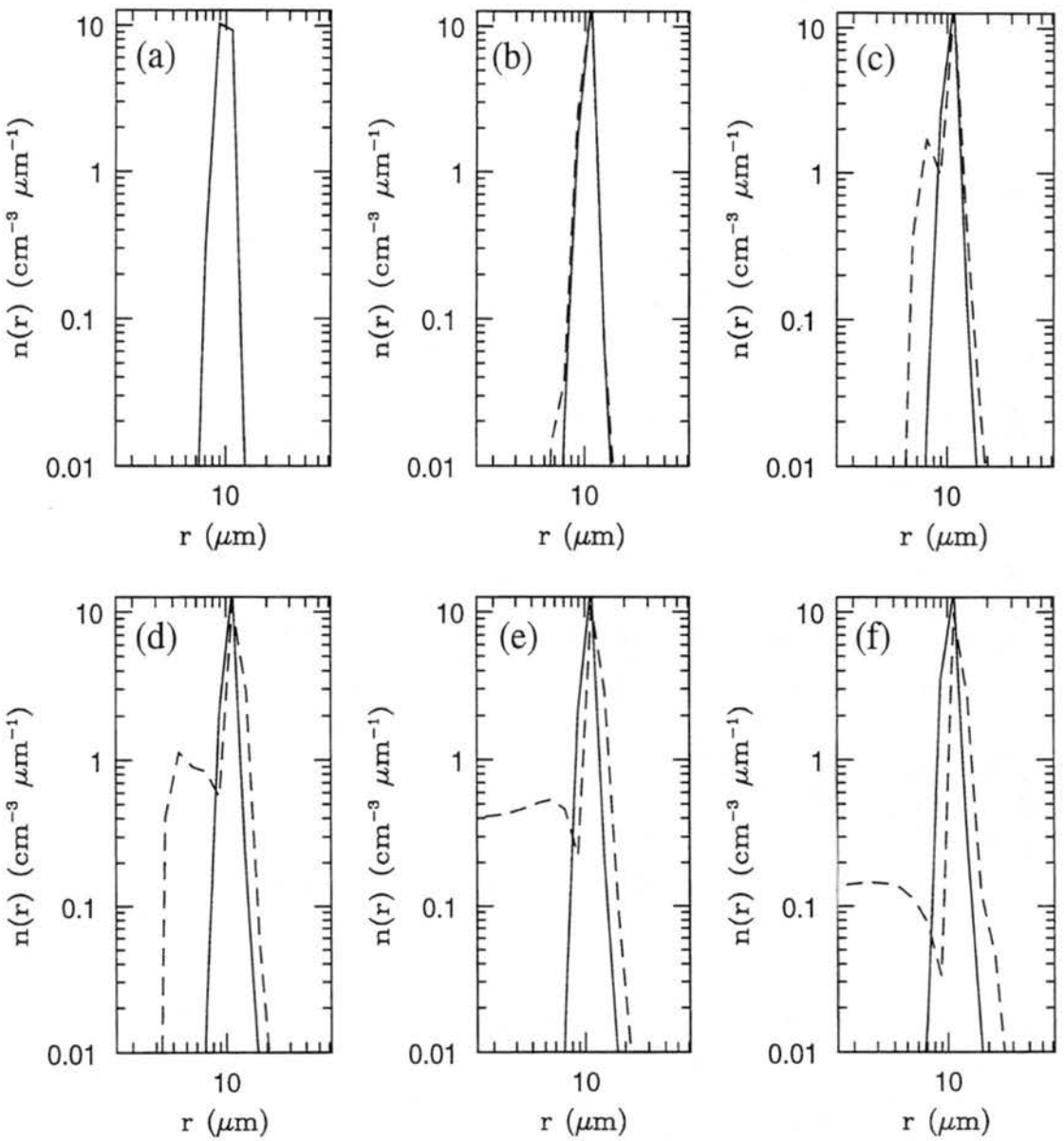

Figure 6.8: Plots of $n(D)$ for selected times during the control run (TAP). Panel (a) is for 4.1 hours, (b) is for 4.2 hours, (c) is for 4.4 hours, (d) is for 4.6 hours, (e) is for 4.8 hours and (f) is for 5.0 hours. The dashed line and solid line are for runs with (TAP) and without (TNR) radiation, respectively.

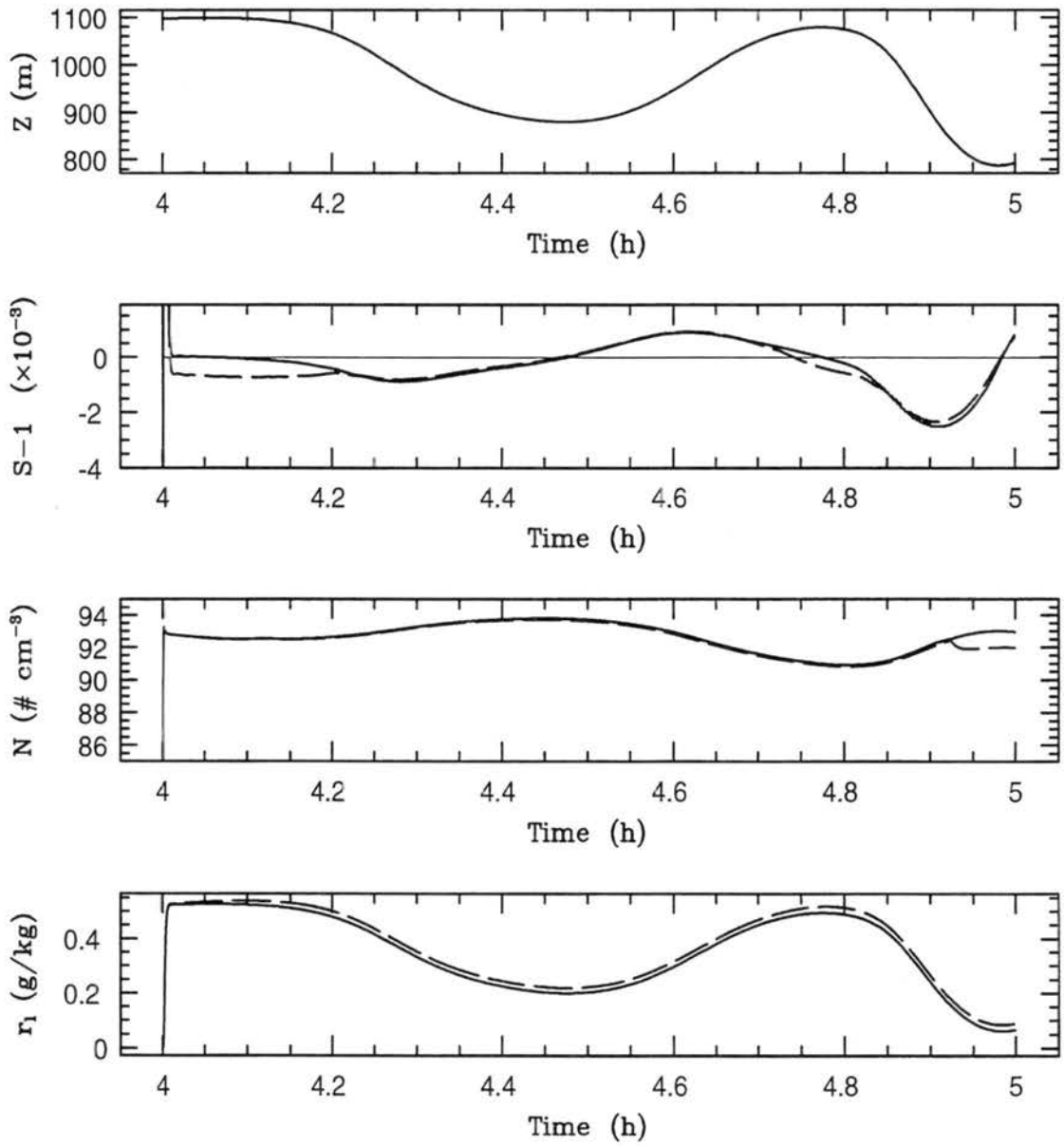

Figure 6.9: Time-series of the microphysical results for the control run (CAP). The vertical location, Z, in m, supersaturation (S), concentration of drops (N) and water mixing ratio (r_l) are shown for the case without radiation (CNR, solid line) and with radiation (CAP, dashed line).

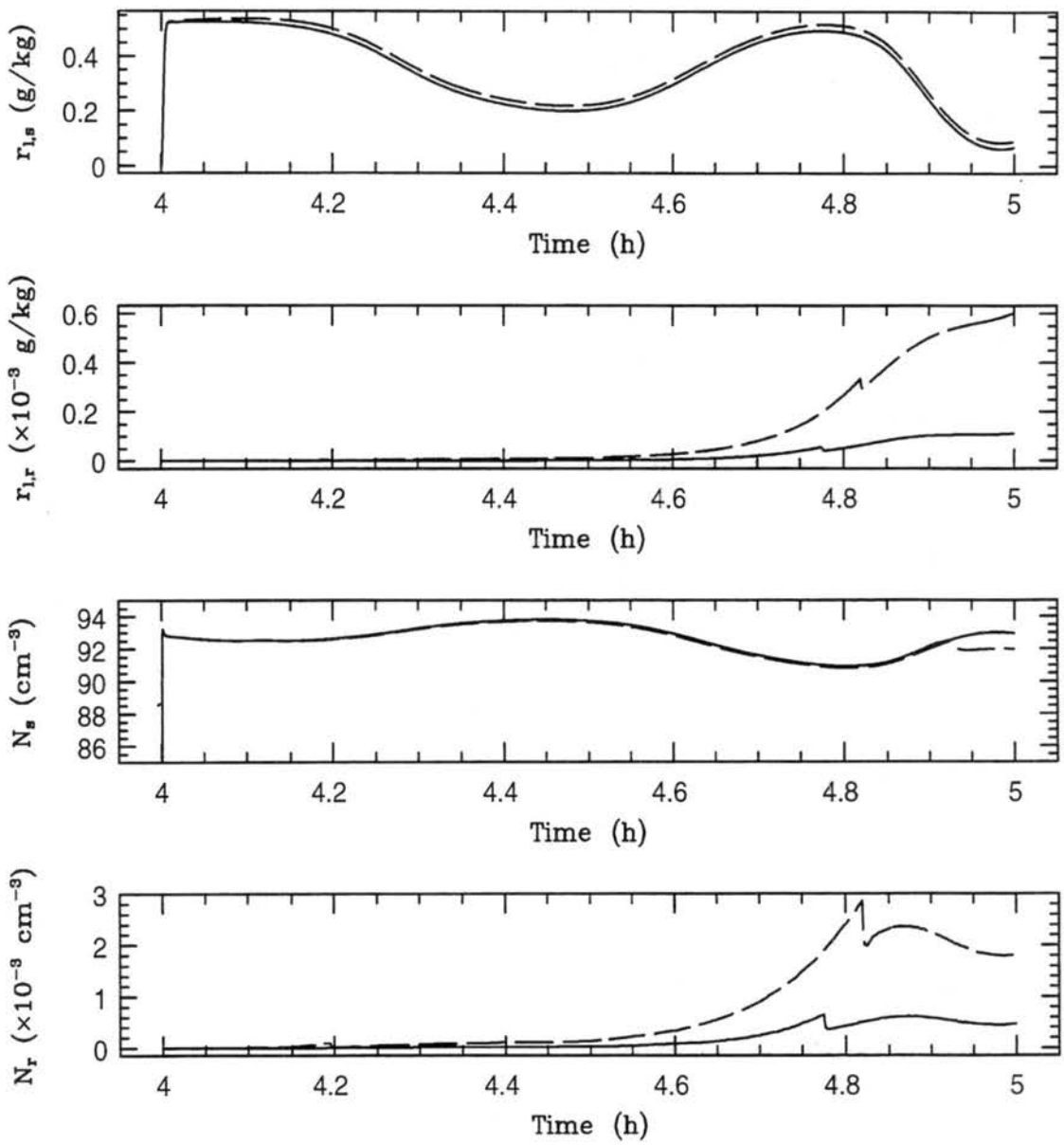

Figure 6.10: Time-series of the results for drizzle and cloud droplet number concentration and mixing ratio for control run (CAP). Results for $r \geq 25\ \mu m$ drops ($r_{l,r}$ and N_r) and for $r < 25\ \mu m$ drops ($r_{l,s}$ and N_s) are shown. The solid line and dashed line are for runs without (CNR) and with (CAP) radiation, respectively.

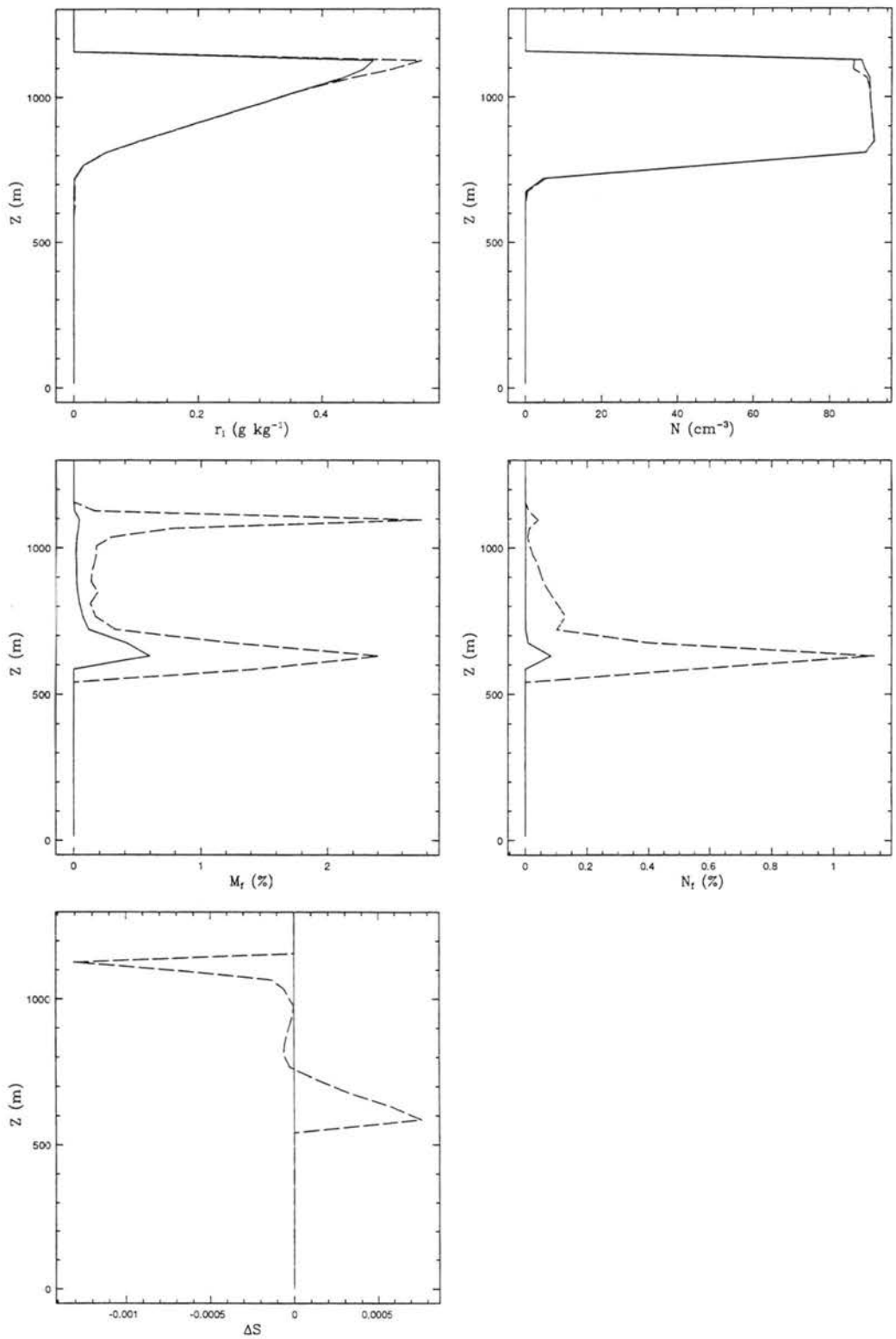

Figure 6.11: Ensemble results for AP. Profiles are shown of liquid water mixing-ratio (r_l), drop concentration (N), drizzle drop mass percentage (M_f), drizzle drop concentration percentage (M_f) and water saturation difference $\Delta S = S_{NR} - S_{AP}$ for the no-radiation (NR, solid line) and radiation (AP, dashed line) simulations.

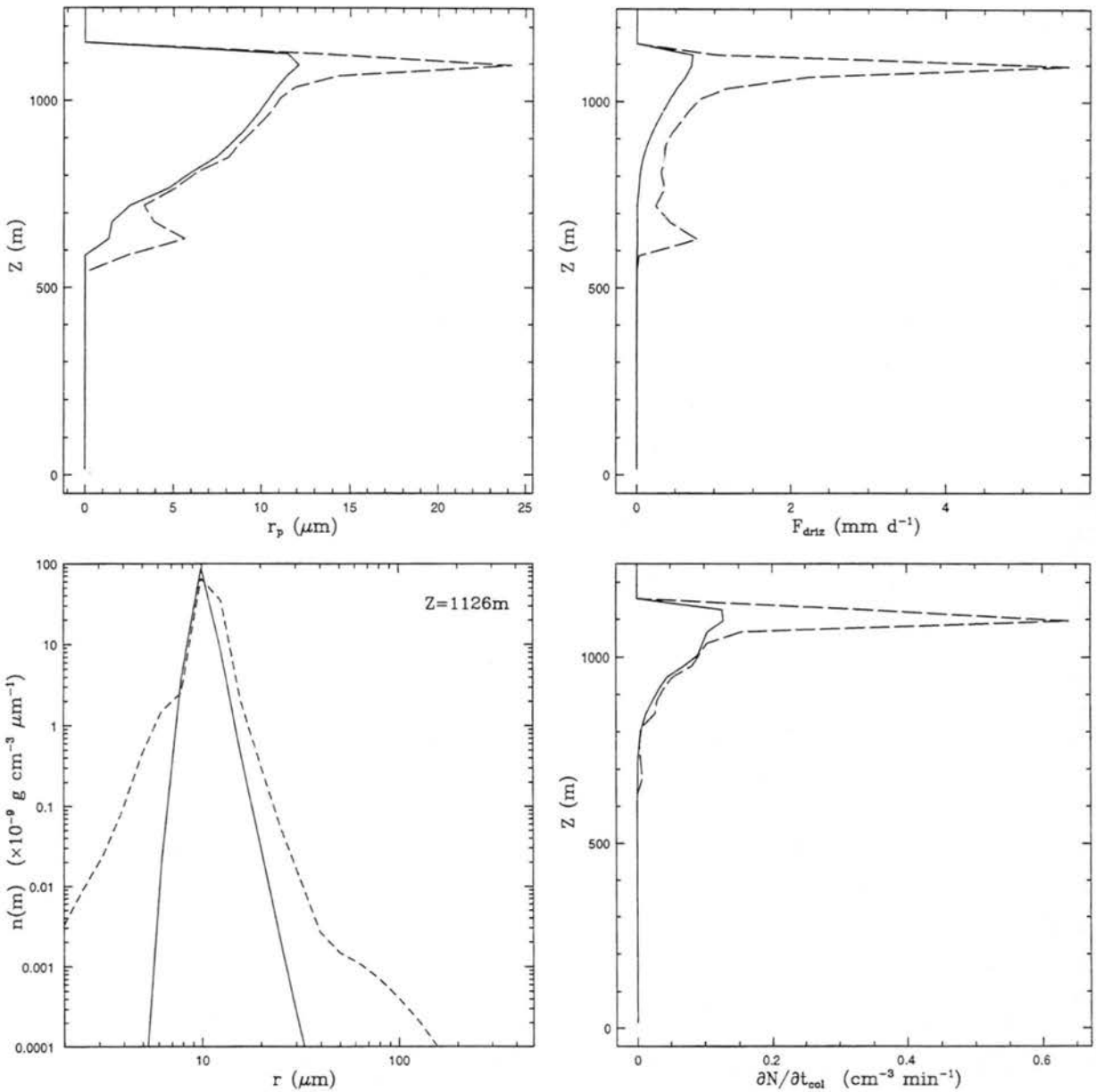

Figure 6.12: Ensemble results for AP. Profiles are shown of predominate radius (r_p), drizzle flux (F_{driz}), cloud top drop distribution ($n(m)$) and collection rate ($\partial N/\partial t_{col}$) and for the no-radiation (NR, solid line) and radiation (AP, dashed line) simulations.

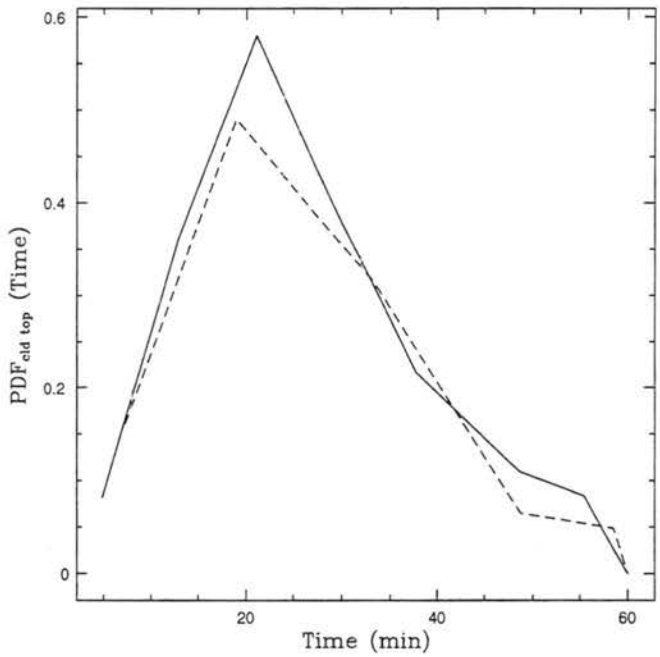

Figure 6.13: PDF of cumulative time spent at cloud top for 100 cm^{-3} (solid line) and 500 cm^{-3} (dashed line) simulations.

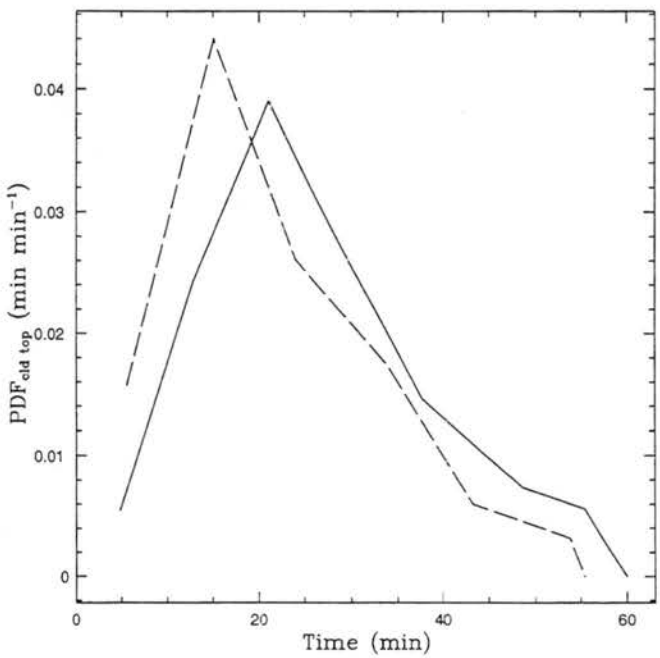

Figure 6.14: PDF of cumulative time spent at cloud top for 100 cm^{-3} (solid line) and of continuous time spent at cloud top for 100 cm^{-3} (dashed line).

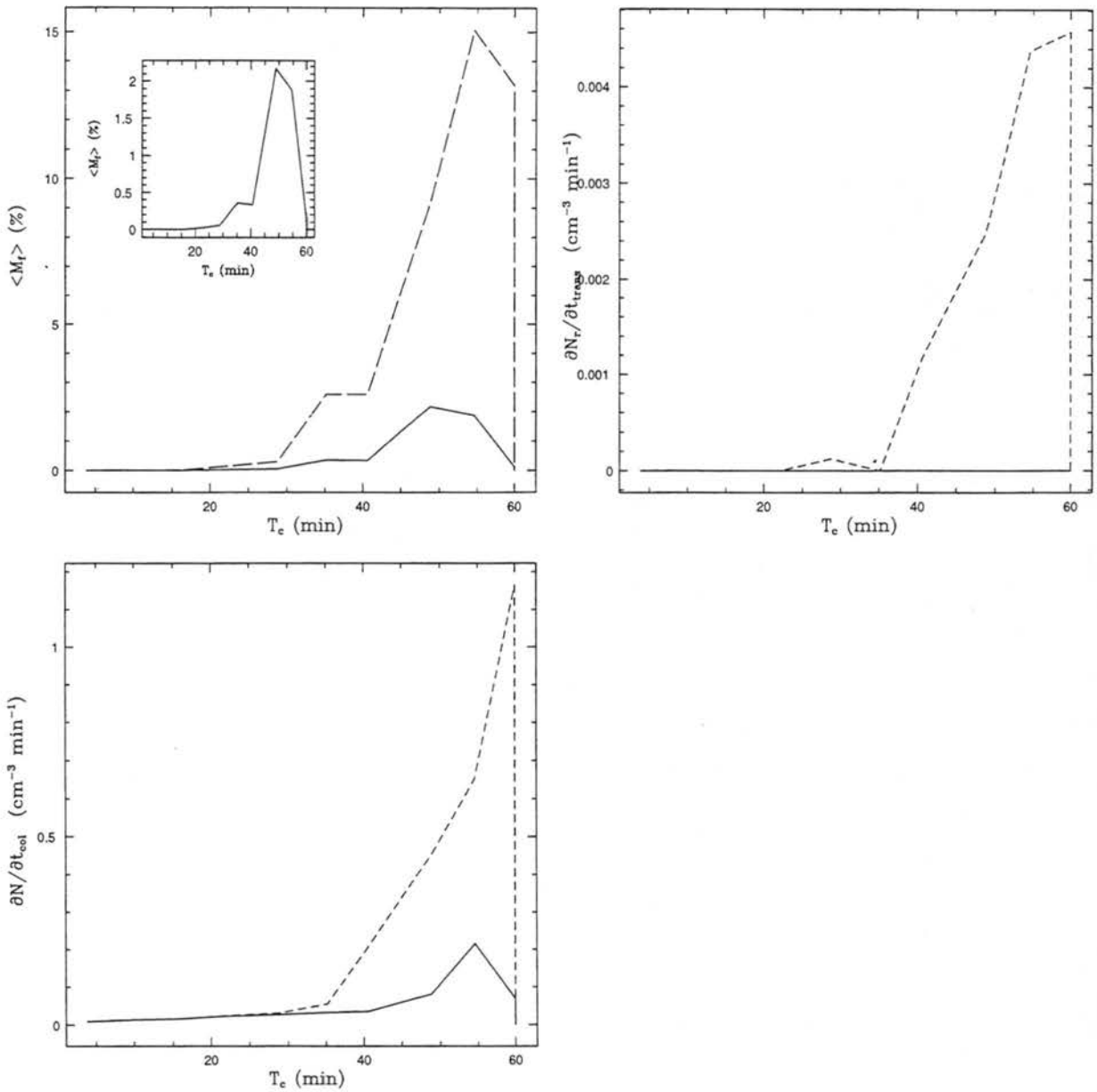

Figure 6.15: Ensemble results for AP. T_c is the cumulative cloud top residence time. Profiles of drizzle drop mass percentage (M_f), transfer rate ($\partial N_r/\partial t_{trans}$), and collection rate ($\partial N/\partial t_{col}$) are shown for the no-radiation (NR, solid line) and radiation (AP, dashed line) simulations. The inset in M_f is for NR.

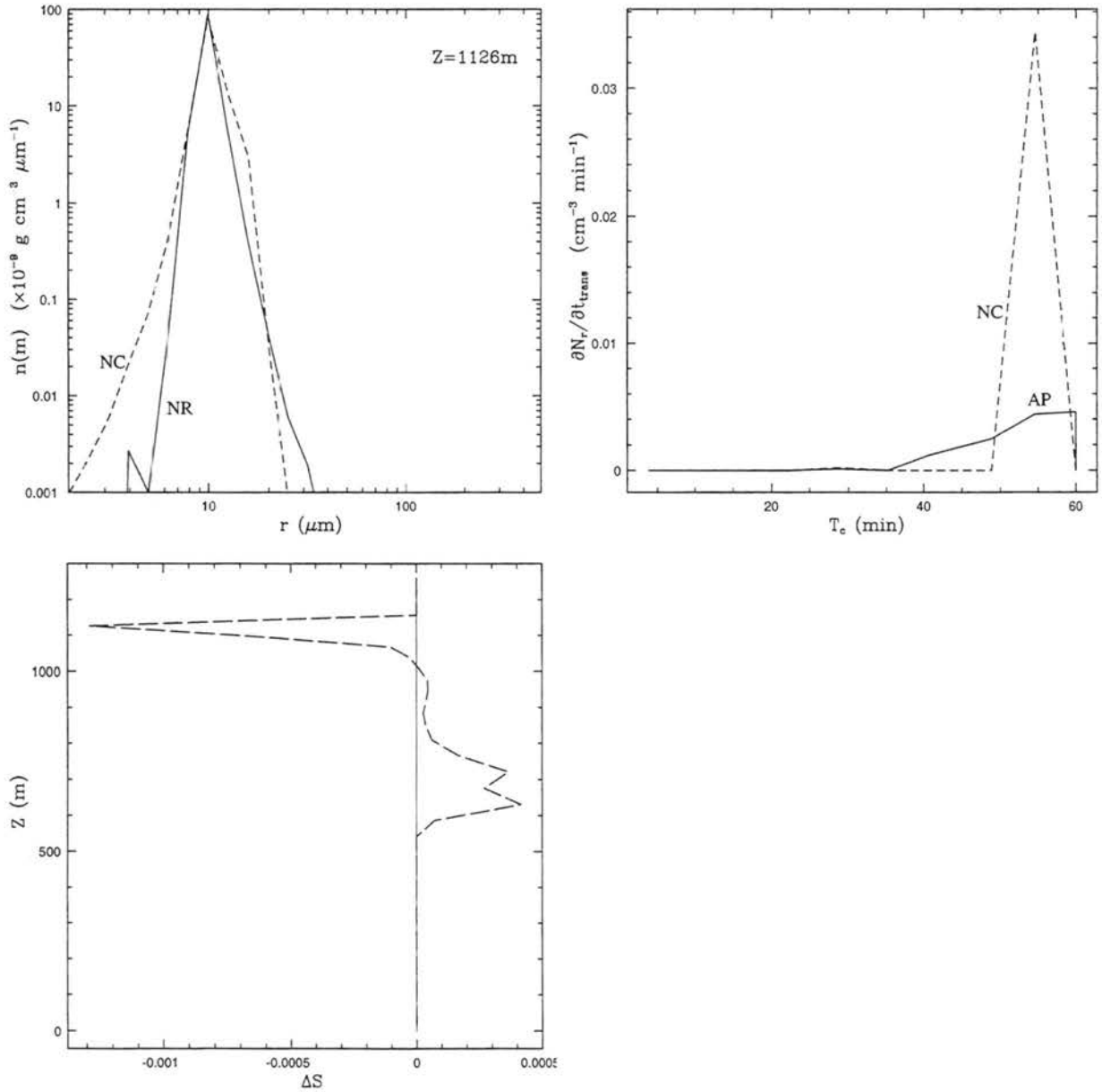

Figure 6.16: Ensemble results for NC, T_c is the cumulative cloud top residence time. Profiles of drop distribution function($n(m)$), transfer rate ($\partial N_r/\partial t_{trans}$) and water saturation difference ($\Delta S = S_{NR} - S_{NC}$) are shown. Identifying acronyms are contained within the panels.

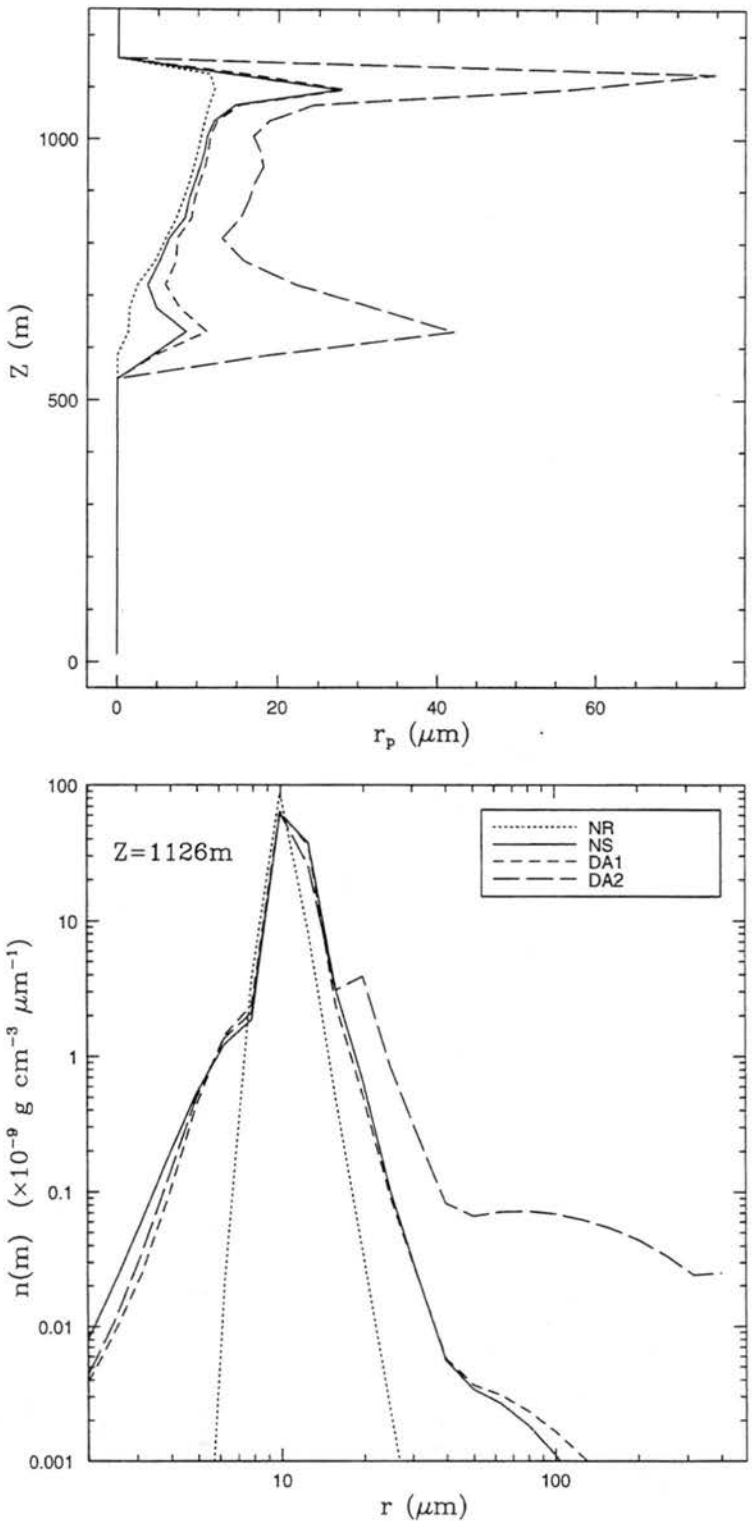

Figure 6.17: Ensemble results for NS and DA. Profiles of predominate radius (r_p) and drop distribution ($n(m)$) are shown for NR (dotted line), NS (solid line), DA1 (short dashed line) and DA2 (long dashed line).

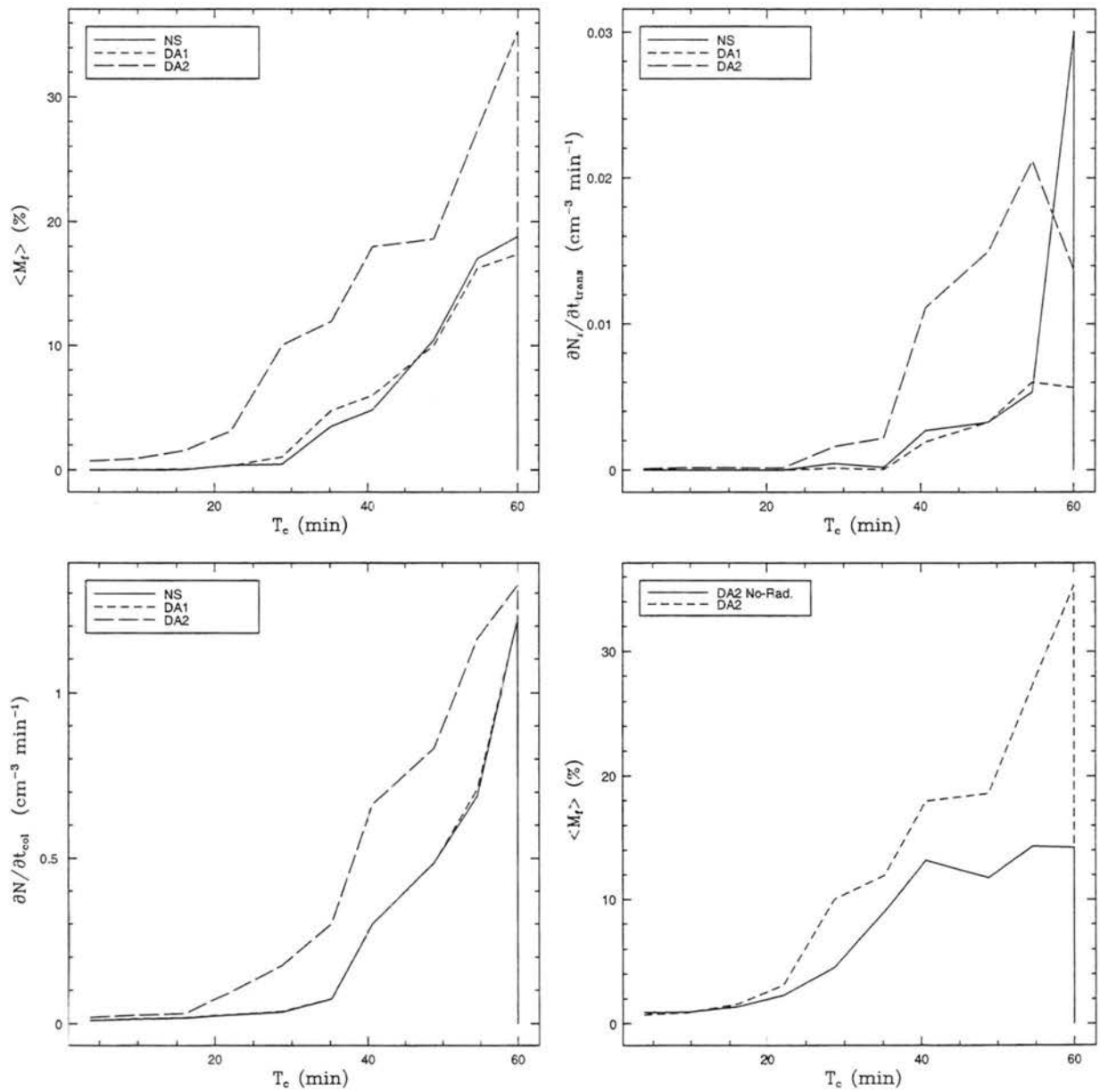

Figure 6.18: Ensemble results for NS and DA, T_c is the cumulative cloud top residence time. Profiles of drizzle mass percentage (M_f), transfer rate ($\partial N_r/\partial t_{trans}$) and collection rate ($\partial N/\partial t_{col}$) are shown for NS (solid line), DA1 (short dashed line) and DA2 (long dashed line). For comparison, M_f is shown for DA2 with and without the radiative term (DA2 and DA2 No-Rad.).

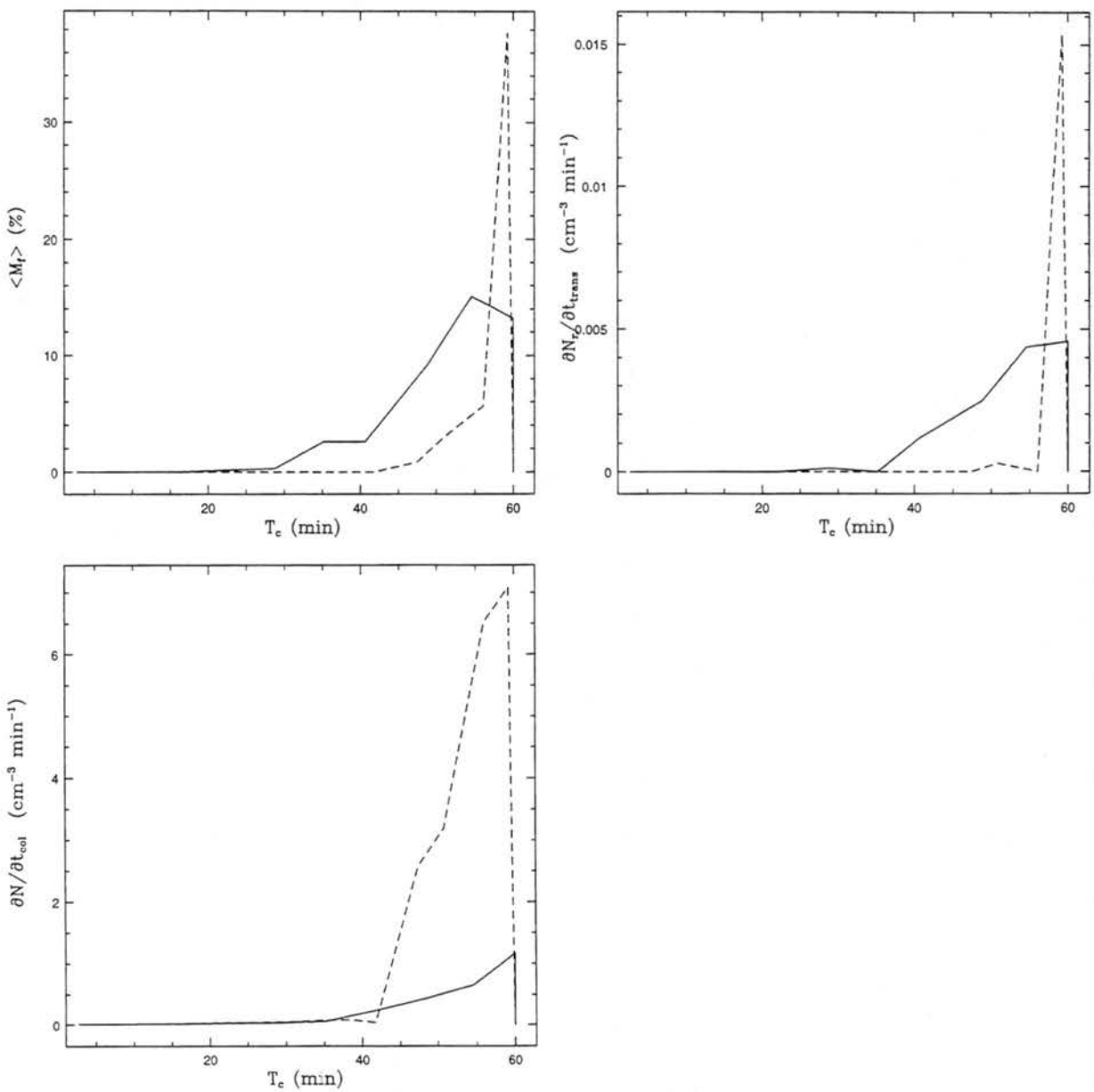

Figure 6.19: Ensemble results for 500AP. T_c is the cumulative cloud top residence time. Profiles of drizzle mass percentage (M_f), transfer rate ($\partial N_r/\partial t_{trans}$) and collection rate ($\partial N/\partial t_{col}$) are shown for AP (solid line) and 500AP (dashed line).

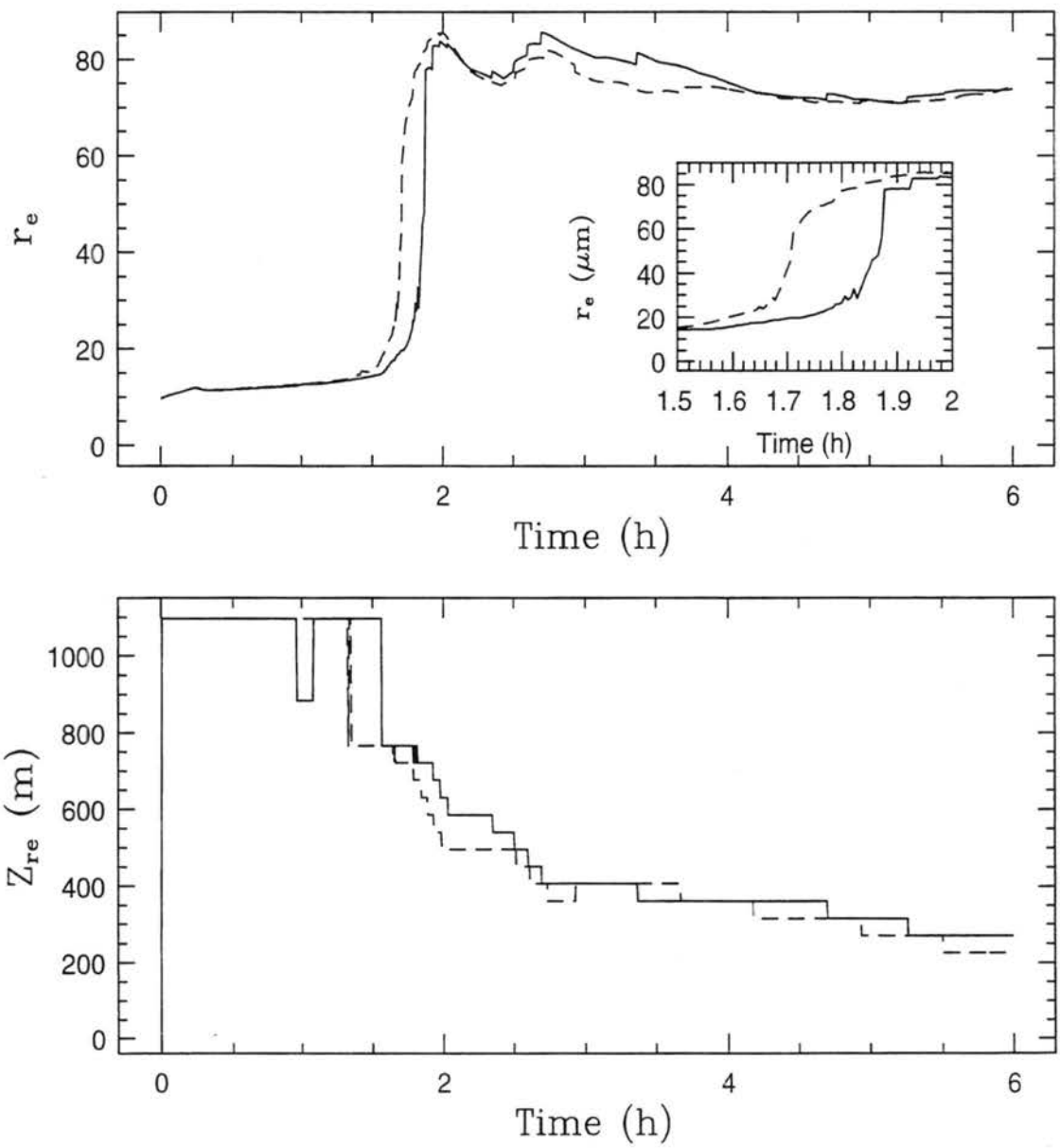

Figure 6.20: Time-series of maximum effective radius (r_e) and its associated model height, Z_{re} for 100R (dashed line) and 100NR (solid line).

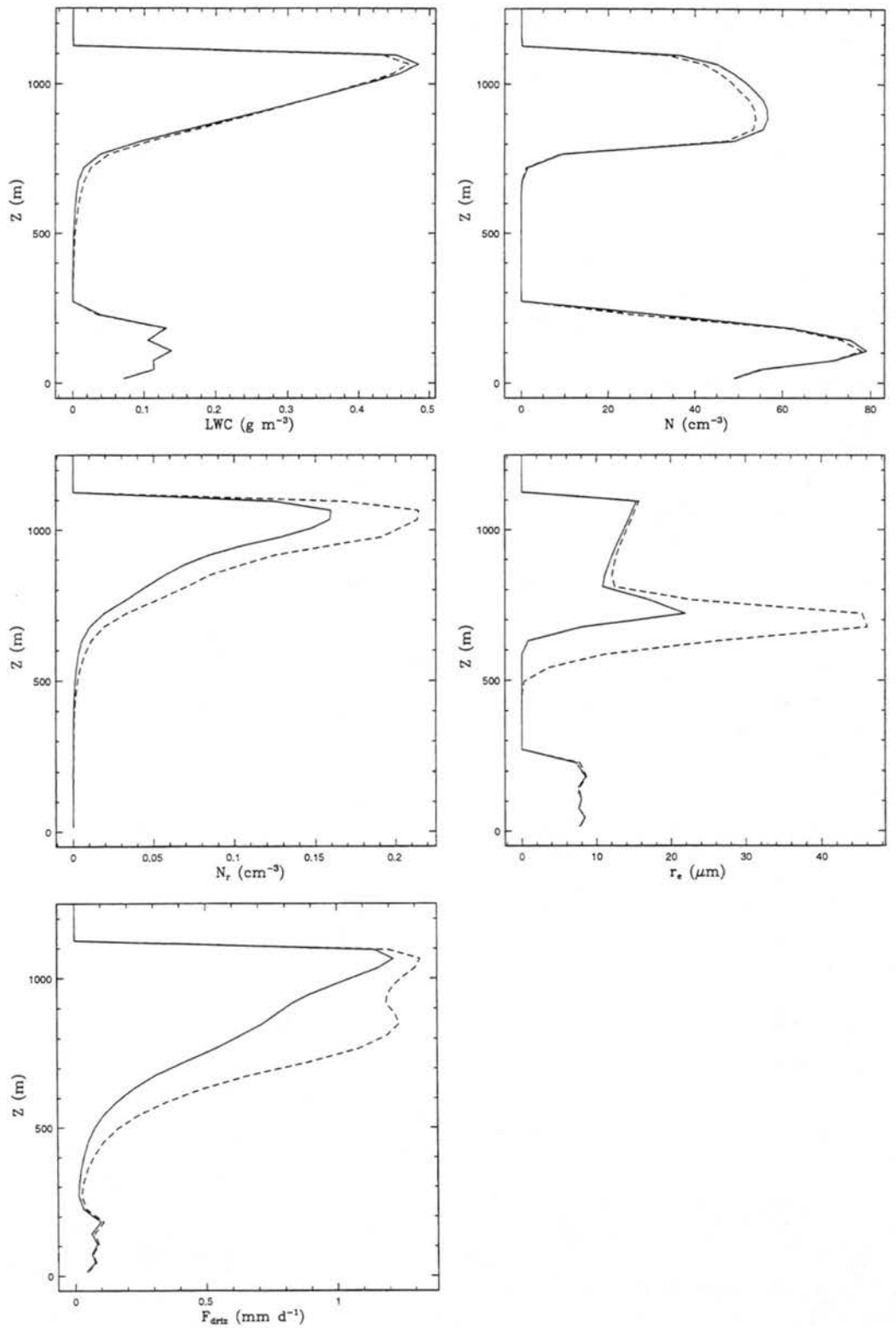

Figure 6.21: CRM profiles at 2 hours of LWC, concentration (N), drizzle drop concentration (N_r), effective radius (r_e), and drizzle flux (F_{driz}) for 100NR (solid line) and 100R (dashed line).

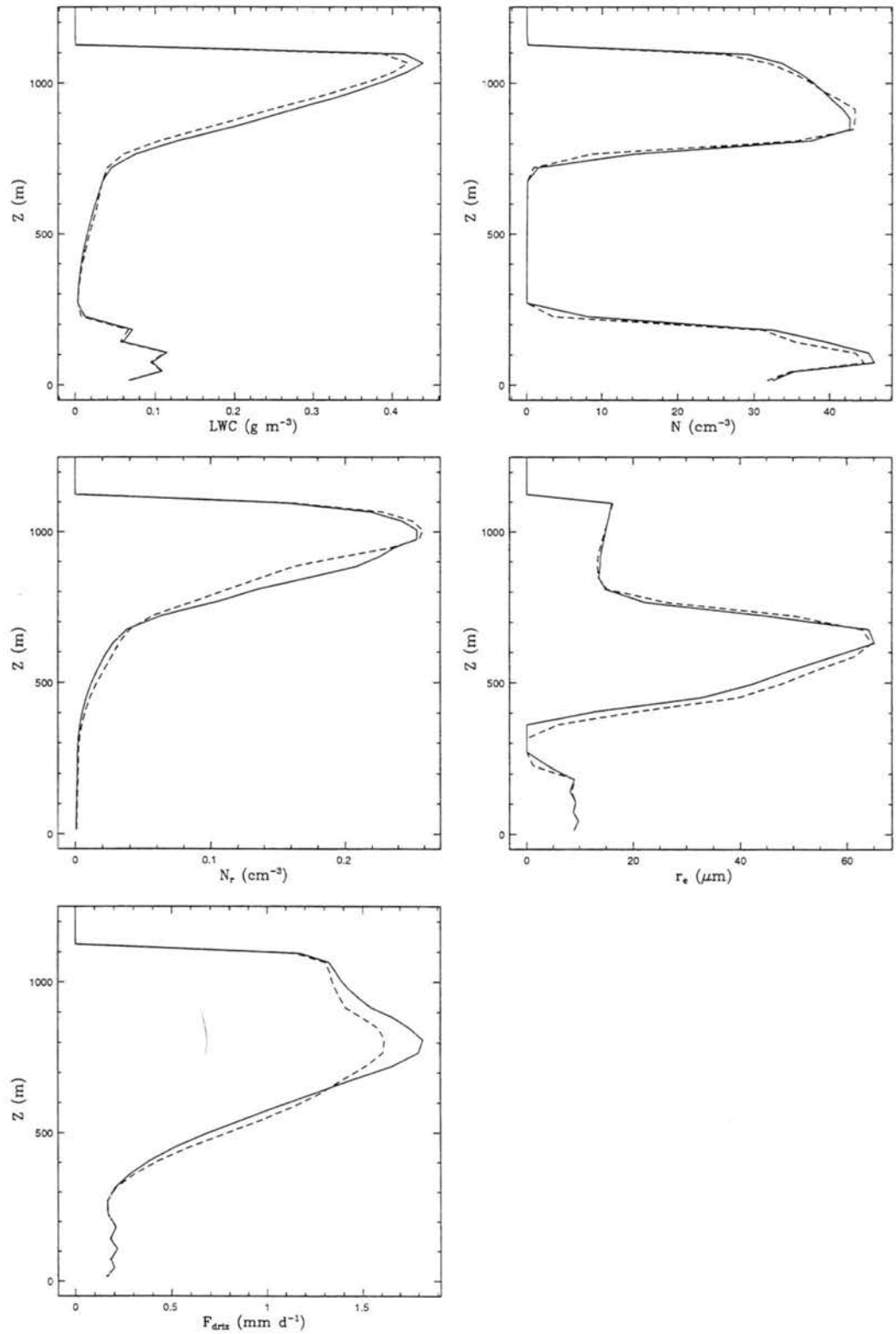

Figure 6.22: CRM profiles at 3 hours of LWC, concentration (N), drizzle drop concentration (N_r), effective radius (r_e), and drizzle flux (F_{driz}) for 100NR (solid line) and 100R (dashed line).

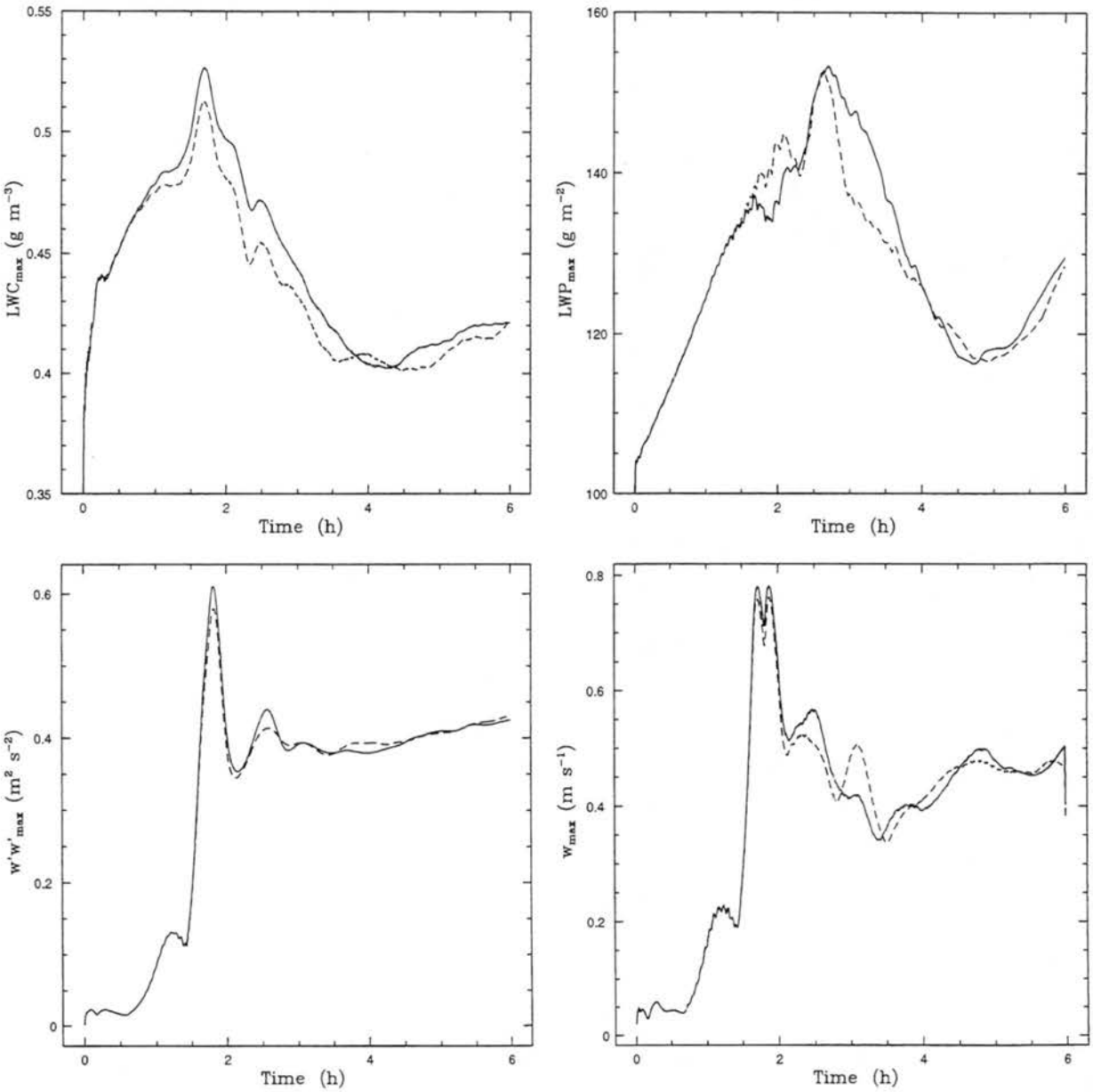

Figure 6.23: CRM time-series of maximum LWC, LWP, $< w'w' >$ and updraft speed (w) for 100NR (solid line) and 100R (dashed line).

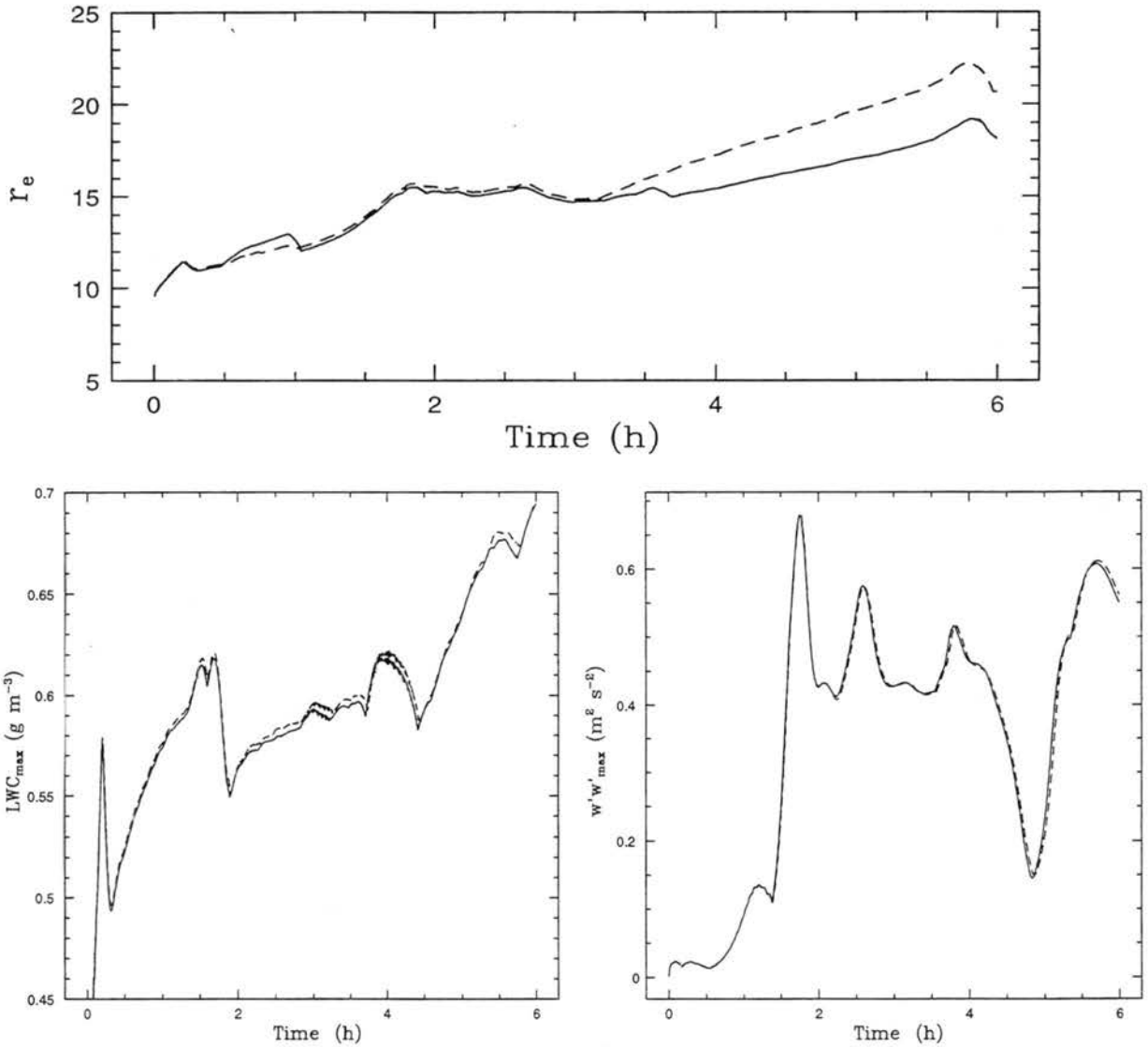

Figure 6.24: CRM time-series of maximum r_e , LWC, and $< w'w' >$ for 100NRNC (solid line) and 100RNC (dashed line).

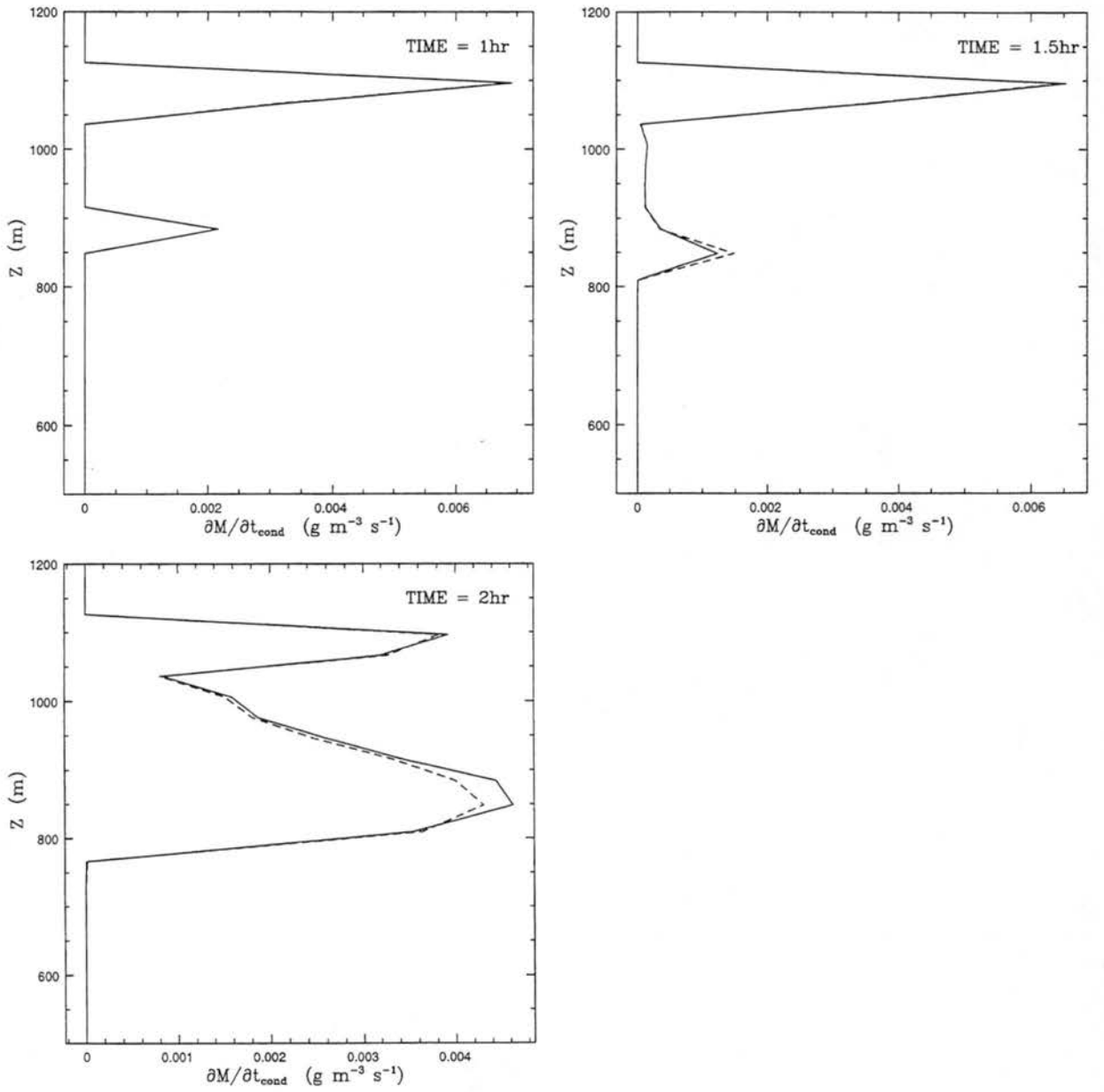

Figure 6.25: CRM condensation rates for 1 hour, 1.5 hours and 2 hours into the the the simulation. The solid line denotes the no-radiative feedback simulation while the dashed line denots the simulation with radiative feedback.

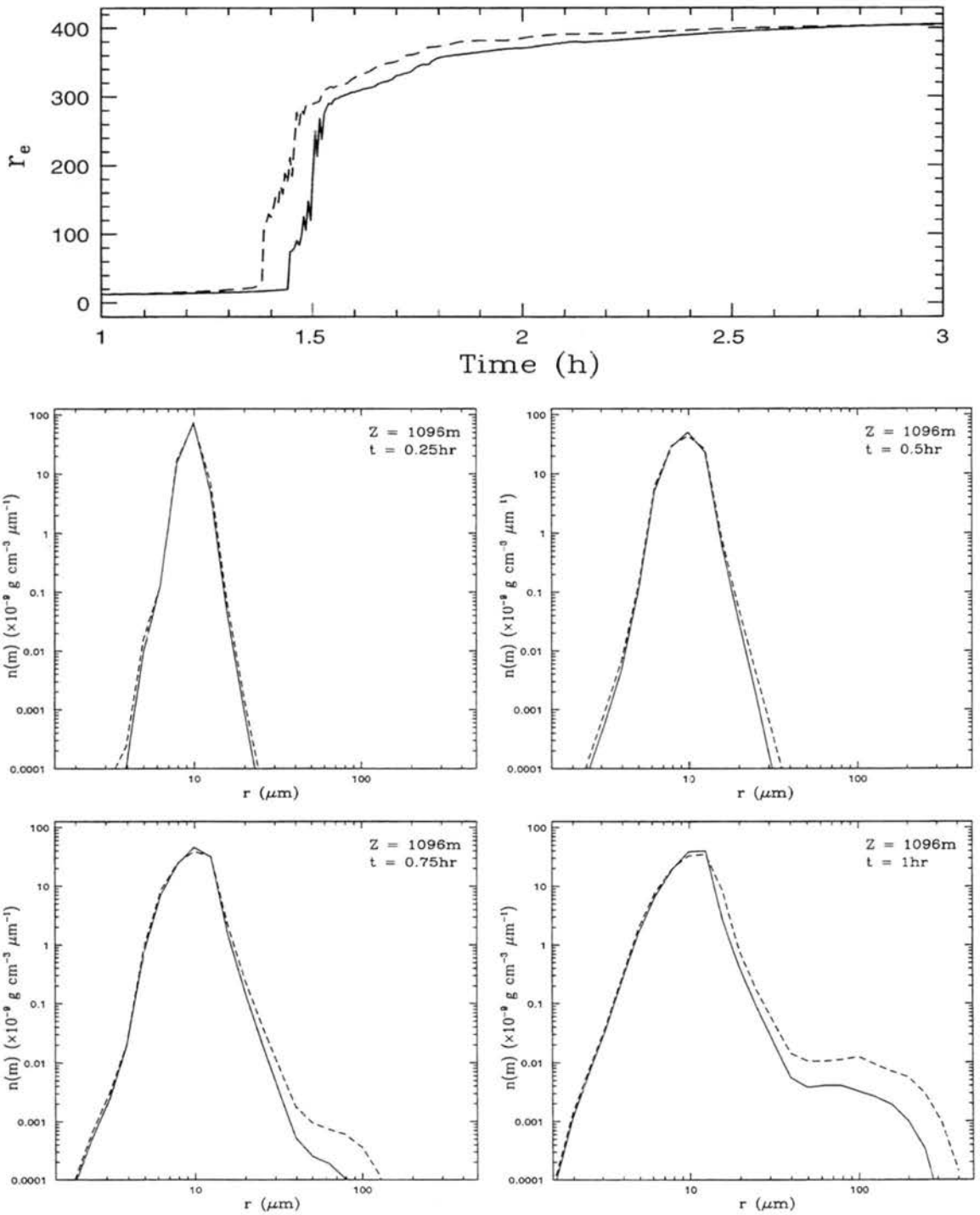

Figure 6.26: CRM no precipitation results. Time-series of maximum r_e and cloud-top mass distribution functions at various times are shown. Simulation without radiative effects is denoted by the solid line while the simulation with radiative effects is denoted with the dashed line.

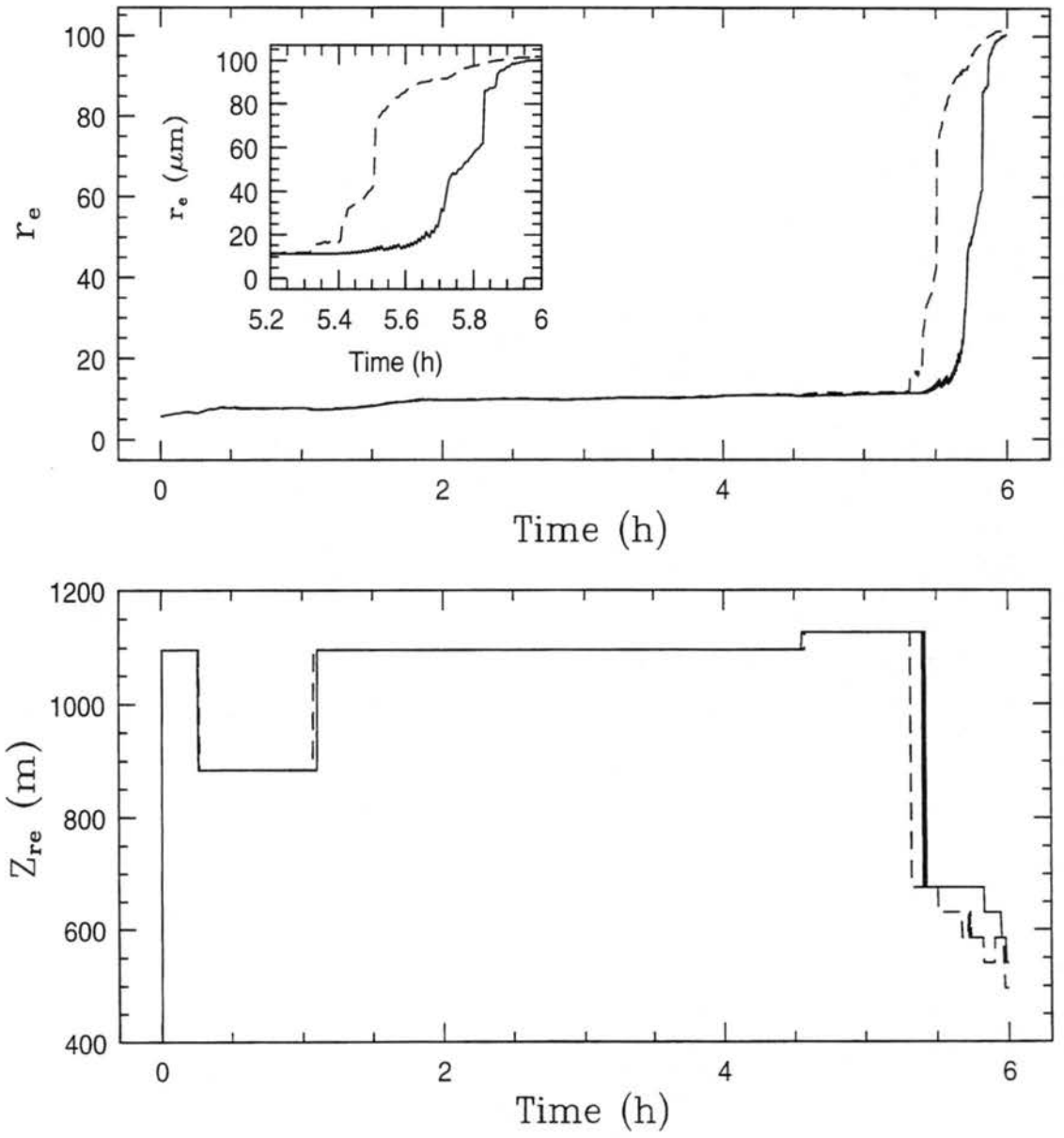

Figure 6.27: Time-series of maximum effective radius (r_e) and its associated model height, Z_{re} for 500R (dashed line) and 500NR (solid line).

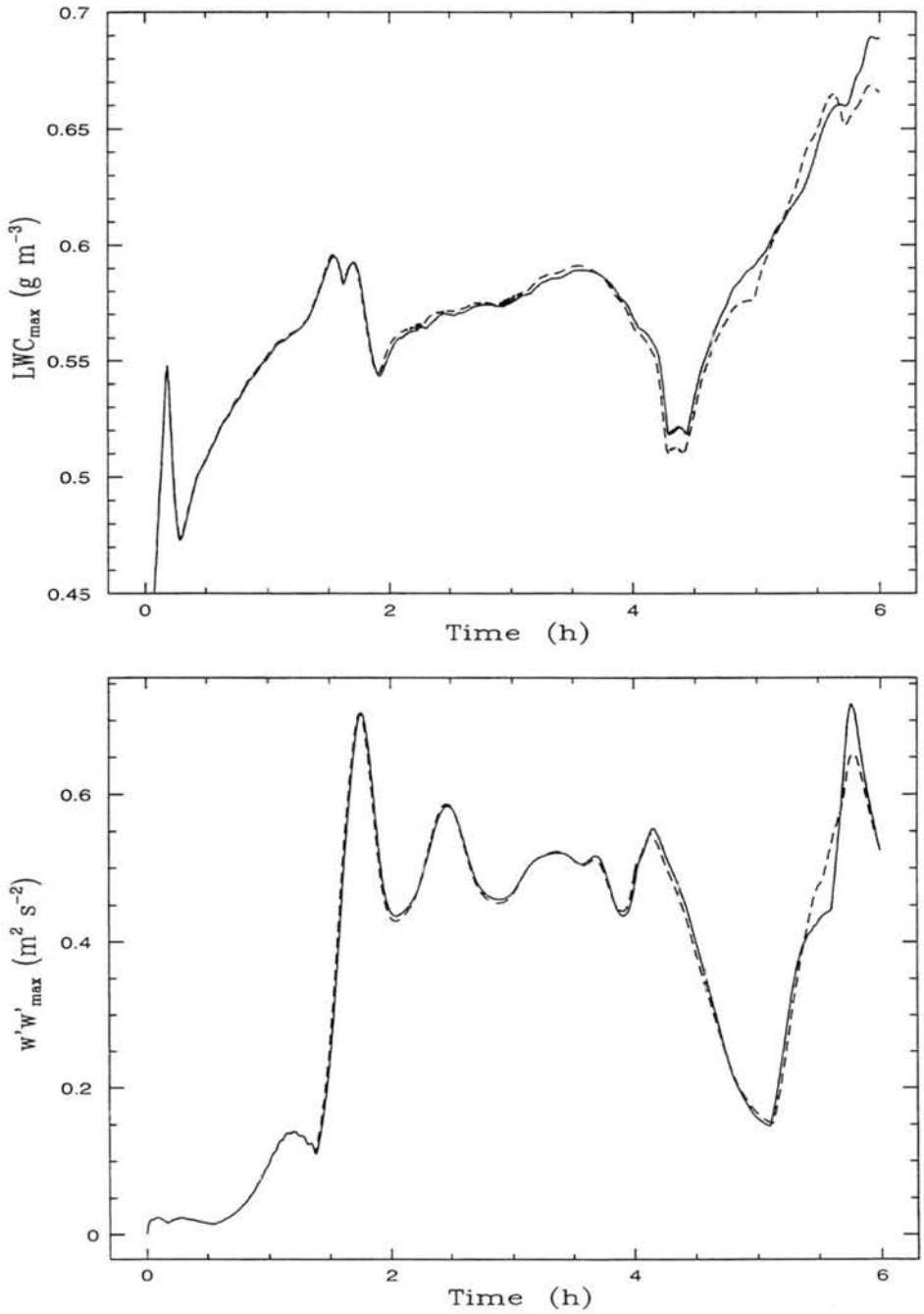

Figure 6.28: CRM time-series of maximum LWC and $< w'w' >$ for 500NR (solid line) and 500R (dashed line).

Chapter 7

TRANSITION-SEASON SIMULATIONS OF ARCTIC STRATUS

In this Chapter we explore the nature of the transition from a liquid dominated ASC to a mixed-phase ASC that may exist during the fall transition period. Specifically, we explore the microphysical conditions necessary to produce self-maintaining mixed-phase systems and collapsing boundary layers during a simulated transition from predominately liquid to mixed-phase ASC. This is accomplished by consistently cooling the sounding used to produce the liquid summertime cloud of Chapter 5. Mixed-phase clouds are produced that either persist for the entire 8 hour simulation period or completely collapse causing all circulations within the boundary layer to cease. Examinations of the dependence of boundary layer stability to the ice phase is examined by conducting sensitivity experiments in which ice nuclei (IN) concentrations are altered, model processes are removed, and habit of the ice crystals is changed.

7.1 Initiation of the transition season clouds

Since cloud top temperatures for the June 28, 1980 case hovered just a few degrees above zero, we explore the effects of the ice process by cooling the sounding used in the summer season ASC simulations (Chapter 5). A natural transition is obtained by reducing θ-values in 5 C increments while the relative humidity of the air is kept constant so that similar relative moisture contents are achieved. Cloud systems are produced for two reductions in θ of the representative sounding; the first is cooled by $5C$ while the second is cooled by $10C$. Figure 7.1 shows the profiles of θ and θ_v used as initial input in the model. The initial horizontal wind profiles are, as shown in Fig. 7.1, the same as that used as input for the summertime simulation. Profiles of θ show the same features as those measured by Pinto (1997) during the 1994 BASE experiment; a deep well mixed layer (constant θ) with

strongly stable layers both below and above the mixed layer. Pinto's observations show water vapor mixing-ratios that increase with height above cloud top, which is a characteristic of the sounding used in these simulations. As in the cases presented here, Pinto's (1997) observed wind shear is strong within $300m$ from the ground with little shear within the mixed layer. Thus, the systems simulated here appear to have similar characteristics to at least one observed transition-season cloud layer.

The model is initialized with the above fields and simulations are conducted for a four hour period as in the summertime cases. For these cases, however, we use the bulk microphysics of Walko *et al.* (1994) in order to initialize a cloud composed of both liquid water and ice. Since these simulations are used to spin-up a cloud field, we allow only cloud water and pristine ice crystals to form during the simulation. The upper bound on the pristine ice sizes (normally set at 125 μm, see Harrington *et al.* , 1994) is removed so that the distribution may evolve freely. The shape of the distribution function is set to $\nu = 6$ for the water drops and $\nu = 2$ for the pristine ice crystals which is qualitatively similar to distributions presented by Pinto (1997). In all simulations, only the effects of infrared radiation are considered as solar zenith angles are quite small during the Arctic autumn.

7.1.1 Results for the initialized clouds

Profiles of the relevant liquid water variables are shown in Fig. 7.2 after four hours of the initial spin-up simulation. All profiles are averaged over the horizontal domain and temporally in 15 minute blocks. After four hours, the 5C cooled simulation produces a cloud with greater LWC spread over a greater depth than the 10C cooled case. Droplet distributions are more narrow in the 10C case, illustrated by the smaller r_e values, as the bulk microphysical scheme utilizes a constant cloud droplet number concentration. The ice microphysical profiles shown in Fig. 7.2 illustrate that the ice cloud produced in the 10C cooled simulation contains more ice and has a greater vertical extent than that produced in the 5C cooled case. Note that the maximum in ice mass exists much below that of the maximum in LWC in the 10C cooled case while it is not true in the 5C cooled case. The positioning of the maximum in ice mass in each case is due to the

size of the ice hydrometeors; in 10C (as is shown by the profiles of the effective radius for ice, $r_{e,i}$) the hydrometeors have larger sizes and, therefore, attain larger settling velocities than the 5C cooled case. The cloud structures simulated here have similar characteristics to those presented in Pinto (1997) with small ice persisting within the liquid layer and large ice maxima near cloud base. Note that more ice hydrometeors are nucleated in the 10C cooled case which produces a prominence in ice concentration (N_i) at about 300 m showing the effects of sedimentation. The fact that more ice is nucleated and more ice mass is produced in the $10C$ cooled simulation is due to a combination of the cooler temperatures and the way that ice and water grow and evaporate as a function of these temperatures. Figure 7.3 shows the predicted IN activated in the model for the nucleation of ice crystals (by freezing and contact methods) as discussed by Meyers *et al.* (1992). This plot shows that IN concentrations are a strong function of ice supersaturations. Note that even though this formula is derived from measurements taken at mid-latitudes, it does produce IN concentrations in the range of some measurements quoted in Chapter 1. At the colder temperatures, higher ice supersaturations are produced (10% in the 10C cooled case compared to 6.5% in the 5C cooled case). The larger ice supersaturations in the 10C cooled case allows for larger deposition[1] rates and, therefore, the production of larger ice masses and sizes. It is also true, however, that in the lower parts of the $10C$ cooled simulated cloud (where ice masses are the greatest), LWC is being depleted through the Bergeron-Findeisen process. That this effect is more pronounced in the 10C cooled case can be seen by examining Fig. 7.3 in which the difference between the equilibrium[2] vapor pressure over water (e_s) and ice (e_i) is plotted. The point where the difference between e_s and e_i is maximized is approximately where the growth of ice at the expense of liquid water is maximized. Since cloud top temperatures in the 10C cooled case are about -13°C

---

[1]Here, we adopt the standard terminology in the vernacular proposed by McDonald (1958). The terms *condensation* and *evaporation* are, as is standard, reserved for vapor-liquid growth mechanism while *deposition* and *sublimation* are used for the analogous vapor-ice growth mechanism.

[2]Here, we adopt the terminology of Bohren (1987) in which the standard phrase, "saturation vapor pressure," is replaced by, "equilibrium vapor pressure." Indeed, as discussed by Bohren (1987), the word equilibrium better describes the physics of the vapor pressure derivation.

while the 5C cooled case are about -6 $°C$, ice will grow more rapidly at the expense of liquid in the 10C cooled case. This fact assists the growth of the ice crystals in the 10C cooled case and is the reason for the reduction in LWC and cloud depth in this case.

Differences between the LWCs of the cases are not extreme as ice contents have not become large by the fourth hour of the simulation. The bulk microphysical simulations were intentionally stopped at this 4 hour point because LWCs are somewhat similar, thus, comparisons between the bin microphysical simulations initiated from this point are not strongly dependent upon the initial LWC. Also, about 1.5 hours after the 4 hour point the two simulations rapidly diverge with the $10C$ cooled simulation undergoing collapse while the $5C$ simulation continues unabated. Thus, the 4 hour termination point for the bulk simulations is chosen with forsight to the bin simulations that are to follow.

Even though the 10C cooled case has smaller LWC than the 5C cooled case, the total surface area is actually greater and the cloud top LWC gradient is stronger which leads to a larger IR cooling rate maximum in the 10C cooled case. The 5C cooled case, which has larger LWC contents and weaker gradients of cloud top LWC produces a smaller IR cooling rate maximum. However, in the 5C cooled case much more of the IR cooling lies within the mixed-layer, indicating that larger buoyancy production should be occurring in this case. That this is the case may be ascertained from Fig. 7.5 which shows that the 5C cooled simulation produces stronger eddies (larger $< w'w' >$) that penetrate deeper into the boundary layer.

In the next set of sections we explore the evolution of the cloud systems utilizing the bin microphysical model. For these discussions we adopt the general procedure of analyzing the cases in a hierarchical order; the simulations cooled by 5 C are discussed firsts followed by simulations that utilized the 10 C cooled sounding.

7.2 Control Simulations

After 4 hours of simulation time with the bulk microphysical model, the bin microphysical model of Reisin *et al.* (1995) is utilized. Two control simulations are run for both the 5C and 10C cooled cases (which will be denoted 5CTRL and 10CTRL) in which all

of the physics considered standard within the bin microphysical model is utilized (*i.e.* we have not tuned any parameterizations or turned off any physical processes). In this section we discuss the control simulations for the 5C and 10C cooled cases along with the large differences that occur between the cases. Both simulations use the appropriate four hour initialized clouds (either 5C or 10C) as a common point of departure and are conducted for 4 hour time periods. Experiments which explore the sensitivity of these control simulations to ice microphysical processes are discussed in the next chapter.

7.2.1 The 5 C cooled control simulation

Since the mixed-phase system is colloidally unstable, we expect that the coexistence of liquid water and ice will cause depletions of liquid water amounts over some period of the simulated system. Indeed, in order for these clouds to attain some sort of self-maintaining state, some balance between liquid water and ice must be maintained within the system.

A time-series plot of LWC and IWC[3] over the last four hours of the eight hour simulation period is shown in Fig. 7.6 . During the first 0.5 hours of the period shown, LWC within the cloud layer and the liquid cloud depth decreases while IWC rapidly increases and sediments out of the cloud layer. After this period, LWC begins to slowly increase over the course of the remaining four hours. Ice water is continually produced within the liquid layer which is a constant source of weak ice precipitation from the cloud layer. Even though little data exist for mixed-phase systems, evidence of such mixed-phase system behavior exists. Shown in Fig. 7.7 is lidar imagery taken during March, 1997 at Barrow, Alaska (Grund, personal communication) and shows a tenuous liquid water topped ASC which is producing ice crystals which fall from the liquid layer (as shown by the fall streaks below the liquid layer). This appears qualitatively analogous to the situation shown in Fig. 7.6. The production of ice crystals within an upper level cloud deck with precipitation fall streaks emanating from the cloud layer is quite similar to the situations normally encountered in cirrus uncinus clouds.

---

[3]The ice water content (IWC) is defined as the total ice mass through the integral, $\int m(L)n(L)dL$, where $m(r)$ is the mass of an ice crystal of size L.

Figure 7.8 illustrates the effects of the rapid reduction in LWC over the 4 to 5 hour period of the simulation (time period which is critical to cloud stability in these cases). The LWC is rapidly depleted through the growth of ice crystals. Subsequently, number concentrations of water drops (total concentration, N_t and concentration of drops with radii larger than 25 μm, N_r) are reduced as drops evaporated due to the existence of the ice crystals. At the end of the fifth hour, LWC begins to increase within the lower layers of the cloud, however, total concentrations of drops (N_t) continues to be reduced while the concentration of large drops, N_r, increases. This fact is corroborated by the increase in effective radius (r_e) of the droplets by hour five. The production of larger drops appears to be due to the increases in LWC with time concomitant with the reduced number concentrations. Thus, fewer drops are competing for the available vapor and drop sizes may increase rapidly through condensation and collection processes.

The large losses in LWC during the fifth hour of simulation is due to the coexistence of large ice particles with significant mass which produce large deposition rates. As the ice crystals grow, $r_{e,i}$ of the ice becomes large rapidly (Fig. 7.9) through deposition and collection, causing rapid reductions in ice concentrations (N_i) and rapid sedimentation. The IWC of collected ice (aggregates) is quite small as shown by the profiles of IWC_{agg} over the 4 to 5 hour period. Even though total aggregate mixing ratios are much smaller than those for pristine ice, this does not preclude the importance of collection events. Indeed, aggregates sediment at a rapid rate and, therefore, unlike pristine ice, may not have areas of large IWC convergence. The possible importance of this pathway for ice removal from the cloud layer will be explored in the next chapter. Similarly, the collection of liquid water drops by ice crystals is quite small (IWC_{graup}) as the majority of LWC is associated with small drops that have small collection efficiencies. Thus, the major removal path is through the Bergeron-Findeisen process. The limited observations of mixed-phase clouds have also shown that rimed ice makes up a small fraction of the IWC in ASC (Jayaweera and Ohtake, 1973; Reuter, personal communication). Whether or not significant riming occurred during the cases discussed by Pinto (1997) was not discussed by that author.

The large sedimentation rates of the ice crystals produces a continuous supply of hydrometeors to the subsaturated sub-cloud layer. Sublimation of these ice crystals supplies

the layers below cloud base with significant moisture (see Fig. 7.10) as shown by the large increases in r_v below 600 m over the 4 to 5 hour period. Ice supersaturations (S_i) are maintained near cloud top at around 6% but are reduced below about 850 m; this minimum is consistent with the production of a dip in the r_v profile and relatively constant θ-values in this region with time. Equilibrium vapor pressures are higher and, therefore, S_i values are lower. The increase in θ within this region is due to large deposition rates caused by large amounts of ice near cloud base (Fig. 7.9) while the decrease in the θ values near cloud top are due to radiative cooling that exists within that region. Indeed, as the LWC gradient and cloud drop concentration at cloud top are reduced, the cooling rate maximum decreases while the total cooling rate occurs over a deeper layer (Fig. 7.11). The production and sedimentation of ice crystals from the liquid layer causes the stabilization of the layers below cloud base (as shown by the succession of θ profiles).

The production of $< w'w' >$, which is considered a measure of eddy strength, in stratus clouds is strongly related to increases and decreases in buoyancy (Stull, 1988). As LWC at cloud top and within the cloud layer is reduced, the overall production of buoyancy is decreased over the 4 to 5 hour period (Fig. 7.12). This is due to the reduction in cloud top radiative cooling along with increases in depositional heating rates ($\partial\theta/\partial t_{mic}$) over this period (Fig. 7.11). This causes a decrease in the vigor of the cloud-scale circulations over the first 0.5 hour (as shown in $< w'w' >$). The cloud continues to cool, overall, near cloud top ($d\theta/dt$) as radiative cooling is stronger than microphysical heating. Ice water settles to lower layers (around 500 m) increasing the buoyancy production through large evaporative cooling rates and mass loadings in this region (Fig. 7.11), causing increases in the circulation strengths. This lower level circulation does not last long, however, as ice contents continue to sediment leaving little water content to maintain the circulations (we will see in a later section that this can produce a lower liquid cloud layer). Circulations begin to increase near the top of the liquid cloud at the end of the fifth hour of simulation time as buoyancy production increases because of increasing LWC, radiative cooling and decreases in microphysical heating.

The increase in LWC occurs as more water vapor is added to the liquid layer that has been substantially cooled through radiation over this one hour period (shown as the

decrease in θ in Fig. 7.10). The source of r_v to the cloud layer is the positive turbulent fluxes of water vapor (see Fig. 7.12) from below cloud base. Water vapor amounts have been increased substantially in these regions due to the sublimation of sedimenting ice crystals (Fig. 7.10), thus, the increase in the water vapor amounts in the sub-cloud region adds vapor to the liquid layer through positive upward fluxes which are driven by the cloud-scale circulations. In addition, turbulent liquid water fluxes ($< w'r_l' >$), while smaller than the fluxes of water vapor, supplies the upper levels of the cloud from lower regions. The circulations, continually produced by the liquid water layer, are increased as the LWC of the upper layer is increased through the water vapor fluxes, lower θ-values, and positive liquid total liquid water fluxes (F_{liq}) at cloud base. The total fluxes of a given condensed species is just the sum of the turbulent fluxes ($< w'r_l' >$, for example) and the drizzle fluxes (F_{driz}) which is defined after Stevens (1996) as,

$$F_{driz} = \sum_{k=1}^{25} m_k v_k \tag{7.1}$$

where m_k and v_k are the mass and terminal fall-speed of bin k. Since the total ice water fluxes (F_{ice}) are dominated by drizzle within the liquid layer ($F_{driz,i}$), there is less competition for the available water vapor, allowing cloud drops to grow substantially.

Thus, we see that an ASC consisting of a mixture of liquid water and ice may persist even under conditions of rapid glaciation without complete dissipation of the liquid water layer. How the ice phase affects the evolution of the layer remains to be discussed. As is shown in Fig. 7.13, sedimentation of the ice crystals is fast enough to allow the liquid layer to remain, however it is slow enough so that ice sublimation in the sub-cloud layer produces substantial moistening. The continued existence of cells associated with the liquid layer produces positive upward fluxes of water vapor and liquid amounts, thus re-supplying the cloud with moisture. Cooling of the upper layers through radiation is sufficient for condensation of the increasing water vapor amounts.

Figure 7.6 shows that the liquid water layer continues to increase after 5 hours in both magnitude of LWC and depth. Ice is continually produced and appears to be quite steady for most of the time period. Towards the eighth simulation hour, however, IWC is

again increasing concomitantly with LWC. The deepening of the liquid layer is illustrated more dramatically in Fig. 7.14 in which the production of liquid drizzle from the layer may easily be seen. Over the course of the 5 to 8 hour period, enough condensation is occurring so that the drop effective radii (r_e) increases. By the eighth hour, significant drizzle is produced as the concentrations of drops (N_t) are low, therefore allowing the available condensation to affect drop size more strongly. The constant low IWC over the course of the 5-7 hour period is also shown in this figure, as the profiles of IWC, N_i and $r_{e,i}$ are relatively constant with height. This suggests the continued production and growth of ice crystals within the liquid water layer with a relatively constant stream of ice to the surface occurring with time. After 8 hours of simulation, the ice amounts increase, but the profile retains its quasi-constant in height characteristics. Ice water contents within the liquid layer are low enough so that liquid water is not readily depleted. In addition, the small ice concentrations (N_i in Fig. 7.14) ensure the production of large ice crystals (shown by large values of $r_{e,i}$) that rapidly sediment.

The production of few, large crystals with low IWC existing within and sedimenting from the liquid layer is consistent with some observations of ASC with cloud temperatures just below freezing (Reuter, personal communication; Pinto, 1997). Indeed, Pinto (1997) observed maximum LWC for two mixed-phase clouds colocated with cloud top with maximum values ranging from 0.09 to 0.2 $g\ m^{-3}$. Both liquid layers appeared to be very thin with cloud depths ranging from $150m$ to 350 m which is qualitatively similar to our simulated cases. Ice water contents for Pinto's observations show the same constant with height characteristic illustrated in these simulations. Values of IWC for these profiles, existing between 0.04 and 0.2 $g\ m^{-3}$, are within the ranges produced by these simulations. The largest discrepancy between the results shown by Pinto's observations and the simulated system are the ice concentrations. Pinto (1997) reports concentrations of what they define as snow between 40 L^{-1} and 20 cm^{-3} (20,000 L^{-1}) with most of this snow concentration existing at or below cloud base. Cloud ice (similar to the pristine ice simulated here) have ice concentrations more in-line with conventional nucleation results (values between 0.1 and 10 L^{-1}).

The effects of the ice on the sub-cloud region appears to be two-fold. First, sedimenting ice crystals supply vapor and cooling to the lower layers through the process of sublimation (as was shown to occur during the 4 to 5 hour period). This causes the stabilization of the layers below cloud base. After ice saturation is reached, water vapor amounts are not increased and cooling is not enhanced through the sedimentation of ice crystals (although drizzle drops passing through the layers will enhance sub-cloud cooling). Thus, cooling must be enhanced by other mechanisms in order for supersaturations with respect to ice (S_i) to be realized. Not only do the ice crystals decrease temperatures throughout the sub-cloud layer by sublimation (see θ in Fig. 7.15), they also indirectly set the stage for increased radiative cooling within the mixed-layer. As concentrations of drops decrease during the 4 to 5 hour period due to the Bergeron-Findeisen process, radiative cooling rate maxima decrease while the radiative cooling layer depths increase. This remains relatively unchanged over the last 3 hours of the simulation (Fig. 7.16). Since IWC is continually produced, it appears that ice crystals have an indirect control on the radiative cooling maxima and depth by effecting the size and mass of liquid water drops produced. Radiative cooling profiles shown in Pinto (1997) illustrate similar characteristics (maxima of about -2 $K\ h^{-1}$ with radiative cooling depths similar to those presented here). Over the 4 to 8 hour period, the change in the θ profiles show that the production and sedimentation of ice crystals slowly causes stabilization of the layer. Thus, a transition from a θ profile associated with a strongly mixed boundary layer to a more stable regime is caused by the existence of the ice phase. It appears possible that cases of mixed-phase clouds which produce strongly mixed-layers, such as those illustrated by Pinto (1997), may undergo transitions to more stable regimes through ice crystal production.

Microphysical cooling rates ($\partial\theta/\partial t_{mic}$), which include the effects of both water drops and ice crystals, and total cooling rates ($d\theta/dt$) show that cooling continues to occur over the entire depth of the boundary layer through the course of the last 3 simulation hours. Radiative cooling which is spread deeper within the mixed-layer is easily redistributed throughout the mixed-layer through eddy motions. Not only this, but more of the cooled air is available for the generation of buoyancy that drives downdraft cells. That the layer is

being cooled rapidly within the upper-portions of the liquid cloud, as shown by changes in the θ profiles, is evidence of this downward mixing of cool air. Alterations in the θ profiles due to ice sedimentation also appears to be occurring in the observations of Pinto (1997). One of the θ profiles observed shows an increase with height (at about 17 $K\ km^{-1}$) which is qualitatively similar to that produced by the simulation after 8 hours (θ lapse rate of about 5 $K\ km^{-1}$). It is not known whether Pinto's observed lapse rate is produced through ice sedimentation as is the case here, however, since the sedimentation mechanism appears to produced similar effects in other simulations (to be presented further in the text), it seems a plausible hypothesis.

Buoyancy production rates (Fig. 7.17) illustrate how the ice phase affects circulation strengths over time. Note that, as a consequence of the deeper radiative cooling layer, the depth of the circulations increase ($< w'w' >$). This illustrates why decreases in θ occur over deeper layers in time; the cloud top generated cooling produces deeper penetrating cells that mix cooled air deeper into the boundary layer. In time, $< w'w' >$ maxima decrease as the cloud layer deepens and cools due to the production of liquid and ice drizzle (Fig. 7.14). Even though radiative cooling rates are maintained near cloud top, evaporative cooling by the hydrometeors ($\partial\theta/\partial t_{mic,d}$), which also feed downdrafts with buoyancy, begins to deepen as drizzle rates increase. Figure 7.16) shows that evaporative cooling within downdrafts maintain a peak near cloud top during the period up to hour 7 of the simulation. After this time, significant precipitation is being produced which distributes the evaporative cooling rates over a deeper layer. This assists the production of deeper penetrating circulations as shown by the $< w'w' >$ profiles.

Cloud LWCs continue to increase, as is shown in Fig. 7.6, until about 7.5 hours and is due to a couple of factors, the first of which is that the mixing of radiatively-cooled air at cloud top throughout the layer. This mixing causes equilibrium vapor pressures to drop and continues to produce an ice supersaturated environment. The second factor that increases LWCs is the mixing of water vapor (generated by ice sublimation) from below cloud base into the liquid cloud deck which causes increases in total water content. Fluxes of water vapor (shown in Fig. 7.18) illustrates that continual convergence of water vapor

is occurring in the vicinity of cloud base. This flux convergence continually adds vapor to the liquid layer over the 6 to 8 hour period. Total fluxes of liquid water (F_{liq}) within the cloud layer shows that drizzle fluxes dominate near cloud top while upward turbulent fluxes ($< w'r_l' >$) dominate the fluxes near cloud base over the period up to 7 hours. Thus, a fairly constant cycling of liquid is occurring throughout the cloud layer. In time, drop sizes increase to the point where sedimentation of water drops from the cloud layer dominates the total liquid flux (at 8 hours). When this occurs, eddy strength (Fig. 7.17) decreases while the depth of the circulation increases. Over time, the cycling of ice crystals within the liquid layer increases as is shown by the dominance of the turbulent fluxes of ice ($< w'r_i' >$) in the total ice budget (F_{ice}). Continuous ice precipitation ($F_{driz,i}$) continues to occur and dominates the fluxes below cloud base.

Thus, the effects of the ice phase on the cloud layer may be summarized in the following manner. The sublimation of ice crystals, by redistributing water vapor and enhancing cooling, primes the sub-cloud layers for the extension of the liquid cloud to lower levels. As the lower layers become more stably stratified, turbulent fluxes decrease. Radiative cooling rates, which appear important to the maintenance of the layer, remain relatively constant as IWC produced within the liquid layer mitigate the strength of the cooling. Large cooling rates and increased water vapor contents below cloud base allows for condensation to occur as saturations rise and vertical motions are extended downwards. As the ice continues to sediment moistening the lower levels, and radiatively cooled air is continually mixed throughout the layer, the liquid cloud base is able to descend.

7.2.2 The 10 C cooled control simulation

The four-hour bulk microphysical simulation used for the 10C control initialization produces larger fractions of total water in the ice phase than the 5C cooled case. The effects of larger initial ice water contents and cooler temperatures in the 10CTRL simulation are illustrated in the 2 hour continuation with the bin microphysical model. The 10C control simulation (10CTRL) produces rapid conversions of LWC to IWC over the 4-5 hour period of the 6 hour simulation. As is shown in Fig. 7.19, the reduction of LWC and the increase in IWC is rapid enough to produce boundary layer collapse (analogous to Ackermann

et al. , 1995 for warm stratocumulus) in a one hour period with no changes occurring throughout the course of the last (sixth) hour of the simulation. This rapid collapse is not a function of the switch over to the bin microphysical model from the bulk microphysical model. Simulations which simply turn on the affects of aggregation within the bulk model at hour 4 also produce a rapidly collapsing boundary layer with similar structure to the one produced by the bin model. It was also noted by Pinto (1997) that rapid glaciation of mixed-phase cloud decks is strongly temperature dependent , as was illustrated by one of their cases that produce large IWC (up to 0.2 $g\ m^{-3}$).

Ice water contents at four hours (Fig. 7.19) are quite small, however increase rapidly within only a 15 minute period. As larger ice contents are produced, LWC decreases rapidly over the 0.5 hour period. By 4.5 hours, the LWC has been almost completely depleted. Ice crystals grow large quickly, as is illustrated by the large $r_{e,i}$ values shown in Fig. 7.20. Comparison with the values in Fig. 7.9 for the 4-5 hour period of the 5CTRL simulation show that IWC are larger in the 10CTRL simulation, however $r_{e,i}$ values are about 100 μm less than 5CTRL because of the existence of higher ice concentrations (N_i). Larger ice nucleation rates, due to higher ice supersaturations (S_i in Fig. 7.21), produce larger ice concentrations in the 10CTRL simulation. Thus, ice sedimentation rates are lower in 10CTRL, which allows the ice crystals longer exposure to the supersaturated environment than those in the 5CTRL simulation. The combination of lower sedimentation rates, larger IWC and larger concentrations causes the liquid layer to be depleted more rapidly that in 5CTRL. This is evidenced by the more rapid decrease in ice supersaturations in this case than in 5CTRL. Larger ice supersaturations are produced in this case as cloud temperatures are lower (-13 C as compared to -6 C in 5CTRL) however initialized relative humidities are the same. Depletion of LWC is more rapid not only because of the larger ice amounts and slower ice fall speeds, but also because of the fact that the difference between the equilibrium vapor pressures of ice and water are maximized at -12 C (see Fig. 7.3). Ice growth at the expense of water drops is maximized, therefore increasing liquid water depletion. This point will be elaborated upon further in the sensitivity study chapter.

As ice deposition occurs rapidly within the cloud layer, water vapor amounts are rapidly depleted as compared to the 4 hour values (Fig. 7.21), more so than in 5CTRL

(compare with Fig. 7.10) in which case IWC spend less time within the liquid layer. Large deposition rates within the cloud layer produce significant heating which causes θ-values shown in Fig. 7.21 to increase over the 4 hour profile. This is in sharp contrast to 5CTRL in which the cloud layer is cooled over the same period (Fig. 7.10).

As the ice sediments out of the liquid layer, sublimation of ice produces increases in r_v and reductions in θ within the sub-cloud layer. The overall effects are not as pronounced as shown in 5CTRL (Fig. 7.10), however both comparisons are relative to r_v and θ profiles at the 4 hour time. In 10CTRL, a substantially deep ice layer already existed (Fig. 7.2), thus the sub-cloud layer had already been affected by evaporating ice. Overall, it appears that the effects of the sublimation on the sub-cloud layer are similar between the cases.

The in-cloud warming in the 10CTRL case, which is in contrast to 5CTRL, appears to be related to the alterations of the radiative cooling profile caused by the rapidly diminishing LWC. Figure 7.22 shows that within 15 minutes the cloud top cooling has rapidly decreased due to reductions in LWC. What radiative cooling does exist is spread deeply over the mixed-layer, however this is not enough to offset the strong ice depositional heating that is occurring throughout the cloud layer by 4.25 hours ($\partial\theta/\partial t_{mic}$ in Fig. 7.22). Strong evaporative cooling of the hydrometeors is occurring within the downdrafts at 4 hours, however as IWC increase even the cores of the downdrafts begin to warm through deposition ($\partial\theta/\partial t_{mic,d}$ at 4.25 hours). The overall effect is the production of significant total warming ($d\theta/dt$) over the period of the collapse.

Since deposition of vapor onto ice surfaces within the liquid layer dominates over radiative cooling as the LWC is depleted, the production of buoyancy (Fig. 7.23) is rapidly reduced. Note that the layer below 1000 m is rapidly being stabilized through the effects of depositional heating (negative area in the buoyancy production profile), which causes reductions in $< w'w' >$ with time.

The fluxes of water vapor, given in Fig. 7.23, indicate that vapor is being fed into the cloud layer from sub-cloud regions (where strong ice sublimation had occurred, thus supplying vapor). The positive water vapor fluxes are similar in magnitude to those produced in the 5CTRL simulation (Fig. 7.13), however are not large enough to initiate condensation

alone. This suggests that the cooling of the liquid layer through the mixing of radiatively-cooled cloud top air dominates the process of enhanced condensation in 5CTRL, allowing the layer in that case to persist. The fluxes of condensed species (Fig. 7.24) illustrates the point that ice precipitation fluxes ($F_{driz,i}$) are smaller in 10CTRL than 5CTRL (Fig. 7.13). These smaller ice precipitation rates, which are due to larger numbers of small ice crystals in 10CTRL, allows for larger turbulent fluxes of ice ($< w'r_i' >$) which dominates the total ice fluxes (F_{ice}) in the lower portion of the liquid cloud. Thus, unlike 5CTRL, the liquid cloud layer is exposed to significant numbers of small ice crystals through cycling by the turbulent eddies. Even though vapor is supplied to the layer through turbulent fluxes, the persistence of ice within the cloud layer continually removes the vapor (and liquid water) through deposition. Liquid water fluxes rapidly diminish as the water is depleted by deposition.

Thus, we may summarize the effects of the ice phase within the $10C$ cooled boundary layer as follows. The $10C$ cooling allows for larger nucleation rates as ice supersaturations become larger than those in 5CTRL. Ice crystal growth rates, therefore, become larger than in 5CTRL and, in addition, ice crystal growth at the expense of liquid water is maximized at the cloud temperatures of the 10CTRL simulation. Because of this, more deposition occurs due to the larger ice concentrations and produces larger IWC but smaller effective sizes ($r_{e,i}$) than 5CTRL. The smaller ice crystal sizes allow for longer in-cloud residence times as eddy cycling of ice dominates the fluxes. The large deposition rates rapidly deplete the water vapor and LWC; radiative cooling rates are reduced quickly and, therefore, cannot balance the strong heating due to deposition that is occurring. This leads to substantial warmings within the whole of the liquid water deck and, therefore, reductions in the buoyancy production rates and $< w'w' >$. The warming within the cloud layer suppresses condensation as equilibrium vapor pressures of water rise. Eventually, after one hour (Fig. 7.19), the turbulent cloud layer collapses.

It appears that temperature differences, which affect the growth of the ice crystals, IN concentrations, and the indirect mitigation of cloud top radiative cooling rates by the ice crystals seem to strongly affect the stability of the cloud decks. Indeed, Pinto (1997)

showed that for the two mixed-phase systems presented there, radiative cooling rates at cloud top were quite important for the maintenance of the mixed-phase systems. Those results also suggested that IWC was a major factor in mitigating the cloud top radiative cooling rates, as shown in the simulations presented above. This effect will be explored within a set of sensitivity studies presented in the next chapter.

As Pinto (1997) shows that ice concentrations and sizes are much smaller than those presented here, it must be the case that in-cloud residence times are much greater in their observed cases than in our idealized case (as turbulent fluxes of microphysical data are not given it is not possible to do a direct comparison). As will be illustrated in the next chapter, an increase in ice concentrations greatly affects layer stability by increasing ice in-cloud residence times and deposition rates. Since Pinto's (1997) observed temperatures are not much different from those in the $10C$ cases presented here, ($\theta = 265$ vs. 270 $K$for observed vs. modeled cloud top values), the persistence of the mixed-phase layer in their case must be related to effects other than those on the cloud-scale. Indeed, Pinto (1997) shows that large scale moisture convergence continually occurs in his cases.

In the next Chapter, we explore sensitivities around the 5CTRL and 10CTRL simulations in order to further elucidate some of the processes discussed here. The idea is to examine how strong some of the above mechanisms are in producing stable and collapsing cloud layers.

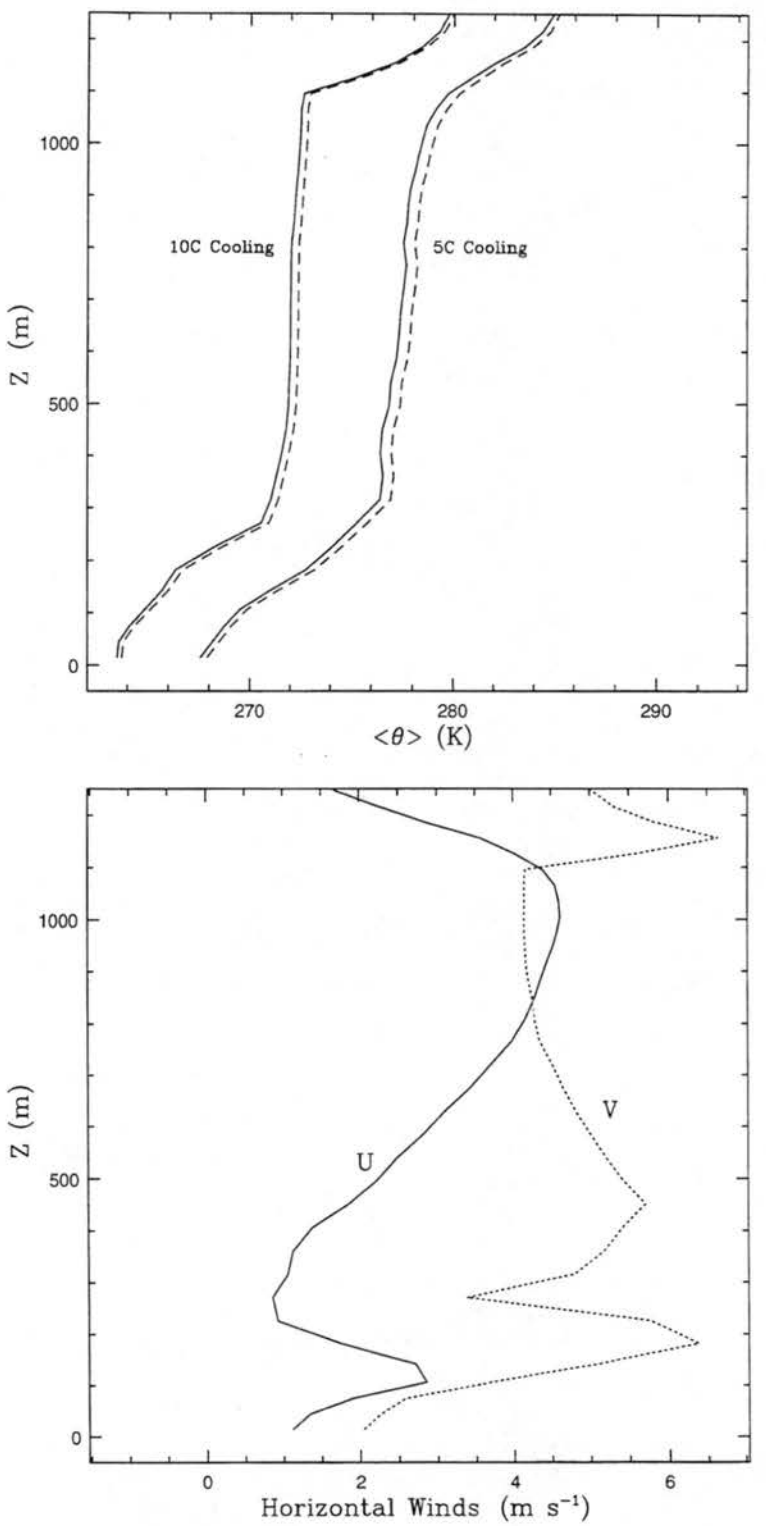

Figure 7.1: Initialization: θ is given by the solid line while θ_v is given by the dashed line. Horizontal winds (U and V components) used in the model initialization are also shown.

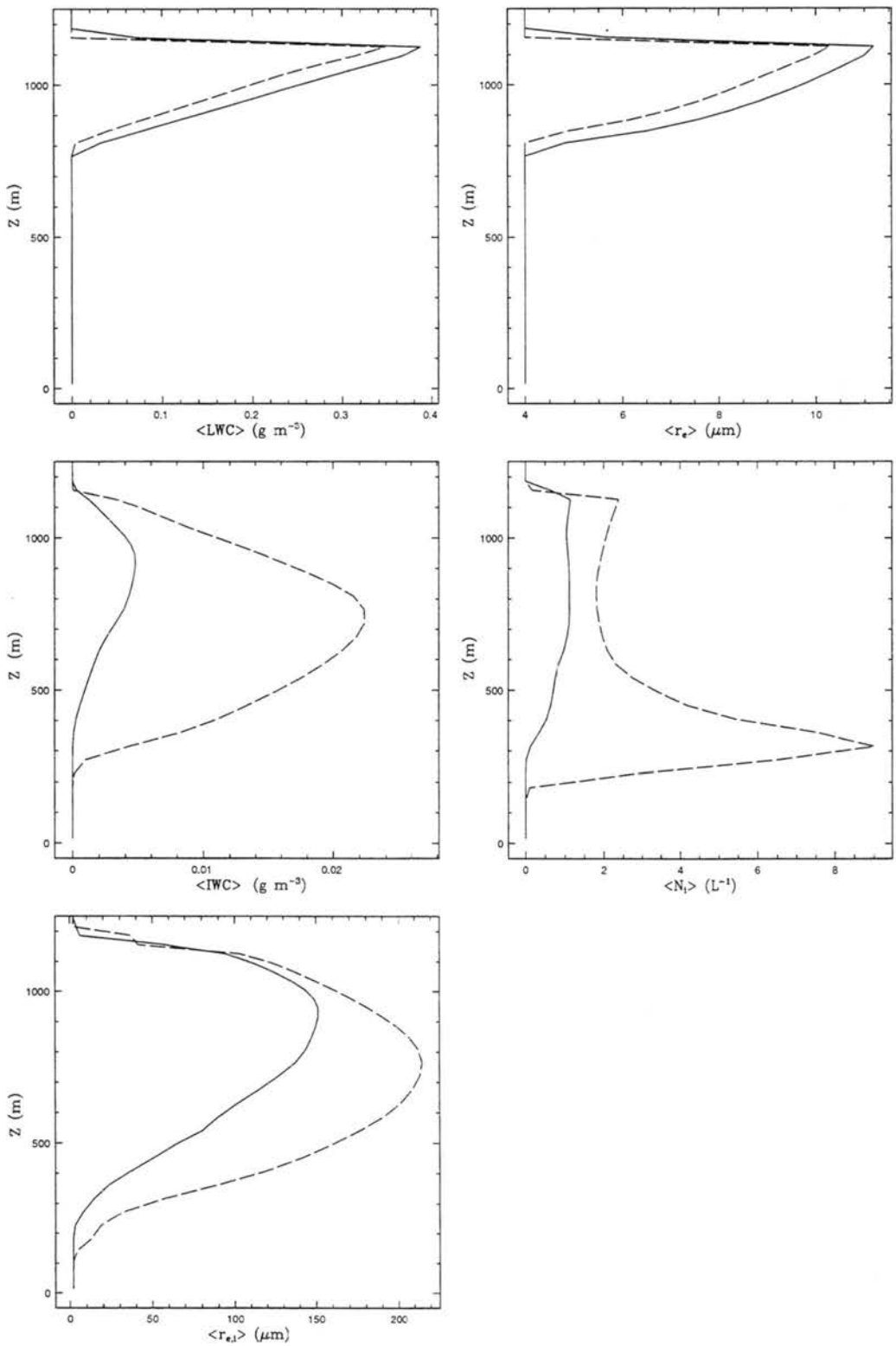

Figure 7.2: Microphysical profiles after four hours for LWC, effective radius (r_e), IWC, ice concentration (N_i), and ice effective radius ($r_{e,i}$). The solid line denotes the 5 C cooled simulation while the dashed line denotes the 10 C cooled simulation.

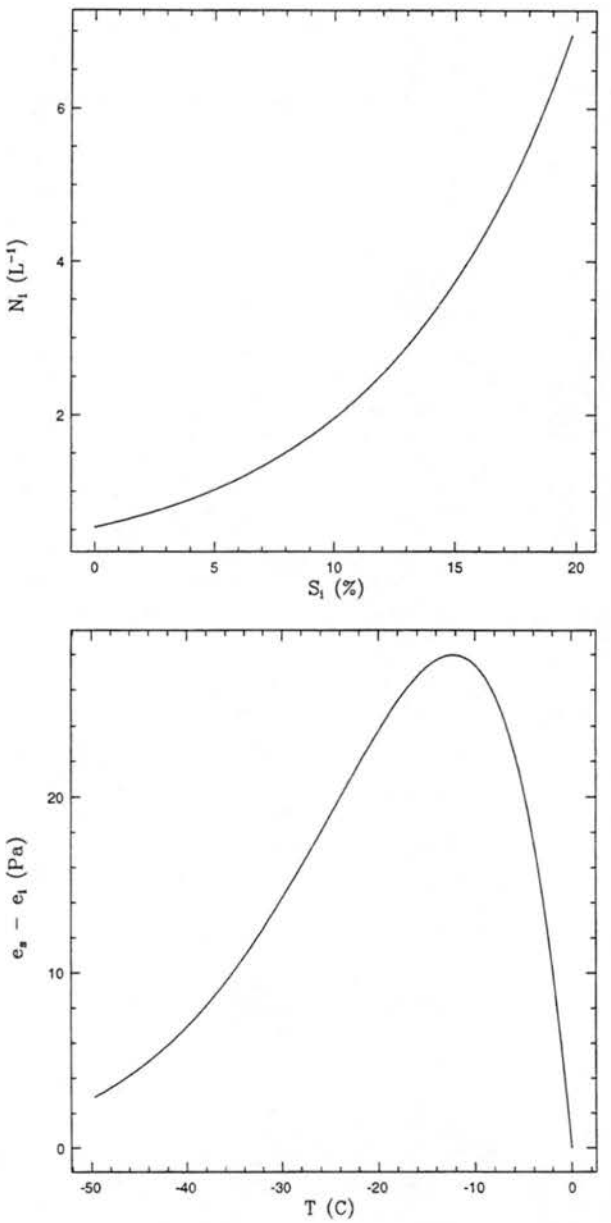

Figure 7.3: Ice nuclei function describing freezing and contact nuclei (after Meyers *et al.* , 1992). Difference in the equilibrium vapor pressure over water (e_s) and over ice (e_i).

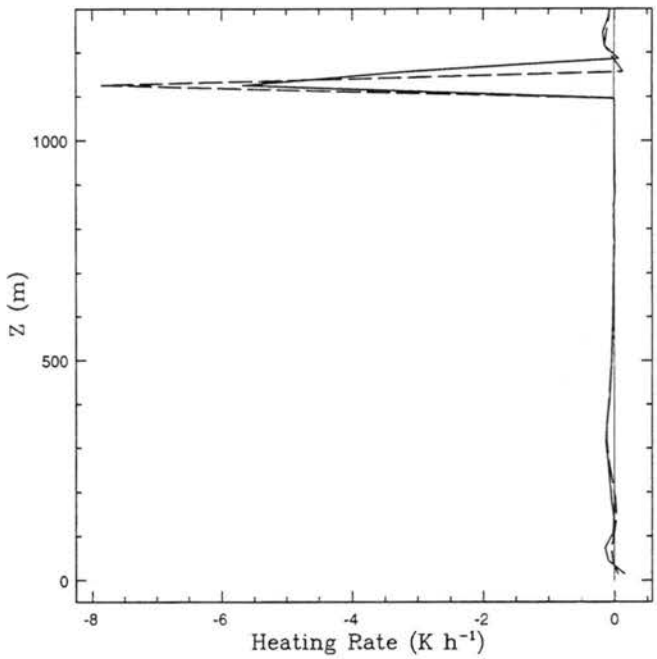

Figure 7.4: Radiative heating rates after four hours. Lines have the same meaning as in Fig. 7.2.

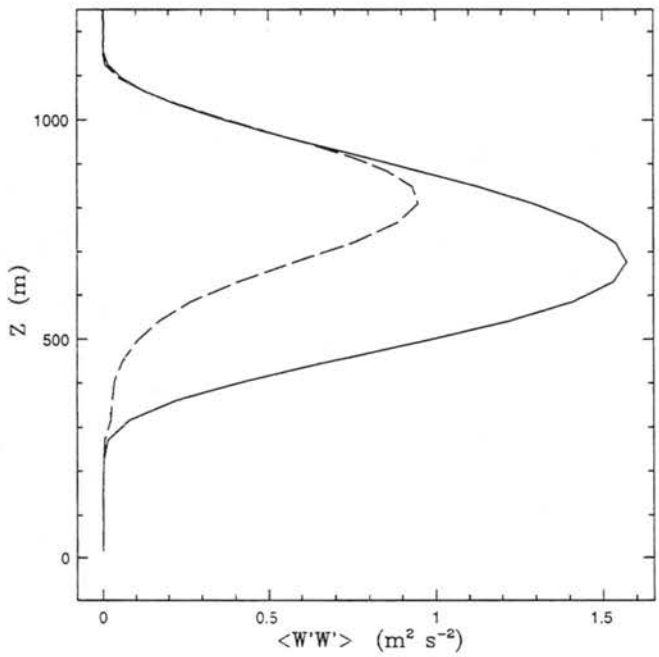

Figure 7.5: $< w'w' >$ after four hours. Lines have the same meaning as in Fig. 7.2.

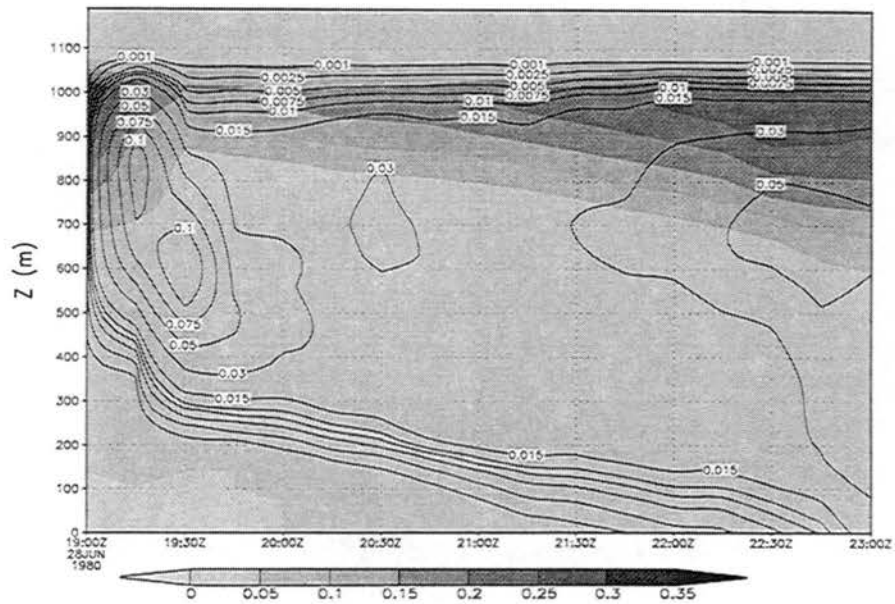

Figure 7.6: Time Series: LWC (shaded) and IWC (contoured) for 5CTRL in $g\ m^{-3}$.

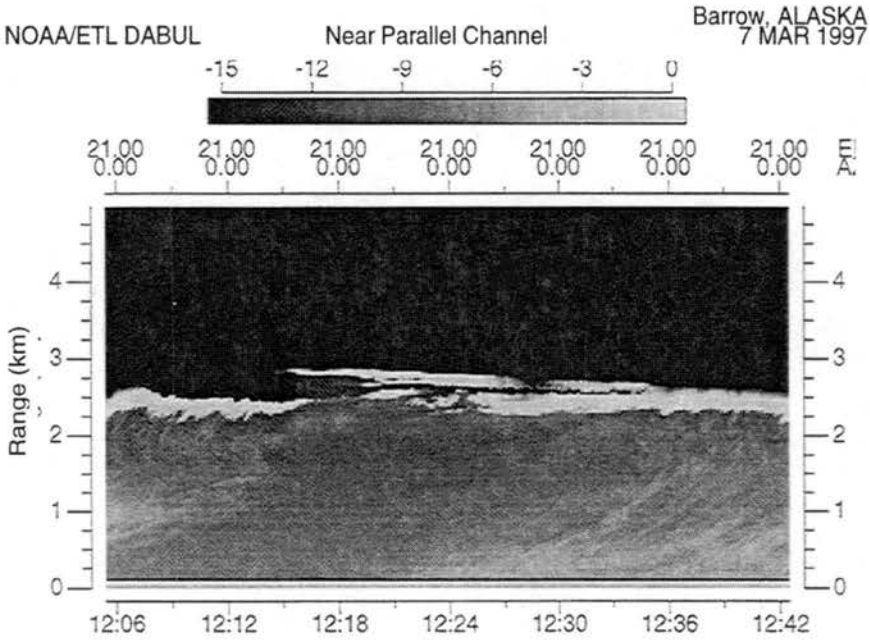

Figure 7.7: Time series of ASC observed over Barrow, AK. The bright cloud top is a tenuous liquid cloud layer composed of relatively small drops. The fall streaks from the cloud are large ice particles that are sedimenting to the surface (image by Chris Grund of NOAA).

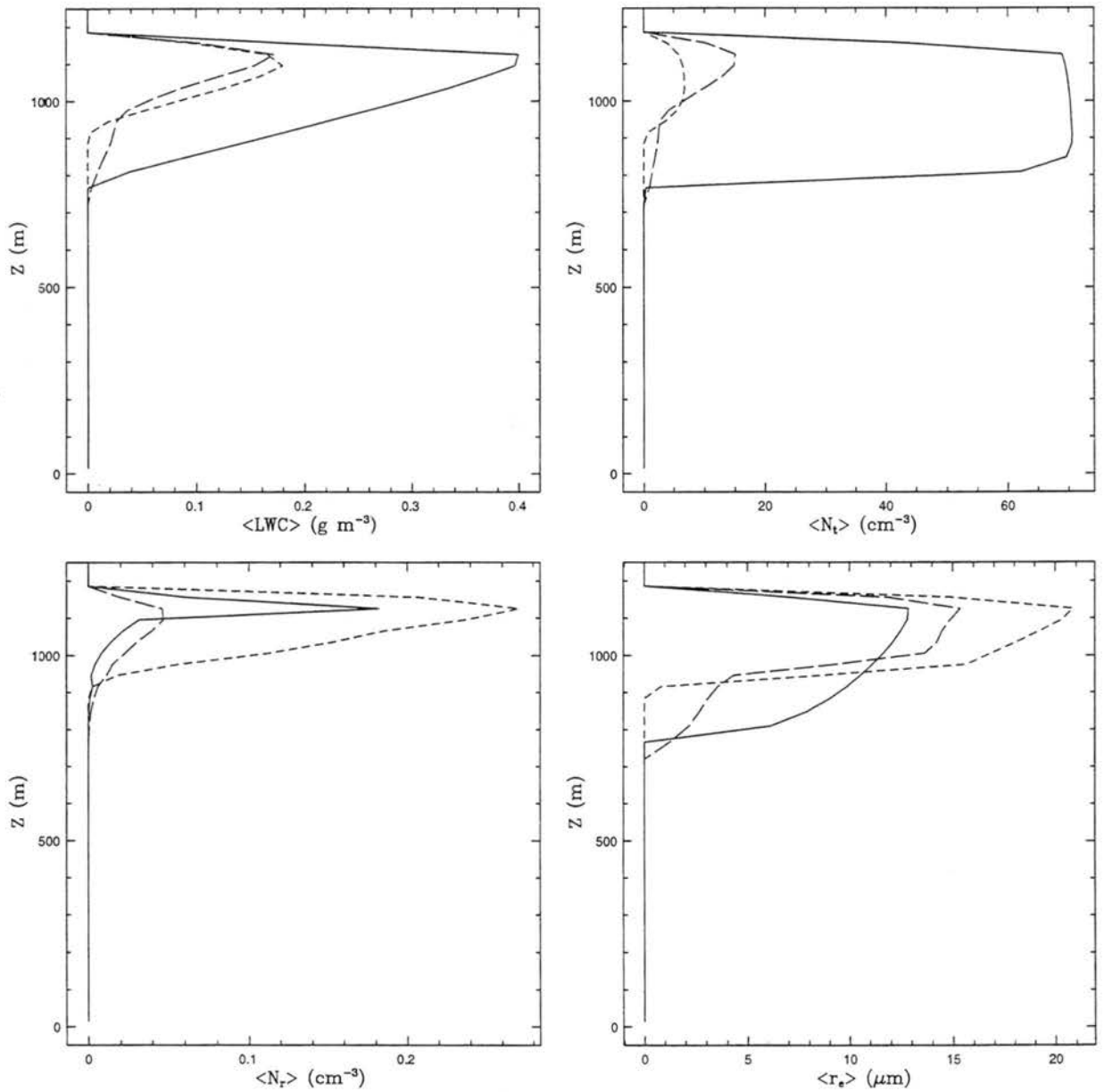

Figure 7.8: Profiles of LWC, total concentration (N_t), concentration of large drops (N_r) and effective radii (r_e) for 5CTRL for the fifth hour of simulation time in 0.5 hour increments. The solid line denotes fields at hour 4, long-dashed line denotes 4.5 hours, and short-dashed line denotes 5 hours.

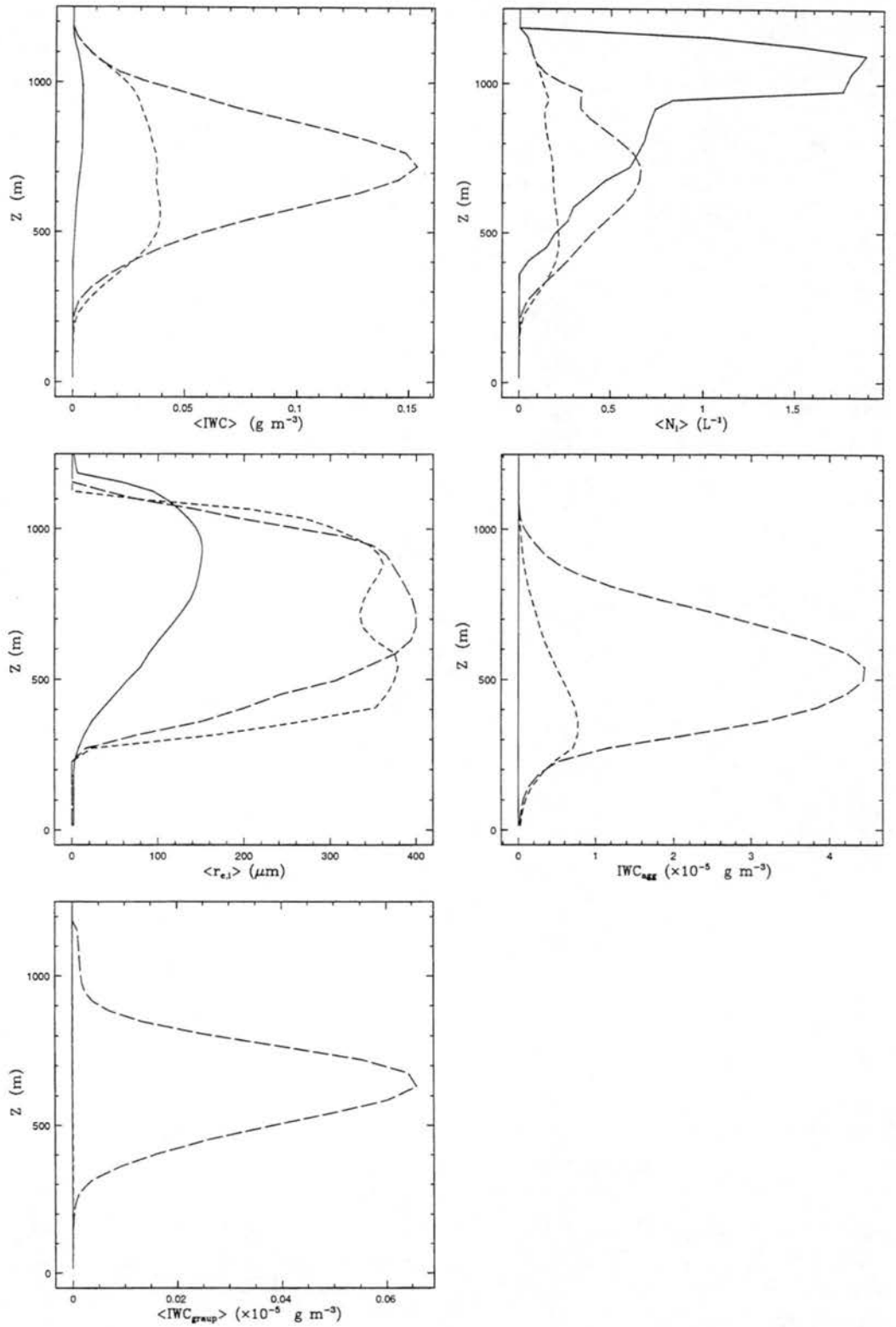

Figure 7.9: Profiles of IWC, total ice concentration (N_i), ice effective radii ($r_{e,i}$), IWC of aggregates (IWC_{agg}), and IWC of graupel (IWC_{graup}) for 5CTRL for the fifth hour of simulation time in 0.5 hour increments. The solid line denotes fields at hour 4, long-dashed line denotes 4.5 hours, and short-dashed line denotes 5 hours.

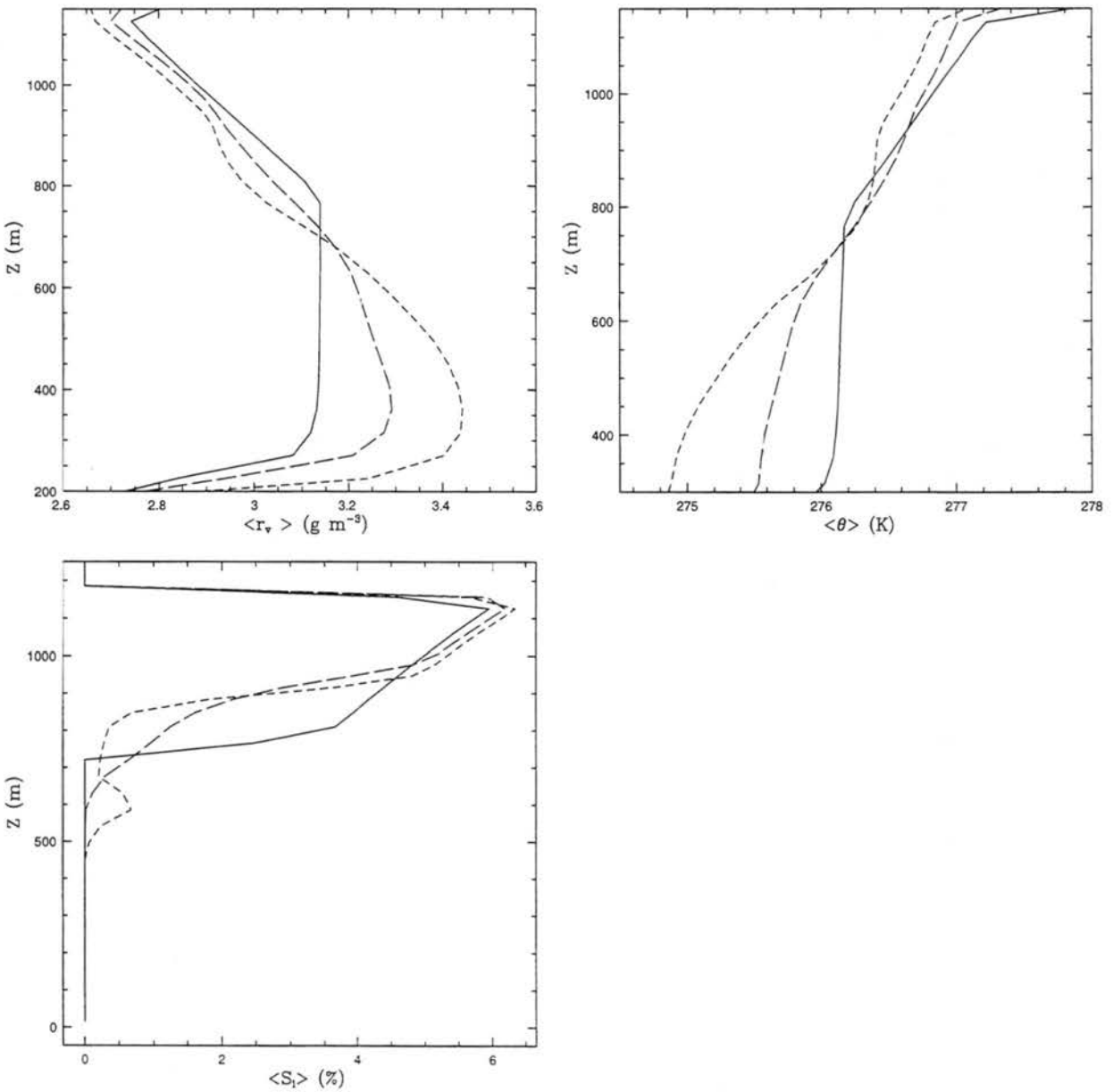

Figure 7.10: Profiles of r_v, θ and S_i for 5CTRL for the fifth hour of simulation time in 0.5 hour increments. The solid line denotes fields at hour 4, long-dashed line denotes 4.5 hours, and short-dashed line denotes 5 hours.

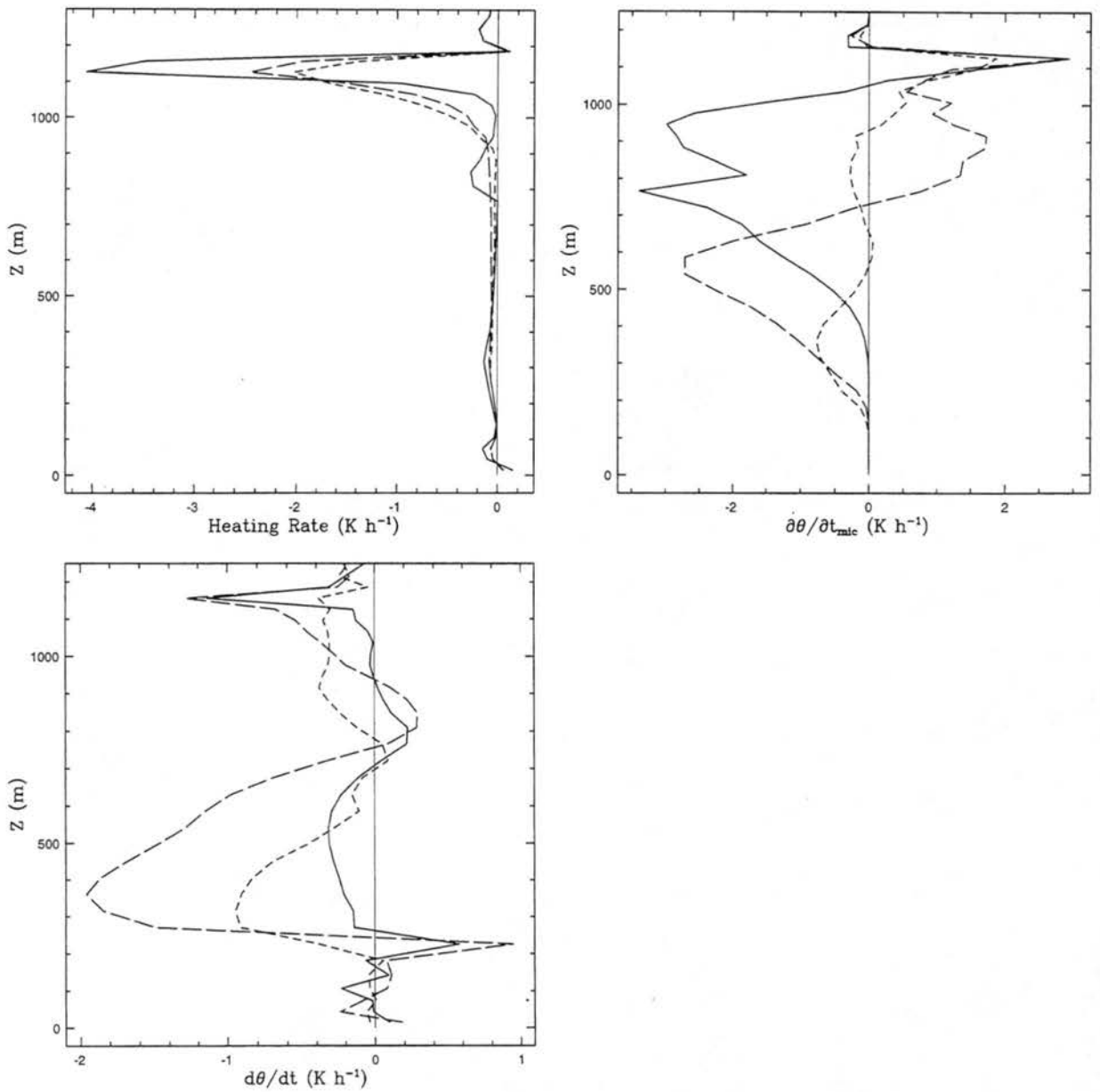

Figure 7.11: Profiles of θ-tendencies including the radiative heating rate (Heating Rate), heating due to microphysics ($\partial\theta/\partial t_{mic}$), and total heating rate ($d\theta/dt$) for 5CTRL for the fifth hour of simulation time in 0.5 hour increments. The solid line denotes fields at hour 4, long-dashed line denotes 4.5 hours, and short-dashed line denotes 5 hours.

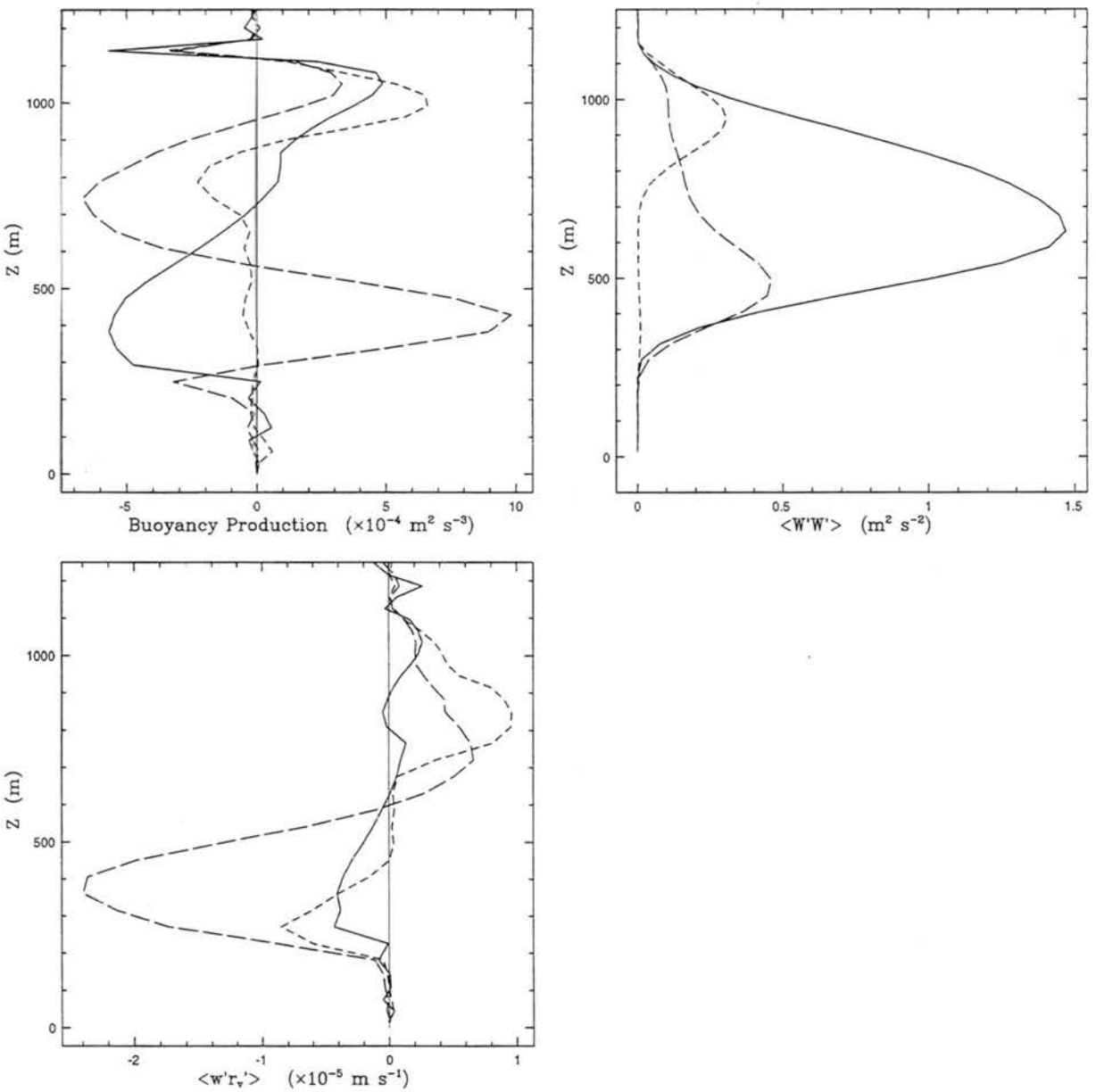

Figure 7.12: Profiles of buoyancy production,. $< w'w' >$ and $< w'r_v' >$ for 5CTRL for the fifth hour of simulation time in 0.5 hour increments. The solid line denotes fields at hour 4, long-dashed line denotes 4.5 hours, and short-dashed line denotes 5 hours.

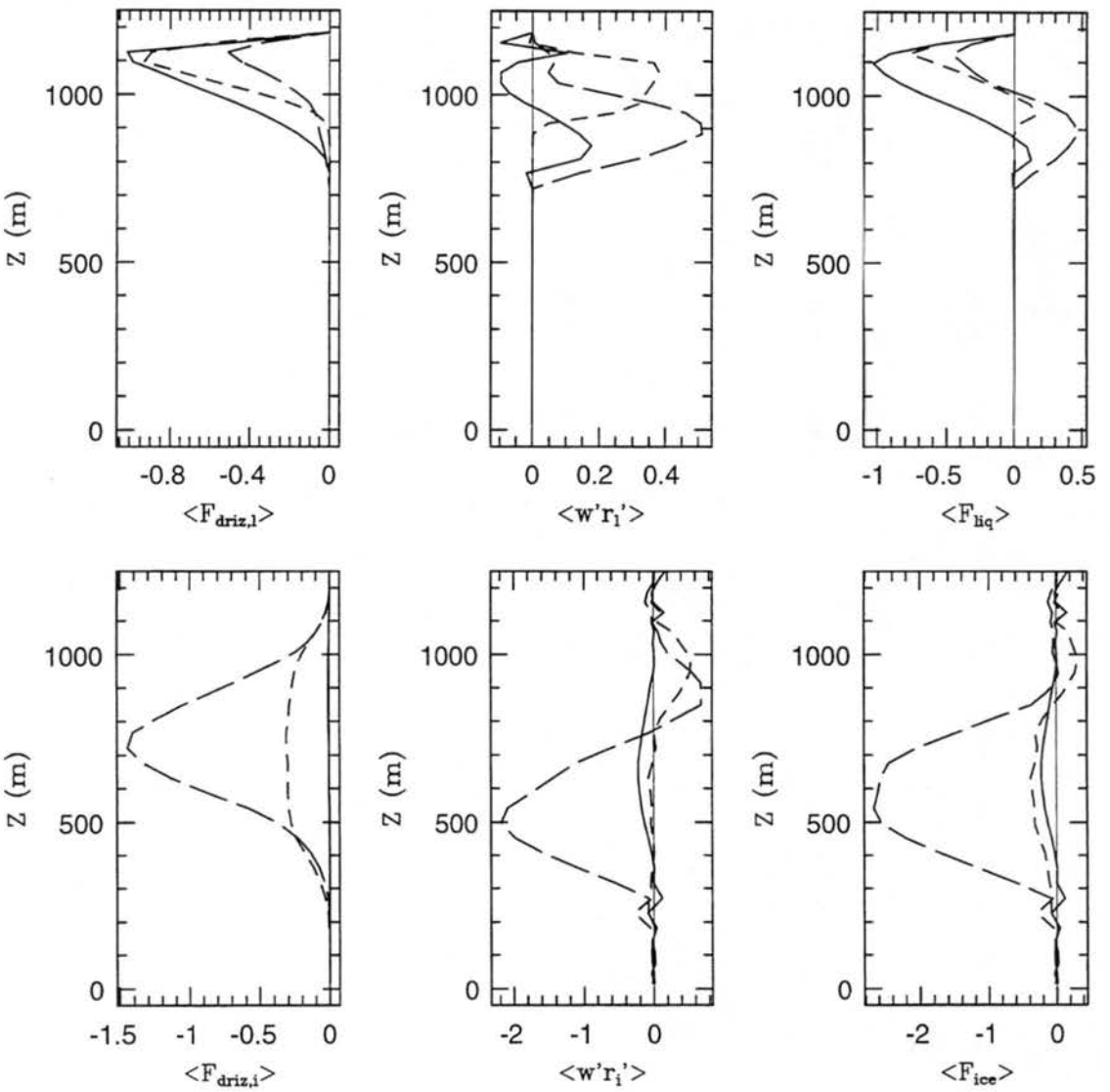

Figure 7.13: Profiles of fluxes of condensed species for 5CTRL for the fifth hour of simulation time in 0.5 hour increments. Units are in $kg\ kg^{-1}\ m\ s^{-1} \times 10^{-5}$. The solid line denotes fields at hour 4, long-dashed line denotes 4.5 hours, and short-dashed line denotes 5 hours.

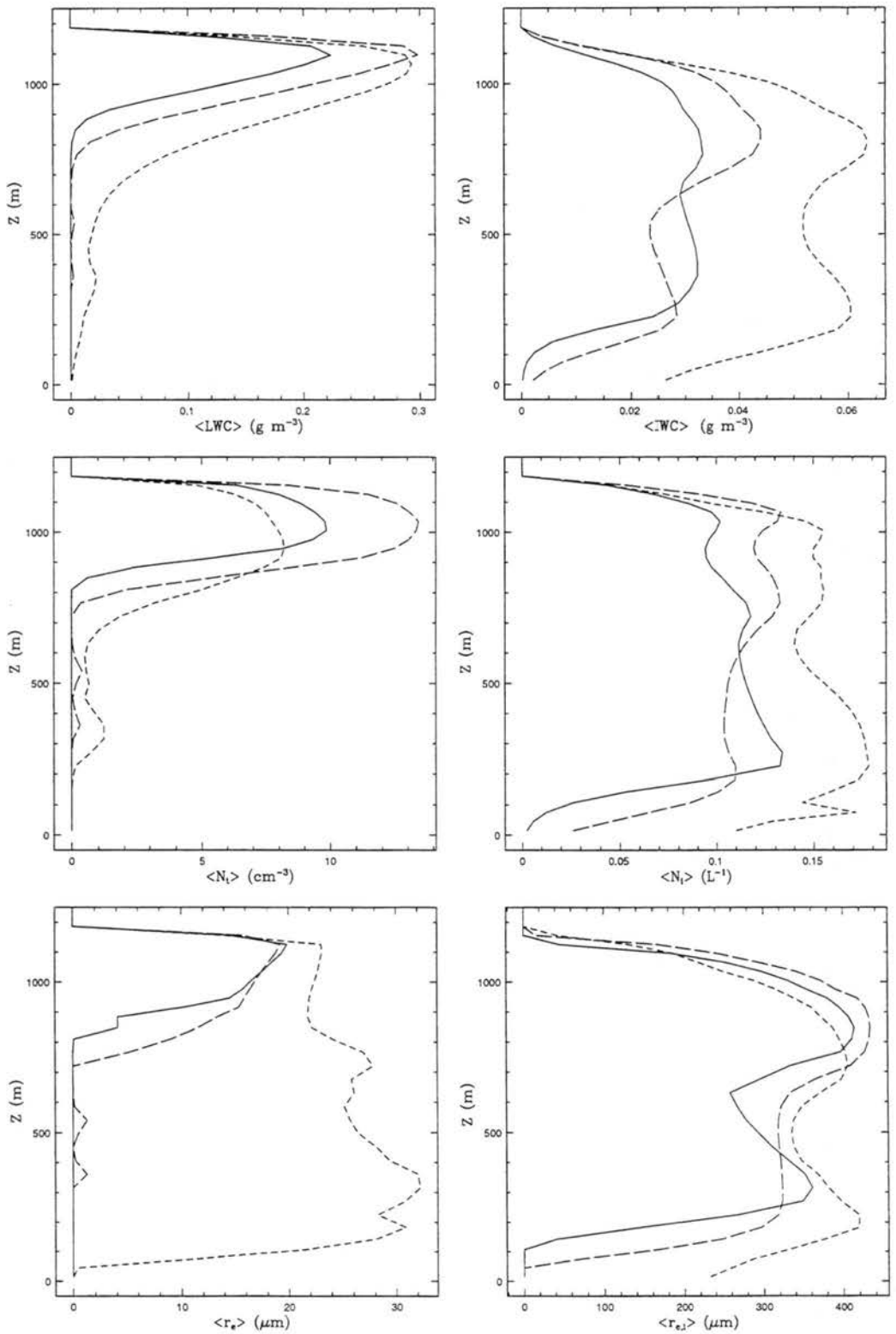

Figure 7.14: Microphysical profiles for hours 6 through 8 for LWC, IWC, drop concentration (N_t), ice concentration (N_i), drop and ice effective radii (r_e and $r_{e,i}$). Solid line denotes sixth hour, long-dashed line denotes seventh hour and the short-dashed line denotes eighth hour of simulation time.

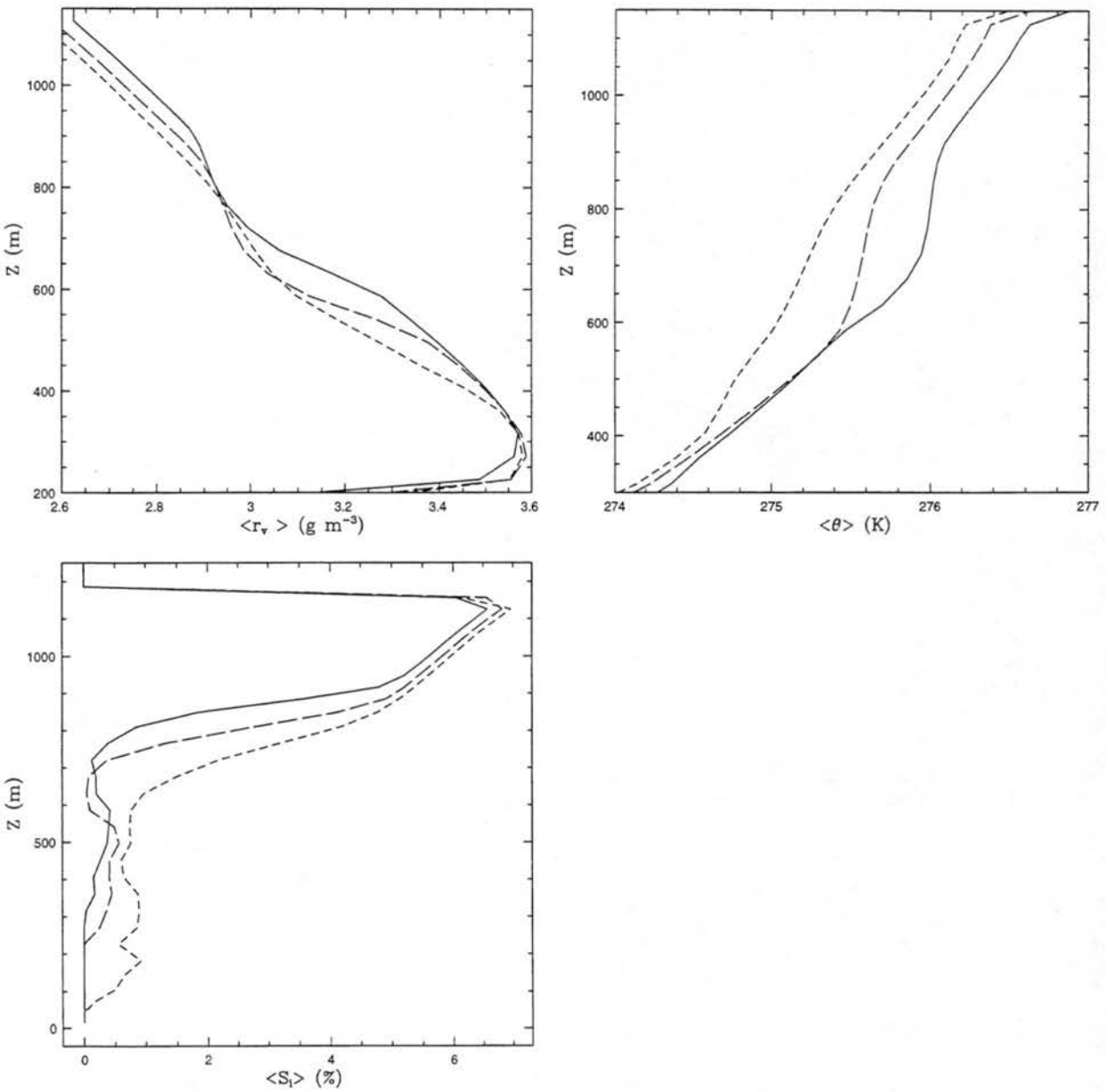

Figure 7.15: Profiles of water vapor, θ, and S_i for 5CTRL for the 6-8 hour period of simulation time in 1 hour increments. The solid line denotes fields at hour 6, long-dashed line denotes 7 hours, and short-dashed line denotes 8 hours.

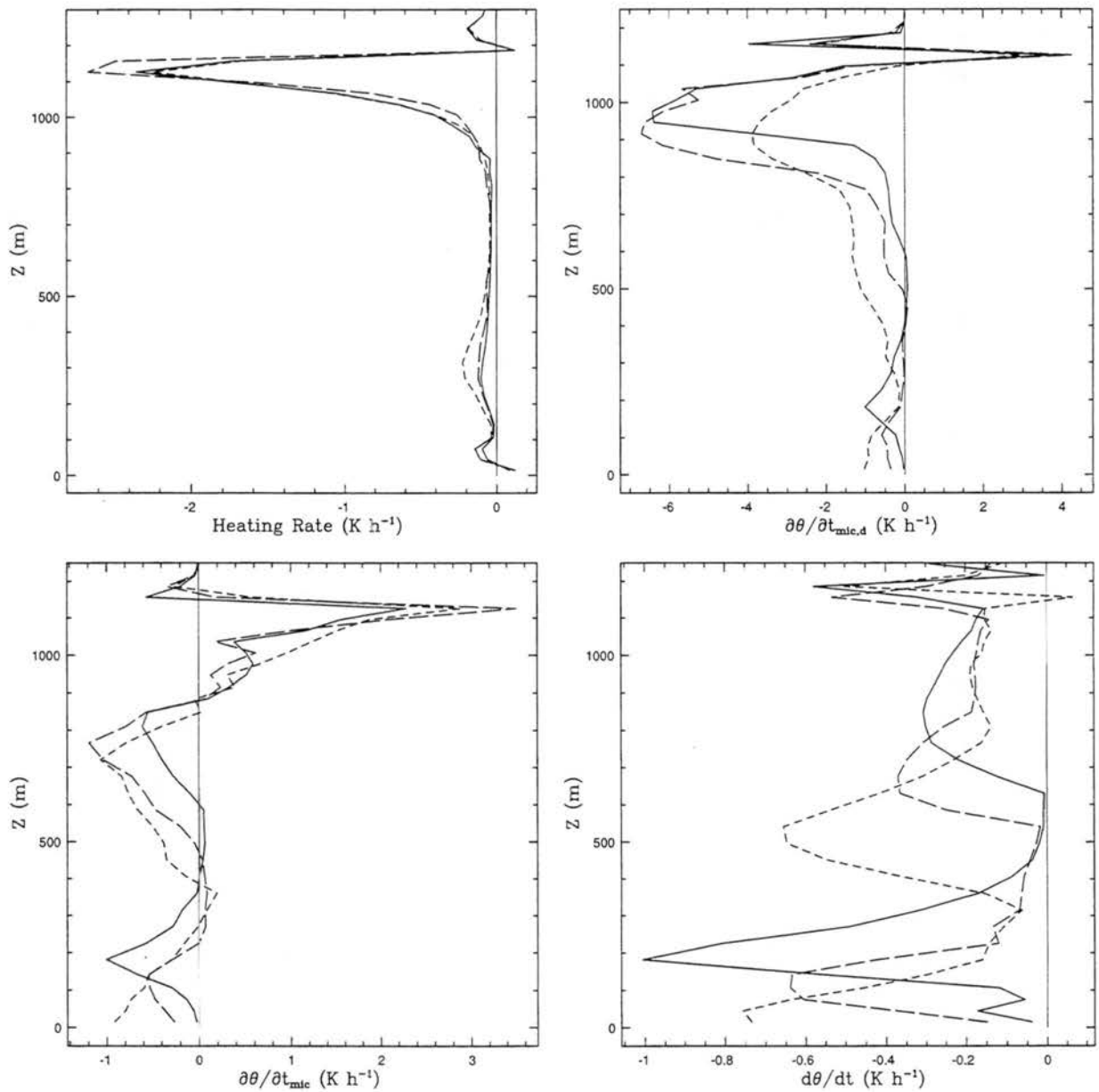

Figure 7.16: Profiles of radiative heating rates (Heating Rate), microphysical cooling within downdrafts ($\partial\theta/\partial t_{mic,d}$), total microphysical heating ($\partial\theta/\partial t_{mic}$), and total cooling rates ($d\theta/dt$) for 5CTRL for the 6-8 hour period of simulation time in 1 hour increments. The solid line denotes fields at hour 6, long-dashed line denotes 7 hours, and short-dashed line denotes 8 hours.

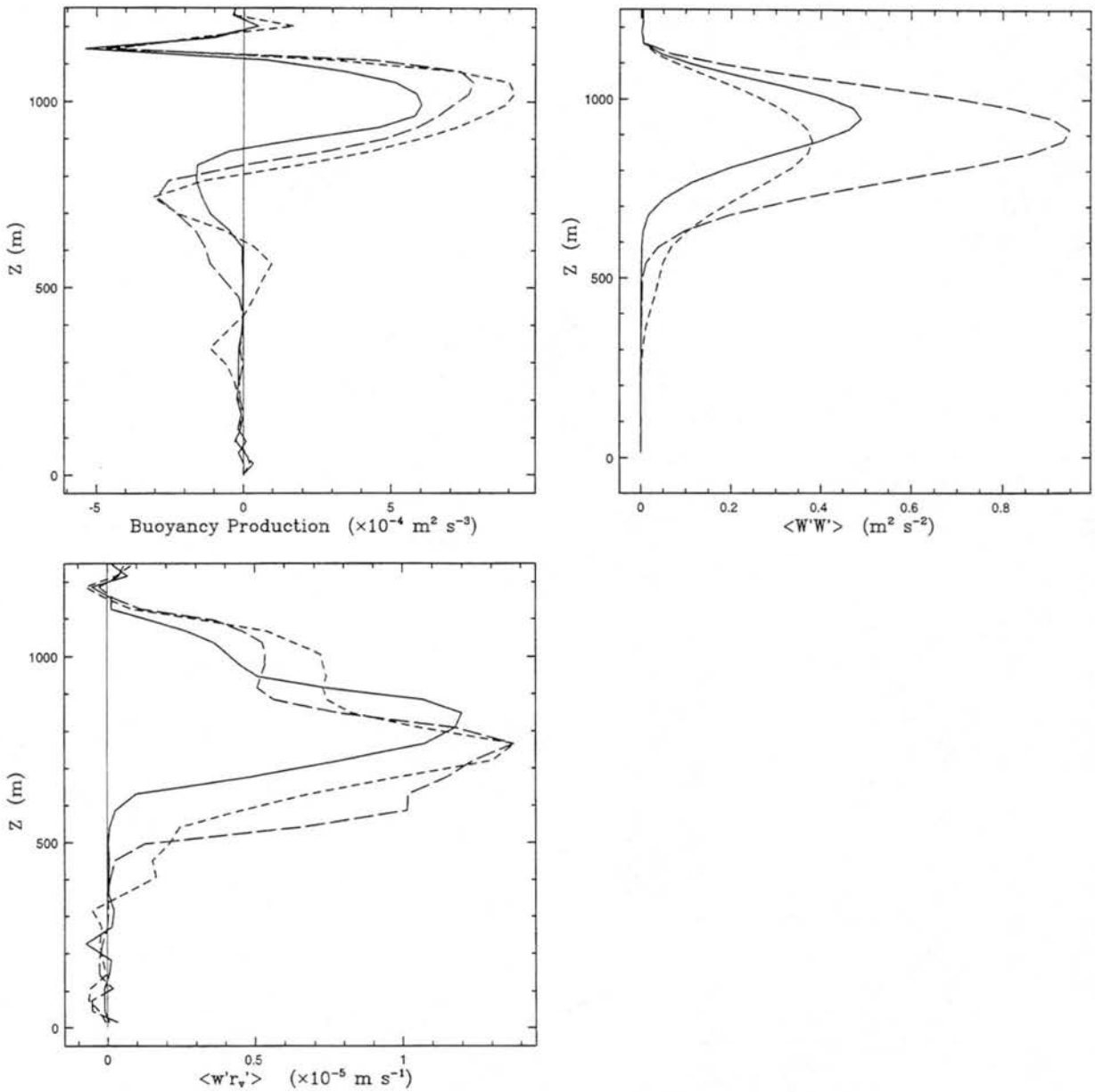

Figure 7.17: Profiles of buoyancy production, $< w'w' >$ and $< w'r_v' >$ for 5CTRL for the 6-8 hour period of simulation time in 1 hour increments. The solid line denotes fields at hour 6, long-dashed line denotes 7 hours, and short-dashed line denotes 8 hours.

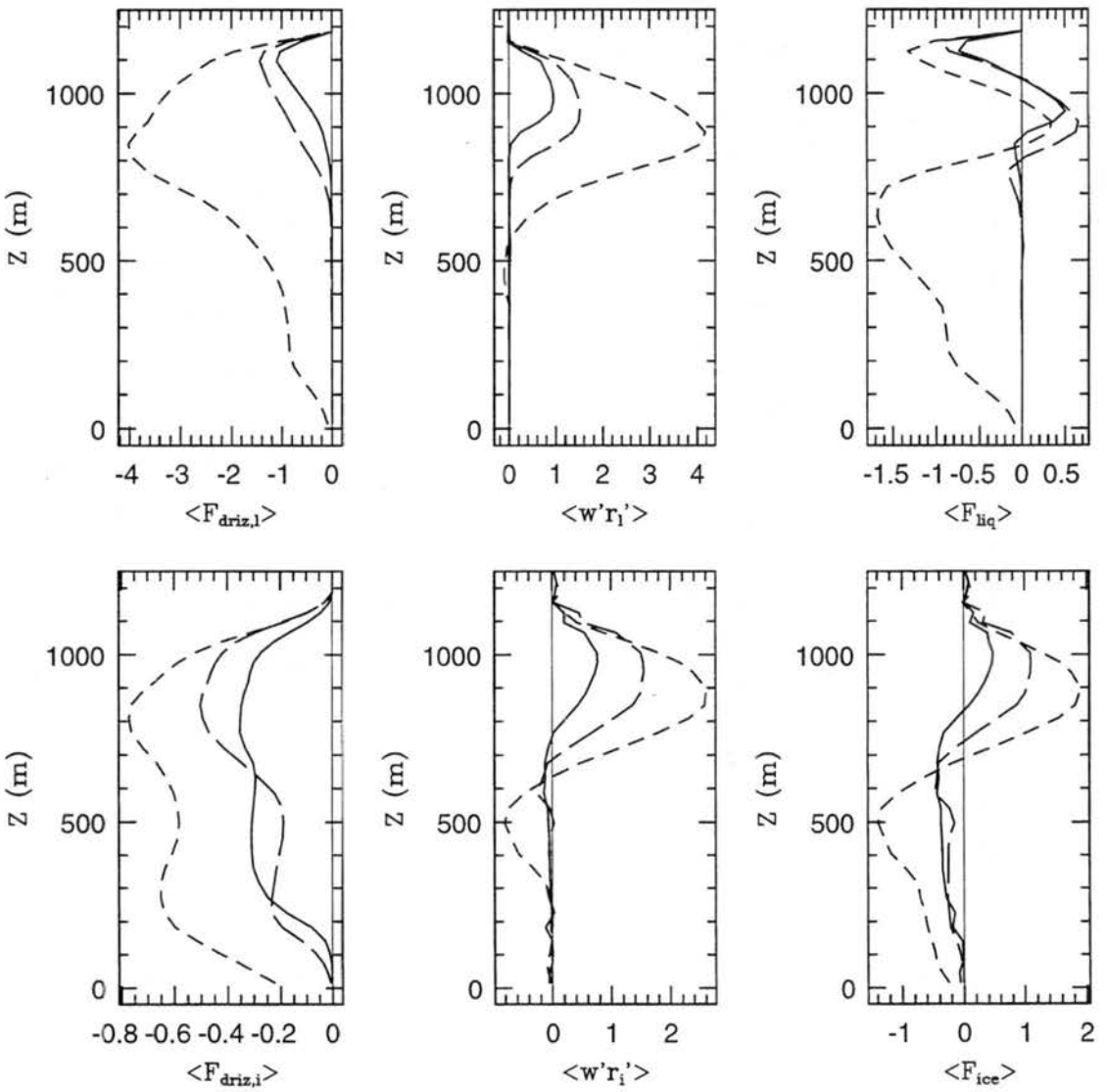

Figure 7.18: Profiles of fluxes of condensed species for 5CTRL for the 6-8 hour period of simulation time in 1 hour increments. Units are in $kg\ kg^{-1}\ m\ s^{-1} \times 10^{-5}$. The solid line denotes fields at hour 6, long-dashed line denotes 7 hours, and short-dashed line denotes 8 hours.

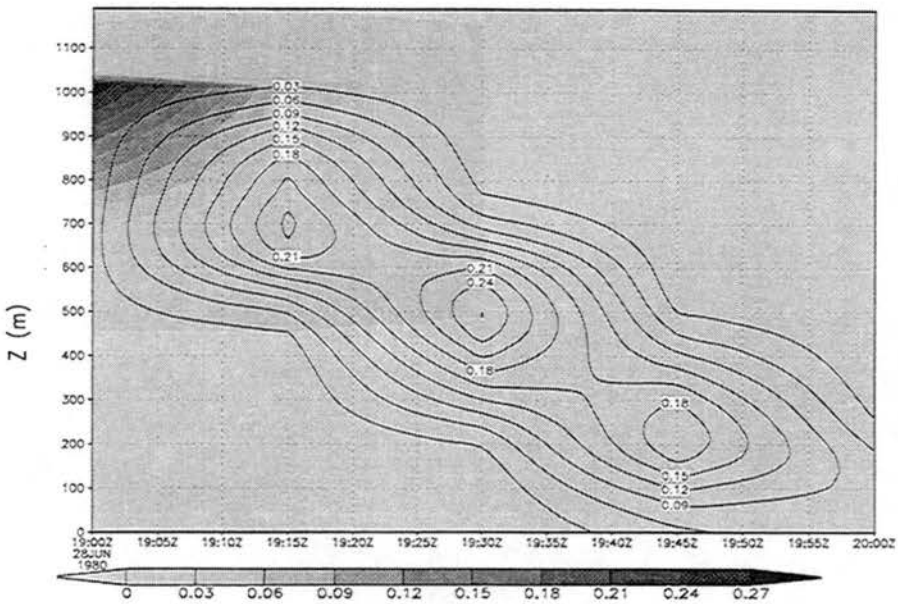

Figure 7.19: Time Series: LWC (shaded) and IWC (contoured) for 10CTRL in $g\ m^{-3}$.

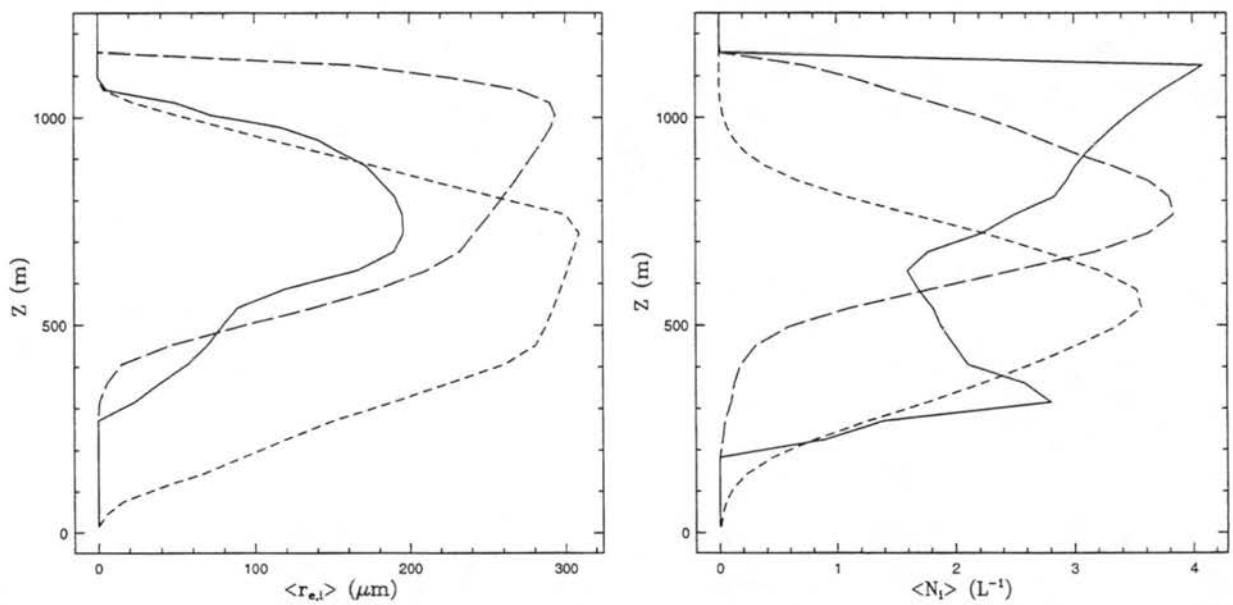

Figure 7.20: Profiles of ice effective radius ($r_{e,i}$) and ice concentration (N_i) for 10CTRL over the coarse of 0.5 hour of bin simulation. Solid line denotes 4 hours, long-dashed line denotes 4.25 hours, and short-dashed line denotes 4.5 hours of simulation time.

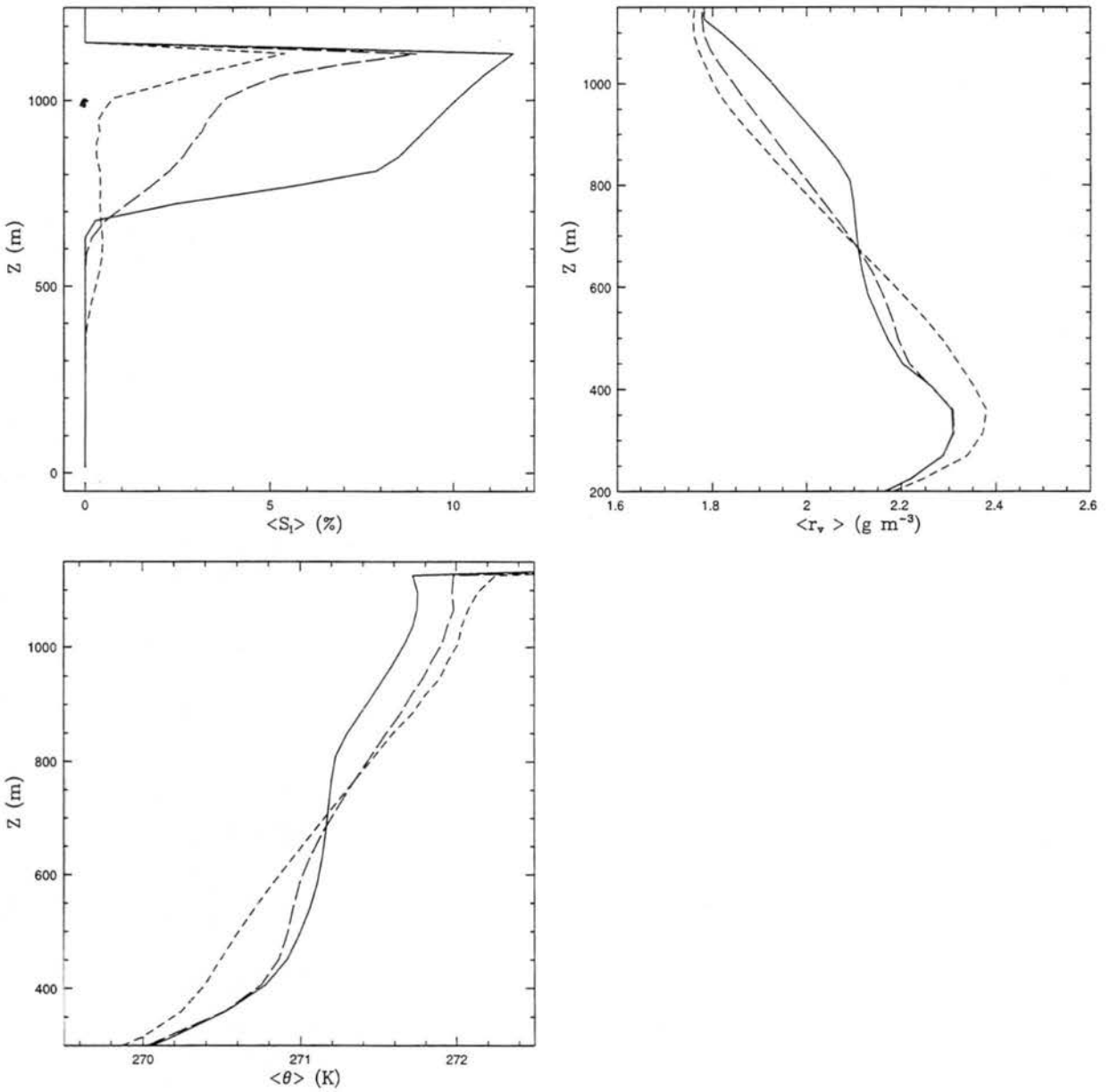

Figure 7.21: Profiles of ice supersaturation (S_i), θ, and water vapor mixing ratio (r_v) for 10CTRL over the coarse of 0.5 hour of bin simulation. Solid line denotes 4 hours, long-dashed line denotes 4.25 hours, and short-dashed line denotes 4.5 hours of simulation time.

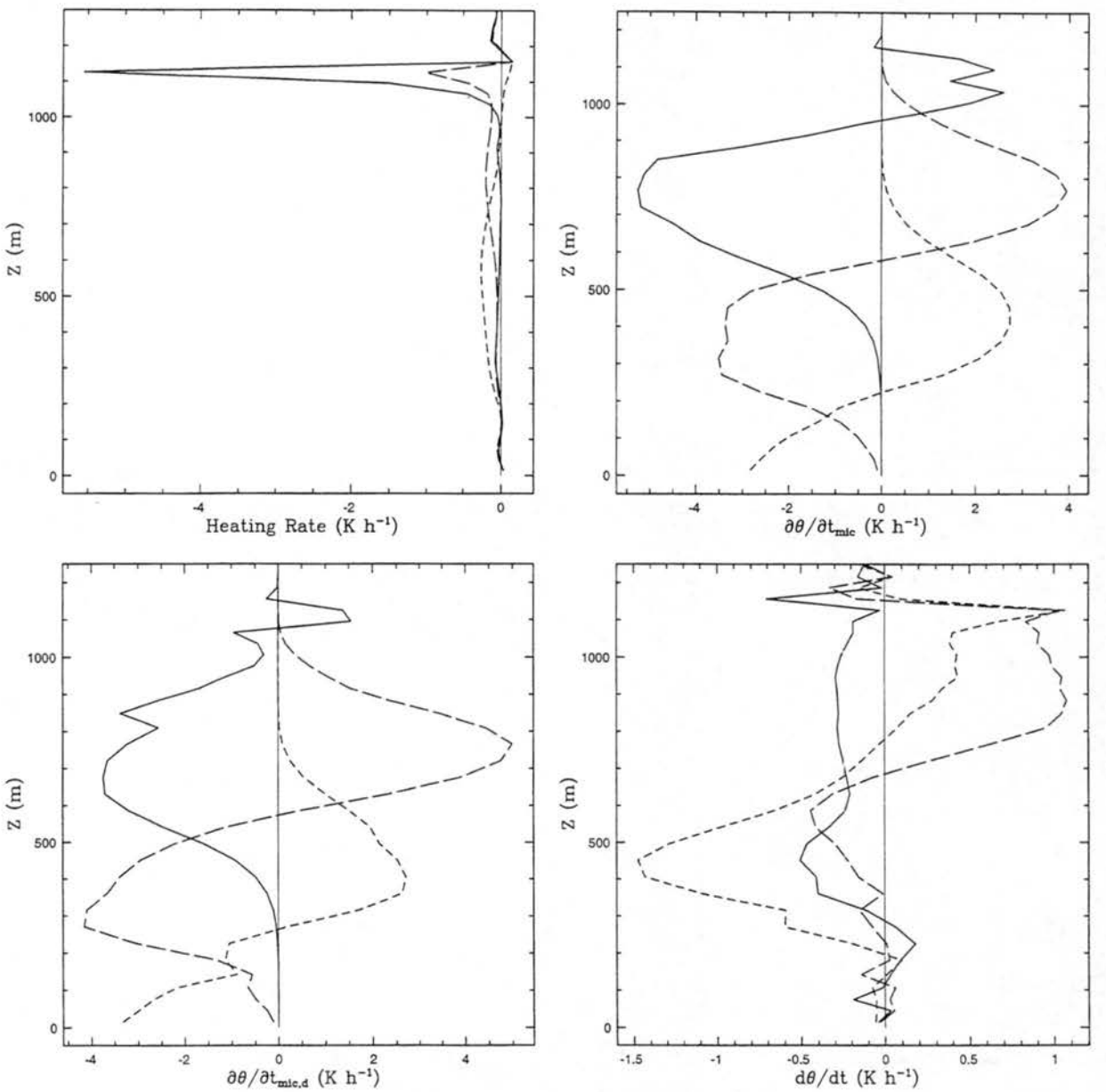

Figure 7.22: Profiles of θ-tendencies including radiative heating rate (Heating Rate), microphysical heating rate ($\partial\theta/\partial t_{mic}$), microphysical heating within downdrafts ($\partial\theta/\partial t_{mic,d}$) and total heating rate ($d\theta/dt$) for 10CTRL over the coarse of 0.5 hour of bin simulation. Solid line denotes 4 hours, long-dashed line denotes 4.25 hours, and short-dashed line denotes 4.25 hours of simulation time.

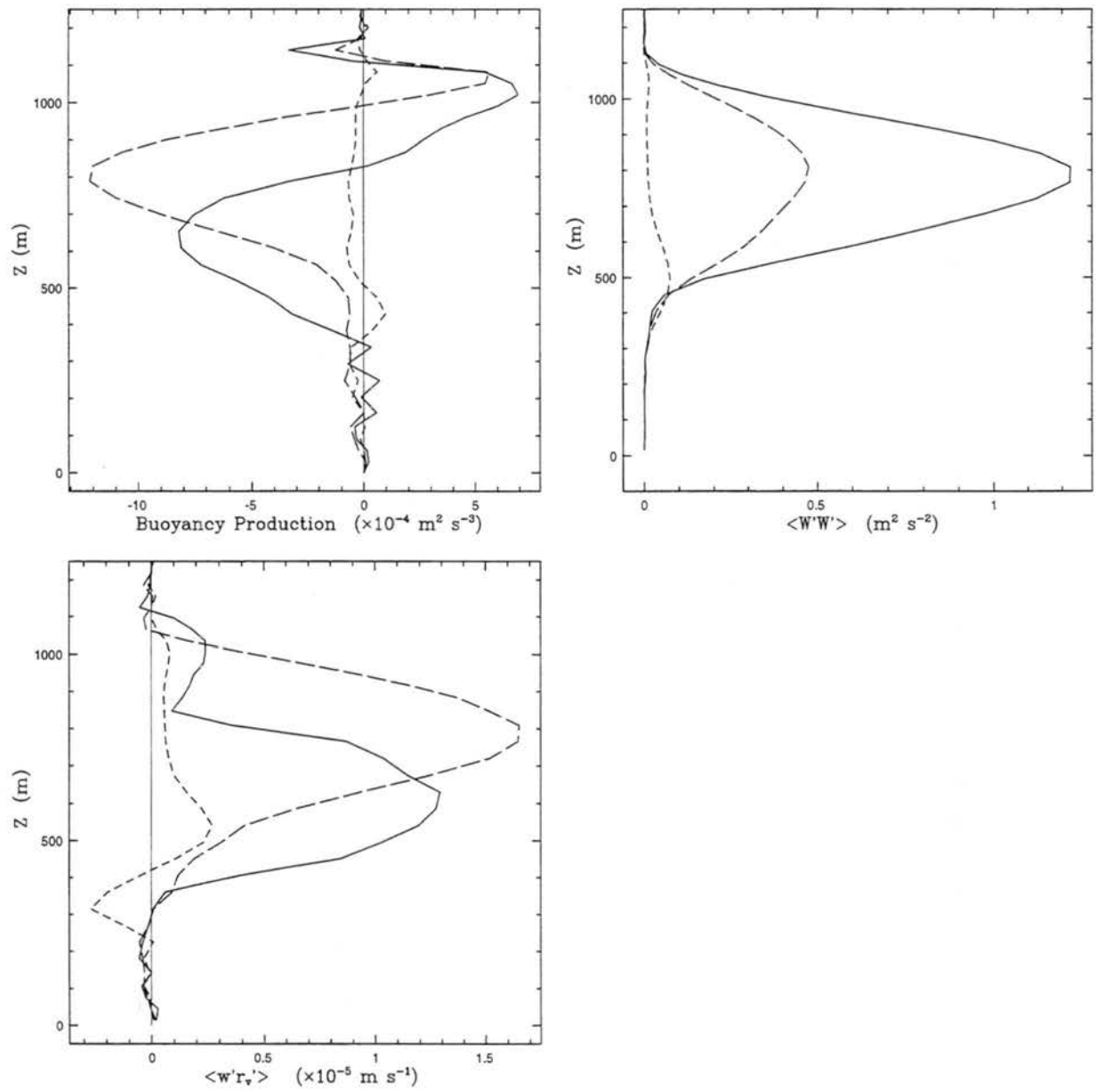

Figure 7.23: Profiles of buoyancy production, $< w'w' >$ and $< w'r_v' >$ for 10CTRL over the coarse of 0.5 hour of bin simulation. Solid line denotes 4 hours, long-dashed line denotes 4.25 hours, and short-dashed line denotes 4.5 hours of simulation time.

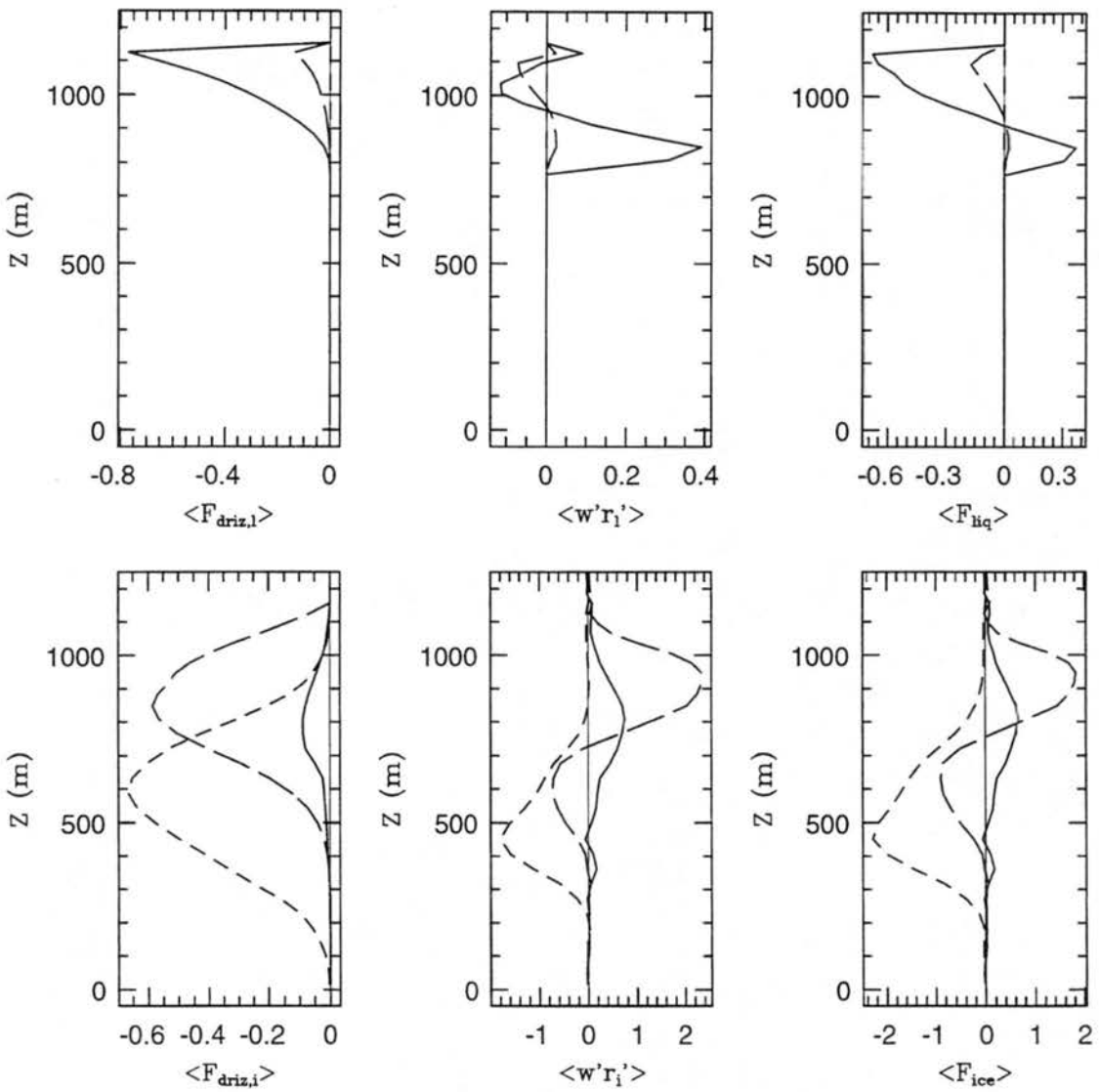

Figure 7.24: Profiles of fluxes of condensed species for 10CTRL for the 4 - 4.5 hour period of simulation time in 15 minute increments. Units are in $kg\ kg^{-1}\ m\ s^{-1} \times 10^{-5}$. The solid line denotes fields at hour 4, long-dashed line denotes 4.25 hours, and short-dashed line denotes 4.5 hours.

Chapter 8

TRANSITION SEASON ARCTIC STRATUS: SENSITIVITY SIMULATIONS

In this chapter we explore the ice processes that contribute to the differing behavior between the simulations. As connections between ice concentration, vapor growth rates, and indirect effects on radiative cooling are important to layer stability, we focus particular attention on these areas. As the ice bin microphysical computations are extremely costly (taking 150 CPU seconds to compute a single 2 second time-step), we attempt to exercise some foresight since the simulations may only be done for a few portions of parameter space.

8.1 Sensitivity simulation designs

Table 8.1 lists the set of sensitivity simulations conducted with the bin microphysical model (the control simulations of the last chapter are included as a reference). We adopt the general procedure of examining the sensitivities to 5CTRL first, following the natural flow of the simulated temperature transition. This table lists the physical processes which are considered to be the most important in the production of the stable and unstable cloud layers. Of course, temperature changes are already implicit in the different simulations. Numerical experiments are conducted in which physical processes are systematically removed or perturbed in order to examine the effects on the system. Many simulations are listed in the table, however, in a lot of the cases the important difference may be illustrated with few figures (thus, the list is not as daunting as it may first appear).

As ice production mechanisms appear to be of paramount importance in terms of liquid water reduction, mitigation of cloud top radiative cooling, and cloud-scale dynamics, we alter processes within the ice bin microphysical framework in order to ascertain their

Simulation	N_{IN}	N_{ccn} cm^{-3}	Collection	Sedimentation	Habit
5CTRL	Stand.†	100	Yes	Yes	Oblate‡
10CTRL	Stand.	100	Yes	Yes	Oblate
5NC	Stand.	100	No	Yes	Oblate
5NS	Stand.	100	No	No	Oblate
5C2IN	Twice	100	Yes	Yes	Oblate
10NC	Stand.	100	No	Yes	Oblate
10INH	Half	100	Yes	Yes	Oblate
10INT	Tenth	100	Yes	Yes	Oblate
10HAB	Stand	100	Yes	Yes	Sphere

Table 8.1: Transition-season simulations. Listed is the acronym for the simulation and the physical processes utilized. † Stand. means than standard ice nucleation formulas are utilized; sensitivities either increase or decrease these amounts as specified. ‡ Oblate spheroids are the habit used for most simulations; the second habit option is that of spheres.

importance in the production of self-maintained systems. Since the production of large ice crystals and sedimentation appear to be quite important to the differences between the 5CTRL and 10CTRL simulations, computations are done which systematically remove these processes in the $5°C$ cooled simulations. The ice collection mechanism is removed in the 5NC simulation, while both ice collection and ice sedimentation are removed in 5NS. Between these two simulations the importance of ice fall speeds and ice growth is exposed. This is also considered in the 5C2IN experiment in which ice nuclei concentrations are doubled. In this simulation, not only are sedimentation rates decreased, but ice concentrations are similar to those in 10CTRL. By comparison with 10CTRL, the importance of temperatures and ice concentrations on layer stability is ascertained.

A set of somewhat different simulations is conducted for the $10°C$ cooled case. Once again, the effects of collection mechanisms on the cloud layer are explored in the 10NC simulation. Runs without sedimentation are not included as this would increase the rapidity of cloud collapse and therefore would not produce any significant information as concerns the reasons for the collapse. Simulations that systematically reduce the IN concentrations by half (10INH) and one tenth (10INT) the values at four hours illustrate the effects of larger ice crystals with less integrated surface area (which affects deposition) on the system stability. We expect that ice crystal habit may also play a role in the cloud collapse, and

it is felt that the biggest influence of habit may be on the residence time of the ice crystals in the liquid layer. In order to explore this, a simulation is conducted with ice spheres (10HAB) as they have the largest terminal fall speed of any ice crystal and, thus, using them sets an upper limit on this process.

We begin, in the succession shown in Table 8.1, by examining the $5°C$ sensitivity simulations in the next section.

8.2 Sensitivity to collision-coalescence: 5NC

The similarity between the LWC and IWC content time-series for 5NC (Fig. 8.1) and 5CTRL in Fig. 7.6 shows that the effects of collection on the evolution of the mixed-phase cloud system are small. Both systems evolve in similar fashions with an initial period of rapid ice production followed by a somewhat constant period of ice production and sedimentation from the liquid layer. Liquid water contents in 5NC, however, maintain larger values as compared to those in 5CTRL, throughout the simulation period. Without the effects of collection, ice effective radii ($r_{e,i}$ in Fig. 8.2) increase more slowly than in 5CTRL (Fig. 7.9). Ice growth at the expense of liquid is, therefore, suppressed in 5NC as a comparison of $\partial\theta/\partial t_{mic}$ for each case shows (Fig. 8.3). Only within a narrow region at cloud top is ice growth larger in 5NC which is due to the smaller sedimentation rates in 5NC.

Collection affects appear to have a significant impact on the radiative budget, however a weaker impact on the thermodynamic structure of the mixed-phase layer. As was noted in the last chapter, cloud LWCs are influenced by the amount of cooling that occurs within the mixed-layer. Differences between control and sensitivity profiles are illuminating as small effects can be quantified. For the remainder of this chapter, profiles of differences are done with respect to the control simulations and defined as,

$$\Delta X = X_{ctrl} - X_{sensitivity} \tag{8.1}$$

where X is some physical quantity. The 5NC layer is consistently cooler than 5CTRL (as $\Delta\theta$ shows) and is due to two factors. First, the depositional heating of the majority of the cloud layer is greater in 5CTRL. Second, cloud top cooling rates are greater in 5NC

with values that persist near -2.8 $K\ h^{-1}$ in 5NC (Fig. 8.3), whereas in 5CTRL (Fig. 7.11) maximum cooling rates drop from about -2.5 $K\ h^{-1}$ at 4.5 hours to -2.0 $K\ h^{-1}$ at 5 hours (Fig. 7.16). These greater cooling rates, as much as 0.8 $K\ h^{-1}$ ($\Delta Heating\ Rate$), produces the cooler cloud top in 5NC ($\Delta\theta$). The regions below cloud base also cool more in 5NC because of the slower settling velocities of the ice crystals.

If ice precipitation is important for the stability of the liquid cloud layer, then what is the the approximate time period required for the removal of ice by sedimentation before cloud collapse occurs (once significant ice production is initiated)? By deactivating the ice sedimentation process, we can gain an upper estimate on this time scale.

8.3 Sensitivity to sedimentation: 5NS

The importance of ice sedimentation to the stability and structure of the mixed-phase layer is ascertained by removing the effects of sedimentation during the simulation. With the effects of sedimentation removed, ice crystals quickly deplete all of the liquid water (Fig. 8.4) within a 0.5 hour time period (4 to 4.5 hours) and shows how fast the conversion of LWC to IWC through the Bergeron-Findeisen process occurs. Thus, the sedimentation of IWC during the 0.5 hour time period is crucial to the stability of the liquid layer. Ice crystals grow rapidly in size (Fig. 8.4) through deposition to around 400 μm and retain this size throughout the 4 to 6 hour simulation period. This limiting size of ice crystal depositional growth is in accord with the results of Harrington (1994) which showed a theoretical limiting size for deposition of about 500 μm.

The thermal and moisture structure of the cloud and sub-cloud regions are strongly affected by sedimentation. Ice crystal deposition rates cause rapid reductions in water vapor amounts (r_v in Fig. 8.5) through the fifth hour of the simulation, however are not affected during the 5 to 6 hour period. Even though the microphysical heat rates are large at 4 hours ($\partial\theta/\partial t_{mic}$), these values are rapidly reduced as LWCs are depleted. Values of θ are only slightly affected by the deposition rates between 4 and 5 hours as continued radiative cooling (Fig. 8.5) offsets the total depositional heating. Continuous radiative cooling rates which have smaller magnitudes (about 0.5 $K\ h^{-1}$) but occur over greater

depths than the liquid cloud layer causes gradual cooling of the cloud and sub-cloud layers. Thus, ice sedimentation is quite important for the redistribution of moisture along with the cooling and stabilization of the boundary layer. In addition, the pure ice cloud cools at a much lower rates since radiative effects are reduced through lower ice concentrations and smaller projected areas (see Chapter 3).

The importance of sedimentation for mixed-phase layer stability is punctuated by simulations with the bulk microphysics of Walko *et al.* , (1994) (discussed in Chapter 2). In these cases, ice is allowed to sediment in two ways; the first method uses an integrated value of the terminal fall velocity while the second method uses a more accurate bin sedimentation routine (thus large ice crystals can fall faster). The bulk sedimentation formulation causes both $5°C$ and $10°C$ cooled cases to collapse by the fifth hour of the simulation while the bin sedimentation produces a cloud layer which is in rough agreement with the temporal evolution in 5CTRL and 10CTRL. The reason for the difference is that the bulk formula increases the in-cloud residence time of the ice crystals. Since ice depletion of liquid water through deposition occurs quickly, accurately computing the sedimentation of ice crystals is crucial for mixed-phase cloud stability in this case.

Since ice sedimentation is important during the 0.5 hour period after the initial production of significant IWC, ice concentrations should have a strong effect on the stability of the cloud layer. This effect is studied in the next section.

8.4 Sensitivity to ice concentration: 5C2IN

The doubling of ice concentrations in the $5°C$ simulation not only elucidates the importance of IN concentrations, but also shows that multiple liquid cloud layers may be formed through ice microphysical, radiative and dynamical interactions. The larger ice concentrations increase in-cloud residence times by reducing ice precipitation, thus causing more rapid reductions in LWCs than 5CTRL (Fig. 8.6). By the fifth hour of the simulation all that remains is a thin, tenuous cloud layer of about 150 m depth (Fig. 8.7). The doubling of ice concentrations from maxima of 2 L^{-1} to 4 L^{-1}, which is well within the range of observed IN concentrations in the Arctic (Curry *et al.* , 1996), not only

causes rapid reductions in LWC but also assists in the production of a lower liquid cloud layer. This layer is not transient and, therefore, its formation and maintenance constitutes a potentially new mechanism of layer formation in Arctic low-cloud systems. This section is broken into two parts, the first contrast the ice production in this case with the control while the section focuses on the layer formation mechanism.

8.4.1 Comparison with 5CTRL and 10CTRL

Even though ice concentrations are similar to 10CTRL within the vicinity of cloud top (compare Figs. 8.7 and 7.20) ice production rates are slower in 5C2IN because the equilibrium vapor pressure differences are greater in 10CTRL, allowing ice to grow faster at the expense of liquid drops in that case. Low concentrations of liquid water drops remain at cloud top after four hours of simulation (Fig. 8.7) as ice growth affects small drops the most causing them to rapidly evaporate.

As ice contents are increased through enhanced deposition rates, in-cloud water vapor amounts are reduced while θ-values are increased over 5CTRL because of the larger deposition rates ($\partial\theta/\partial t_{mic}$ in Fig. 8.8). This contrasts 5CTRL in which θ decreases in time due to relatively constant cloud top radiative cooling. Only near cloud top is θ reduced over the 4 to 5 hour period through radiative cooling, as depositional heating does not dominate the cloud top heat budget (Fig. 8.8). Lower layers begin to cool in time through radiation as the upper cloud layer becomes thin. The sub-cloud layer is rapidly cooled and moistened through increased sublimation (Fig. 8.8) brought about by longer periods of ice precipitation. The rapid stabilization processes apparently cause a transition from a predominately mixed boundary layer to one with a larger stable layer. Thus, it seems plausible that some of the stable autumnal cloud regimes observed by Pinto (1997) may be produced through ice precipitation (which was continually occurring in his cases).

Circulation strengths ($< w'w' >$) weaken as buoyant production of TKE is reduced concomitantly with radiative cooling (Fig. 8.9). By 5 hours, the circulations are confined to a shallow layer near $1000m$.[1] Lower level circulations are initiated by 4.5 hours as

[1]Such shallow, coherent structures have recently been detected in thin, tenuous ASC (Reuter, personal communication). Previous work in the literature have shown deep eddy structures within thick ASC.

cooling, moistening and ice mass loading increase buoyancy production of TKE. Once the ice has been removed, these circulations are maintained by radiative cooling at the top of the ice-produced humidity inversion (Fig. 8.8). The low level circulations produced water vapor flux convergence ($< w'r_v' >$) at 5 hours, thus setting the stage for the initiation of the lower cloud deck.

8.4.2 Multi-layer formation and maintenance

The cooling and moistening of the 200-400m layer, along with the production of circulations through radiative cooling, causes the formation of a second liquid cloud after 5.5 hours of model integration (Fig. 8.6). Once the majority of the ice mass precipitates out of the region, particularly the small ice crystals which have long in-cloud residence times (r_e in Fig. 8.10), water saturations can build up. Droplets are initiated as vertical motions produce water supersaturations ($r_v > r_{v,s}$ in Fig. 8.10) by about 5 hours. These droplets are formed by activation, not drizzle processes as the small number of drizzle drops (N_r) in the lower layer, along with the the small drop sizes in the distribution function ($n(D)$ at 5 hours indicates.

Once the upper layer has thinned, and the lower layer has formed, significant θ-reductions occur within each cloud layer (Fig. 8.11). This cooling is caused by radiative cooling which strongly influences the total cooling rate ($d\theta/dt$ in Fig. 8.11). The high correlation between the total and radiative cooling rates indicates that condensational heating must be small; this is corroborated by the small reductions in r_v and increases in N_t with time. The weakness of the circulations (Fig. 8.12) shows that continued condensation is caused by cooling through radiation. As condensation processes are slow, both layers remain quite tenuous as the infrared optical depth ($\tau_{infrared}$) shows. In time, the lower liquid layer forms a cloud-top inversion through the strong differential in radiative cooling and takes on the character of a cloudy mixed-layer.

The slow changes in LWC and IWC for both the upper and lower decks suggests a balance between in-cloud production and drizzle. Indeed, the relatively constant N_t values (Fig. 8.10) with time and the constant-with-height N_i profiles corroborate this. The fact that the drop distribution, $n(D)$, varies slowly in the lower cloud deck suggests that

the microstructure here is also fairly constant. Ice crystals precipitating from the upper layers are dominated by large ice crystals ($r_{e,i}$ in Fig. 8.10) which is to the benefit of the lower liquid layer as these crystals quickly fall through the layer with little impact. Such behavior appears to be characteristic of autumnal mixed-phase cloud layers, as suggested by the data of Pinto (1997).

The maintenance of the upper and lower deck, in the presence of continued loss of water mass through precipitation, appears to be mostly due to radiative cooling effects which allows for further condensation and the maintenance of buoyancy production. Convergence of water vapor fluxes ($< w'r_v' >$ in Fig. 8.12) below both cloud decks adds vapor to the liquid layers and, in conjunction with the cooling, assists the slow condensation process. As the upper deck attains larger water mass, circulations within the deck strengthen and deepen in response to the stronger cooling rates and larger water mass loadings. This leads to a continual increase in buoyancy production which fuels the circulations ($< w'w' >$). Unlike the upper deck, buoyancy production within the lower deck diminishes in time (Fig. 8.12) as does the associated fluxes. The LWC of the lower deck does not change rapidly (Fig. 8.6), and appears to be maintain by continued radiative cooling (Fig. 8.11).

This potential form of layering falls outside the classification regime defined by Curry *et al.* , (1988) as the lower and upper cloud decks show characteristics of shallow mixed-layers. The classification scheme of Curry *et al.* , (1988) includes combinations of stable-layers and mixed-layers but not two liquid mixed-layers. The production of this lower layer is dependent upon the rapid glaciation of the upper cloud deck and reduction of its optical depth in time. Whether such glaciation periods occur within true mixed-phase ASC is not known, although the results of Pinto (1997) and the lidar observations of Grund (personal communication, Fig. 7.7) show that observed mixed-phase systems undergo rapid periods of glaciation. In addition to this, the results shown above illustrate that transitions from mixed-layers to stable-layers may occur through the ice precipitation and sublimation. This may occur in autumnal boundary layers such as those discussed by Pinto (1997).

8.5 Sensitivity to collision-coalescence: 10NC

As we have seen in the $5°C$ cooled simulations, combinations of ice concentrations, sizes, and sedimentation rates are important for mixed-phase cloud stability. Thus, we explore the effects of large ice crystals on the $10°C$ cooled simulation through the deactivation of the ice collection processes in order to ascertain its importance to boundary layer collapse.

Collection processes, as in the 5NC case, have little effect on the evolution of the $10°C$ cooled system. The suppression of collection events causes the production of fewer large ice crystals which affects the sedimentation and deposition processes within the liquid cloud layer. The cloud topped boundary layer still collapses, however LWCs are larger in 10NC (Fig. 8.13) than in 10CTRL (Fig. 7.19) by a small amount at 4.25 hours; this appears to be the only microphysical difference between the simulations. The main effect of the suppression of collection events is the reduction in deposition rates, which affects the thermodynamic structure of the boundary layer. Temperatures within the region of the liquid cloud layer rise more rapidly (while r_v values decrease more rapidly) in the 10CTRL case as shown by profiles of the differences between the θ and r_v variables of the 10CTRL and 10NC cases ($\Delta\theta$ and Δr_v, Fig. 8.13). Water vapor mixing ratios increase more rapidly below cloud in the control simulation (10CTRL) as quickly sedimenting large ice crystals increase sublimation rates, and therefore r_v values, within the sub-cloud layer. Even though the profiles of the heating rates due to deposition are similar between the two cases (compare $\partial\theta/\partial t_{mic}$ between Figs. 8.13 and 7.22), in-cloud deposition rates and sub-cloud sublimation rates are shown to be larger in 10CTRL ($\Delta\partial\theta/\partial t_{mic}$). Although the suppression of collection reduces deposition, the effect is quite small and attributed to the fact that, as concentrations are weakly affected by collection in these cases, the production of a few large ice crystals in 10CTRL allows for slightly more deposition in that case.

Since the effect here is small, it would be difficult to argue that the production of large ice crystals enhances the collapse of the boundary layer. This analysis does, however, shed light on the fact that simply increasing ice sizes may not result in increasing the mixed-phase cloud stability. In order to explore the effects of large ice crystals further we examine sensitivities to concentrations in the next sections.

8.6 Sensitivity to reduced concentrations: 10INH

The discussion presented above suggests a three-fold importance of ice concentrations. First, ice concentrations affect net depositional growth and, thus heating (cooling) and drying (moistening). Second, ice concentrations affect the production of large ice crystals and, therefore the vertical structure of the IWC. In-cloud residence times of IWC feeds into the importance of depositional growth. Third, ice concentrations directly and indirectly affect cloud top radiative cooling rates by converting large numbers of droplets to smaller numbers of ice crystals (thus, reducing the integrated surface area) which have smaller projected areas than liquid drops (see Chapter 3). If increasing ice concentrations decreases stability in the $5°C$ simulations, then reductions in ice concentrations should increase it in the $10°C$ cases.

Reducing concentrations in this simulation by half, so that ice concentration maxima match those of the 5CTRL simulation (N_i in Fig. 8.14), still produces a collapsing boundary layer, however it occurs more gradually. Ice water contents produced are larger than those produced in 5CTRL (Fig. 7.9) over the 4 to 5 hour period, since the vapor pressures are lower in the $10°C$ cooled cases. Ice production rates are reduced in this case as compared to 10CTRL because the larger ice crystals produced precipitate much more quickly from the layer. This causes a reduction in the depositional heating of the cloud layer in this case (compare Fig. 8.14 and 7.22). Depositional heating still dominates the θ-tendencies causing increases in θ as compared to 4 hour values (Fig. 8.14).

Comparisons of IWCs are somewhat limited as IWC amounts are larger at 4 hours in the $10°C$ cases, thus a comparison of the total rate of change in IWC among the simulations may be illuminating (Fig. 8.15). As expected, clouds which collapse have the strongest IWC production rates. However, a comparison amongst the cases which produce the greatest ice amounts (*i.e.* 10CTRL, 10INH and 5C2IN) shows similar rates of IWC production rates. In fact 5C2IN, which was on the verge of collapse, has an IWC production rates just below those of the $10°C$ cases. Comparing the 4.25 hour values, it would appear that an IWC production rate exceeding 0.05 $g\ m^{-3}\ h^{-1}$ is required for cloud collapse in these cases.

Since ice concentrations similar to those in 5CTRL still produce a collapsing layer, it is evident that even lower ice concentrations are required in the cooler case to produce a stable cloud layer. The next section reduces concentrations further to explore this possibility.

8.7 Sensitivity to concentrations: 10INT

The reduction of ice concentrations by 1/10 the initialization values produces a mixed-phase system that is colloidally stable (Fig. 8.16). In this case, IWCs are produced more slowly than in 10CTRL (Fig. 7.19) and precipitate much more quickly from the liquid layer. In fact, IWCs are less than half that produced in 10CTRL (Fig. 7.19) and are even slightly less that those produced in 5CTRL (Fig. 7.9). Behavior of the LWC layer over the 4 to 5 hour time period is similar to that of 5CTRL (compare Figs. 8.16 and 7.6), however reductions in LWC are much less owing to the small ice concentrations (Fig. 8.17).

The rapid removal of large ice crystals from the upper layers of the cloud clouds affects the water vapor (r_v) and θ profiles (Fig. 8.18) differently than in 10CTRL (Fig. 7.21). Because IWC production rates (Fig. 8.18) are smaller than 10CTRL, but similar to 5CTRL (Fig. 8.15), net depositional heating ($\partial\theta/\partial t_{mic}$) does not offset cloud top radiative cooling. Thus, the layer is able to cool ($d\theta/dt$ and θ) , unlike 10CTRL. The continued radiative cooling produces strong cloud top negative buoyancy which continually feeds the circulations. The weaker ice production rates, in conjunction with rapid sedimentation, causes less moistening and cooling of the sub-cloud layer ($d\theta/dt$, θ and r_v) than in the 5CTRL or 5C2IN cases. The weaker stabilization of the lower layers, due to smaller ice production and greater precipitation rates, produces a boundary layer structure which is much more similar to that of a pure liquid phase mixed-layers.

Since ice sedimentation is so important, it is natural to expect that ice habit will play a role in cloud stability. This is explored in the next section.

8.8 Sensitivity to ice habit: 10HAB

Since alterations in deposition and sedimentation rates significantly affect cloud stability, changes in ice crystal habit may be an important effect. Ice crystals have a broad spectrum of terminal fall speeds with dendrite crystals (which fall slowly) and ice spheres

(which fall quickly) making up the two extremes (Pruppacher and Klett, 1997). Since oblate spheroids have fall speeds more closely associated with plate crystals (and, thus, have slower fall speeds), we choose to use ice spheres so that the two simulations, 10CTRL and 10HAB, will approximately cover the two extremes. Since ice sedimentation velocities are large in 10HAB, in-cloud residence times of ice crystals are reduced dramatically as ice crystals quickly sediment out of the liquid layer (Fig. 8.19). The initial thinning of the liquid layer is greater than the 5CTRL simulation (Fig. 7.6), however enough LWC persists to drive cloud circulations through cloud top radiative cooling. Ice content reduction occurs rapidly (Fig. 8.20) as ice spheres precipitate quickly from the cloud layer at smaller sizes ($r_{e,i}$). Thus, less IWC needs to be produced before rapid sedimentation occurs.

Ice crystals precipitate rapidly enough away from the cloud top region so that depositional heating ($\partial\theta/\partial t_{mic}$) does not dominate the total heat budget ($d\theta/dt$), thus cloud top cools in time through radiative effects (θ in Fig. 8.21). The weak deposition rates produce only slight reductions in water vapor contents (r_v) at cloud top. This contrasts the 10CTRL simulation in which rapid reductions in r_v and increase in θ occur because of the large deposition rates. Ice convergence (Fig. 8.20) at mid-cloud levels (700 to $900m$) increases deposition rates causing rapid LWC and r_v reductions and, thus, heating of the mid-cloud layer. The precipitation of large amounts of ice through the sub-cloud regions causes rapid cooling and moistening ($\partial\theta/\partial t_{mic}$, θ and r_v) which stabilizes the layer. The effect is not as strongly pronounced as it is in the $5°C$ cases since ice spheres precipitate much more rapidly. Since LWCs at cloud top are not completely depleted, radiative cooling (Heating Rate in Fig. 8.21) continues to drive circulations allowing the persistence of the upper cloud deck. As Fig. 8.19 shows, IWC production was on the verge of completely converting all of the LWC. Ice production rates ($d(IWC)/dt$, not shown) maximize at $0.046\ g\ m^{-3}\ h^{-1}$, just slightly below the $0.05\ g\ m^{-3}\ h^{-1}$ value deemed necessary for cloud collapse to occur.

Thus, if ice crystals with large sedimentation velocities are produced by the cloud layer, a cooler layer can accommodate larger ice concentrations (in this case, up to 10 times as much) and still retain its stability. It appears that the key to stability of the

cloud layer may be related to whether or not ice crystals within the vicinity of cloud top have deposition rates that are large enough to deplete the LWC there. If this is not the case, and as long as the LWC is sufficient to continue to drive some weak eddies (as in the 5C2IN simulation) through radiative cooling, the cloud layer may persist without collapse of the boundary layer.

8.9 Summary of sensitivity study results

In this chapter we discussed sensitivities to the control simulations presented in Chapter 7 in order to ascertain how important ice phase processes are to the maintenance of mixed-phase ASC layers. From the previous chapter, we found that at $5°C$ cooling a self-maintaining mixed-phase ASC system was produced while larger ice production rates in the $10°C$ cooled case caused the collapse of the cloud layer. In the case of the non-collapsing system (5CTRL), it was found that the ice phase redistributes moisture and cools the lower boundary layer through the sedimentation and sublimation of the ice crystals. The amount of cooling that occurs is dependent upon the amount of ice produced within the liquid layer and on the rate of precipitation. If ice amounts are great enough, and sedimentation rates slow enough, the lower portion of the boundary layer can be stabilized by this process. Ice crystals that sediment slowly (such as hexagonal plates) have the greatest potential for modification of the lower boundary layer. Ice crystals that sediment quickly (such as spheres) modify the lower boundary layer little. In fact, clouds that produce small amounts of ice precipitation (such as 10INT) show the same small effects on the lower layer as the case with quickly sedimenting ice crystals. The effects of collection on the layer evolution were shown to be small. Even though IWC became large through condensation, ice concentrations were small enough so that significant collection did not occur.

Radiative cooling rates that exceed warming through deposition were shown to be important for the maintenance of the mixed-phase layers. In cases where the deposition rates were high ($10°C$ cooling with large ice concentrations), ice production within the liquid cloud is large and, thus, the cloud layer warms as liquid water amounts are depleted. Ice crystal concentrations were determined to be highly important for the maintenance

of the liquid cloud layer as deposition rates and in-cloud residence times are affected by this quantity. Indeed, a small range of ice concentrations (0.4 to 4 L^{-1}) exists over which stable mixed-phase layers may persist. The warmer clouds ($5°C$ cooling) showed that a doubling of ice concentrations did not produce collapse of the boundary layer. In fact, enhanced ice production rates assisted in the production of a lower liquid cloud layer. Ice crystals performed two functions in the production of the second cloud layer; the first was the reduction in the upper cloud optical depths so that lower portions of the boundary layer can cool in the infrared. The second function was the modification of the lower boundary layer through moistening and cooling (sublimation) which produced a moist layer at about $400m$. The liquid layers produced in this case do not fall into the multiple layer categories set forth in Curry *et al.* (1988) as the lower cloud layer produces a lower, shallow mixed-layer.[2] Colder clouds ($10°C$ cooling) glaciate much more rapidly and, thus, ice concentrations must be lower in order to form persistent mixed-phase layers. Indeed, ice concentrations lower than $1L^{-1}$ were needed in order to stop the collapse of the boundary layer in these cases. The predominate affect of reducing concentrations was the reduction in net deposition rates, thus allowing the ice produced within the liquid layer to sediment before significant LWC removal occurred. The $10°C$ cooled system was able to produce a persistent mixed-phase cloud with larger ice concentrations if an ice habit with greater terminal fall-speeds was utilized. Even with rapid sedimentation rates, significant LWC was depleted through the Bergeron-Findeisen process.

It is interesting to note that Pinto (1997), by using a similar heat budget analysis, shows that the stability of an observed autumnal mixed-phase system is highly dependent upon the balance between the condensational growth of drops, the depositional growth of ice, and the maintenance of cloud top radiative cooling. Pinto concludes that ice nuclei concentrations are highly important for the stability of the mixed-phase layer; which is similar to the conclusions drawn here for idealized mixed-phase ASC. In addition, Pinto's (1997) case is similar to our idealized case in thermodynamic and microphysical structure.

---

[2]The summertime ASC cases discussed by Curry *et al.* (1988) show lower cloud layers that exist predominately in a stable environment.

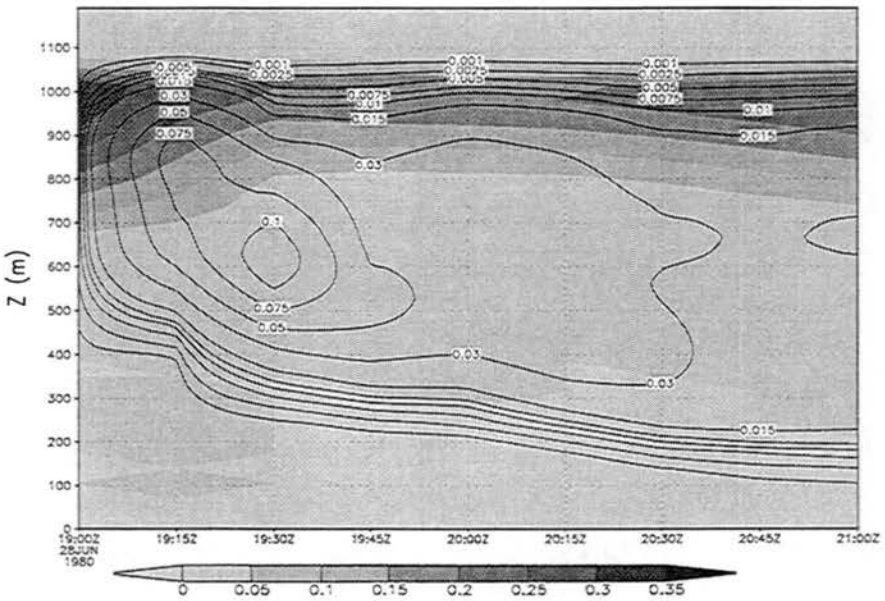

Figure 8.1: Time Series: LWC and IWC for 5NC. Values of LWC are shaded while IWC are contoured, values are in $g\ m^{-3}$.

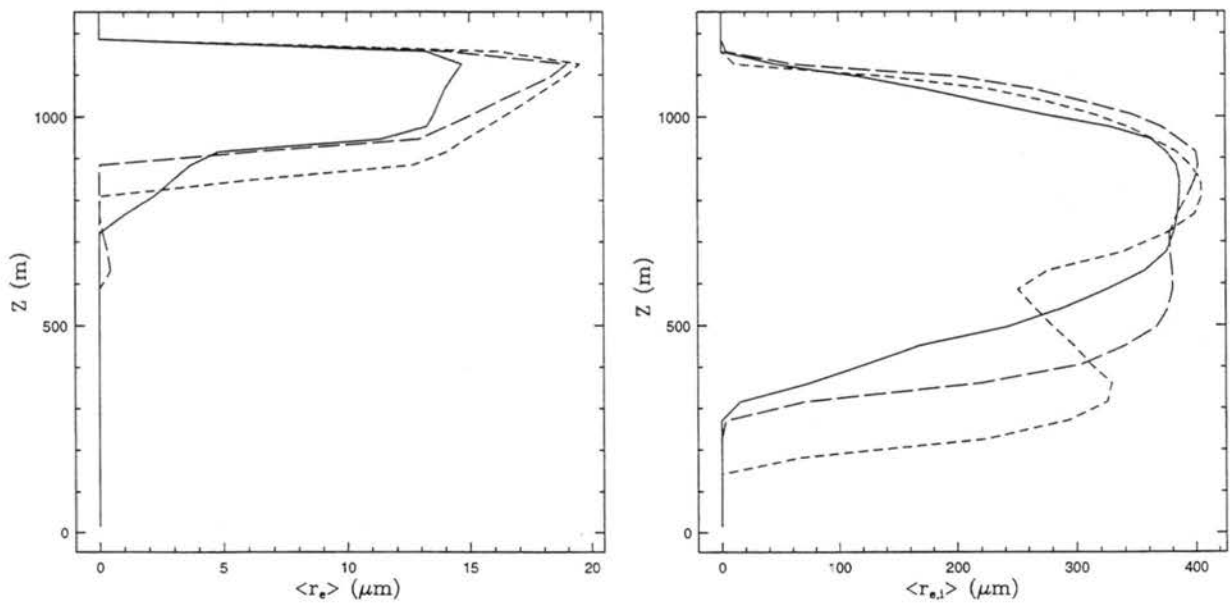

Figure 8.2: Profiles of liquid (r_e) and ice ($r_{e,i}$) effective radii for 5NC over the coarse of 2 hours of bin simulation. Solid line denotes 4.5 hours, long-dahsed line denotes 5 hours, and short-dashed line denotes 6 hours of simulation time.

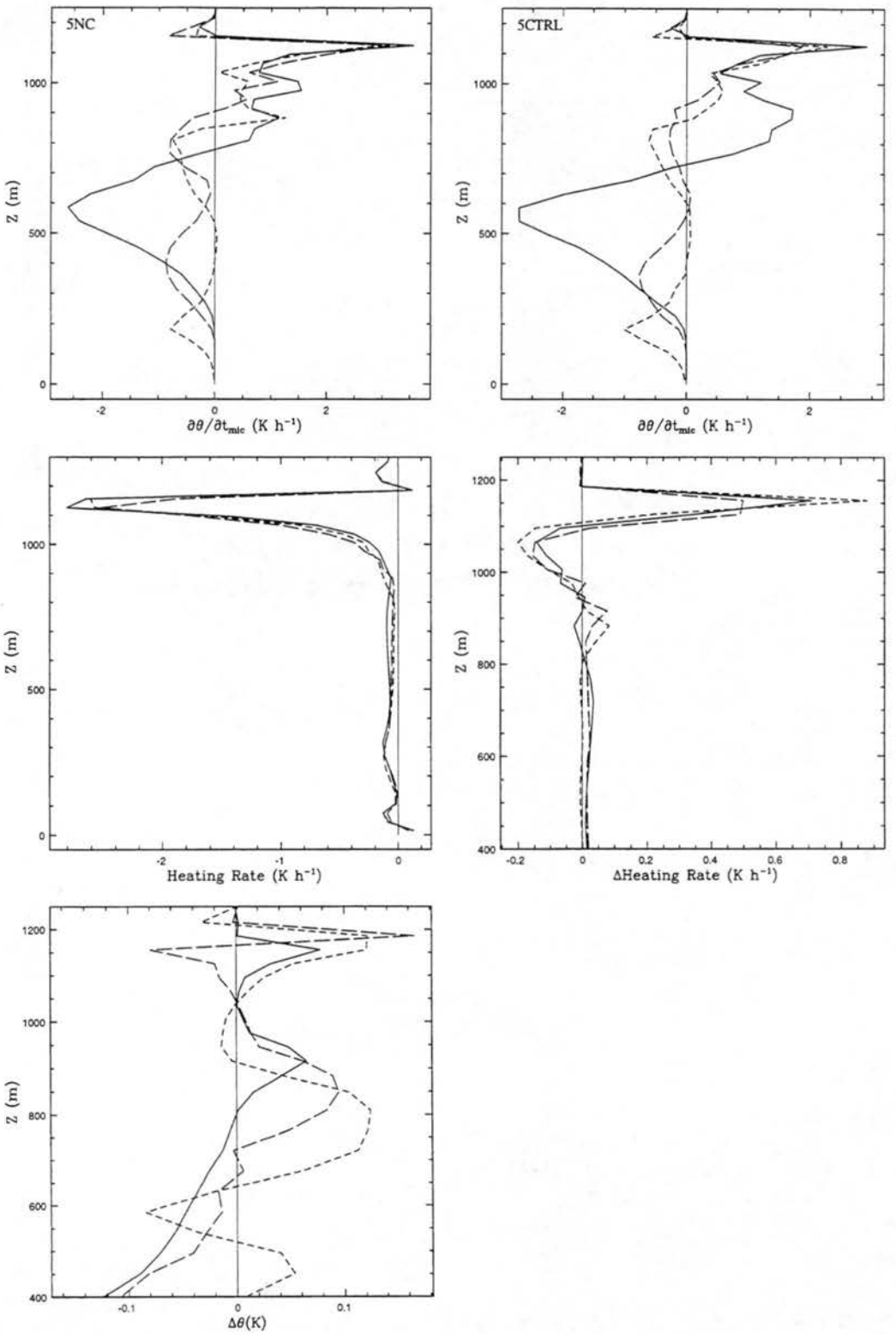

Figure 8.3: Profiles of θ-tendencies for 5NC over the coarse of 2 hours of bin simulation. Panels show microphysical heatinf for 5CTRL and 5NC, radiative heating rates (Heating Rate), and differences in θ and radiative heating rates between 5CTRL and 5NC. Solid line denotes 4.5 hours, long-dahsed line denotes 5 hours, and short-dashed line denotes 6 hours of simulation time.

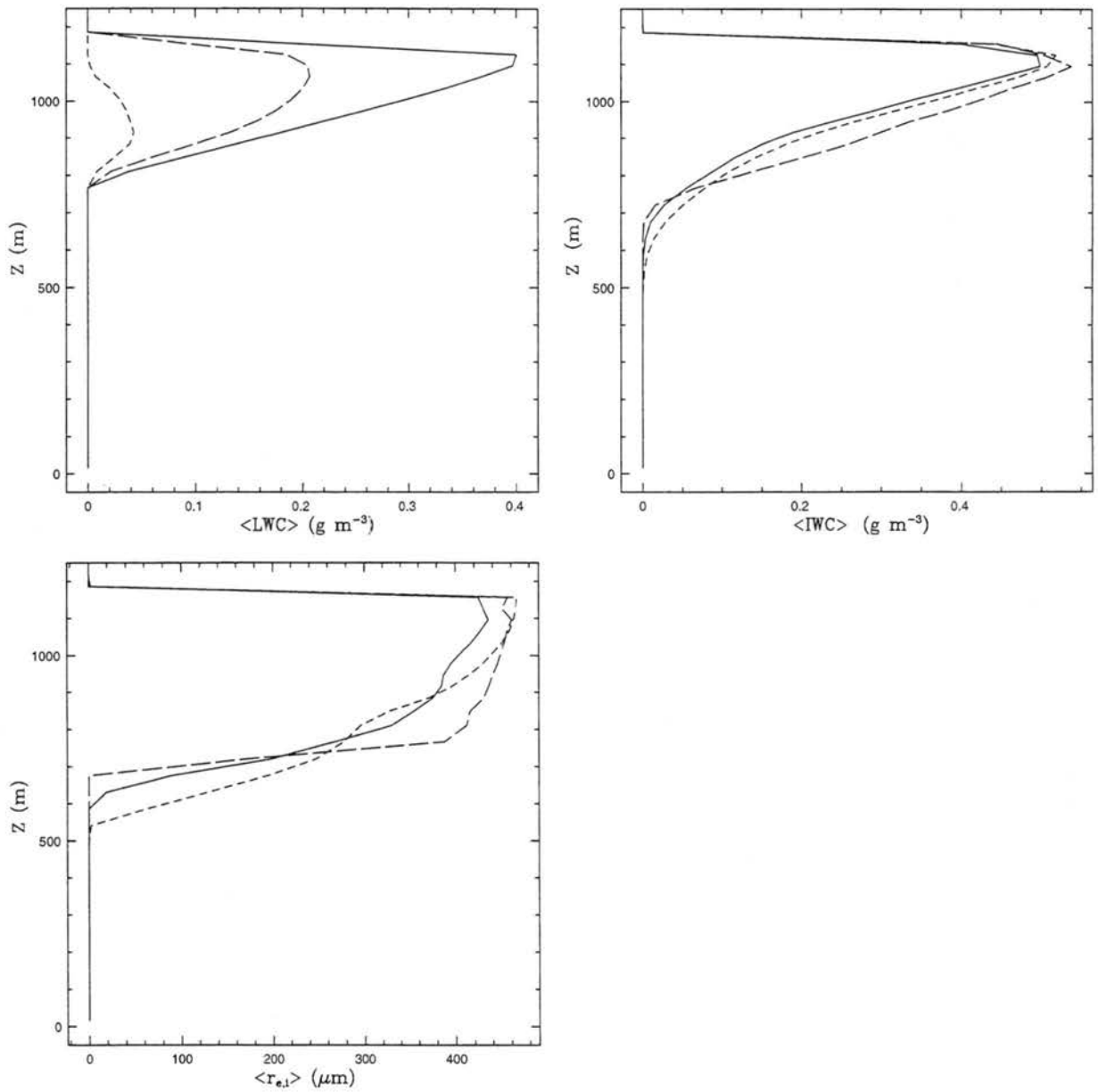

Figure 8.4: Profiles of LWC, IWC, and ice effective radii ($r_{e,i}$) for 5NS over the coarse of 2 hours of bin simulation. Solid line denotes 4.5 hours, long-dahsed line denotes 5 hours, and short-dashed line denotes 6 hours of simulation time except for LWC. LWC lines are denoted as solid for 4 hours, long-dashed for 4.25 hours and short-dashed for 4.5 hours.

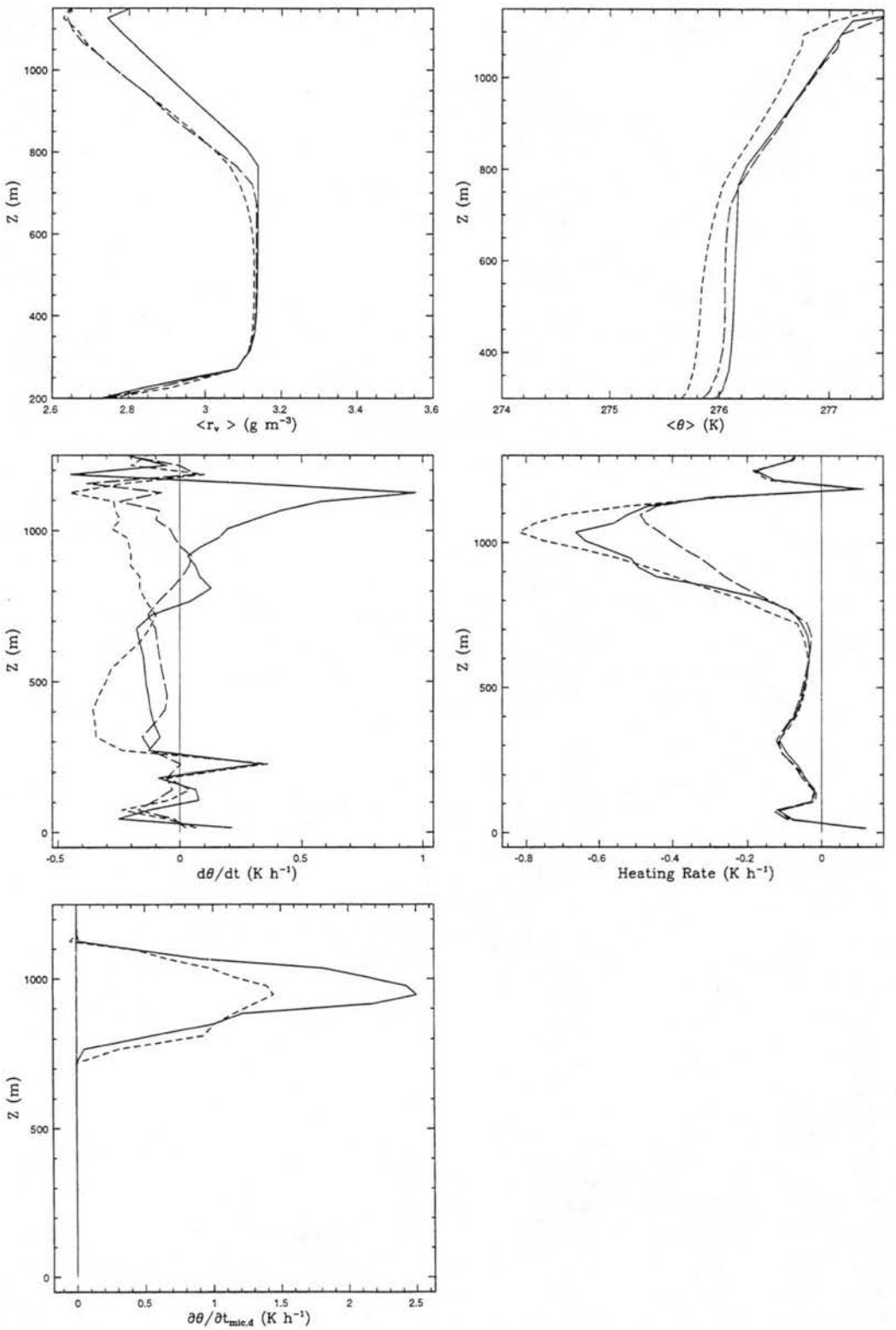

Figure 8.5: Profiles of water vapor mixing-ratio, θ, total θ-tendency ($d\theta/dt$), microphysical heating rate ($\partial\theta/\partial t_{mic}$), and radiative heating rate (Heating Rate) for 5NS over the coarse of 2 hours of bin simulation. Solid line denotes 4 hours, long-dahsed line denotes 5 hours, and short-dashed line denotes 6 hours of simulation time.

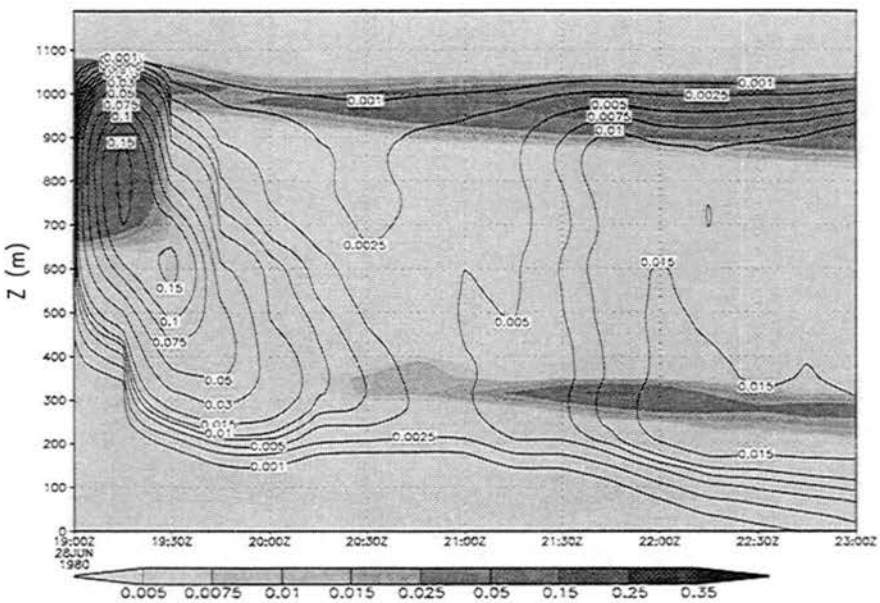

Figure 8.6: Time Series: LWC (shaded) and IWC (contoured) for 5C2IN in $g\ m^{-3}$.

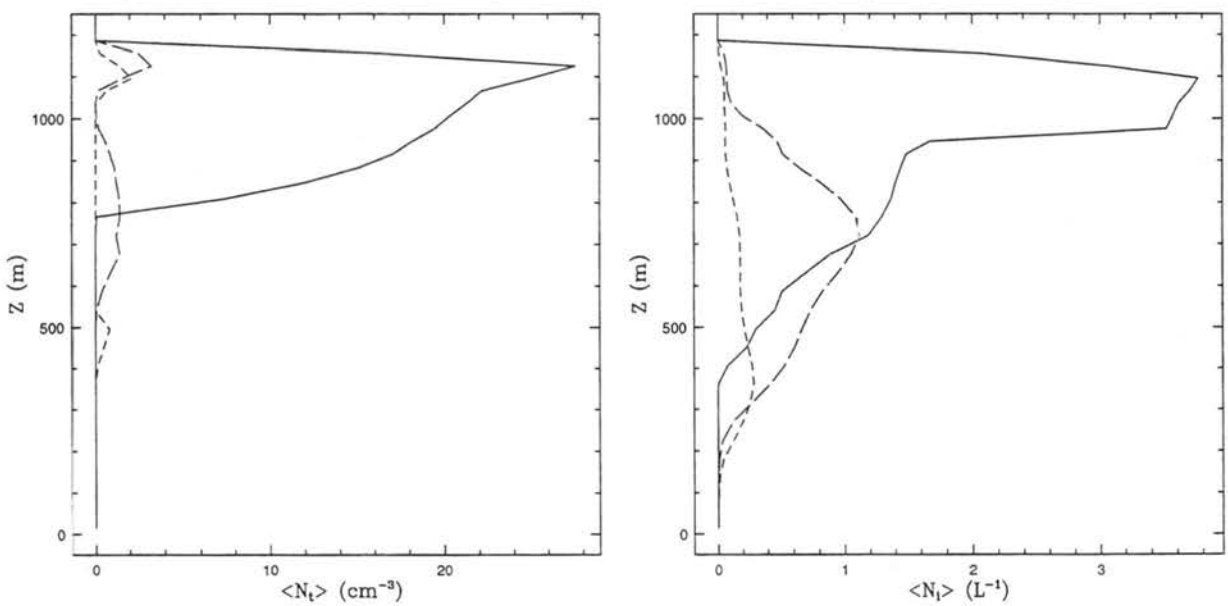

Figure 8.7: Profiles of water drop (N_t)and ice crystal (N_i) concentration for 5C2IN. Solid line denotes 4.25 hours, long-dahsed line denotes 4.5 hours, and short-dashed line denotes 5 hours of simulation time for N_t. N_i is similar except that the solid line denotes 4 hours.

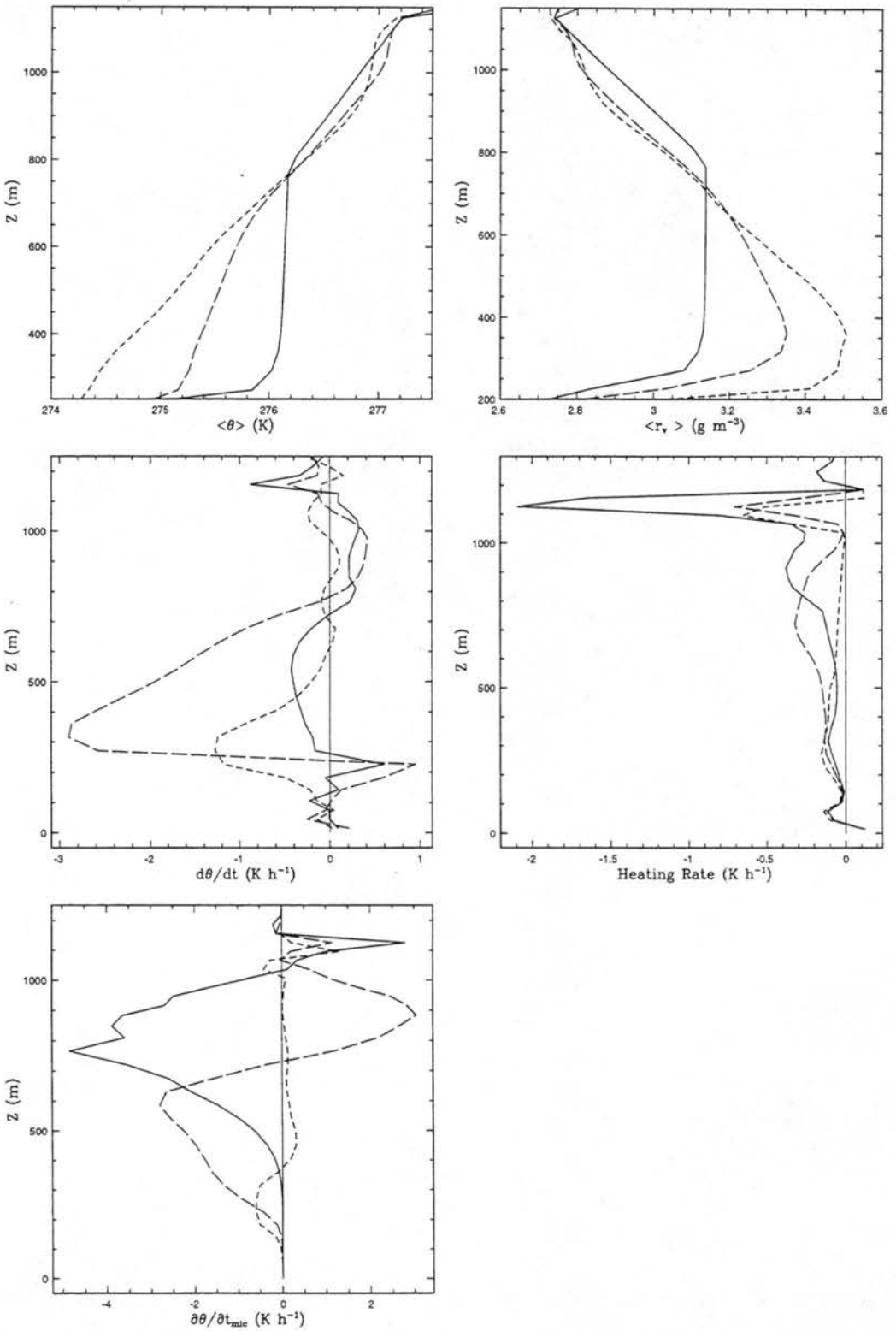

Figure 8.8: Profiles of water vapor mixing-ratio, θ, total θ tendency ($d\theta/dt$), microphysical heating rate ($\partial\theta/\partial t_{mic}$), and radiative heating rate (Heating Rate) for 5C2IN during the 4 to 5 hour period. Solid line denotes 4 hours, long-dahsed line denotes 4.5 hours, and short-dashed line denotes 5 hours of simulation time.

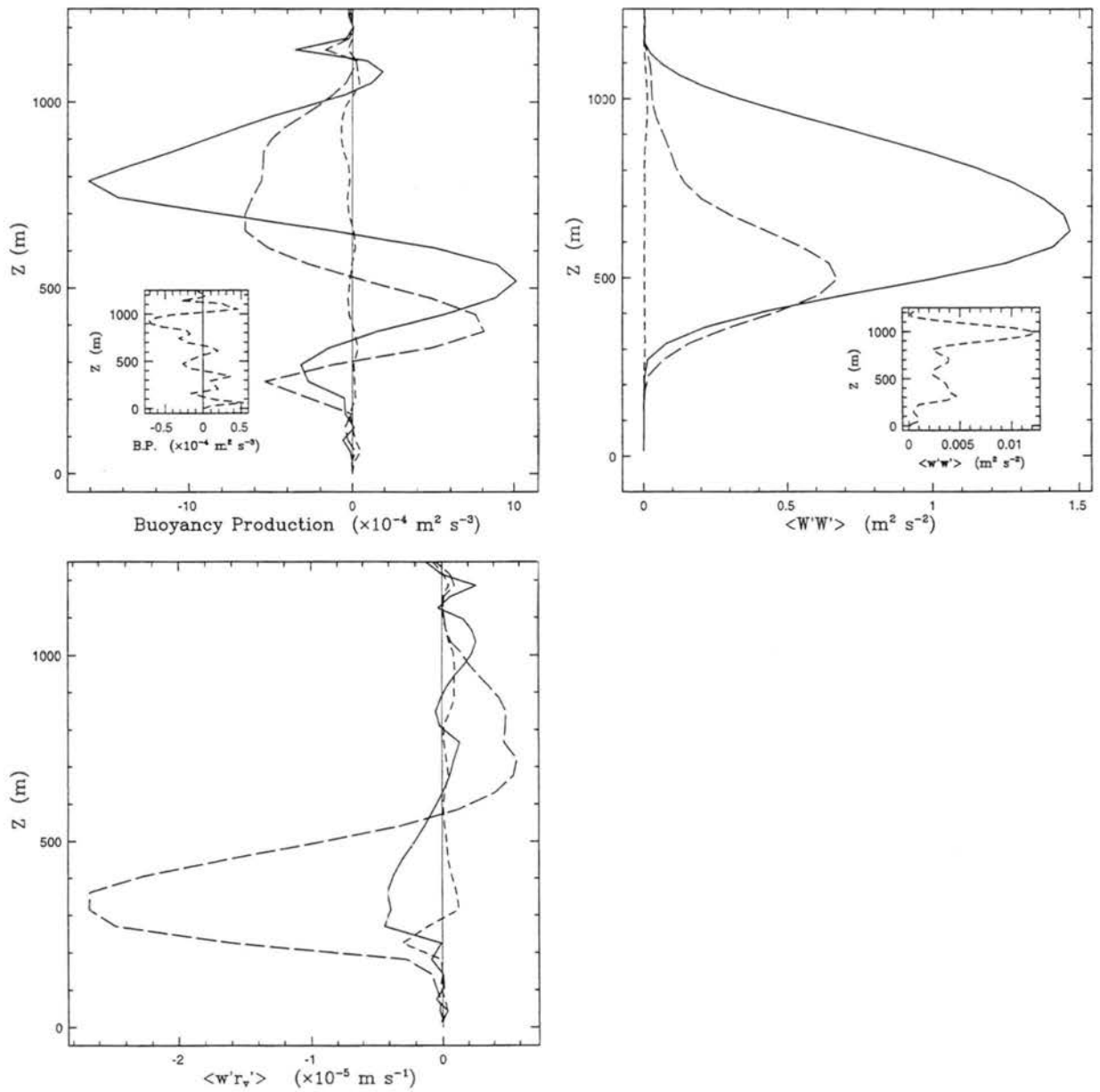

Figure 8.9: Profiles of buoyancy production, $< w'w' >$ and $< w'r_v' >$ for 5C2IN over the 4 to 5 hour period of the simulation. Solid line denotes 4.25 hours, long-dahsed line denotes 4.5 hours, and short-dashed line denotes 5 hours of simulation time.

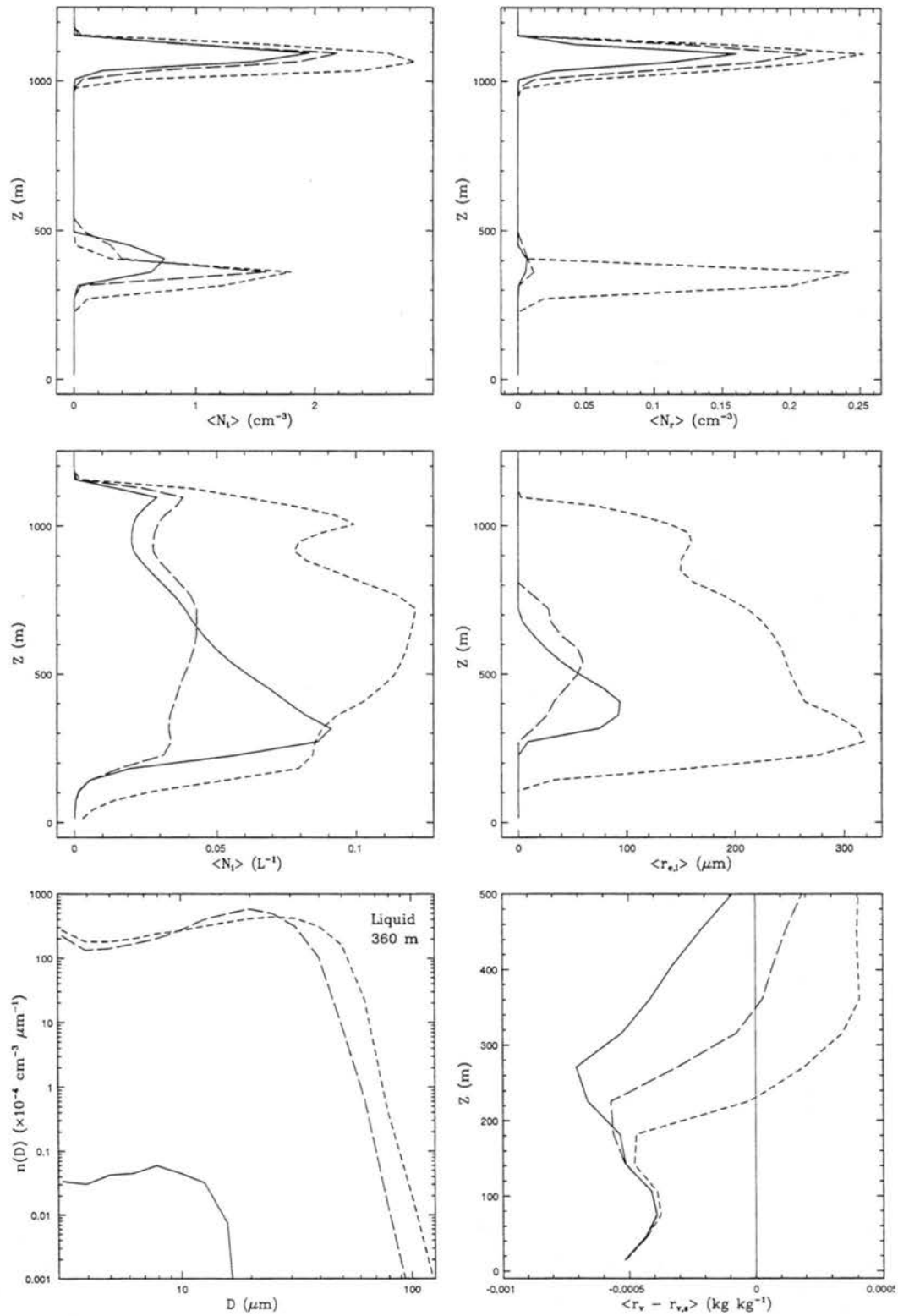

Figure 8.10: Profiles of microphysics consisting of drop concentration (N_t), drizzle concentration (N_r), ice concentration (N_i), ice effective radius ($r_{e,i}$) and drop distributions ($n(D)$) for 5C2IN. Solid line denotes 5.5 hours, long-dahsed line denotes 6 hours, and short-dashed line denotes 7 hours of simulation time. Times are similar for the distributions except that the solid line is for 5 hours. Plot of water vapor excess ($r_v - r_{v,s}$) are for 5 hours (solid line), 5.5 hours (long-dahsed line) and 6 hours (short-dashed line).

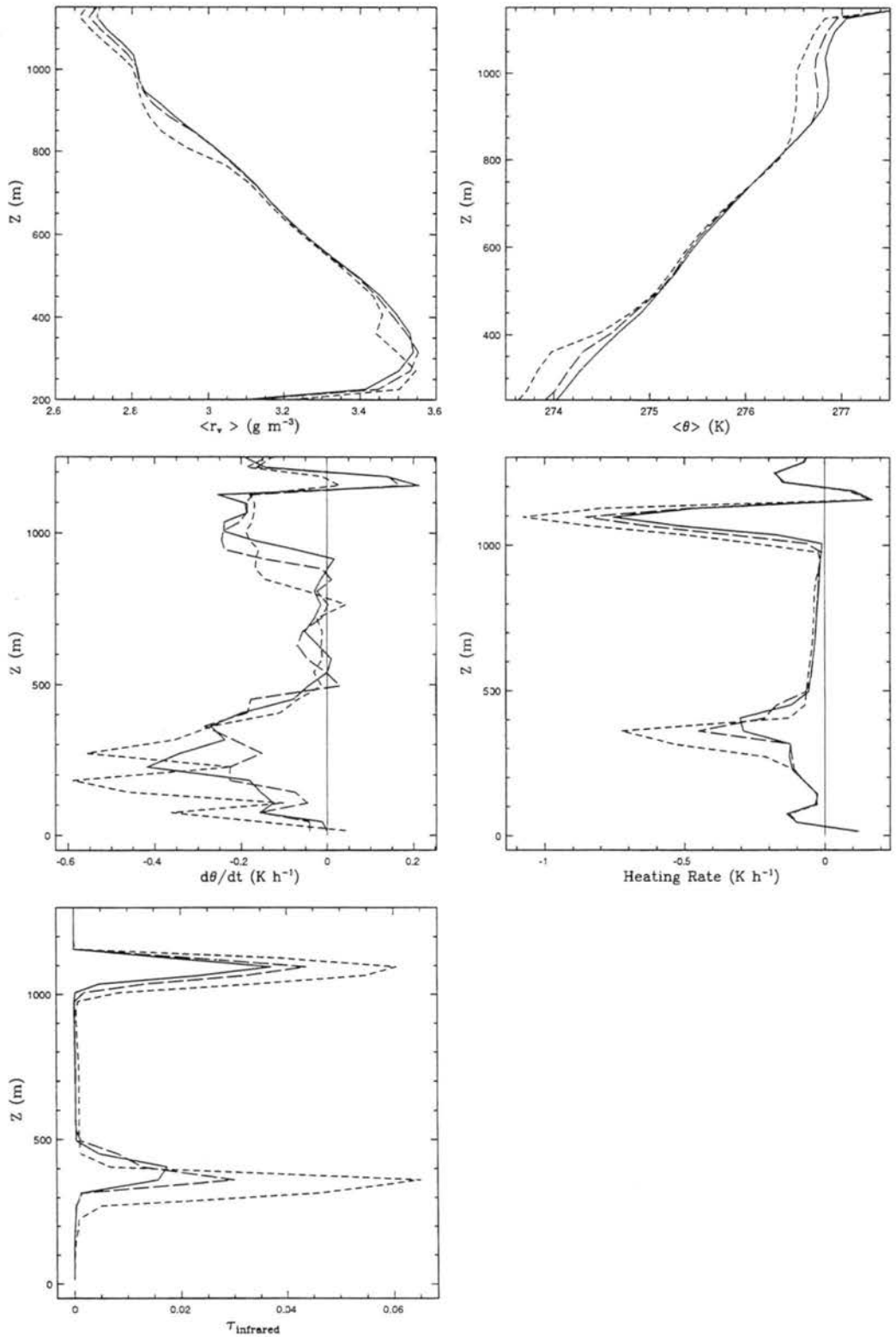

Figure 8.11: Profiles of θ, water vapor mixing-ratio, total cooling rate ($d\theta/dt$), radiative heating rate (Heating Rate), and ifrared optical depth ($\tau_{infrared}$) for 5C2IN over the coarse of hours 5-8. Solid line denotes 5.5 hours, long-dahsed line denotes 6 hours, and short-dashed line denotes 7 hours of simulation time.

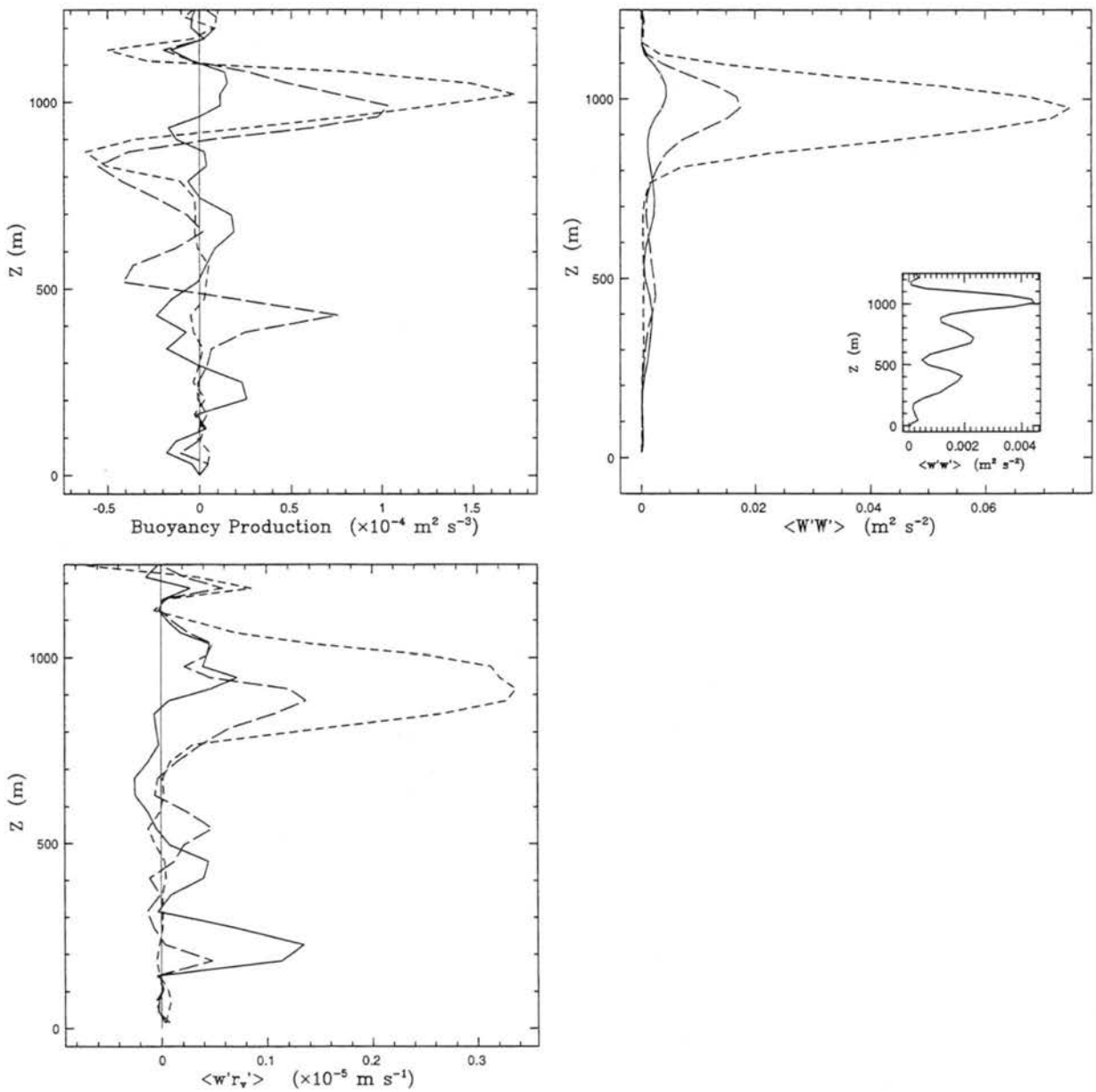

Figure 8.12: Profiles of buoyancy production, $< w'w' >$ and $< w'r'_v >$ for 5C2IN over the coarse of 5-8 hours of bin simulation. Solid line denotes 5.5 hours, long-dahsed line denotes 6 hours, and short-dashed line denotes 7 hours of simulation time.

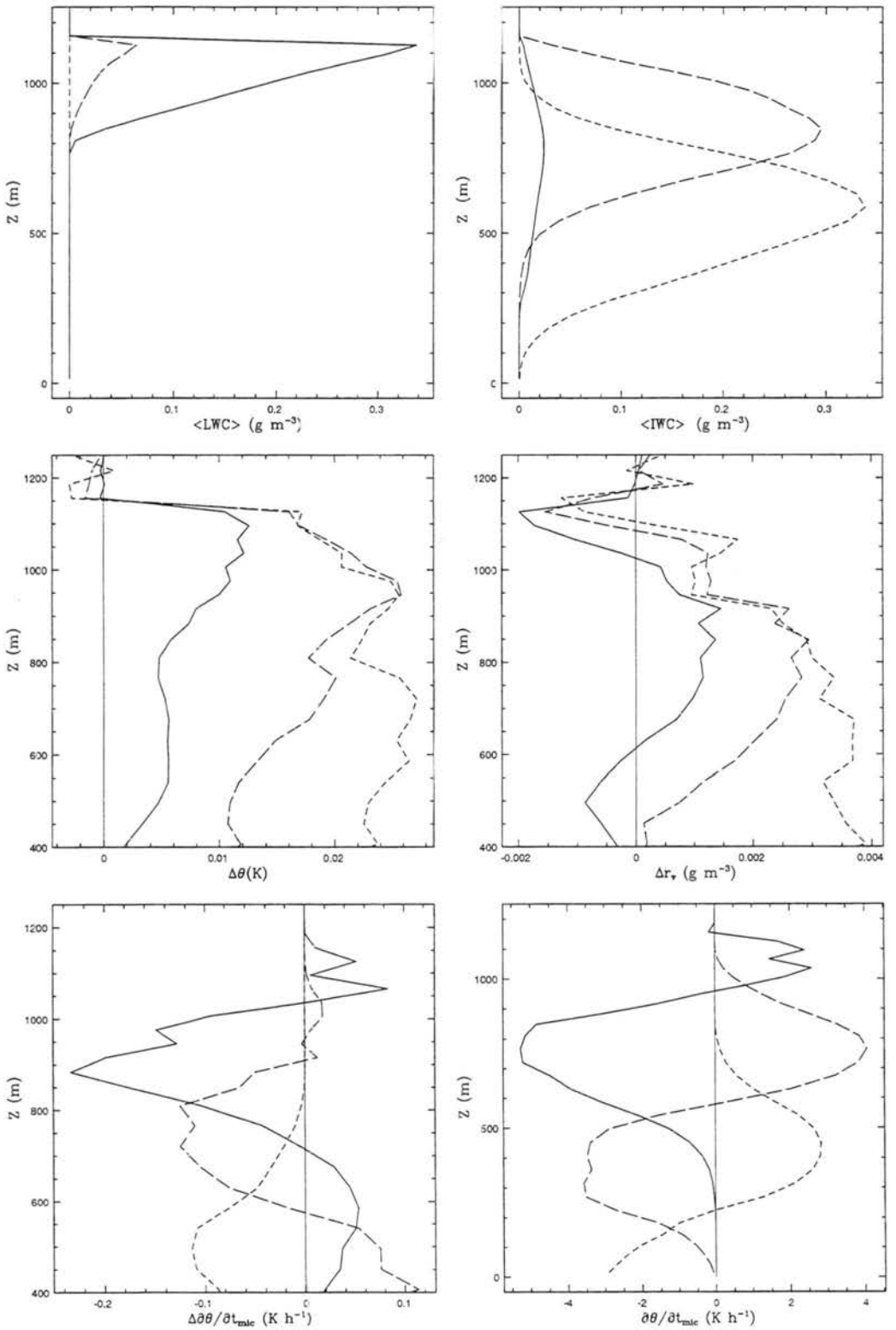

Figure 8.13: Profiles for 10NC of LWC, IWC, microphysical heating rates ($\partial\theta/\partial t_{mic}$) and difference quantities. All differences are computed as $X_{10CTRL} - X_{10NC}$. Solid line denotes 4 hours, long-dahsed line denotes 4.25 hours, and short-dashed line denotes 4.5 hours of simulation time.

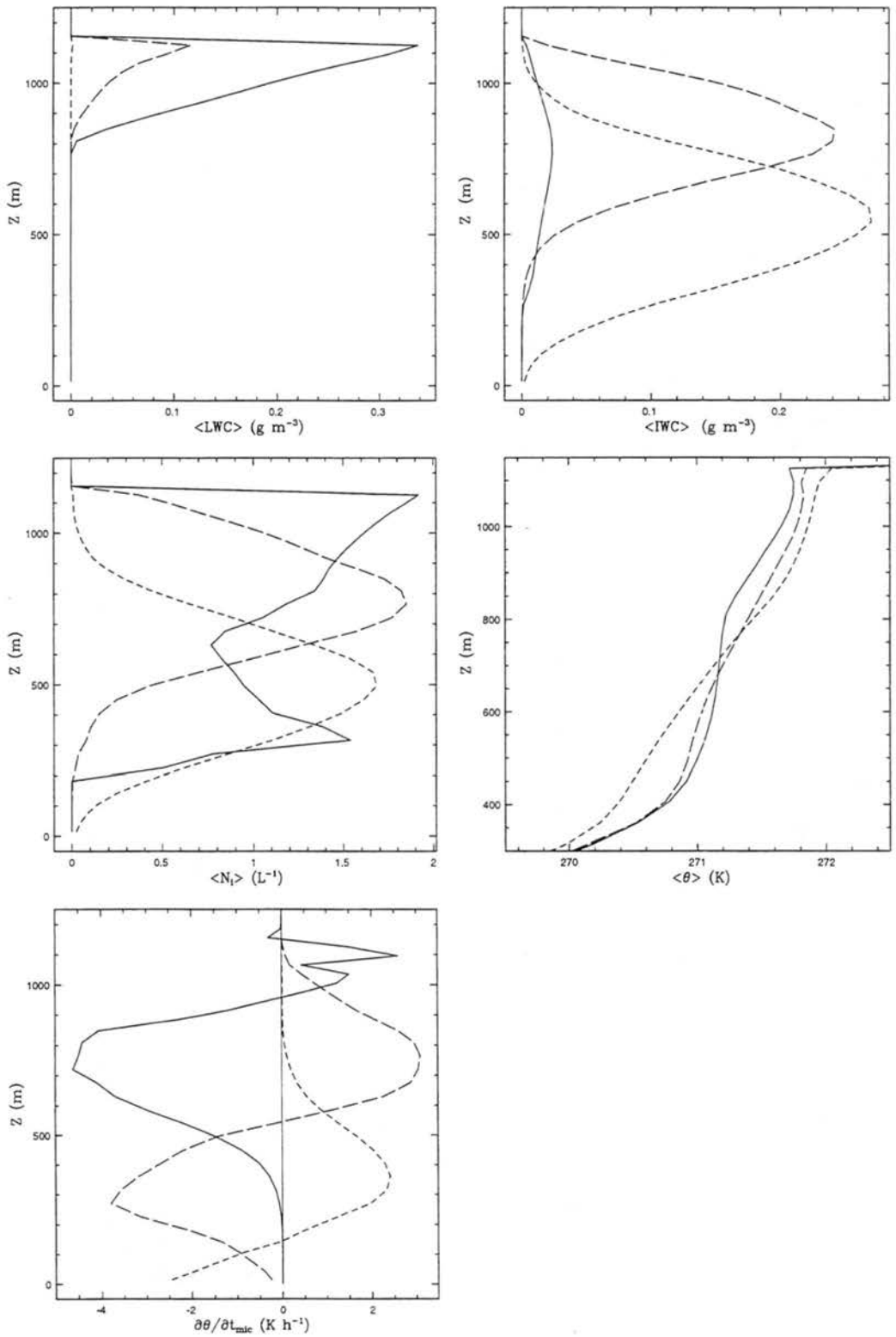

Figure 8.14: Profiles for 10INH of LWC, IWC, ice concentration (N_i), θ and microphysical heating rate ($\partial\theta/\partial t_{mic}$) at 4 hours (solid line), 4.25 hours (long-dashed line), and 4.5 hours (short-dashed line) of simulation time.

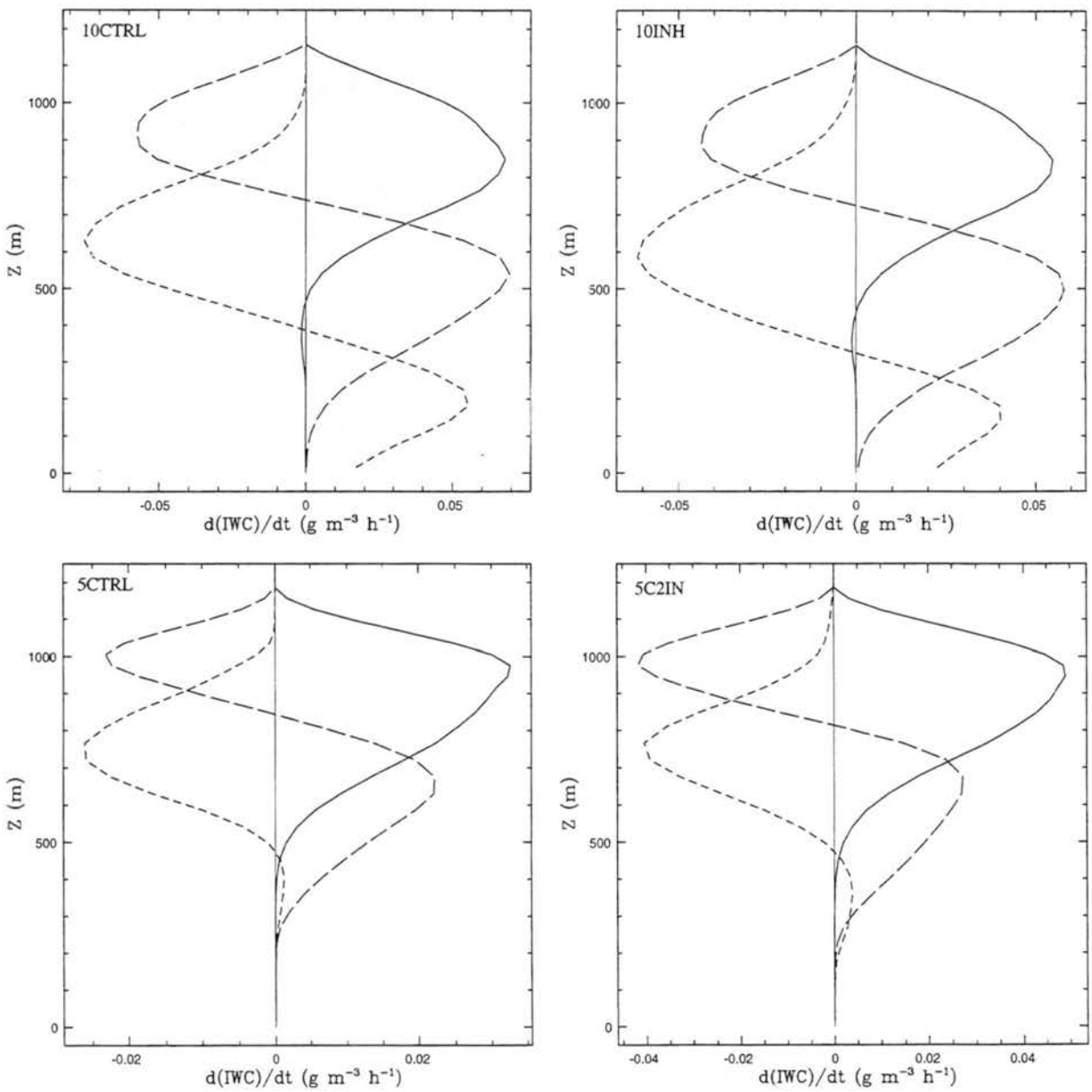

Figure 8.15: Profiles of total tendency for IWC for relevant $5C$ and $10C$ cases. Simulation acronyms identify each figure. Solid line denotes 4.25 hours, long-dahsed line denotes 4.5 hours, and short-dashed line denotes 5 hours of simulation time.

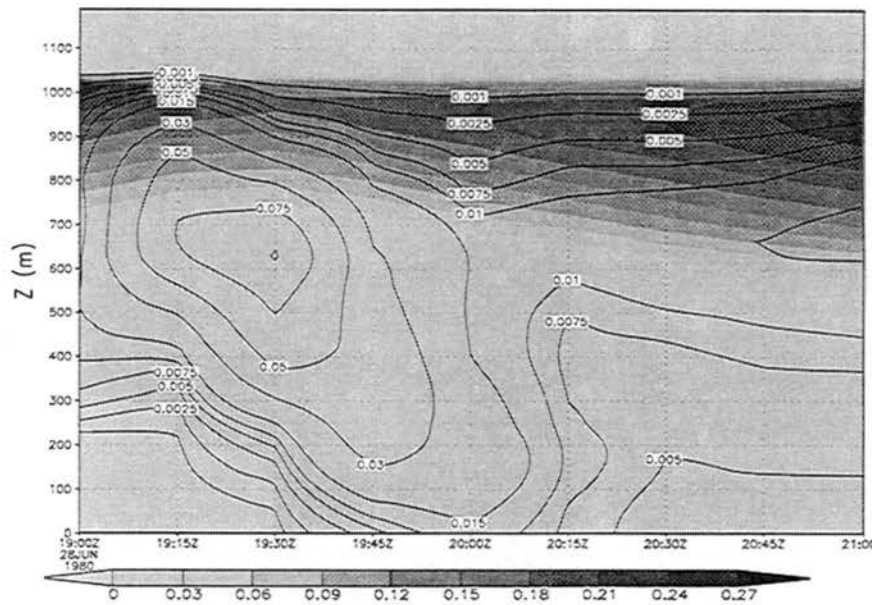

Figure 8.16: Time Series: LWC (shaded) and IWC (contoured) for 10INT in $g\ m^{-3}$.

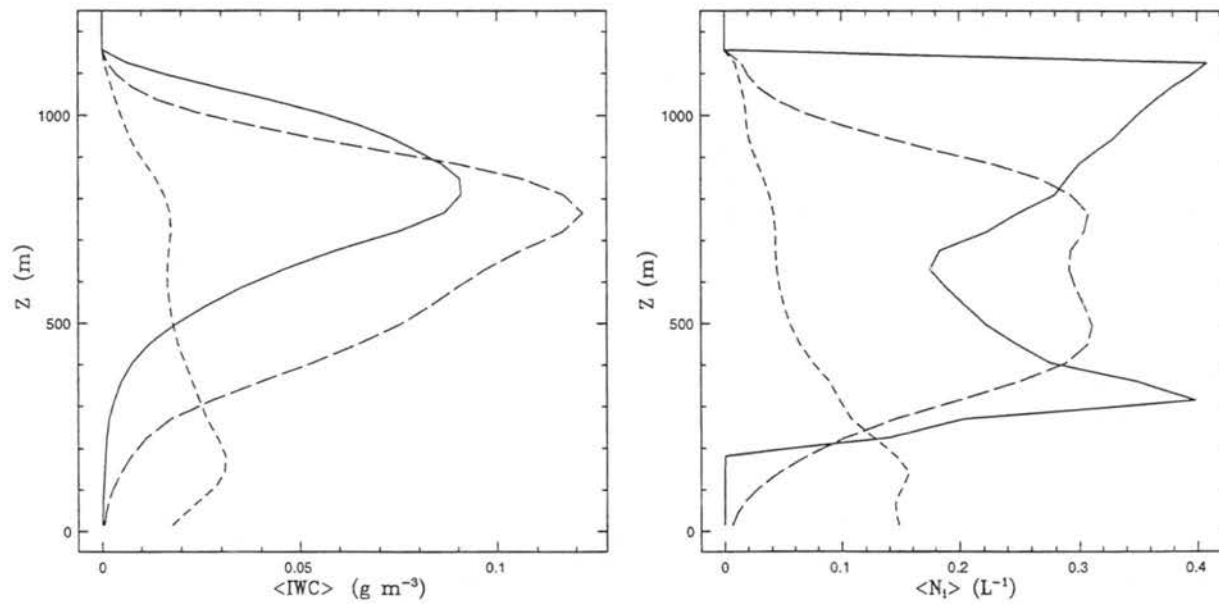

Figure 8.17: Profiles of IWC and ice concentration (N_i) for 10INT over the coarse of 2 hours of bin simulation. Solid line denotes 4.25 hours, long-dahsed line denotes 4.5 hours, and short-dashed line denotes 5 hours of simulation time.

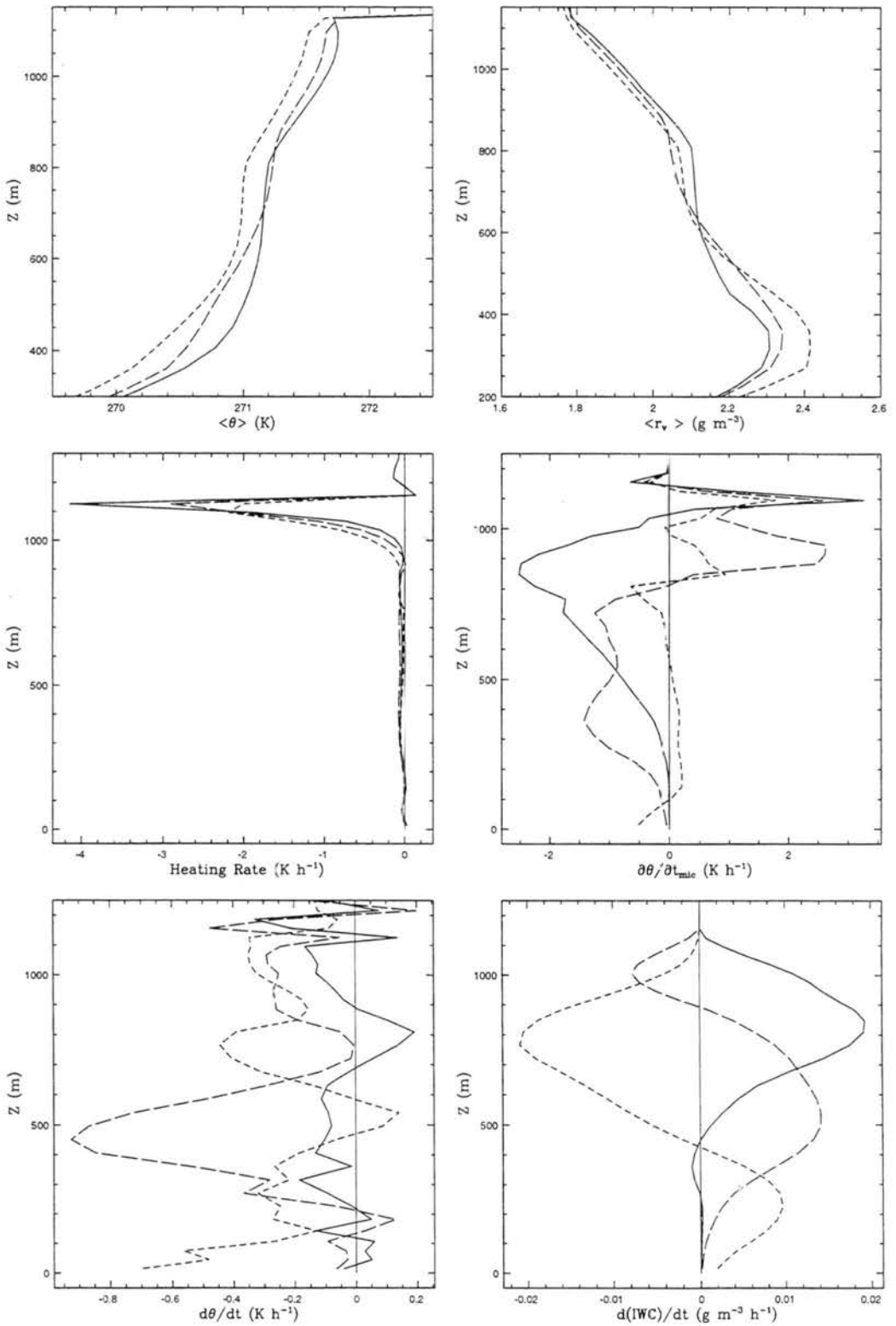

Figure 8.18: Profiles of θ, water vapor mixing-ratio (r_v), total cooling rate ($d\theta/dt$), microphysical heating rate ($\partial\theta/\partial t_{mic}$), radiative heating rate (Heating Rate), and ice production rate ($d(IWC)/dt$) for the 4 to 5 hour period of simulation 10INT. Solid line denotes 4 hours, long-dahsed line denotes 4.5 hours, and short-dashed line denotes 5 hours of simulation time.

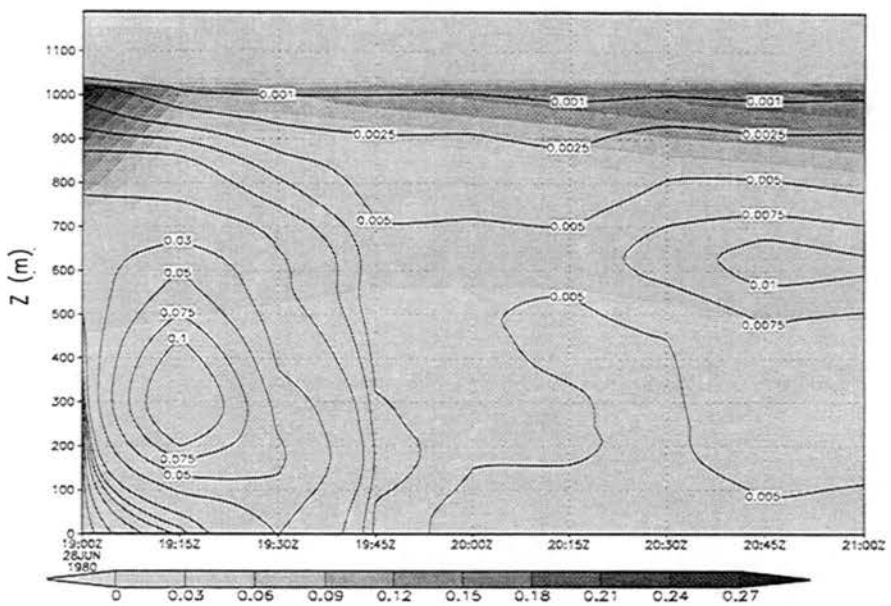

Figure 8.19: Time Series: LWC (shaded) and IWC (contoured) for 10HAB $g\ m^{-3}$.

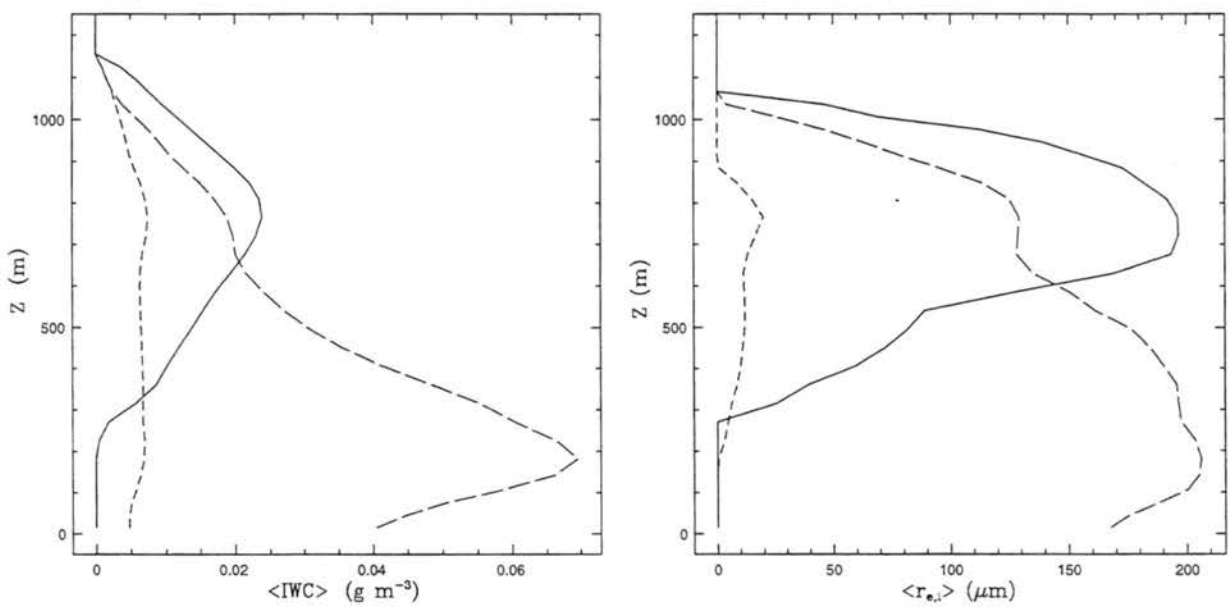

Figure 8.20: Profiles of IWC and ice effective radius ($r_{e,i}$) for 10HAB over the coarse of 2 hours of bin simulation. Solid line denotes 4 hours, long-dahsed line denotes 4.5 hours, and short-dashed line denotes 5 hours of simulation time.

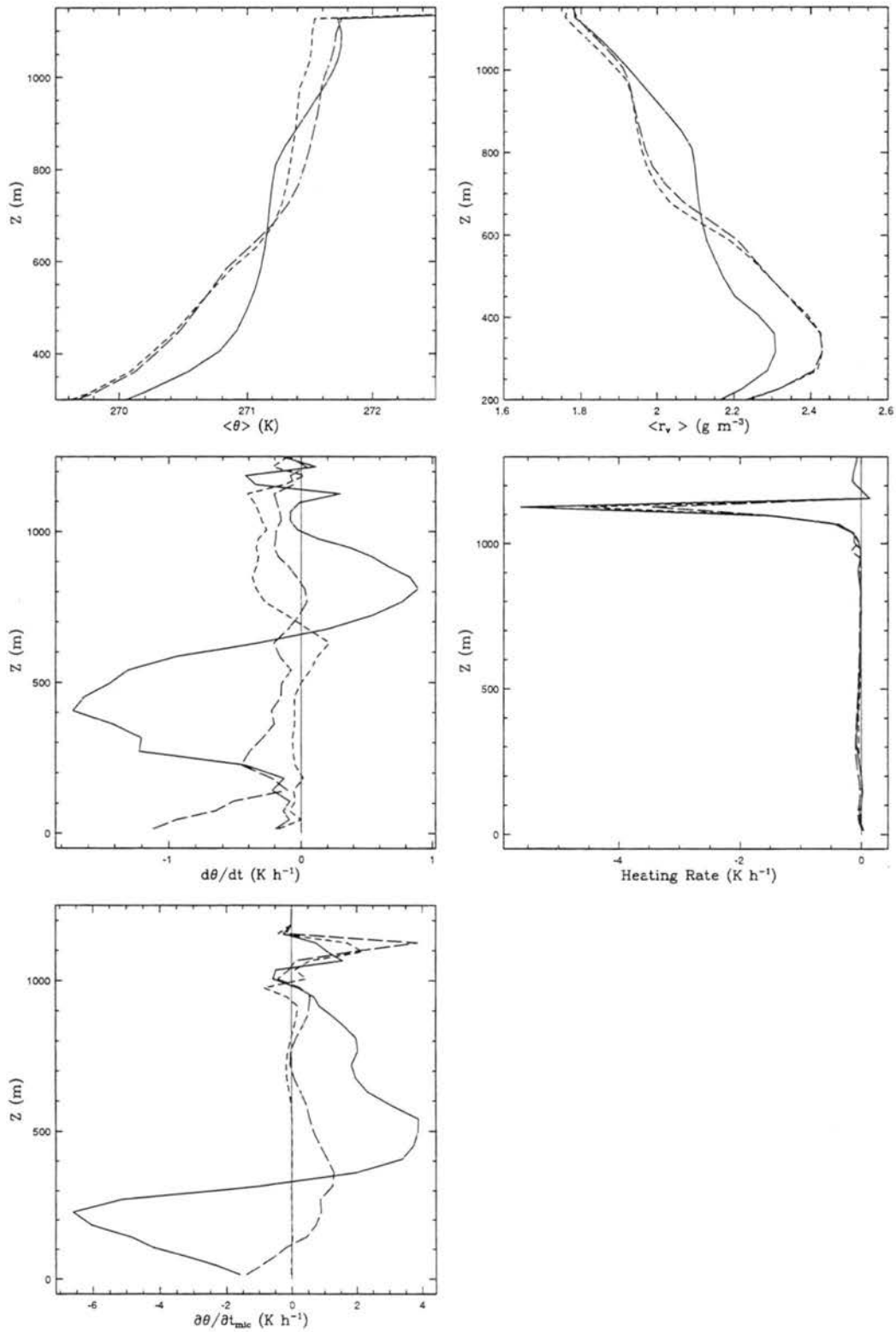

Figure 8.21: Profiles of θ, water vapor mixing-ratio (r_v), total cooling rate ($d\theta/dt$), radaitive heating rate (Heating Rate) and microphysical heating rate ($\partial\theta/\partial t_{mic}$) for the 4 to 5 hour period of simulation 10HAB. Solid line denotes 4 hours, long-dahsed line denotes 4.5 hours, and short-dashed line denotes 5 hours of simulation time.

Chapter 9

SUMMARY, CONCLUSIONS AND FUTURE WORK

9.1 Summary and Conclusions

A cloud-resolving model (CRM) version of RAMS, coupled to explicit bin resolving microphysics and a new two-stream radiative transfer code was used to study various aspects of Arctic stratus clouds (ASC). The two-stream radiative transfer model is coupled in a consistent fashion to the bulk microphysical parameterization of Walko *et al.* (1995) and includes computations of scattering and absorption of water drops (Mitchell, 1997) and ice crystals (Mitchell and Arnott, 1994). Coupling to the explicit liquid bin microphysical model (*e.g.* Feingold *et al.* 1996a) and the mixed-phase microphysical model (Reisin *et al.* , 1996) includes a new bin optical property method which does not need distribution shape specification. The method was shown to have excellent accuracy with errors never greater than about 2%. This method has a large advantage over earlier methods (*e.g.* Feingold *et al.* , 1994; Stevens *et al.* , 1996; Kogan *et al.* , 1995) in that the radiation is able to accurately respond to variations in the distribution function. In addition, SW radiation is modeled, a process that is usually not studied. These models were used to study both warm (summer) season and transition (fall and spring) season ASC. Simulations of transition season ASC, which require the use of a detailed mixed-phase microphysical model coupled to the CRM framework along with radiation is, to our knowledge, a first attempt. Equations for drop condensational growth in the explicit model include the term for radiative heating (cooling) and is coupled to the radiation through the bin optical properties, thus leading to a detailed and consistent coupling. The effects of this process are examined in two frameworks, the first being a trajectory parcel model (TPM) the second being the CRM. The TPM is driven with 500 parcels generated during 2 hours

of the warm season ASC runs and for two different CCN concentrations ($100cm^{-3}$ and $500cm^{-3}$).

Arctic stratus simulated with the new CRM framework compared well with the observations of Curry (1986). Previous studies (*i.e.* Albrecht, 1989; Ackerman *et al.* , 1993; Stevens, 1996) have addressed the importance of CCN concentration on microphysical and dynamical structure of stratocumulus clouds. Indeed, as Shaw (1986) shows, CCN concentration variations occur widely in the Arctic and, therefore, could play a strong role in regulating ASC cloud structure. Important points brought out by this research includes:

- In addition to CCN concentrations, it was shown that drop distribution shape can strongly impact cloud evolution.

- Distributions with broad tails absorb more shortwave (SW) radiation; this constrains the depths of the cloud through reductions in circulation strength and depth. Drizzle formation is reduced in these cases. It is also shown that large SW absorption may have a stronger stabilizing effect than drizzle in weakly drizzling situations.

- Narrow distributions, in contrast, absorb less SW radiation which leads to deeper clouds through stronger and deeper circulations. Drizzle formation tends to be enhanced in these cases.

- Partitioning of LW radiation between the inversion and mixed layers is important for buoyancy production and appears to have a distribution shape dependence.

In conjunction with these results, whether or not the effective radius (r_e) is a good characterization of the cloud optical properties was examined as this has been considered a characterization method for some time (*e.g.* Stephens, 1978; Hu and Stamnes, 1993). Modeling results showed that:

- Fixing distribution shapes (even though gamma function derived r_e values match bin values) and conserving LWC and drop concentrations produced clouds that evolved along a different path than the accurate, bin optical property method.

- The effective radius method of Hu and Stamnes (1993), which conserves r_e and drop concentration, was shown to produce acceptable results in an evolving cloud as compared to the detailed bin optical property method.

Thus, methods used in GCMs such as Slingo's (1989) method, where LWC and r_e are conserved and optical properties are derived for a specific distribution shape, may work well for such applications. Utilizing them in CRM simulations is likely to produce erroneous results (since r_e is often derived from the relation between the LWC and concentration using the gamma function). In addition, bulk microphysical models (*e.g.* Walko *et al.* , 1995; Ferrier *et al.* , 1995) which fix the distribution shape may not properly capture the cloud evolution. Even new hybrid methods such as Feingold *et al.* (1997), which better characterizes the drizzle process, must rebuild a gamma function at the end of the microphysical computations and this requires distribution shape specification. Thus, even these methods will be susceptible to problems associated with cloud top radiative dependence on distribution shape. This effect most likely does not bear strongly on nocturnal simulations as LW cooling is not as strongly affected by drop distribution shape as is SW heating. Thus, this effect is of primary importance to summertime ASC and diurnal simulations of stratocumulus which have a strong radiatively driven circulation.

The TPM analysis using the radiative effect on drop condensational growth showed the following:

- Parcels which spend at least 12 minutes at cloud top undergo spectral broadening which is due not only to large drops growing faster, but also to the evaporation of drops with $r < 10\ \mu m$. The evaporation of these drops is strongly forced by the growth of drops within $r = 10$ to $20\ \mu m$ in a process similar to the ice-phase Bergeron-Findeisen process.

- The time for the onset of drizzle can be reduced by as much as 30 minutes and is weakly dependent upon SW heating, but strongly dependent on cloud top cooling and the size of the activated drops.

- These results show a weaker reduction in the time for drizzle onset as compared to Austin *et al.* (1995) and is due to drop activation, as Austin *et al.* (1995) started with initial drop size distributions which reduced drizzle onset times.

- Drizzle production is highly correlated with cloud top residence times of the parcels and corroborates the hypotheses of Feingold *et al.* (1996a) and Stevens *et al.* (1996) that this should be the case.

- Radiative effects enhance drizzle production, however, only within the same subset of cloud trajectories that produce drizzle in the no-radiation cases.

- Simulations with greater CCN concentrations show that much longer cloud top residence times are needed to form drizzle in these cases, so much so that drizzle production can be sufficiently suppressed in both the radiation and no-radiation simulations.

- Computations with the CRM show that drizzle production can occur as much as one hour earlier with radiative effects. The character of the simulated clouds is not, however, greatly altered.

Simulations of transition season, mixed-phase ASC shows that:

- The cloudy boundary layer is quite sensitive to ice phase processes. Colloidally stable and unstable clouds were produced thus illustrating that the rapid reduction in stratus cloudiness during fall may be forced, at least in part, through microphysical processes.

- Many of the simulated features of the stable cloud compare well with observations of Pinto (1997) for an autumnal mixed-phase ASC.

- The stability of the mixed-phase cloud layer is shown to be strongly dependent upon the cloud temperature, ice concentration, precipitation rate and the indirect effects of ice crystals on cloud top radiative cooling while aggregation has little effect on cloud stability.

- Ice precipitation causes large cooling and moistening of the lower boundary layer through sublimation which results in layer stabilization. Frequently observed autumnal stable layers may be formed in this fashion (Pinto, 1997). The effect is strongly dependent on ice mass amount and terminal fall speed as slower falling ice habits have the greatest potential for lower layer stabilization, but also for causing cloud collapse.

- Layer stability is shown to exist in a small range of ice concentrations (0.4 to 4 L^{-1}) with cooler clouds needing the smallest concentrations as they glaciate more rapidly. Interestingly enough, Pinto (1997) uses a simple microphysical model to argue that the stability of observed autumnal mixed-phase ASC is highly sensitive to ice concentrations.

- A potentially new process of multiple cloud layer formation was explored . The lower layer cloud is formed through ice precipitation which moistens and cools the lower layers while optically thinning the upper cloud layer. Radiative cooling of the lower layers causes droplet activation and cloud formation. Persistence and maintenance of the lower layer occurs through cloud top radiative cooling.

9.2 Future Research

While this dissertation has addressed many issues related to microphysical and radiative processes in ASC, the limitations of the microphysical-dynamical and radiative framework, and the limitations of time leave many questions to future studies.

The dependence of warm ASC microphysical and dynamical structure on the distribution of both LW cooling and SW heating, particularly the latter, should be addressed in detail. The dependence of the radiative profiles on idealized distribution parameters can easily be explored, thus setting a framework for simulations with a CRM or LES model. The LES framework would be the most likely candidate for such studies as 3-D simulations are less susceptible to grid spacing issues (Stevens *et al.* , 1996).

Aerosol properties, which may vary widely both temporally, spatially, and with respect to mid-latitude measurements (Shaw, 1986), most likely have important impacts on the

microphysical structure of the cloud. Proper aerosol species, along with sufficient representation in the numerical model, could help elucidate issues related to Arctic aerosol and cloud processing. However, further measurements and experiments that examine Arctic aerosol properties, especially in terms of drop activation, need to be explored.

In terms of the radiative effects on cloud drop growth, the 10 μm boundary around which spectral broadening occurs kept showing up in our simulations. Whether or not this spectral broadening occurs in real clouds, including if it is centered around a preferential radius such as was shown here, is not known. Measurements in the vicinity of cloud top may be able to shed light on this. [1] Even though the dependence of enhanced collection on cloud top residence times was quantified to some degree, the question of what processes cause drizzle production for an increasing subset of the total parcels is left unanswered. In addition to this, spurious supersaturation production, advective and diffusive problems at cloud top may be swamping the effects in the CRM. How strongly these effects alter the drizzle process, and whether it is to the advantage or disadvantage of the radiative effect, is not known.

Few studies have examined the effects of radiative transfer on the depositional growth of ice crystals in cirrus clouds, with Stephens (1983) being the only exception. That work showed the importance of the term in the heat budget of an individual crystal at certain radiative extremes. It would appear that an analysis such as has been executed here for warm season ASC (i.e. the TPM) could effectively elucidate these processes in cirrus clouds and cold-season ASC. The development necessary should mirror that of Chapter 6.

More observations of mixed-phase ASC from the perspective of microphysical processes and with an outlook to numerical modeling need to be undertaken as the data are quite sparse at this time (with Pinto's (1997) paper being the only published information on these cloud systems). Better observations may also answer some of the following questions. Are self-maintaining mixed-phase systems realized in nature, or does large scale forcing always play an important role in cloud maintenance? Are collapsing autumnal boundary layers

---

[1] Although, it should be noted that Tsay and Jayaweera (1984) showed minima in cloud drop spectra near cloud top at 9.4 μm for this ASC case.

observed and, if so, is microphysical forcing important. Are multiple cloud layers formed by the mechanism simulated here? Further observations should also shed light on ice nuclei (IN) effects, their relation to chemistry, concentrations of CCN and their activation all of which will affect the stability of the mixed-phase layers, if cloud stability is as sensitive as the simulations here suggest. In addition, Pinto's (1997) work has shown extremely high ice crystal concentrations at and below cloud base (up to $20cm^{-3}$). These ice crystal concentrations are much higher than the ambient IN concentrations observed in the Arctic (usually up to $10L^{-1}$). Investigations of the origin of these high ice concentrations and their relation to IN concentrations (and whether or not they are produced erroneously through aircraft sampling) are necessary. Mixed-phase bin microphysical models, while being accurate, are extremely computationally expensive. Efficient and accurate bulk models, scrutinized with bin model results, need to be developed, thus allowing for the accurate study of the 3-D nature of these systems. More efficient codes would allow for longer simulations and more realistic transitions that could address the following questions. How strongly is mixed-phase cloud maintenance dependent upon large scale effects? How important are ice leads to the development and maintenance of these clouds? Does stratus cloud cover really, essentially disappear during the winter months? How important is the cycling of IN along with precipitation removal to the stability of the system? Better IN parameterizations suitable for the Arctic are needed to address these questions.

Appendix A

TWO-STREAM SOLUTION

All forms of the two-stream equation may be written in the following, compact form,

$$\begin{aligned} \frac{d\mathbf{F}}{d\tau} &= \mathbf{A}\mathbf{F}(\tau) + \mathbf{S}(\tau), \\ \frac{dF_s}{d\tau} &= \frac{F_s}{\mu_0}, \end{aligned} \tag{A.1}$$

where the matrices are defined as,

$$\begin{aligned} \mathbf{F} &= \begin{bmatrix} F^+ \\ F^- \end{bmatrix} \qquad \mathbf{A} = \begin{bmatrix} \gamma_1 & -\gamma_2 \\ \gamma_2 & -\gamma_1 \end{bmatrix} \\ \mathbf{S} &= \begin{bmatrix} S^+ \\ S^- \end{bmatrix}, \end{aligned} \tag{A.2}$$

and F^+ and F^- are the upward and downward directed diffuse fluxes, respectively, S^+ and S^- are the upward and downward source contributions (either single scattered solar or infrared emission) to the diffuse fluxes, and γ_1 and γ_2 are coefficients that are related to the reflection and transmission functions (the above mentioned approximations lie in these two terms). The source functions, $\sigma^{\pm}$, are given by

$$\begin{aligned} S^+ &= -\gamma_3 \pi \omega_0 F_s e^{-\tau/\mu_0} \\ S^- &= \gamma_4 \pi \omega_0 F_s e^{-\tau/\mu_0}, \end{aligned} \tag{A.3}$$

for solar radiation and

$$\begin{aligned} S^+ &= \gamma_3 \pi U (1-\omega_0) B(\tau, T) \\ S^- &= \gamma_4 \pi U (1-\omega_0) B(\tau, T), \end{aligned} \tag{A.4}$$

for infrared radiation where U is the diffusivity factor, $B(\tau, T)$ is the Planck function integrated between the band limits λ_i to λ_{i+1} (truncated Planck function) the temperature dependence of which is given in §2.3, and γ_3 and γ_4 will be defined in the next subsection.

Now, one must solve this set of equations for an inhomogeneous atmosphere; within the framework of a numerical model, this consists of a number of plane-parallel layers each with different optical properties which are usually constant over the layer (Fig. A.1). Most

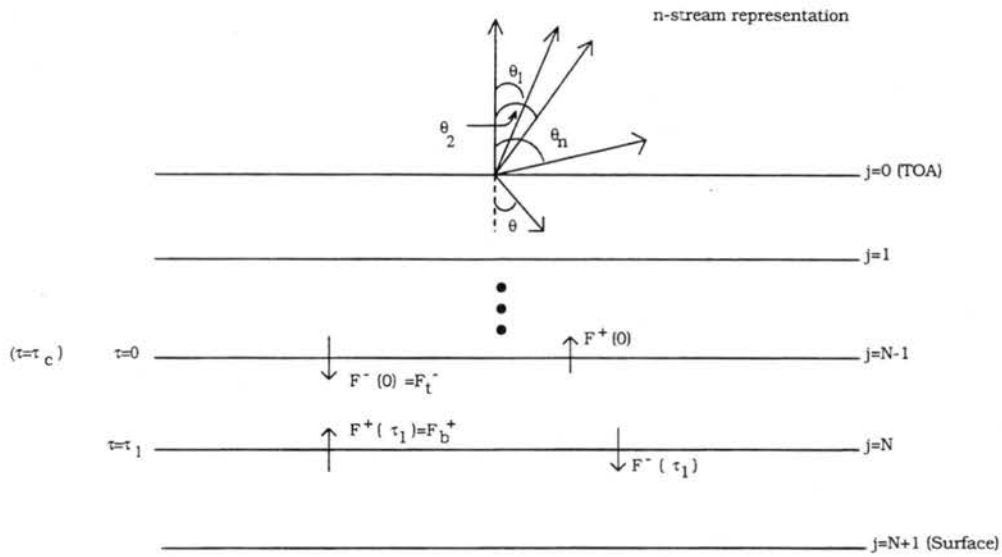

Figure A.1: The representation of multiple layers and streams. For two-stream model integrals over all zenith angles must be evaluated to obtain equations for the fluxes. The equations are solved for each layer given F_b^+ and F_t^- as boundary conditions.

numerical model grids are staggered containing points at which velocities are computed (momentum points) and points in between thermodynamic quantities are computed (thermodynamic points). As we need to computed the heating rates at the thermodynamic points, fluxes at the surrounding momentum points are required. Thus, the two-stream equations are solved over a layer in which the layer edges are defined by the upper and lower bounding momentum points. The optical properties of the medium in between the layers (gases and particulates) are assumed to take on a single value for that particular thermodynamic point. It is therefore advantageous to solve the equation set given above for each layer independently and use the adding method (Liou, 1992) to computed the

total fluxes for each model level. This may be done by separating out the term $e^{-\tau_c/\mu_0}$ from the solar source function (as defined below) where τ_c is the cumulative optical depth up to the top of the layer in question (Fig. A.1). We consider a single layer bounded by $\tau = 0$ and $\tau = \tau_1$ with flux boundary conditions being the fluxes incident on the layer, F_b^+ and F_t^-. We now multiply each side of the Eq. A.1 by the matrix exponential, $e^{-\mathbf{A}z}$, and integrate over the layer from $\tau = 0$ to $\tau = \tau_1$ finding,

$$\mathbf{F}(\tau_1) = e^{\mathbf{A}\tau_1}\mathbf{F}(0) + e^{\mathbf{A}\tau_1}\int_0^{\tau_1} e^{-\mathbf{A}\tau}\mathbf{S}(\tau)d\tau. \tag{A.5}$$

This is known as the propagator form of the solution (Flatau and Stephens, 1988). The form is elegant mathematically, however it contains the desired solution, $F^+(0)$ and $F^-(\tau_1)$, and the boundary conditions, $F^+(\tau_1)$ and $F^-(0)$, on each side of the equation. We, therefore, need to rearrange the solution so that the boundary conditions end up on the right hand side and the unknowns on the left; this form is know as the interaction form of the equation set. To do this, one can use a theorem from matrix calculus (Bronson, 1969; Flatau and Stephens, 1988) to rewrite the matrix exponential; rearranging the solution gives,

$$\begin{bmatrix} F^+(0) \\ F^-(\tau_1) \end{bmatrix} = \begin{bmatrix} t(\tau_1,0) & r(\tau_1,0) \\ r(\tau_1,0) & t(\tau_1,0) \end{bmatrix} \begin{bmatrix} F_b^+ \\ F_t^- \end{bmatrix} + \begin{bmatrix} \sigma^+ \\ \sigma^- \end{bmatrix}. \tag{A.6}$$

The r and t terms are the reflection and transmission functions defined for each local layer and are given in the following numerically stable form (Flatau and Stephens, 1988),

$$\begin{aligned} r(\tau,0) &= r_\infty \frac{(1-e^{-2\kappa\tau})}{1-r_\infty^2 e^{-2\kappa\tau}} \\ t(\tau,0) &= \frac{(1-r_\infty^2)e^{-\kappa\tau}}{1-r_\infty^2 e^{-2\kappa\tau}} \end{aligned} \tag{A.7}$$

where the reflectance for $\tau \to \infty$ is given by $r_\infty = \gamma_2/(\kappa+\gamma_1)$ and the eigenvalue, κ is given by the relation $\kappa = \sqrt{\gamma_1 - \gamma_2}$.

The source functions for the layer, $\sigma^\pm$, are determined by solving the integral in Eq. A.5,

$$e^{\mathbf{A}\tau_1}\int_0^{\tau_1} e^{-\mathbf{A}\tau}\mathbf{S}(\tau)d\tau \tag{A.8}$$

for solar and infrared source terms. The $\sigma^{\pm}$ functions contain this integral plus other terms that originate from the manipulations that produced Eq. A.6. For the case of the solar source function, the integration and rearrangement gives,

$$\begin{bmatrix} \sigma^+ \\ \sigma^- \end{bmatrix} = R \begin{bmatrix} c_s - r(\tau_1,0)d_s & -t(\tau_1,0)c_s \\ -t(\tau_1,0)d_s & d_s c_s - r(\tau_1,0)c_s \end{bmatrix} \begin{bmatrix} e^{-\tau_c/\mu_0} \\ e^{-(\tau_c+\tau_1)/\mu_0} \end{bmatrix} \tag{A.9}$$

where τ_c is the cumulative optical depth of the atmosphere above the layer being considered and the other various coefficients are given as,

$$\begin{aligned} R &= \frac{F_s \omega_0}{\kappa^2 - 1/\mu_0^2} \\ c_s &= \gamma_3(\gamma_1 - 1/\mu_0) + \gamma_4\gamma_2 \end{aligned}$$

and

$$d_s = \gamma_4(\gamma_1 + 1/\mu_0) + \gamma_3\gamma_2. \tag{A.10}$$

Note that the coefficient, R, contains the so-called "resonance" condition which occurs when $\kappa^2 = 1/\mu_0^2$. This condition is avoided by adding an increment, $\epsilon = 1. \times 10^{-6}$, when this denominator becomes small.

The equation of transfer for solar radiation was easily solved as the source function is a known function of τ. This, however, is not true for the infrared source function, in which case we have knowledge only of the source function at the points where the temperature is defined (top and bottom of the layer). For simplicity, we make the assumption that B is a linear function of τ within the layer,

$$B(\tau, T) = B_t + \left(\frac{B_b - B_t}{\tau_1}\right)\tau \tag{A.11}$$

where B_t and B_b are the truncated Planck functions for the top and bottom of the layer, respectively, as determined from the fits given in §2.3. Integration and rearrangement using this infrared source term gives,

$$\begin{bmatrix} \sigma^+ \\ \sigma^- \end{bmatrix} = D \begin{bmatrix} c_i t(\tau_1,0) - d_i r(\tau_1,0) + e_i & -d_i t(\tau_1,0) + c_i r(\tau_1,0) + c_i \\ -d_i t(\tau_1,0) + c_i r(\tau_1,0) + c_i & c_i t(\tau_1,0) - d_i r(\tau_1,0) + e_i \end{bmatrix} \times \begin{bmatrix} B_t \\ B_b \end{bmatrix} \tag{A.12}$$

where the coefficients are given as,

$$\begin{aligned} D &= \frac{\pi U(1-\omega_0)}{\kappa^2} \\ c_i &= 1/\tau_1 \\ d_i &= \gamma_1 + \gamma_2 + 1/\tau_1 \\ e_i &= \gamma_1 + \gamma_2 - 1/\tau_1. \end{aligned} \tag{A.13}$$

The infrared source function approximated as a linear function of optical depth obviously breaks down at small optical depths as some of the above terms can approach infinity as $\tau \to 0$. Simulations over a broad range of optical depths and temperatures seem to show that the limiting value of τ, below which non-physical solutions result, is $\tau_{lim} \simeq 4 \times 10^{-2}$. In these cases, since the Planck function at the top and bottom of the layer are about the same, we approximate the source functions by a simple averaging of the two Planck functions,

$$\begin{bmatrix} \sigma^+ \\ \sigma^- \end{bmatrix} = \pi U \frac{1}{2}(B_t + B_b).$$

Since this condition is rarely encountered in the modelling framework, and it appears to work well when it is encountered, this form appears justified.

Equation A.6 is the solution for the required fluxes at the layer boundaries of a single layer. This solution must now be generalized to the case of many atmospheric layers such as one would encounter in a numerical model. This may be done either by solving a tri-diagonal system or by utilizing the well known adding method (Liou, 1992). Since the method of adding gives a physical picture of the process, we will demonstrate it here for a two-layer system. The generalization to the n-layer system should be obvious. We will use notation here similar to the variables used in the RAMS code for ease of comparison. Many excellent references exist that shed light on adding for many layers; one may consult Liou (1992) for further explanation and examples.

Let us start by examining the two-layer system shown in Fig. A.2. Here, we see that the fluxes for each layer are defined at the model momentum points while the reflection, transmission and source functions are defined between these layers (thermodynamic

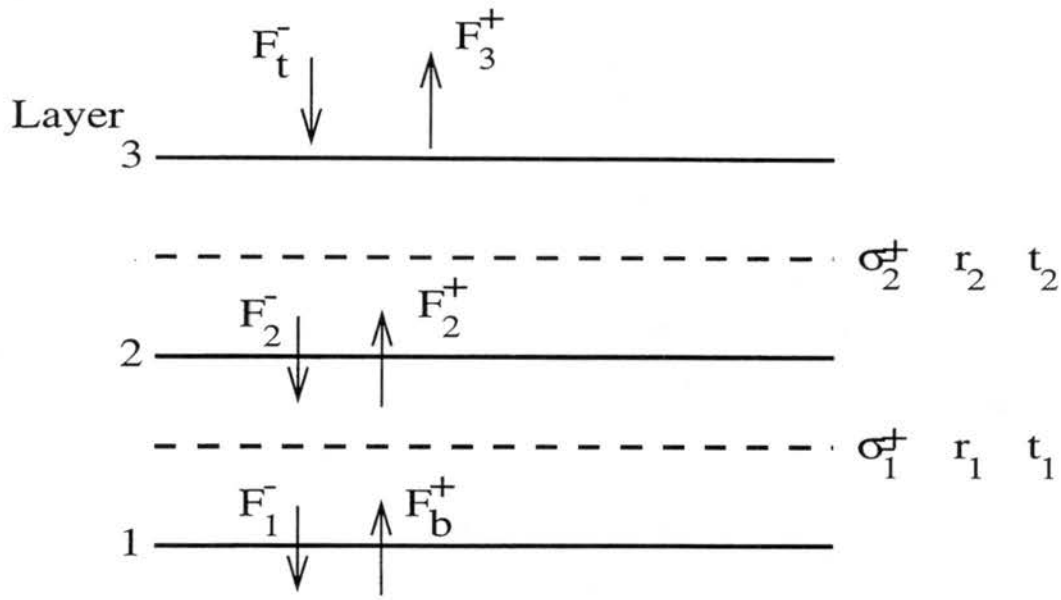

Figure A.2: Two layer system for illustration of the adding method. The boundary conditions are the upwelling flux at the surface, F_b^+, and the downwelling flux at the top, F_t^-.

points). Our goal is to define equations that consider the interactions of the fluxes from each of these levels to produce the final fluxes at each level in terms of the boundary conditions, F_t^- and F_b^+. Ultimately we wish to find the upwelling flux at the top and the downwelling flux at the bottom of a given layer; as our boundary conditions are in terms of the downwelling flux at the top and the upwelling flux at the bottom of the given layer. We will solve for the fluxes at the top and bottom of the lower layer as the resulting expressions are similar to the coded version. We begin by writing out Eq. A.6 for each layer in matrix form. For the top layer we have,

$$\begin{bmatrix} F_3^+ \\ F_2^- \end{bmatrix} = \begin{bmatrix} t_2 & r_2 \\ r_2 & t_2 \end{bmatrix} \begin{bmatrix} F_2^+ \\ F_t^- \end{bmatrix} + \begin{bmatrix} \sigma_2 \\ \sigma_2 \end{bmatrix}. \tag{A.14}$$

For the bottom layer we have,

$$\begin{bmatrix} F_2^+ \\ F_1^- \end{bmatrix} = \begin{bmatrix} t_1 & r_1 \\ r_1 & t_1 \end{bmatrix} \begin{bmatrix} F_b^+ \\ F_2^- \end{bmatrix} + \begin{bmatrix} \sigma_1^+ \\ \sigma_1^- \end{bmatrix}. \tag{A.15}$$

Doing the matrix multiplication we find that the fluxes at each level are coupled and we must rearrange in order to produce a set of equations in terms of the known boundary

conditions. Doing this gives us the following equations for F_2^+ and F_1^-, our fluxes at the top and bottom of the lower layer,

$$\begin{aligned} F_2^+ &= \frac{t_1}{T_d} F_b^+ + V_2^+ \\ F_1^- &= R_e F_b^+ + V_1^- \end{aligned}$$

where we have defined

$$\begin{aligned} T_d &= 1 - r_1 r_2 \\ R_e &= r_2 + \frac{t_2^2 r_1}{T_d} \\ V_2^+ &= \frac{\sigma_1^+}{T_d} + \frac{r_1 \sigma_2^-}{T_d} \\ V_1^- &= \sigma_1^- + \left[\frac{t_1 r_2}{T_d} \sigma_1^+ + \frac{r_1}{T_d} V_2^- \right]. \end{aligned}$$

Note that the upwelling flux at the top of the layer contains two terms; the first is a weighted transmission function multiplying the lower boundary condition while the section contains the contributions from the reflected and transmitted diffuse source terms. The downwelling flux at the base of the layer also contains two terms with the first consisting of a weighted reflection/transmission factor multiplying the lower boundary condition and the second term containing the contributions from the diffuse source terms. The general form of the adding method used for the two-stream model is quite similar to the above example and may be written in the following form for a layer bounded by n and $n-1$,

$$\begin{aligned} F_n^+ &= \frac{t_n}{T_d^{(n)}} F_{n-1}^+ + V_{n-1}^+ \\ F_{n-1}^- &= R_e^{(n-1)} F_{n-1}^+ + V_{n-1}^- \end{aligned}$$

where we have defined

$$\begin{aligned} T_d^{(n)} &= 1 - R_e^{(n)} r_n \\ R_e^{(n-1)} &= r_n + \frac{t_n^2 R_e^{(n)}}{T_d^{(n)}} \\ V_{n-1}^+ &= \frac{\sigma_n^+}{T_d^{(n)}} + \frac{r_n V_n^-}{T_d^{(n)}} \\ V_{n-1}^- &= \sigma_n^- + \left[\frac{t_n R_e^{(n)}}{T_d^{(n)}} \sigma_n^+ + \frac{r_n}{T_d^{(n)}} V_n^- \right]. \end{aligned}$$

Again we see that the upwelling and downwelling fluxes at the layer boundaries are computed in terms of combined reflection and transmission functions that include the contributions from the multiple reflections of diffuse radiation.

Appendix B

GASEOUS ABSORPTION, RAYLEIGH SCATTERING AND CONTINUUM ABSORPTION

In a numerical model, it is important to capture all of the major features of absorption and emission by gases without having to resort to complex line by line computations. To reduce computational costs, one normally computes the fluxes in an absorbing and scattering atmosphere within broad-bands. These broad-bands cover a given range of wavelength space, the scattering and absorbing properties calculated in some appropriate manner for the gases and particulates active within that band.

The version of the model currently in use has the same band structure as Ritter and Geleyn (1992), the wavelength limits of which are listed in Table B. There are 3 solar bands covering the solar, $\lambda = 0.245 \rightarrow 0.7\mu m$, and near-IR, $\lambda = 0.7 \rightarrow 4.64\mu m$, regions of the spectra. The IR region begins in our model at $4.64\mu m$ and extends to $104\mu m$; the energy at wavelengths larger than this is insignificant for our purposes. The spectra given above is divided up according to specific gaseous and cloud hydrometeor scattering and absorbing characteristics (Table B). This table also serves as illustration of the gases that absorb within each band in the two-stream model. The issue of these absorption coefficients will be addressed shortly.

The emission source function for the IR two-stream equation as parameterized by Eq. A.4 requires knowledge of the band-integrated Planck function. This truncated integral is expensive to compute, thus we utilize code developed by Piotr Flatau (personal communication) to fit the Planck function integrated over each band with a third order polynomial in temperature (180 to 320 K),

$$B(\tau, T) = b_0 + b_1 T + b_2 T^2 + b_3 T^3, \tag{B.1}$$

Band	1	2	3	4	5	6	7	8
λ_{low}	1.53	0.7	0.245	20.0	12.5	8.33	9.01	4.64
λ_{high}	4.64	1.53	0.7	104.0	20.0	9.01	10.3	8.33
k_{H_2O}	5	5	1	5	4	2	2	5
k_{CO_2}	3	1	1	0	4	1	1	1
k_{O_3}	0	0	3	0	0	0	3	0

Table B.1: Radiation Band Structure. Given are the wavelength limits for each band and the number of gaseous absorption coefficients, k, for each gas that absorbs in the band.

where the coefficients, b_0 to b_3, are determined from the fit. Values for these coefficients are give in Table B.

The treatment of the gaseous absorption coefficients for each band follows Ritter and Geleyn's (1992) method of exponential sum fitting of transmission functions. In this method, the gaseous absorption problem is treated by finding fits to the transmission function for a given gas, within a certain spectral interval, $\Delta\lambda$, at a reference temperature, T_0, and pressure, P_0:

$$T_{\Delta\lambda}(u) = \sum_{i=1}^{N_p} w_i e^{-k_i u} \tag{B.2}$$

where u is the path length (gas amount) in Pascals, N_p is the number of terms in the fit, w_i is the weight and k_i is the "pseudo"-absorption coefficient. Inhomogeneous paths are treated by varying the temperature and pressure to produce new transmission data. This is subsequently fit by modifying the k_i term in the exponential,

$$\begin{aligned} T_{\Delta\lambda}(u) &= \sum_{i=1}^{N_p} w_i e^{\tau_i(P,T,u)} \\ \tau_i(P,T,u) &= -k_i \left(\frac{P}{P_0}\right)^{\alpha_i} \left(\frac{T_0}{T}\right)^{\beta_i} u \end{aligned} \tag{B.3}$$

where α_i and β_i are the fit coefficients for variations of pressure and temperature along a given path. This method may be used for any set of specific model band widths; Table B lists the number of terms in the fit for each gas. Ritter and Geleyn (1992) use more terms in their fits, up to 7 for strongly absorbing gases, as compared to our maximum number of 5. We have found that by using a sophisticated fitting routine we can produce the same accuracy with less terms in the fits. We have also compromised our accuracy somewhat

here by using only one pseudo-absorption coefficient for many of the weakly absorbing gases. Reducing the number of terms in the fits is of paramount importance as we are able to pick up a factor of about 4 in computation speed with the reduced number of terms. Figure B.1 shows the heating rates computed with extremely accurate fits containing many terms as compared to the fits given in Table B. We should note here that the comparison

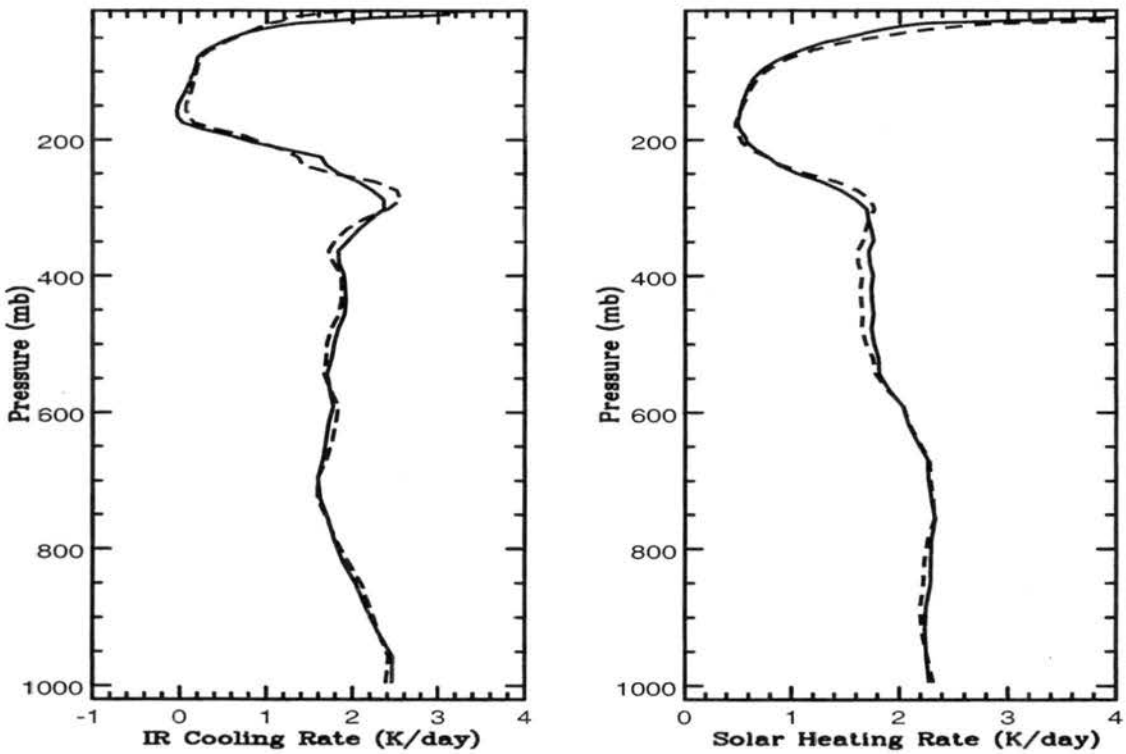

Figure B.1: Comparison of the solar and infrared heating rates for ESFT with accurate absorption (solid line) to FESFT with reduced number of absorption coefficients (dashed line).

is also between the ESFT and FESFT methods described below so the comparison is not strictly between the data with larger number of terms in the fits to our above tabulated values. However, almost all of the deviation shown in Fig. B.1 is due to the reduction in the number of pseudo-absorption coefficients. This computation was done for a mid-latitude summer atmosphere of McLatchy (1970) at a solar zenith angle of $\theta_0 = 30°$. Note the small error between the heating rates computed with the lower number of fit terms. This is corroborated by Fig. B.2 for the fluxes, showing that the error in the fluxes by using significantly less terms in the fits to the spectral transmission functions is quite small.

Band	4	5	6	7	8
b_0	1.073	37.41	18.45	6.12	-106.96
b_1	-9.042×10^{-2}	-0.539	-0.162	-2.418×10^{-2}	1.602
b_2	9.553×10^{-4}	2.219×10^{-3}	-1.201×10^{-5}	-3.281×10^{-4}	-8.145×10^{-2}
b_3	-8.219×10^{-7}	-1.149×10^{-6}	2.1481×10^{-5}	1.612×10^{-6}	1.415×10^{-5}

Table B.2: Planck function fit coefficients.

Once the transmission functions fits are found for each gas and within each band, then the fluxes may be computed. Let us define a two-stream solver as $F^{\pm}_{2s}(\tau)$ which uses as input the optical properties of a given layer and produces the upwelling and downwelling fluxes at some height, z; this is of course a function of other things but, for our illustrative purposes, τ is all that is needed. The standard method to compute the fluxes at an arbitrary model level, z, for a band that has n-overlapping gases is the following,

$$F^{\pm}(z) = \sum_{i1}^{N_1}\sum_{i2}^{N_2}\cdots\sum_{in}^{N_n}[w_{i1}w_{i2}\cdots w_{in}F^{\pm}_{2s}(\tau_g + \tau_{i1} + \tau_{i2} + \cdots + \tau_{in}). \tag{B.4}$$

where $w_{i,n}$ is the weight from the transmission fits for gas n. Of course, this is quite computationally cumbersome even for as few as 3 overlapping gases since the number of required solutions of the two-stream equations is $N_1 \times N_2 \times \cdots \times N_n$. To reduce cost, we employ a method of effective transmission functions (the FESFT method in Ritter and Geleyn, 1992). This method approximates the flux solution by making a substitution of variables and then dropping the small terms (see Edwards, 1996 for a full discussion of the method). Consider two gases of optical depths τ_1 and τ_2 and say that there exists some cloud hydrometeors that are considered grey (independent of wavelength across the band) given by τ_g.

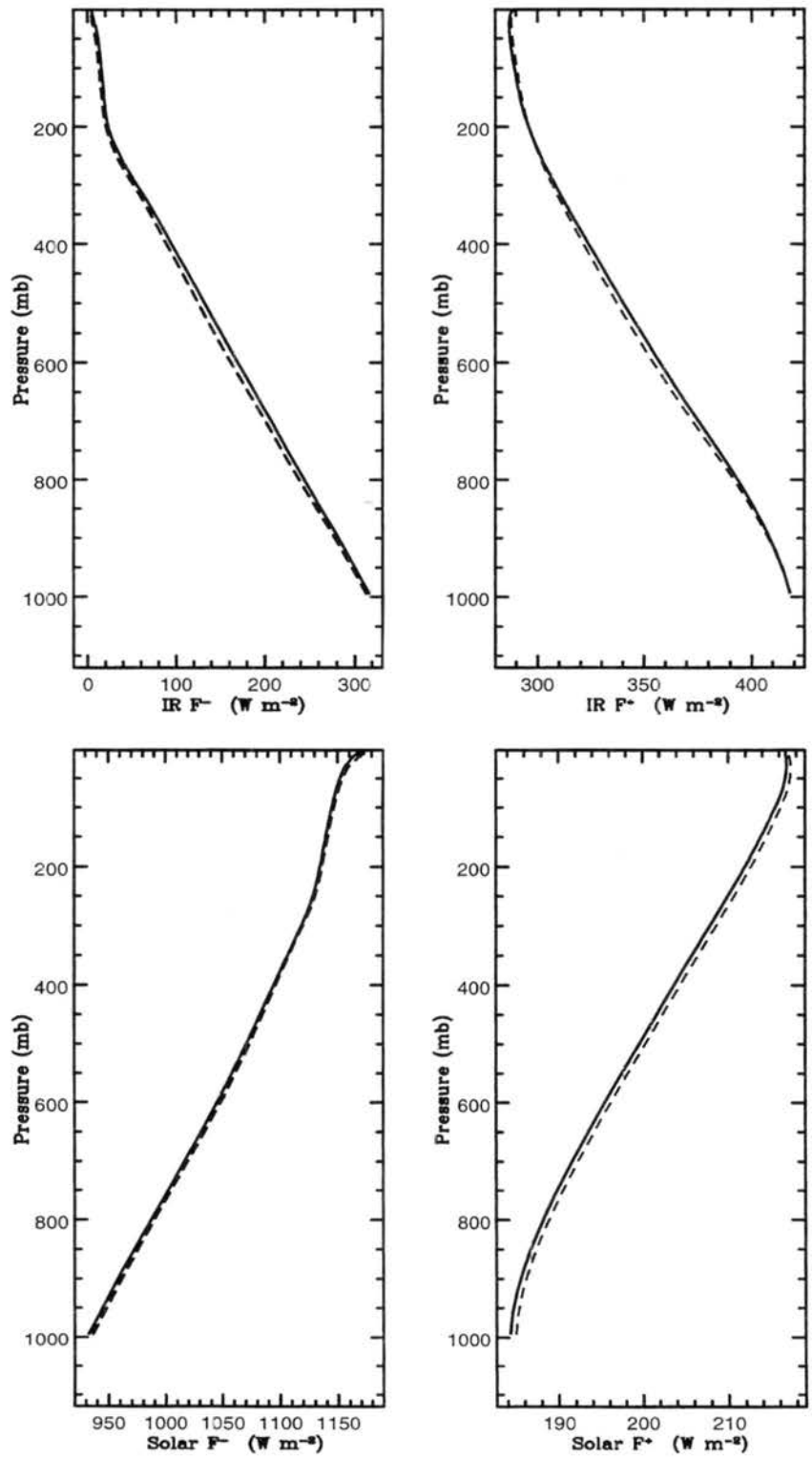

Figure B.2: Comparison of the fluxes for ESFT with accurate absorption (solid lines) and FESFT with reduced number of absorption coefficients (dashed lines). Upwelling and downwelling solar and infrared fluxes are shown for a mid-latitude McLatchy (1970) atmosphere are shown.

One then considers separating the fluxes for each gas by using a substitution that is multiplicative,

$$\begin{aligned} F_n^{\pm} &\equiv \frac{F^{\pm}(\tau_1+\tau_g)}{F^{\pm}(\tau_g)} F^{\pm}(\tau_2+\tau_g) \\ &= \frac{F_1^{\pm}}{F_g^{\pm}} F_2^{\pm} \\ &= \left(\frac{F_1^{\pm}}{F_g^{\pm}}\right)\left(\frac{F_2^{\pm}}{F_g^{\pm}}\right) F_g^{\pm} \\ &= T_1^{\pm} T_2^{\pm} F_g^{\pm} \end{aligned} \tag{B.5}$$

where we define the effective transmission functions for the upwelling and downwelling fluxes in terms of the T functions given above. Note the difference in definition as compared to a standard transmission function. If one rearranges the two-stream equations so that the equations are in terms of the newly defined flux matrix $\mathbf{F}_n$ then we find,

$$\mathbf{F}_n = \mathbf{A}\mathbf{F}_n + \mathbf{S} + \mathbf{R}, \tag{B.6}$$

where $\mathbf{R}$ contains the extra terms after the change of variables. If the switch in variables had produced an equation without this $\mathbf{R}$ term, then the methods of FESFT and ESFT would be equivalent. Fortunately, as is stated in Edwards (1996), this $\mathbf{R}$ term is quite small and may be neglected to a good approximation. The neglect of this term allows us to write the fluxes for many overlapping gases in a band as,

$$F^{\pm}(z) = (T_1^{\pm} T_2^{\pm} \cdots T_n^{\pm}) F_g^{\pm} \tag{B.7}$$

for the solar bands and

$$\begin{aligned} F^{-}(z) &= (T_1^{-} T_2^{-} \cdots T_n^{-}) F_g^{-} \\ \bar{F}(z) &= (\bar{T}_1 \bar{T}_2 \cdots \bar{T}_n) \bar{F}_g \end{aligned} \tag{B.8}$$

for the infrared bands. Note that the $\bar{F}$ is the net flux and $\bar{T}_i$ is the net transmission function for the i^{th} gas. As per the above example for two gases, the effective transmission functions for the i^{th} gas is defined as,

$$T_i = \frac{\sum_j^{N_i} w_j F_{2s}(\tau_g + \tau_j)}{F_g}. \tag{B.9}$$

In the case of solar radiation we may use the method for both the upwelling and the downwelling fluxes, however, in the case of infrared radiation we may only use the method for the downwelling flux and the net flux. It is quite fortunate that we can compute the downwelling fluxes in addition to the net fluxes in the infrared with this method, since the fluxes themselves are needed for other computations (such as vapor deposition enhancement/suppression). For a discussion of the effectiveness of this method, we refer the reader to Edwards (1996).

The advantage of the FESFT method is that the number of solutions required is now $1 + N_1 + N_2 + \cdot + N_n$ for n-gases. This results in about an order of magnitude decrease in computational cost as compared to the more accurate ESFT method. The FESFT method may produce unrealistic values for both the solar and the infrared bands. In the solar, F_g is never zero but T_i can become greater than one in some cases. A first examination may suggest that the T_i functions should be bounded between 0 and 1, however, we have run into cloud cases in which using values of the T_i functions that are greater than 1 give better results as compared to the explicit method given by Eq. B.4. Experimentation has shown that bounding the T_is between 0 and 1.1 give very accurate results for many cloud test cases.

In the infrared region of the spectrum, we have the possibility that $\bar{T}_i$ can become greater than 1 by virtue of $\bar{F}_g \to 0$. Experimentation has shown that if we bound $\bar{F}_g$ to be greater than some small value and if we bound the effective transmission between -1 and $+1$ we are able to produce excellent accuracy over a variety of test cases. Computations with FESFT as compared to ESFT show that FESFT is quite accurate with errors in the fluxes is less than 1 Wm^{-2}. Figures B.1 and B.2 are illustrative of the accuracy of FESFT coupled with a set of drastically reduced number of absorption coefficients which produces over an order of magnitude reduction in computational costs.

B.1 Rayleigh scattering and continuum absorption

The properties of Rayleigh scattering and continuum absorption are treated as grey properties and parameterized in the following manner. The effects of Rayleigh scattering

are computed via a simple formula as suggested by Slingo and Schrecker (1982). For each solar band, i_s, the Rayleigh optical depth is found by applying the formula,

$$\tau_{Ray,i_s} = C_{Ray,i_s} \Delta z \frac{P}{T} \tag{B.10}$$

where $\beta_{Ray,i_s} = C_{Ray,i_s} \frac{P}{T}$ is the Rayleigh volume extinction coefficient integrated over the band, i_s, and weighted with the amount of solar energy per wavelength.

The effects of the water vapor continuum in the 8 to 12μm window region is parameterized by utilizing the formula given in Liou (1992). The band integrated form of this equation is given by,

$$\begin{aligned} \tau_{con} &= \sigma_{con}[e_v + 0.002(P - e_v)] exp\left[c\frac{T_r}{T} - c\right] \\ \sigma_{con} &= \frac{\int_{\Delta\lambda}(a + be^{-\beta\nu})B(\lambda, T_r)d\lambda}{\int_{\Delta\lambda} B(\lambda, T_r)d\lambda} \end{aligned} \tag{B.11}$$

where e_v is the vapor pressure of pure water, $c = 6.08$, $T_r = 296K$, $a = 4.18$, $b = 5578$, $\beta = 7.87 \times 10^{-3}$, ν is the wavenumber in cm^-1, and $B(\lambda, T_r)$ is the Planck function evaluated at T_r.

References

Ackermann, Andrew S., Owen B. Toon, and Peter V. Hobbs, 1993: Dissipation of marine stratiform clouds and collapse of the marine boundary layer due to the depletion of cloud condensation nuclei by clouds. *Science*, **262**, 226-229.

Ackermann, Andrew S., Owen B. Toon, and Peter V. Hobbs 1995: A model for particle microphysics, turbulent mixing and radiative transfer in the stratocumulus-topped marine boundary layer and comparisons with measurements. *J. Atmos. Sci.*, **52**, 1204-1236.

Albrecht, Bruce A., 1989: Aerosols, cloud microphysics and fractional cloudiness. *Science*, **245**, 1227-1230.

Ambromowitz, Milton, and Irene A. Stegun, 1972: *Handbook of Mathematical Functions.* Dover Publications, New York, 1046pp.

Austin, P. H., S. Siems, and Y. Wang 1995: Constraints on droplet growth in radiatively cooled stratocumulus. *J. Geophys. Res.*, **100**, 14231-14242.

Barkstrom, Bruce R., 1978: Some effects of 8-12μm radiant energy transfer on the mass and heat budgets of cloud droplets. *J. Atmos. Sci.*, **35** ,665-673

Beard, K. V., and H. T. Ochs, 1993: Warm-rain initiation: An overview of microphysical mechanisms. *J. Appl. Meteor.*, **32**, 608-625.

Berry, Edwin X. and Richard L. Reinhardt, 1974: An analysis of cloud drop growth by collection: Part I. Double distributions. *J. Atmos. Sci.*, **31**, 1814-1824.

Bohren, Craig F., 1987: *Clouds in a glass of beer.* Wiley Science Editions, 195 pp.

Borys, Randolph D., Studies of ice nucleation by Arctic aerosol on AGASP-II. *J. Atmos. Chem.*, **9**, 169-185.

Bott, A., U. Sievers, and W. Zdunkowski 1990: A radiation fog model with a detailed treatment of the interaction between radiative transfer and fog microphysics. J. Atmos. Sci., 47, 2153-2166.

Bougeault, Philippe, 1985: The diurnal cycle of the marine stratocumulus layer: A higher-order model study. *J. Atmos. Sci.*, **42**, 2826-2843.

Bronson, 1969: *Matrix Methods: An Introduction.* Academic Press, 284pp.

Chandresakar, 1960: *Radiative Transfer.* Dover Publications, New York, 393pp.

Clark, Terry L., 1973: Numerical modeling of the dynamics and microphysics of warm cumulus convection. *J. Atmos. Sci.*, **30**, 857-878.

Clark, Terry L., 1974: On modelling nucleation and condensation theory in Eulerian spatial domain. *J. Atmos. Sci.*, **31**, 2099-2117.

Coakly, James A. and Petr Chylek, 1975: The two-stream approximation in radiative transfer: Including the angle of the incident radiation. *J. Atmos. Sci.*, **32**, 409-428.

Curry, J. A., and G. F. Herman, 1985a: Infrared radiative properties of summertime Arctic stratus clouds. *J. Climate Appl. Meteo.*, **24**, 525-538.

Curry, J. A., and G. F. Herman, 1985b: Relationship between large-scale heat and moisture budgets and the occurrence of Arctic stratus clouds. *Mon. Wea. Rev.*, **113**, 1441-1457.

Curry, Judith A. 1986: Interactions among turbulence, radiation and microphysics in Arctic stratus clouds. J. Atmos. Sci., 43, 90-106.

Curry, J. A., E. E. Ebert, and G. F. Herman 1988: Mean and turbulence structure of the summertime Arctic cloudy boundary layer. Quart. J. R. Met. Soc., 114, 715-746.

Curry, J. A., F. G. Meyer, L. F. Radke, C. A. Brock, and E. E. Ebert, 1990: Occurrence and characteristics of lower tropospheric ice crystals in the Arctic. *International J. Climatology*, **10**, 749-764.

Curry, Judith A. and Elizabeth E. Ebert, 1992: Annual cycle of radiation fluxes over the Arctic Ocean: Sensitivity to cloud optical properties. *J. Climate*, **5**, 1267-1280.

Curry, J. A., J. L. Schramm, and E. E. Ebert, 1993: Impacts of clouds on the surface radiation balance of the Arctic ocean. *Meteo. Atmos. Phys.*, **51**, 197-217.

Curry, Judith A., 1995: Interactions among aerosols, clouds, and climate of the Arctic Ocean. *Sci. Total Env.*, **160**,777-791.

Curry, Judith A., William B. Rossow, David Randall, and Julie L. Schramm 1996: Overview of Arctic cloud and radiation characteristics. J. Climate, 9, 1731-1764.

Deardorff, James W., 1981: On the distribution of mean radiative cooling at the top of a stratocumulus-capped mixed layer. *Q. J. R. Meteorol. Soc.*, **107**, 191-202.

Dergach, A.L., G.M. Zabrodsky, and V.G. Morachevsky, 1960: The results of a complex investigation of the type st-sc clouds and fogs in the Arctic. *Bull. Acad. Sci. USSR, Geophys. Ser.*, **1**, 66-70.

Dümenil, L. and S. Schröder, 1989: The impact of an ice-free Arctic ocean on the general circulation in winter. Research Activities in atmospheric and oceanic modelling no. 13, WMO/TD no. 332, WMO, GEneva, 7.42-7.43.

Ebert, Elizabeth E. and Judith A. Curry, 1992: A parameterization of ice cloud optical properties for climate models, *J. Geophys. Res.*, **97**, 3831-3836.

Ebert, Elizabeth E. and Judith A. Curry, 1993: An intermediate one-dimensional thermodynamic sea ice model for investigating ice-atmosphere interactions. *J. Geophys. Res.*, **98**, 10085-10109.

Eddington, A.S., 1916: On the radiative equilibrium of the stars. *Mon. Not. Roy. Astronom. Soc.*, **77**, 16-35.

Edwards, J.M., 1996: Efficient calculation of infrared fluxes and cooling rates using the two-stream equations. *J. Atmos. Sci.*, **53**, 1921-1932.

Feingold, G., S. Tzivion, and Z. Levin, 1988: The evolution of raindrop spectra. Part I: Stochastic collection and breakup. J. Atmos. Sci., 45, 3387-3399.

Feingold, G., B. Stevens, W.R. Cotton, and R.L. Walko, 1994: An explicit cloud microphysics/LES model designed to simulate the Twomey effect. *Atmos. Res.*, **33**, 207-233.

Feingold, Graham, Bjorn Stevens, W.R. Cotton, and A.S. Frisch, 1996a: The relationship between drop in-cloud residence time and drizzle production in numerically simulated stratocumulus clouds. *J. Atmos. Sci.*, **53**, 1108-1122.

Feingold, Graham, Sonia M. Kreidenweis, Bjorn Stevens, and W.R. Cotton, 1996b: Numerical simulations of stratocumulus processing of cloud condensation nuclei through collision-coalescence. *J. Geophys. Res.*, **101**, 21,391-21,402.

Feingold, Graham, R.L. Walko, Bjorn Stevens, and W.R. Cotton, 1997: Simulations of marine stratocumulus using a new microphysical parameterization scheme. Submitted to *Atmos. Res.*

Ferrier, Brad Schoenberg, 1994: A double-moment multi-phase four-class bulk ice scheme. Part I; Description. *J. Atmos. Sci.*, **51**, 249-280.

Finger, Jörg E. and Peter Wendling, 1990: Turbulent structure of Arctic stratus clouds derived from measurements and calculations. *J. Atmos. Sci.*, **47**, 1351-1373.

Flatau, P.J., and G.L. Stephens, 1988: On the fundamental solution of the radiative transfer equation. *J. Geophys. Res.*, **93** 2134-2156.

Flatau, Piotr J., 1992: *Scattering by Irregular Particles in Anomalous Diffraction and Discrete Dipole Approximations.* Ph.D. dissertation, Colorado State University, Fort Collins Colorado, USA, 140pp.

Frisch, A.S., C.W. Fairall, and J.B. Snider, 1995: Measurement of stratus cloud and drizzle parameters in ASTEX with a K_α-band doppler radar and a microwave radiometer. *J. Atmos. Sci.*, **52**, 2788-2799.

Fu. Qiang and K.N. Liou, 1992: Parameterization of the radiative properties of cirrus clouds. *J. Atmos. Sci.*, **50**, 2008-2025.

Fuchs, N. A., 1959: *Evaporation and droplet growth in gaseous media.* Pergamon Press, 72pp.

Gabriel, Philip, Jerry Y. Harrington, Graeme L. Stephens, and Timothy Schneider, 1997: Adjoint Perturbation method applied to two-stream radiative transfer. *J. Quant. Spectros. Rad. Trans.*, Accepted.

Gabriel, Philip, Philip Partain, and Graeme L. Stephens, 1998: Refinement, Validation and Application of Cloud-Radiation Parameterizations in a GCM. In preparation for *J. Atmos. Sci.*

Guzzi, Rodolfo and Rolando Rizzi, 1980: The effect of radiative exchange on the growth of a population of droplets. *Contrib. Atmos. Phys.*, **53**, 351-365.

Harshvardhan and Michael D. King, 1992: Comparative accuracy of diffuse radiative properties computed using selected multiple scattering approximations. *J. Atmos. Sci.*, **50**, 247-259

Harrington, Jerry Y., Michael P. Meyers, Robert L. Walko, and William R. Cotton, 1995: Parameterization of ice crystal conversion processes due to vapor deposition for mesoscale models using double-moment basis functions. Part I: Basic formulation and parcel model results. *J. Atmos. Sci.*, **52**, 4344-4366.

Hegg, Dean A., Ronald J. Ferek, and Peter V. Hobbs, 1995: Cloud condensation nuclei over the Arctic Ocean in early spring. *J. Appl. Meteo.*, **34**, 2076-2082.

Herman, Gerald and Richard Goody, 1976: Formation and persistence of summertime Arctic stratus clouds. *J. Atmos. Sci.*, **33**, 1537-1554.

Herman, G. F., 1980: Thermal radiation in Arctic stratus clouds. *Quart. J. R. Met. Soc.*, **106**, 771-780.

Herman, G. F. and J. A. Curry, 1984: Observational and theoretical studies of solar radiation in Arctic stratus clouds. *J. Climate and Appl. Meteo.*, **23**, 5-24.

Hu, Y.X., and K. Stamnes, 1993: An accurate parameterization of the radiative properties of water clouds suitable for use in climate models. *J. Climate*, **6**, 728-742.

Jayaweera, Kolf, and T. Ohtake, 1973: Concentration of ice crystals in Arctic stratus clouds. *J. De Recherches Atmospheriques*, **9**, 199-207.

Joseph, J.H., W.J. Wiscombe, and J.A. Weinman, 1976: The Delta-Eddington Approximation for Radiative Flux Transfer. *J. Atmos. Sci.*, **33**, 2452-2459.

King, Michael D., and Harshvardhan, 1986: Comparative accuracy of selected multiple scattering approximations. *J. Atmos. Sci.*, **43**, 784-801.

Kogan, Y. L., M. P. Khairoutdinov, D. K. Lilly, Z. N. Kogan, and Qingfu Liu, 1995: Modeling of stratocumulus cloud layers in a large eddy simulation model with explicit microphysics. *J. Atmos. Sci.*, **52**, 2923-2940.

Liou, K.N., 1992: *Radiation and Cloud Processes in the Atmosphere.* Oxford University Press, New York, 487pp.

McDonald, James E., 1958: Nomenclature of phase change. *J. Chem. Ed.*, **35**, 205-206.

McInnes, Kathleen L. and Judith A. Curry, 1995: Modelling the mean and turbulent structure of the summertime Arctic cloudy boundary layer. *Boundary-Layer Meteo.*, **73**, 125-143.

Meador, W.E. and W.R. Weaver, 1980: Two-stream approximations to radiative transfer in planetary atmospheres: A unified description of existing methods and a new improvement. *J. Atmos. Sci.*, **37**, 630-643.

Meyers, Michael P., Paul J. Demott, and William R. Cotton, 1992: New primary ice-nucleation parameterizations in an explicit cloud model. *J. Appl. Meteo.*, **31**, 708-721.

Meyers, Michael P., Robert L. Walko, Jerry Y. Harrington and William R. Cotton, 1997: New RAMS cloud microphysics parameterization. Part II: The two-moment scheme. Accepted to *Atmos. Res.*

Mitchell, David L., and W. Patrick Arnott, 1994: A model predicting the evolution of ice particle size spectra and radiative properties of cirrus clouds. Part II: Dependence of absorption and extinction on ice crystal morphology. *J. Atmos. Sci.*, **51**, 817-832.

Mitchell, David L., Andreas Macke, and Yangang Liu, 1996: Modeling cirrus clouds. Part II: Treatment of radiative properties. *J. Atmos. Sci.*, **53**, 2967-2988.

Mitchell, L. David, 1997: Parameterization of the Mie extinction and absorption coefficients: A process oriented approach. Submitted to *Applied Optics.*

Nicholls, S., 1988: The structure of radiatively driven convection in stratocumulus. *Q. J. R. Meteorol. Soc.*, **115** , 487-511.

Ohtake, Takeshi, Kolf Jayaweera, and Ken-Ichi Sakurai, 1982: Observation of ice crystal formation in the lower Arctic atmosphere. *J. Atmos. Sci.*, **39**, 2898-2902.

Olsson, Peter Q., Jerry Y. Harrington, Graham Feingold, William R. Cotton, and Sonia M. Kreidenweis, 1997: Exploratory cloud resolving simulations of Arctic stratus clouds. Part I: Warm season clouds. Submitted to *Atmos. Res.*

Pielke, R.A., W.R. Cotton, R.L. Walko, C.J. Tremback, W.A. Lyons, L.D. Grasso, M.E. Nicholls, M.D. Moran, D.A. Wesley, T.J. Lee, and J.H. Copeland, 1992: A comprehensive meteorological modeling system- RAMS. *Meteorol. Atmos. Phys.*, **49**, 69-91.

Pinto, James O., Judith A. Curry and Kathleen L. McInnes, 1995: Atmospheric convective plumes emanating from leads 1. Thermodynamic structure. *J. Geophys. Res.*, **100**, 4621-4631.

Pinto, James O., and Judith A. Curry, 1995: Atmospheric convective plumes emanating from leads 2. Microphysical and radiative processes. *J. Geophys. Res.*, **100**, 4663-4642.

Pinto, James O., 1997: Autumnal mixed-phase cloudy boundary layers in the Arctic. *J. Atmos. Sci.*, Submitted.

Potter, John F., 1970: The delta function approximation in radiative transfer theory. *J. Atmos. Sci.*, **27**, 943-949.

Pruppacher, Hans R. and James D. Klett 1997: *Microphysics of Clouds and Precipitation.* Kluwer Academic Publishers, Boston, 954pp.

Reisin, T., Z. Levin, and S. Tzivion, 1996: Rain production in convective clouds as simulated in an axisymmetric model with detailed microphysics. Part I: Description of the model. *J. Atmos. Sci.*, **53**, 497-519.

Ritter, Bodo and Jean-Francois Geleyn, 1992: A comprehensive radiation scheme for numerical weather prediction models with potential applications in climate simulations. *Mon. Wea. Rev.*, *120*, 303-325.

Roach, W.T., 1976: On the effect of radiative exchange on the growth by condensation of a cloud or fog droplet. Quart. J. R. Met. Soc., 102, 361-372.

Royer, J. F., S. Planton, and M. Deque, 1990: A sensitivity experiment for the removal of Arctic sea ice with the French spectral general circulation model. *Climate Dynamics*, **5**, 1-17.

Russell, Bertrand, 1952: *The Problems of Philosophy.* Oxford University Press, Oxford, 167pp.

Schuster, Arthur, 1905: Radiation through a foggy atmosphere. *Astrophysical Journal*, **21**, 1-22.

Shaw, G. E., 1986: Aerosols in Alaskan air masses. *J. Atmos. Chem.*, **4**, 157-171.

Slingo, A. and H.M. Schrecker, 1982: On the shortwave properties of stratiform water clouds. *Q. J. R. Meteorol. Soc.*, **108**, 407-426.

Slingo, A., 1989: A GCM parameterization for shortwave radiative properties of water clouds. *J. Atmos. Sci.*, **46**, 1419-1427.

Smith, W.S., and C.-Y. J. Kao, 1996: Numerical simulation of observed Arctic stratus clouds using a second-order turbulence closure model. *J. Appl. Meteorol.*,**35**, 47-59.

Stephens, G.L., 1978: Radiation profiles in extended water clouds. II: Parameterization schemes. *J. Atmos. Sci.*, **35**, 2123-2132.

Stephens, Graeme L., 1983: The influence of radiative transfer on the mass and heat budgets of ice crystals falling in the atmosphere. *J. Atmos. Sci.*, **40**, 1729-1739.

Stevens, Bjorn, Graham Feingold, Robert L. Walko, and William R. Cotton, 1996a: The spurious production of cloud-edge supersaturations by Eulerian models. *Mon. Wea. Rev.*, **124**, 1034-1041.

Stevens, B., G. Feingold, W.R. Cotton. and R.L. Walko, 1996b: Elements of the microphysical structure of numerically simulated nonprecipitating stratocumulus. *J. Atmos. Sci.*, **53**, 980-1006.

Stevens, Bjorn, 1996: *On the Dynamics of Precipitating Stratocumulus.* Ph.D. dissertation, Colorado State University, Fort Collins Colorado, USA, 140pp.

Stackhouse, Paul W. and Graeme L. Stephens, 1991: A theoretical and observational study of the radiative properties of cirrus: Results from FIRE 1986. *J. Atmos. Sci.*, **48**,2044-2059.

Takano, Yoshihide and Luo-Nan Liou, 1989: Solar radiative transfer in cirrus clouds. Part I: Single-scattering and optical properties of hexagonal ice crystals. *J. Atmos. Sci.*, **46**, 3-19.

Thomas, J.W., 1995: *Numerical Partial Differential Equations: Finite Difference Methods.* Springer, New York, 437pp.

Tsay, Si-Chee and Kolf Jayaweera, 1984: Physical characteristics of Arctic stratus clouds. *J. Climate Appl. Meteo.*, **23**, 584-596.

Tzivion (Tzitzvashvili), Shalva, Graham Feingold, and Zev Levin, 1989: The evolution of raindrop spectra. Part II: Collisional collection/breakup and evaporation in a rainshaft. *J. Atmos. Sci.*, **46**, 3312-3327.

van de Hulst, H.C., 1957: *Light Scattering by Small Particles.* Dover Publications, New York, 470pp.

Walko, R.L., W.R. Cotton, M.P. Meyers, and J.L. Harrington, 1995: New RAMS cloud microphysics parameterization. Part I: the single-moment scheme. Atmos. Res., 38, 29-62.

Walsh, J.E. and R.G. Crane 1992: A comparison of GCM simulations of Arctic climate. *Geophys. Res. Lett.*, **19**, 29-32.

Wiscombe, W.J., 1977: The delta-M method: rapid yet accurate radiative flux calculations for strongly asymmetric phase functions. *J. Atmos. Sci.*, **34**, 1408-1422.

Wielicki B.A., J.T. Suttles, A.J. Heymsfield, R.M. Welch, J.D. Spinhirne, M.-L. C. Wu, D. O'C. Starr, L. Parker and R.F. Arduini, 1990: The 27-28 October 1986 FIRE IFO cirrus case study: Comparison of radiative transfer theory with observations by satellite and aircraft. *Mon. Wea. Rev.*, **118**, 2356-2376.

Witte, H.J., 1968: *Airborne Observations of Cloud Particles and Infrared Flux Density in the Arctic.* MS Thesis, Dept. of Atmospheric Sciences, University of Washington. 102 pp.

Zdunkowski, Wilford G., Ronald M. Welch, and Gunther Korb, 1980: An Investigation of the Structure of Typical Two-Stream Methods for the Calculation of Solar Fluxes and Heating Rates in Clouds. *Contrib. Atmos. Phys.*, **53**, 147-166.